ATOMIC STRUCTURE AND NONELECTRONIC PROPERTIES
OF SEMICONDUCTORS

Thermodynamic Stability of Bulk and Epitaxial CdHgTe, ZnHgTe, and MnHgTe Alloys

V. G. Deĭbuk^, S. G. Dremlyuzhenko, and S. É. Ostapov^^

Fed'kovich National University, ul. Kotsyubinskogo 2, Chernovtsy, 58012 Ukraine

^*e-mail: vdei@chnu.cv.ua*

^^*e-mail: sergey.ostapov@gmail.com*

Submitted January 13, 2005; accepted for publication February 7, 2005

Abstract—The thermodynamic stability of $Cd_{1-x}Hg_xTe$, $Mn_xHg_{1-x}Te$, and $Zn_xHg_{1-x}Te$ alloys is studied. Calculations performed in the context of the δ lattice-parameter model indicate that CdHgTe and ZnHgTe alloys are stable over the entire range of compositions at typical growth temperatures. At the same time, a miscibility gap is found in $Mn_xHg_{1-x}Te$ at $0.33 < x < 1$ at $T = 950$ K, which is consistent with the known experimental data. It is shown that the biaxial strains observed in $Mn_xHg_{1-x}Te/CdTe$ and $Mn_xHg_{1-x}Te/Cd_{0.96}Zn_{0.04}Te$ thin epitaxial films lead to a narrowing of the miscibility gap and to insignificant lowering of critical temperatures. © 2005 Pleiades Publishing, Inc.

1. INTRODUCTION

At present, the CdHgTe compound is the variable-band-gap semiconductor most used in the fabrication of infrared (IR) photodetectors [1]. However, the existence of certain problems related to the use of CdHgTe, in particular, the instability of its lattice, surface, and interphase boundary, have initiated the development of alternative materials for IR detectors. Ternary compounds such as MnHgTe and ZnHgTe occupy a prominent place among these materials, as they have a number of advantages that have been extensively studied both theoretically and experimentally [2, 3]. These advantages include, most importantly, improved structural properties (such as microhardness and dislocation-formation energy) and fairly high mobilities of charge carriers. The composition and temperature dependences of the band gap in these materials are similar to those in CdHgTe [1]. In spite of the current serious problems in growing high-quality MnHgTe and ZnHgTe samples (large segregation coefficients, higher melting temperatures of the corresponding binary compounds, an so on), it seems that new narrow-gap semiconductors based on Hg will gradually replace CdHgTe, especially in applications where stringent requirements are imposed on the stability of a device's parameters. At the same time, epitaxial methods of growth (in comparison with the growth of bulk crystals) make it possible to obtain large-area epitaxial layers and complex multilayer structures at relatively low temperatures, which is especially important for the attainment of good operating characteristics in the next generation of photovoltaic and MIS devices [4, 5].

In addition to analysis of the dependences of the band gap and lattice constant on the alloy composition, it is necessary to take into account the fact that the majority of alloys are unstable in a certain range of compositions. An alloy in the instability region tends to experience a decrease in its free energy as a result of decomposition, i.e., a phase transformation that brings about a disruption in the macroscopic homogeneity of crystals and the formation of a mixture of phases with differing compositions. When decomposition occurs without the formation of nuclei of new phases, it is referred to as spinodal decomposition. The corresponding phase-diagram curve that separates the domain of alloy compositions of that are unstable with respect even to negligible fluctuations is referred to as the spinodal curve [6]. Unordered semiconductor alloys exhibit a positive enthalpy of mixing, which leads to a decomposition that counteracts the stabilizing effect of internal stresses. The conduction- and valence-band offsets at the interface between two semiconductors can be controlled using the corresponding strains, which makes it possible to obtain improved heterostructure-based devices. The strain also ensures an additional degree of freedom when fitting the energy-band structure to experimental data and varying the optical and kinetic properties of semiconductors.

Strains and stresses in materials grown by epitaxial methods (such as molecular-beam epitaxy (MBE) and the deposition of metal–organic chemical compounds from a vapor phase (MOCVD)) are mainly caused by a mismatch between the lattices of the epitaxial layer and the substrate. The presence of elastic relaxation in thin films also affects the phase transformations and stability [7].

The thermodynamic stability of the alloys under consideration has not as yet been adequately studied. Owing to the miscibility gap, one cannot obtain alloys based on II–VI compounds containing an arbitrary composition of components. For example, in $Cd_{1-x}Hg_xTe$

and $Zn_xHg_{1-x}Te$ systems with a slight lattice-constant mismatch, the critical temperature of decomposition is comparatively low, which makes it possible to obtain a more or less regular alloy in the entire range of compositions under normal growth conditions [8]. At the same time, a fairly wide region of phase separation ($0.35 < x < 1$) was has been experimentally observed [9] in a bulk $Mn_xHg_{1-x}Te$ alloy.

CdTe and ZnTe crystals have a zinc blende structure under conventional conditions; at the same time, MnTe has two structural modifications: a high-temperature modification with a cubic NaCl structure and a low-temperature modification with a hexagonal NiAs structure [9]. As ternary compounds grow, they aquire a sphalerite structure. Stresses related to a mismatch in the lattice parameters and compositional fluctuations affect the majority of physical properties, including solubility.

In this paper, we report the results of studying the thermodynamics of strained $Cd_{1-x}Hg_xTe$, $Mn_xHg_{1-x}Te$, and $Zn_xHg_{1-x}Te$ alloys. We analyze the effect of biaxial stresses originating in the substrate and plastic relaxation caused by the formation of misfit dislocations on diagrams of the spinodal decomposition in thin alloy films using the model of the δ lattice parameter [10].

2. CONSIDERATION OF THE ELASTIC ENERGY

In order to thermodynamically describe pseudobinary $A_{1-x}B_xC$ alloys, we consider the Gibbs free energy of mixing (ΔG) per mole,

$$\Delta G = \Delta H - T\Delta S, \tag{1}$$

where ΔH is the enthalpy of mixing, T is the absolute temperature, ΔS is the entropy of mixing and is given by

$$\Delta S = -R[\ln x + (1-x)\ln(1-x)], \tag{2}$$

and R is the universal gas constant. When describing the enthalpy of mixing, two models are most often used: the model of a regular solution [11] and the model of the δ lattice parameter (DLP) [10]. It is well known that the regular-solution model adequately describes the thermodynamic properties of a liquid phase but has limitations in the case of a solid phase, since the interaction parameters depend on the composition (x) in this model. In the DLP model, the enthalpy of mixing ΔH depends only on the lattice parameter a. For $A_{1-x}B_xC$ alloys, ΔH can be expressed as [12]

$$\begin{aligned} \Delta H &= E(\text{alloy}) - xE(\text{BC}) - (1-x)E(\text{AC}) \\ &= K[a_{\text{alloy}}^{-2.5} - xa_{\text{BC}}^{-2.5} - (1-x)a_{\text{AC}}^{-2.5}], \end{aligned} \tag{3}$$

where K is a parameter of the model. A solid solution undergoes spinodal decomposition if the curve describing the composition dependence of the free energy has an inflection point. The criterion for stability of pseudobinary alloys can be written as $\partial^2 G/\partial x^2 > 0$. The domain of instability is defined as the geometric locus for which the condition $\partial^2 G/\partial x^2 = 0$ is satisfied.

For a bulk solid solution, it is necessary to take into account the elastic component of the free energy in addition to the chemical component (the elastic component has its origin in the requirement for coherent matching of the phases [13] with the crystal anisotropy taken into account). When the alloy is in the form of a thin epitaxial film and the thermodynamic process involves the formation of misfit dislocations, biaxial tensile and compressive strains ε arise in the film as a result of a mismatch between the lattice constants of the alloy (a_{alloy}) and the substrate material (a_{sub}); it is important that $\varepsilon_{xx} = \varepsilon_{yy}$. The component of the stress tensor in the perpendicular direction (z) for cubic crystals can be written as

$$\tau_z = C_{12}\varepsilon_{xx} + C_{12}\varepsilon_{yy} + C_{11}\varepsilon_{zz}, \tag{4}$$

where C_{11} and C_{12} are the elastic constants of the film. Taking into account that $\tau_z = 0$ for the free (growth) direction in the film, we use (4) to obtain

$$\varepsilon_{zz} = -\frac{2C_{12}}{C_{11}}\varepsilon_{xx}(x). \tag{5}$$

In the case under consideration, the strain energy per unit volume can be expressed as [14]

$$E_s = \frac{E\varepsilon^2}{1-\nu}, \tag{6}$$

where $\varepsilon = \varepsilon_{xx}$, E is Young's modulus, and ν is Poisson's ratio. In addition, as was shown for the first time by Ipatova *et al.* [15], the elastic strain energy in an epitaxial film varies as a result of relaxation of elastic stresses at the surface. In this case, it is more correct to use the following expression instead of (6):

$$E_s' = \frac{C_{11}}{2(C_{11} + C_{12})}\frac{E\varepsilon^2}{1-\nu}. \tag{7}$$

The strain in a completely stressed epitaxial film is given by

$$\varepsilon(x) = \varepsilon_m(x) = \frac{a_{\text{alloy}}(x) - a_{\text{sub}}}{a_{\text{sub}}}. \tag{8}$$

The composition dependence of an alloy's lattice constant $a_{\text{alloy}}(x)$ was described using Vegard's law, which is satisfied with a good accuracy for alloys from II–VI semiconductors.

However, the situation under consideration is observed only when the film thickness (h) is smaller than the critical thickness (h_c). If $h > h_c$, plastic relaxation occurs in the film and is accompanied by generation of misfit dislocations; the thicker the film, the smaller the strain present in it. With the aim of determining the effect of the above factors on the thermodynamic stability of the alloys under consideration, we note that, according to a model describing the balance of forces [16] acting on dislocations, it can be written that

$$\varepsilon = A/h; \tag{9}$$

i.e., as the thickness of the epitaxial film increases, the strain decreases and the film gradually relaxes. Here, the parameter A is determined from the condition for continuity of the function $\varepsilon(h)$ at the point $h = h_c$. We then use expressions (8) and (9) to find that $A = \varepsilon_m h_c$. The majority of semiconductor heterostructures are grown on a (001) substrate surface; in what follows, we limit the consideration to this substrate orientation.

In our calculations, we used the model of the balance of forces, in which the critical thickness of the epitaxial layer is defined as [16]

$$h_c = \left(\frac{b}{\varepsilon_m}\right)\frac{1}{8\pi(1+\nu)}\left[\ln\left(\alpha\frac{h_c}{b}\right) + \beta\right], \qquad (10)$$

where $\alpha = 4$, β is a phenomenological parameter that serves as a measure of the deviation of stresses in the dislocation core from the linear dependence on elastic constants [7], and b is the magnitude of the Burgers vector. Since 60° misfit dislocations in the (001) plane are most often encountered in epitaxial semiconductor layers, the Burgers vector can be written as $(a/2)\langle 110\rangle$, which means that $b = a/\sqrt{2}$.

Thus, the Gibbs total free energy of the system per unit volume is the sum of the chemical energy ΔG and the elastic energy E_s'; i.e.,

$$G_{tot} = N_v\Delta G + E_s', \qquad (11)$$

where N_v is the number of moles per unit volume of a homogeneous solid solution before its decomposition. An analysis of the Gibbs free energy in relation to the solid-solution composition, epitaxial-layer thickness, and condition for stability make it possible to calculate the miscibility gap. The parameters used in the calculations were taken from [12].

3. AN ANALYSIS OF THERMODYNAMIC STABILITY

3.1. $Cd_{1-x}Hg_xTe$

The known experimental data on the solid-state part of the phase diagrams of the semiconductor alloys under consideration are fragmentary. Although detailed data on high-temperature solidus and liquidus lines are well known [8], the small values of the atomic-diffusion constants at lower temperatures make it difficult to carry out the corresponding studies.

Substitutional $Cd_{1-x}Hg_xTe$ solid solutions can be experimentally obtained for all compositions (all values of x) both in bulk and film forms; therefore, the analysis we have undertaken serves as a check.

The thermodynamic stability of $Cd_{1-x}Hg_xTe$ has been theoretically studied in a number of publications by various methods [17–19]. In particular, in ab initio calculations [17], the critical temperature of the spinodal decomposition is equal to $T_c = 84$ K. In our calculations, we used the DLP model, which is usually
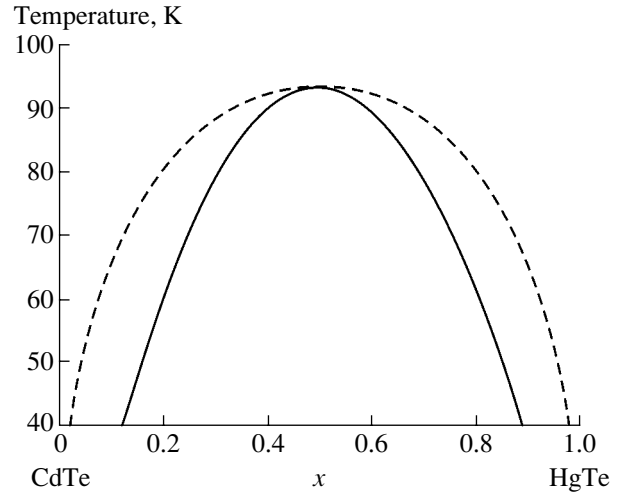
Fig. 1. Phase diagrams of the $Cd_{1-x}Hg_xTe$ decomposition. The dashed line represents the binodal curve and the solid line represents the spinodal curve.

applied to alloys based on III–V compounds, and extended it to epitaxial films (this model was described in detail in [7]). We calculated the critical temperature as being equal to $T_c = 95$ K at $x_c = 0.5$, which accounts for the absence of the miscibility gap in this particular alloy at characteristic growth temperatures for the solid solution and is caused by insignificant internal stresses as a result of a good match between the lattice constants of the compounds that form the alloy ($\Delta a/a \approx 0.3\%$). The decomposition diagram we calculated is shown in Fig. 1, where the binodal curve is represented by the dashed line and the spinodal curve is represented by the solid line. As the film thickness decreases, the significant contribution of biaxial stresses to the strain energy brings about a certain decrease in the critical temperature and an insignificant narrowing of the spinodal-decomposition range.

3.2. $Zn_xHg_{1-x}Te$

This system has been studied rather extensively in recent years, both experimentally and theoretically [3, 4, 18, 20]. Similarly to a $Cd_{1-x}Hg_xTe$ system, $Zn_xHg_{1-x}Te$ alloys form a continuous series of solid solutions [8]. However, the internal local strains arising as a result of mixing of two components (ZnTe and HgTe) with unmatched lattice constants ($\Delta a/a \approx 6\%$) lead to a larger asymmetry of the spinodal-decomposition curves with respect to $x = 0.5$ and to an increase in the critical temperature (Fig. 2, curve 1). In particular, according to our calculations, $T_c = 457$ K at $x_c = 0.53$, which is in good agreement with the results reported by Patrick et al. [18] ($T_c = 455$ K at $x_c = 0.56$). Therefore, it is possible to obtain a continuous series of solid solutions at typical growth temperatures. In Fig. 3, we show the calculated composition dependences of the critical thickness for thin films of $Zn_xHg_{1-x}Te/CdTe$ (dashed

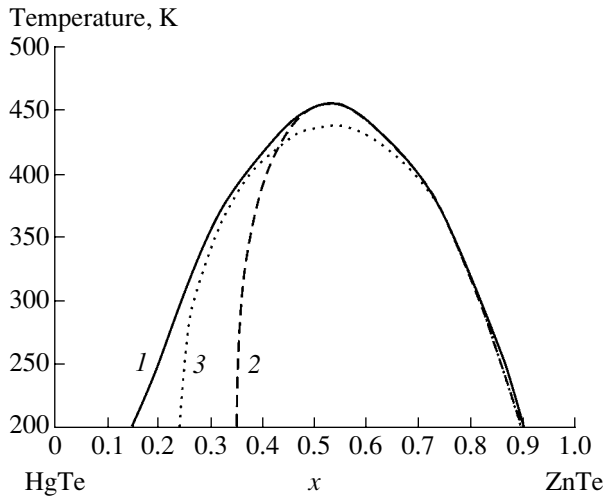**Fig. 2.** Phase diagrams of the $Zn_xHg_{1-x}Te$ spinodal decomposition for (*1*) the bulk alloy, (*2*) a $Zn_xHg_{1-x}Te/CdTe$ system ($h = 0.5$ μm), and (*3*) a $Zn_xHg_{1-x}Te/Cd_{0.8}Zn_{0.2}Te$ system ($h = 0.5$ μm).

Fig. 3. Dependence of the critical thickness (h_c) on the composition (*x*) for $Zn_xHg_{1-x}Te/CdTe$ (dashed line) and $Zn_xHg_{1-x}Te/Cd_{0.8}Zn_{0.2}Te$ (the solid line) epitaxial films.

line) and $Zn_xHg_{1-x}Te/Cd_{0.8}Zn_{0.2}Te$ (solid line). We used the DLP model to calculate the spinodal-decomposition curves for the above films, which, in this case, had a thickness $h = 0.5$ μm (Fig. 2). It follows from our calculations that the film relaxes completely if $h = 1$ μm; i.e., the spinodal curve for this film practically coincides with the corresponding curve for a bulk sample. As the film thickness decreases, the biaxial stresses originating in the substrate affect the shape of the decomposition curves more and more. In particular, the critical temperature of decomposition decreases slightly and the spinodal-decomposition region shifts to higher zinc concentrations. These results thermodynamically account for the higher quality of epitaxial $Zn_xHg_{1-x}Te$ films grown on $Cd_{0.8}Zn_{0.2}Te$ substrate as compared to that of films grown on CdTe substrates and are consistent with the experimental data [4].

3.3. $Mn_xHg_{1-x}Te$

In contrast to the $Cd_{1-x}Hg_xTe$ and $Zn_xHg_{1-x}Te$ systems, $Mn_xHg_{1-x}Te$ alloys have been studied in much less detail due to the difficulties encountered in growing this compound [2, 9, 21]. A wide range of variations in the band gap makes it possible to expect that this alloy will find extensive use, in particular, in photoelectronic devices for the infrared region of the spectrum. Since magnetic Mn ions are present in the lattice, the energy-band parameters can be easily controlled by an external magnetic field. However, a rather wide miscibility gap ($0.35 < x < 1$) appreciably limits the domain of applicability for bulk crystals. Therefore, recent expectations have been linked to the growth of high-quality epitaxial films with a wide variation in their composition. In this case, the search for the optimal substrate is one of the most important technological problems.
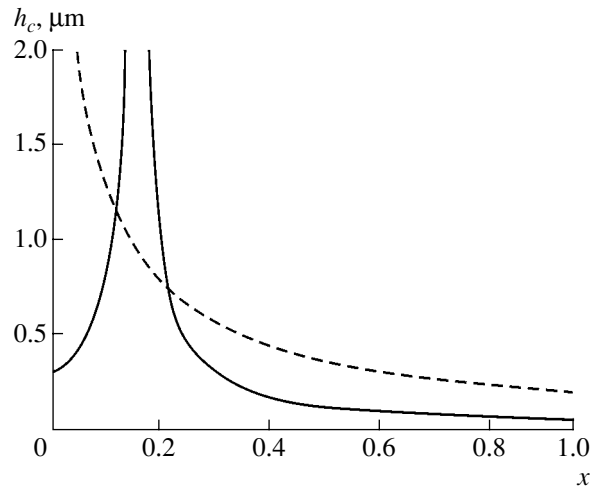

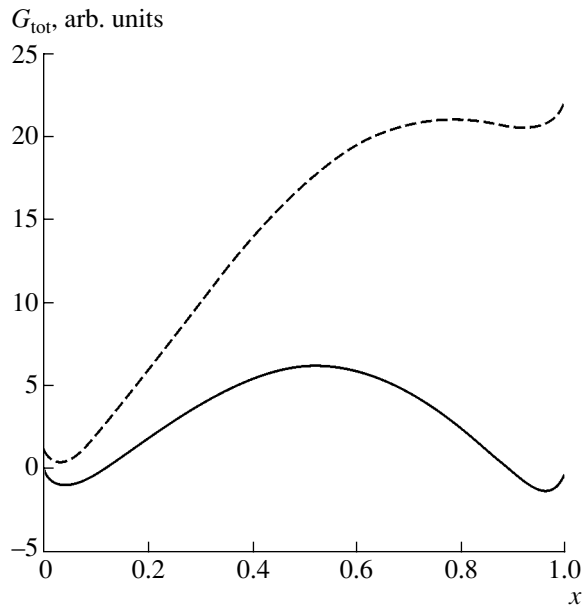**Fig. 4.** Composition dependence of the Gibbs free energy $G_{tot}(x)$ for $Mn_xHg_{1-x}Te/CdTe$ epitaxial films with the thicknesses $h = 1$ μm (the solid line) and $h = 0.1$ μm (dashed line). $T = 600$ K.

We calculated the Gibbs free energies for bulk (Fig. 4, solid line) and epitaxially stressed (Fig. 4, dashed line) $Mn_xHg_{1-x}Te/CdTe$ solid solutions. The biaxial stresses originating in the CdTe substrate increase in an alloy with an increased Mn content and give rise to a pronounced deformation of the compositional dependence of the Gibbs free energy. In turn, this circumstance also affects the spinodal-decomposition curves (Fig. 5) plotted for two substrates: CdTe and
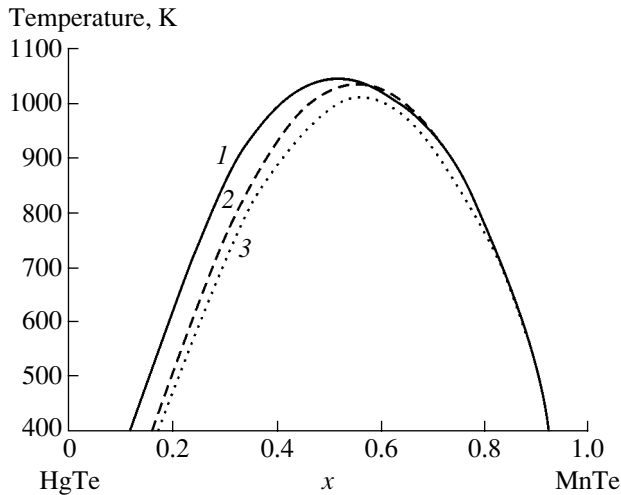
Fig. 5. Phase diagrams of the $Mn_xHg_{1-x}Te$ spinodal decomposition for (*1*) the bulk alloy, (*2*) $Mn_xHg_{1-x}Te/CdTe$ ($h = 0.1$ µm), and (*3*) $Mn_xHg_{1-x}Te/Cd_{0.96}Zn_{0.04}Te$ ($h = 0.1$ µm).

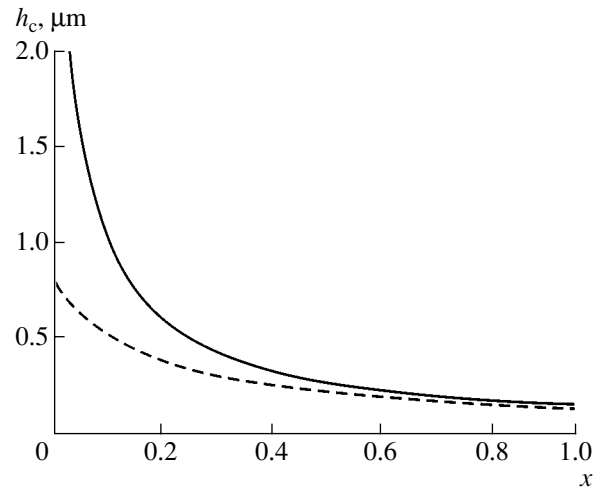**Fig. 6.** Dependences of the critical thickness (h_c) on the composition (x) for epitaxial films of $Mn_xHg_{1-x}Te/CdTe$ (dashed line) and $Mn_xHg_{1-x}Te/Cd_{0.96}Zn_{0.04}Te$ (the solid line).

$Cd_{0.96}Zn_{0.04}Te$. The results of our calculations indicate that the phase separation in this alloy should be observed in a wide concentration range at typical growth temperatures. For example, the spinodal decomposition of relaxed films ($h > 0.5$ µm) should occur at $T = 950$ K if the Mn content is higher than 35%, which is in good agreement with experimental data on the phase separation; according to these data, the corresponding value $x > 0.35$ [8, 9].

If we take into account the biaxial strains originating in the substrate in $Mn_xHg_{1-x}Te/CdTe$ and $Mn_xHg_{1-x}Te/Cd_{0.96}Zn_{0.04}Te$ thin films, the critical temperature decreases insignificantly and the solubility range of Mn extends to $x = 0.41$ for $Mn_xHg_{1-x}Te/CdTe$ and to $x = 0.45$ for $Mn_xHg_{1-x}Te/Cd_{0.96}Zn_{0.04}Te$. In addition, the miscibility gap narrows especially rapidly in the films near the substrate, which was experimentally confirmed in [22, 23]. It is also worth noting that the critical thickness for a film grown on a $Cd_{0.96}Zn_{0.04}Te$ substrate is much larger than this thickness for a film grown on a CdTe substrate (Fig. 6), which also indicates that the former substrate is preferable.

4. CONCLUSION

We studied the thermodynamics of stability for $Cd_{1-x}Hg_xTe$, $Mn_xHg_{1-x}Te$, and $Zn_xHg_{1-x}Te$ solid solutions. Calculations carried out in the context of the δ lattice parameter indicate that the CdHgTe and ZnHgTe solid solutions are stable in the entire range of component concentrations at typical growth temperatures. At the same time, a miscibility gap is observed in MnHgTe, which is consistent with the experimental data.

It is shown that the biaxial strains arising in $Mn_xHg_{1-x}Te/CdTe$ and $Mn_xHg_{1-x}Te/Cd_{0.96}Zn_{0.04}Te$ thin epitaxial films bring about a narrowing of the miscibility gaps and an insignificant decrease in the critical temperatures.

REFERENCES

1. A. Rogal'skiĭ, *Infrared Detectors* (Nauka, Novosibirsk, 2003) [in Russian].

2. A. Rogalski, Infrared Phys. **31**, 117 (1991).

3. A. Rogalski, Prog. Quantum Electron. **13**, 299 (1989).

4. E. J. Smith, T. Tung, S. Sen, *et al.*, J. Vac. Sci. Technol. A **5**, 2043 (1987).

5. N. V. Sochinskii, J. C. Soares, E. Alves, *et al.*, Semicond. Sci. Technol. **11**, 542 (1996).

6. V. I. Fistul', *Decomposition of Supersaturated Solid Solutions* (Metallurgiya, Moscow, 1977) [in Russian].

7. V. G. Deĭbuk, Fiz. Tekh. Poluprovodn. (St. Petersburg) **37**, 1179 (2003) [Semiconductors **37**, 1151 (2003)].

8. V. N. Tomashik and V. I. Grytsiv, *Phase Diagrams of the Systems Based on II–VI Semiconductor Compounds* (Naukova Dumka, Kiev, 1982) [in Russian].

9. J. K. Furdyna, J. Appl. Phys. **64**, R29 (1988).

10. G. B. Stringfellow, J. Phys. Chem. Solids **34**, 1749 (1973).

11. M. Ilegems and M. B. Panish, J. Phys. Chem. Solids **35**, 409 (1974).

12. A. Chen and A. Sher, *Semiconductor Alloys: Physics and Material Engineering* (Plenum, New York, 1995).

13. A. G. Khachaturyan, *The Theory of Phase Transformations and the Structure of Solid Solutions* (Nauka, Moscow, 1974) [in Russian].

14. L. D. Landau and E. M. Lifshitz, *Course of Theoretical Physics*, Vol. 7: *Theory of Elasticity*, 4th ed. (Nauka, Moscow, 1987; Pergamon, New York, 1986), Sect. 5.

15. I. P. Ipatova, V. G. Malyshkin, and V. A. Shchukin, J. Appl. Phys. **74**, 7198 (1993).

16. R. Beanland, D. J. Dunstan, and P. J. Goodhew, Adv. Phys. **45**, 87 (1996).

17. S.-H. Wei, L. G. Ferreira, and A. Zunger, Phys. Rev. B **41**, 8240 (1990).

18. R. S. Patrick, A.-B. Chen, A. Sher, and A. Berding, J. Vac. Sci. Technol. A **6**, 2643 (1988).

19. J. Yang, N. J. Silk, A. Watson, *et al.*, CALPHAD: Comput. Coupling Phase Diagrams Thermochem. **19**, 415 (1995).

20. M. A. Herman and J. T. Sadowski, Cryst. Res. Technol. **34**, 153 (1999).

21. O. M. Bodnaruk, I. N. Gorbatyuk, V. I. Kalenik, *et al.*, Neorg. Mater. **28**, 335 (1992).

22. G. V. Beketov, A. E. Belyaev, S. A. Vitusevich, *et al.*, Fiz. Tekh. Poluprovodn. (St. Petersburg) **31**, 268 (1997) [Semiconductors **31**, 218 (1997)].

23. S. V. Kavertsev and A. E. Belyaev, Fiz. Tekh. Poluprovodn. (St. Petersburg) **31**, 342 (1997) [Semiconductors **31**, 283 (1997)].

Translated by A. Spitsyn

ELECTRONIC AND OPTICAL PROPERTIES
OF SEMICONDUCTORS

Low-Temperature Microwave Magnetoresistance
of Lightly Doped p-Ge and p-Ge$_{1-x}$Si$_x$

A. I. Veĭnger^, A. G. Zabrodskiĭ, and T. V. Tisnek

Ioffe Physicotechnical Institute, Russian Academy of Sciences, St. Petersburg, 194021 Russia
^e-mail: anatoly.veinger@mail.ioffe.ru

Abstract—The magnetoresistance of a lightly doped p-Ge$_{1-x}$Si$_x$ alloy is studied in the range of compositions $x = 1$–2 at %. The results are compared with the available data for lightly doped p-Ge. The studies have been carried out using ESR measurements at a frequency of 10 GHz in the temperature range 10–120 K. It is established that micrononuniformity in the distribution of Si in the Ge lattice (Si clusters) suppresses the interference part of the anomalous magnetoresistance and, in addition, results in an averaging of the effects of light and heavy holes. This observation suggests a sharp decrease in the inelastic scattering time in the case of a Ge$_{1-x}$Si$_x$ solid solution as compared to that of Ge. © 2005 Pleiades Publishing, Inc.

1. INTRODUCTION

Studies of the transport properties of Ge–Si alloys in the range of compositions close to Ge [1] have revealed that, at low temperatures, the charge carriers in these materials are scattered by neutral compositional fluctuations and by energy fluctuations in the bottom of the conduction band (the top of the valence band). This circumstance leads to essential differences between the low-temperature transport properties of such alloys and single-component semiconductors.

One of the most informative effects when studying the transport properties of semiconductors is their magnetoresistance (MR). The field and temperature dependences of MR are closely related to the character of charge-carrier scattering. Recent studies of the microwave MR of lightly doped n- and p-Ge [2] have shown that, at microwave frequencies and low temperatures, this effect is controlled not only by scattering of the carrier momentum but also by scattering of the carrier energy. The latter process manifests itself in the anomalous MR component as well as in intervalley scattering in n-Ge and intersubband scattering in p-Ge.

In this context, it was of interest to clarify the influence of scattering by the neutral compositional fluctuations that are thought to be present in Ge–Si solid solutions on the scattering mechanisms mentioned above. In this paper, we report data on the MR effect in a p-Ge$_{1-x}$Si$_x$ alloy with $x \approx 0.01$–0.02. These data are compared to the results of similar studies of p-Ge [2].

2. EXPERIMENTAL METHOD AND RESULTS

The MR was measured using a procedure previously developed for studying the MR in the microwave range with the use of an ESR spectrometer. This procedure allowed us to considerably improve the sensitivity of

the setup and to obtain a higher accuracy of measurement; as a result, the ESR signal could be reliably detected in the lowest magnetic fields. The procedure was described in detail in [3]. We used an E-112 spectrometer (Varian Co.), which operates at the frequency 10 GHz and whose magnet can produce magnetic fields ranging from 0 to 16 kOe. The spectrometer includes an ESR-9 Oxford Instruments cryostat, which is capable of maintaining the temperature in the range 3–300 K with an accuracy of 0.1 K. It is worth noting that present-day ESR spectrometers record the derivative of the microwave absorption of a sample with respect to the magnetic field as a function of the magnetic field. In turn, this function is proportional to the similar dependence for the derivative of the conductivity or resistivity as defined by the relationship between the resistivity of a sample and the wave impedance of the waveguide.

The MR effect was studied in samples of a rather pure p-Ge$_{1-x}$–Si$_x$ alloy that had a Ga dopant concentration $p \approx (7$–$10) \times 10^{13}$ cm^{-3}. At such a Ga content, the conductivity in the impurity band is negligible in the temperature range under consideration and all the transport processes are controlled by holes in the valence band. A sample $6 \times 1.5 \times 1$ mm in size was placed in the low-temperature region of the cryostat, which was located inside the resonator of the ESR spectrometer. This allowed the dependences of the derivative of the microwave power P absorbed by the sample with respect to the magnetic field H (dP/dH) on the magnetic field to be recorded automatically when the sample was at a particular temperature.

These dependences are shown in Fig. 1. It should be noted that, at $H = 0$, the derivative is $dP/dH = 0$ (curve *1*); however, in order to avoid the superposition of the curves, we have displaced each subsequent curve, starting with curve *2*, from the preceding one by a fixed step
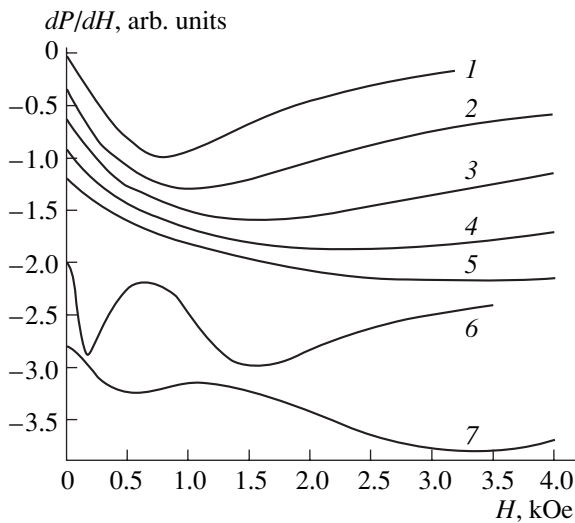
Fig. 1. Magnetoresistance of the p-Ge$_{0.99}$Si$_{0.01}$ alloy (curves *1–5*) and lightly doped p-Ge [2] (curves *6* and *7*) vs. the magnetic field at the temperatures (*1* and *6*) 12 K, (*2*) 20 K, (*3*) 30 K, (*4* and *7*) 50 K, and (*5*) 80 K.

along the ordinate axis. It was found that the field dependences of the derivative of the absorption signal are noticeably weakened with an increase in temperature. In order to visualize the specific features of the field dependences in this case, we have normalized each dependence by setting the change in dP/dH to the minimal value equal to unity instead of its zero-field value. Since the samples were relatively pure and, thus, had high resistivity, the change in the derivative of the microwave absorption was usually proportional to the derivative of the conductivity of the samples.[1] In Fig. 1, similar dependences for lightly doped p-Ge at the same temperatures are shown for comparison.

It is evident that, in contrast to the curves for the solid solutions characterized by one minimum of the derivative dP/dH, the dependences for p-Ge exhibit two minimums. In the both cases, the minimums shift to higher magnetic fields with an increase in temperature.

3. DISCUSSION

It is important to note that, for Ge–Si solid solutions, the observed dependences of the conductivity on the magnetic field, which exhibit one minimum, correspond to the conventional field dependence of classical MR. In fact, it is well known that, under low fields ($H \longrightarrow 0$), the conductivity of a semiconductor decreases as H increases according to the relation

$$\sigma_m = \sigma_0(1 - A\mu^2 H^2), \qquad (1)$$

where σ_0 is the conductivity at $H = 0$, μ is the charge-carrier mobility, and A is a numerical factor dependent on the mechanism of scattering of the charge carriers. It

---

[1] This problem was analyzed in detail in [3].

is also known that, under high fields ($H \longrightarrow \infty$), classical MR is independent of the magnetic field.

From the aforesaid and Eq. (1) it follows that, in low fields, we have

$$dP/dH \propto d\sigma/dH \propto -H; \qquad (2)$$

i.e., the derivative of the microwave absorption is negative and decreases linearly as the magnetic field increases. In line with the asymptotic behavior of the conductivity, the derivative in the range of high fields approaches zero ($dP/dH \longrightarrow 0$) from the negative side.

As is evident from Fig. 1, the above-described field dependences of dP/dH for Ge$_{1-x}$–Si$_x$ solid solutions are observed over the entire temperature range. The dependences for lightly doped p-Ge (curves *6* and *7*) are shown in Fig. 1 for comparison. These dependences are noticeably different from those for the p-Ge$_{1-x}$Si$_x$ solid solutions in that they have an additional minimum under low fields in the low-temperature region. As was established in [2], this minimum is due to the long period of inelastic scattering of light and heavy holes in this temperature range. It should be noted that the curves for p-Ge have been shifted away from the other curves so that the dependences do not intersect each other. In addition, these curves are normalized in the same manner as for the field dependences of the alloy.

The lack of such a minimum in the field dependences of the MR of the Ge–Si alloy leads us to assume that, for this material, the dephasing time is much shorter than that for pure Ge. In the case of the alloy, the dephasing time is so short that, in the course of carrier diffusion, the self-crossing paths that define the quantum corrections to the conductivity do not appear. The same conclusion can be drawn for transitions between the subbands of light and heavy holes. We can believe that the light and heavy holes manifest themselves separately if the time taken for the transition from one subband to the other is much longer than the inverse frequency of the external field. If the frequency of the intersubband transitions is much higher that the frequency of the external field, each hole has an opportunity to become light or heavy many times per period of the field. In this case, the MR value for these subbands is averaged.

Thus, the first conclusion that can be drawn from comparison of the MRs of the pure Ge and Ge–Si alloy is the following: due to the inelastic scattering of holes in the alloy, fast dephasing of the holes and mixing of light and heavy holes occur; as a result, the MR effect is averaged over the corresponding subbands. The enhancement of the inelastic scattering in Ge$_{1-x}$Si$_x$ solid solutions when x increases in the range of compositions close to the Ge side is most likely due to the enhanced effect of compositional fluctuations [1, 4].

As the MR in the Ge–Si alloy exhibits only classical behavior, it allows us to analyze the field dependences

shown in Fig. 1 in more detail. From Eq. (1) it follows that, in the region of low fields, we have

$$d^2P/dH^2 \propto d^2\sigma/dH^2 = -2\sigma_0 A\mu^2 = -2Aep\mu^3. \quad (3)$$

Therefore, the temperature dependence of the second-order derivative of the microwave absorption in low fields is proportional to the hole mobility cubed. Furthermore, the field dependence of the derivative of the MR demonstrates behavior that is different in sign at $\mu^2H^2 \ll 1$ and $\mu^2H^2 \gg 1$; this observation suggests that the minimum of the derivative lies in the region around $\mu^2H^2 \approx 1$. It follows that the magnetic field corresponding to the minimum of the derivative H_{min} is defined by the inverse mobility:

$$H_{min} \propto 1/\mu. \quad (4)$$

Figure 2 shows the temperature dependence of the second-order derivative of the microwave absorption at $H \longrightarrow 0$ for two samples with somewhat different Si concentrations. As is evident from the figure, this dependence can be divided, according to variations in the parameters in formula (3), into two clearly defined regions: (i) a low-temperature region and (ii) a high-temperature region. At low temperatures, the second-order derivative of the microwave absorption increases with temperature because the hole density increases due to thermal ionization of the dopant centers; at higher temperatures, the behavior of the second-order derivative is controlled by the behavior of the carrier mobility. In the latter temperature region, the second-order derivative of microwave absorption decreases as the temperature increases and approaches the dependence $d^2P/dH^2 \propto T^{-2.5}$ at high temperatures. Glicksman [5] has measured the temperature dependence of electron mobility in Ge–Si alloys of various compositions. Under the conditions of scattering by compositional fluctuations, he obtained the dependence $\mu \propto T^{-0.8}$ for $x = 0.03$ in the temperature range 80–300 K. If we assume that the mechanism of scattering in the Ge–Si alloys under study is the same, the temperature dependence is expected to be $d^2P/dH^2 \propto T^{-2.4}$. This dependence is in good agreement with the experimental data.

The above assumption can be verified using formula (4) for the field H_{min} in which the minimum in the derivative of the absorption signal is observed. In Fig. 3, the temperature dependences $H_{min}(T)$ are shown for the same samples as in Fig. 2. At relatively high temperatures ($T \gtrsim 15$ K), the two temperature dependences are close to each other and can be written as $H_{min} \propto T^{0.83}$, in good agreement with the data provided by Glicksman [5]. In the low-temperature region, in which the scattering mechanism is most likely changed from scattering by compositional fluctuations to scattering by impurities, the curves become separated.

It should be noted that the data shown in Fig. 3 are controlled by the temperature dependence of the free-hole mobility from much lower temperatures than the data in Fig. 2. This circumstance is quite understand-
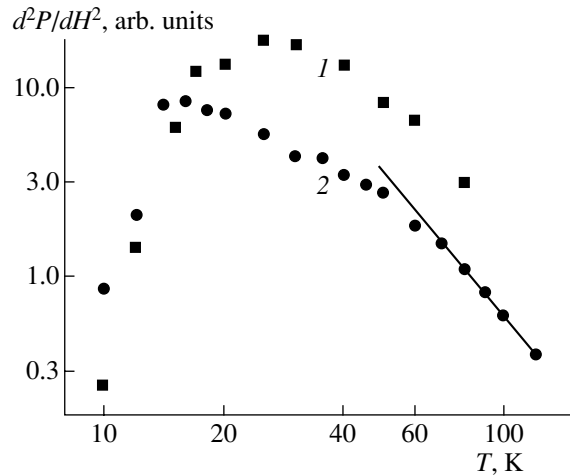
Fig. 2. The second-order derivative of the microwave absorption d^2P/dH^2 vs. the temperature under low magnetic fields for $Ge_{1-x}Si_x$ alloys with (*1*) $x = 0.01$ and (*2*) $x = 0.02$. The straight line refers to the dependence $d^2P/dH^2 \propto T^{-2.5}$.

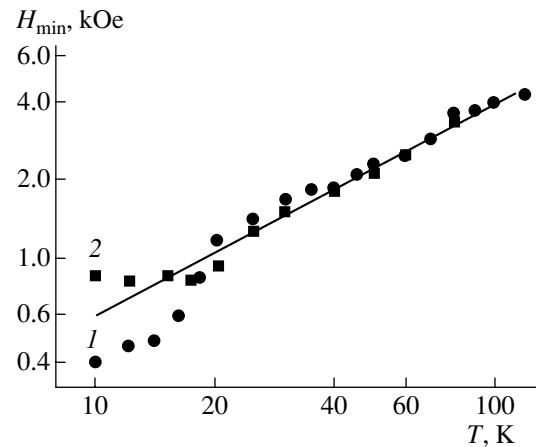**Fig. 3.** Temperature dependences of the magnetic field corresponding to the minimum derivative of the microwave absorption in $Ge_{1-x}Si_x$ alloys with (*1*) $x = 0.01$ and (*2*) $x = 0.02$. The straight line refers to the dependence $H_{min} \propto T^{0.83}$.

able, since dependence (3) involves the free-hole concentration, a change in which influences the field dependences of the MR up to rather high temperatures (60–80 K).

Comparison of the data in Fig. 3 (with regard to the relationship $\mu \propto 1/H_{min}$) with the corresponding experimental dependences in [1] shows that the temperature dependences of the mobilities for different alloys are close to each other in the temperature range 20–120 K but are noticeably different at $T < 20$ K. Specifically, the data of [1] for lower temperatures are characterized by a substantially weaker temperature dependence. As was argued in [1], this is probably due to some extra scattering mechanisms in addition to scattering by compositional fluctuations. (The samples described in [1] were more heavily doped than the samples under study.) In

the case considered in this study, it is the scattering by compositional fluctuations that is probably the most important scattering process. This statement is confirmed by the fact that the temperature dependences of the hole mobility are close to those observed in [5] for the electron mobility, which is precisely due to the scattering by compositional fluctuations.

As far as we know, all the theories on scattering by compositional fluctuations [1, 5] are based on the assumption that the potential of such fluctuations can be described by the δ function. Therefore, these fluctuations are assumed to be neutral objects with vertical walls and represented by clusters of Si atoms embedded in the Ge lattice. In this case, the decrease in mobility resulting from an increase in temperature is governed only by an increase in the thermal velocity of the charge carriers. Then, this decrease is proportional to $T^{-1/2}$.

In experiments, however, a more profound decrease in the mobility is observed as the temperature increases. In order to explain this observation, Glicksman [5] assumed that the above clusters are charged and that their charge is of the same sign as the carrier charge. This assumption is quite reasonable, since the band gap of Si clusters is much wider than the band gap of the basic Ge lattice. However, the conventional description of scattering by charged impurities yields an increase in mobility on interaction of the carrier with either an attractive potential or a repulsive potential [4].

It is possible to envisage another mechanism of inelastic scattering by Si clusters in Ge. This mechanism involves the trapping of a hole by such a cluster and the subsequent thermal release of the hole back into the valence band of Ge. If the cluster has a repulsive potential and contains an allowed energy level, the frequency of the trapping and release will increase as the temperature increases, since, as is well known, the cross section for trapping by repulsive centers increases with an increase in temperature [6].

We analyze the temperature dependence of the probability of the above scattering mechanism by recognizing that, in turn, this scattering process is controlled by the probability W_1 of the carrier encountering the scattering cluster and of its subsequent penetration through the repulsive barrier. The temperature dependence of the first of the two events is controlled by the temperature dependence of thermal velocity of the charge carrier, which is well known to be proportional to $T^{1/2}$. The probability of the second event W_2 is described by the relation

$$W_2 \propto -\exp(T_0/T)^{1/3}, \tag{5}$$

where $T_0 \approx 10^5$ K [6].

If the exponential function in formula (5) is replaced by the increasing dependence $T^{1/3}$, the desired probability of scattering with trapping at the repulsive center W will follow the temperature dependence in the form

$$W = W_1 W_2 \propto T^{1/2} T^{0.33} = T^{0.83}. \tag{6}$$

As can be seen from Fig. 3, this relationship is in excellent agreement with the experimental temperature dependence of the mobility, although the physical grounds for the above substitution remain obscure.

It should be noted that the above-considered mechanisms of interaction of charge carriers with charged impurity clusters are clearly revealed in spin relaxation processes [7]. Recently, we have demonstrated that, when the concentration of the nitrogen dopant centers in 4*H*-SiC is increased, the spin relaxation involves interaction with charged clusters that contain progressively smaller amounts of impurity centers [8].

4. CONCLUSIONS

The transition from *p*-Ge to diluted solid solutions with Si (p-Ge$_{1-x}$Si$_x$ with $x \approx 0.01$–0.02) results in complete elimination of anomalous MR, as has been observed experimentally. In addition, the fine structure of classical MR disappears because of an increase in the frequency of transitions between the subbands of light and heavy holes.

The low-field temperature dependences of the second-order derivatives of microwave absorption that are controlled by changes in the carrier mobility suggest that scattering of holes by compositional fluctuations is the prevailing mechanism of scattering. The same conclusion follows from the temperature behavior of the magnetic fields corresponding to the minimum value of the first-order derivative of microwave absorption. The compositional fluctuations are related to the appearance of Si clusters embedded in the Ge lattice.

The simple relationship between the magnetic field, corresponding to the minimum value of the first-order derivative of the MR, and the hole mobility ($\mu \propto H_{\min}^{-1}$) made it possible to determine the hole mobility to a reasonably high accuracy over the entire temperature range under study.

Analysis of all the experimental data (the field and temperature dependences of the derivatives of microwave absorption in diluted solid solutions of Si in Ge) and comparison of these data with the previously studied MR in Ge [2] show that the inelastic scattering of holes is due to repulsive centers that are assumed to be Si clusters. A mechanism of inelastic scattering of holes by Si clusters is suggested. The mechanism involves trapping of the holes followed by their thermal release into the valence band of Ge. For such processes, the experimental temperature dependence of the hole mobility is consistent with the model of centers with a repulsive potential.

REFERENCES

1. I. S. Shlimak, A. L. Éfros, and I. Ya. Yanchev, Fiz. Tekh. Poluprovodn. (Leningrad) **11**, 256 (1977) [Sov. Phys. Semicond. **11**, 149 (1977)].

2. A. I. Veinger, A. G. Zabrodskii, T. V. Tisnek, and S. I. Goloshchapov, Solid State Commun (2005) (in press).

3. A. I. Veĭnger, A. G. Zabrodskiĭ, and T. V. Tisnek, Fiz. Tekh. Poluprovodn. (St. Petersburg) **36**, 826 (2002) [Semiconductors **36**, 772 (2002)].

4. K. Seeger, *Semiconductor Physics* (Springer, Berlin, 1973; Mir, Moscow, 1977).

5. M. Glicksman, Phys. Rev. **111**, 25 (1958).

6. V. L. Bonch-Bruevich, *Solid State Physics* (Nauka, Moscow, 1959), Part 1, p. 182 [in Russian].

7. A. Honig and E. Stupp, Phys. Rev. **117**, 69 (1960).

8. A. I. Veĭnger, A. G. Zabrodskiĭ, T. V. Tisnek, and E. N. Mokhov, Fiz. Tekh. Poluprovodn. (St. Petersburg) **38**, 816 (2004) [Semiconductors **38**, 782 (2004)].

Translated by É. Smorgonskaya

ELECTRONIC AND OPTICAL PROPERTIES
OF SEMICONDUCTORS

Features of Physical Differentiation with Respect to Light Absorbance in Junction Photovoltage Spectra

L. I. Berezhinskiĭ, E. F. Venger, I. E. Matyash, A. V. Sachenko, and B. K. Serdega^

Lashkarev Institute of Semiconductor Physics, National Academy of Sciences of Ukraine,
Prospekt Nauki 41, Kiev, 03028 Ukraine
^e-mail: serdega@isp.kiev.ua

Abstract—Junction-photovoltage pleochroism is studied in crystalline silicon under the conditions of a conductivity anisotropy induced by a uniaxial compressive strain. Polarization modulation of light has been used: the samples are excited by linearly polarized light, with the polarizations periodically alternating with respect to the optical axis. The spectral characteristics obtained in such a way represent the polarization difference of the photovoltages, which depends on the light absorbance. A heavy dependence of the spectrum shape on the type of *p–n* junctions, which differ in relation to base parameters and emitter technologies, is detected. An analysis of the spectra shows that the condition of physical differentiation with respect to absorbance is satisfied only in *p–n* junctions with a negligible space-charge thickness. © 2005 Pleiades Publishing, Inc.

1. INTRODUCTION

Light absorbance α is one of the main parameters in such effects as transmission and photoconductivity or various photovoltaic effects studied in semiconductor crystals. The dependence of α on photon energy, mainly due to the semiconductor band gap and features of its dispersion in the Brillouin zone, controls the shape of the spectral characteristics of the mentioned effects. The information content of such characteristics is important for studies of the physical properties of materials and their applications. The need to increase their informativity has led to the development of many techniques of physical differentiation, which, together, make up an independent spectroscopy division called modulation spectroscopy [1]. During the development of this line of research, various parameters and physical quantities, such as electric and magnetic fields, temperature, pressure and others, were used in modulations.

However, none of the physical modulation techniques has been found capable of reproducing a derivative of a spectral characteristic of any optical or photoelectric effect with respect to the absorbance. To this end, it would be required to measure the response to a change in the absorbance sequentially at discrete points in a widely varying range of α. However this operation seems impossible, since every used modulation technique causes a change in the absorbance simultaneously at all points of its spectral characteristic due to the modulation effect on the entire crystalline system or any of its elements. Moreover, the kinetic, recombination, and other parameters of a material are subjected to the α-modulation effect simultaneously with an α variation.

Therefore, the conceptual possibility of α modulation (by analogy with λ modulation) can be accomplished only by varying an external-medium modulating parameter that would not change, most importantly, the structural properties of a material under study. Under certain conditions, such a parameter can be (as we showed earlier [2]) the polarization state of the electromagnetic radiation exciting a sample. The essence of these conditions is that the state polarization of light propagating in a sample manifests itself only when the dielectric properties of a used material are anisotropic and the light polarization state is modulated in a certain way. In this case, the propagation and absorption conditions for light with an electric-component vector parallel or perpendicular to the crystal optical axis become different due to anisotropy of the complex refractive index, which causes the linear dichroism effect. If the difference in the corresponding absorbances is much smaller than one of these absorbances alone $(\alpha_\perp - \alpha_\parallel) \ll \alpha_\perp, \alpha_\parallel$ (small-anisotropy condition), according to an analysis carried out in [3] using the example of a transmission spectral characteristic, the measured signal contains the derivative of the transmission function $T(\alpha)$ with respect to the absorbance:

$$\Delta T = (dT/d\alpha)\Delta\alpha. \qquad (1)$$

However, in contrast to the case of transmission, the situation for photoelectric effects becomes complicated due to additional processes. As was shown in [4] using the example of polarization–modulation photoconductivity spectra, a diffusion of excess carriers changes the spatial distribution of electrons and holes generated by light according to the Lambert law, as, in this case, there are different ratios of surface and volume recombination fluxes. Nevertheless, the spectral characteristics of the polarization difference of the photoconductivity exhibit, although with a certain constraint, the property of the derivative with respect to the absorbance.

As for photovoltaic effects, they can add structural inhomogeneity (e.g., a *p–n* junction) to the mentioned factors as well as associated internal electric and strain fields. For this reason, the feasibility of the α modulation (by analogy with the λ modulation) of the spectral characteristics of photovoltaic effects can be problematic. The study of the level of feasibility in this case, using the example of measurements and analysis of the junction photovoltage induced when the *p–n* junction of an anisotropic crystal is exposed to light, is the objective of this paper.

2. EXPERIMENTAL

As follows from the above discussion, α modulation can be experimentally demonstrated in any photovoltaic spectra only in materials with anisotropic dielectric properties. As for the spectra themselves, the most convenient characteristic for simulation seems to be the spectrum of the junction photovoltage induced when a *p–n* junction is exposed to light. Simultaneous satisfaction of these conditions can be attained, e.g., in the *p–n* junction of a Si crystal with the anisotropy controlled by external uniaxial compression.

Silicon crystals with a cubic structure feature isotropic dielectric properties. Therefore, optical or photoelectric effects in them, associated with light polarization, can be caused only by a directed effect that lowers the crystal symmetry. Therefore, in the case under consideration, the experimental configuration is such that the light interacting with the crystal propagates along the normal to its surface and the dichroism $\alpha_\perp - \alpha_\parallel$ or pleochroism $P = (V_\perp - V_\parallel)/(V_\perp + V_\parallel)$ of the junction photovoltage V arises as a result of a change in crystal structure symmetry, in contrast to the photopleochroism induced by an oblique incidence of light [5].

Three types of samples with various preparation conditions were used in the measurements. Their characteristics are listed in the table. In all cases, standard silicon wafers that were 0.4 mm thick and had a (100) surface crystallographic orientation were used. In addition, an opposite-conductivity layer was formed on one of the surfaces using a certain method. Then, rectangular platelets $1 \times 0.5 \times 0.04$ cm in size were prepared by cleaving along {110} cleavage planes. Aluminum electrodes (a continuous electrode on the back surface and a ring electrode on the exposed surface) were used to connect a sample to a measuring circuit. In one case, this circuit represented a reversely connected voltage source and a load resistor (persistent photoconductivity measurement conditions). In another case, it was in the form of a high-resistance input of a selective amplifier (photovoltage measurement conditions). A compressing uniaxial force was applied to the narrow plate faces, and its direction coincided with the sample surface plane exposed to light and was parallel to the [110] crystallographic direction. The samples were fixed in a com-

Table

Sample type	Base type	Resistivity, Ω cm	Emitter fabrication method	Emitter thickness, μm
A	p	1	Epitaxy	5
B	p	10	Diffusion	2
C	n	5×10^3	Implantation	0.5

pressing device to provide for their steady state under compression as well as mechanical stress uniformity.

The measurements were carried out using the optical scheme described in [2]. Its key feature was the use of a polarization modulator based on the photoelastic effect. This device periodically (at a frequency of 50 kHz) transformed light with a circular polarization state to linearly polarized light at the monochromator output. The electric component of the light alternately took on parallel and perpendicular orientations with respect to the sample optical axis. The measured signal represented the difference between two photovoltages $V_\perp$ and $V_\parallel$ excited in a planar *p–n* junction exposed to linearly polarized light in the spectral range near the absorption edge. The measurements were carried out at room temperature in the range of the linear dependence of the photovoltage on the light intensity. The light source was an MDR-12 monochromator with a halogen lamp at the input. The spectral characteristics of the junction photovoltage and transmittance later used to analyze the polarization characteristics were measured using a conventional technique. The measurement data were normalized to a constant intensity of light passed through a sample's front face.

3. RESULTS AND DISCUSSION

In order to analyze the experimental results, we used the theoretical expression for low-signal photovoltage V for the case $V < kT/q$ [6]. This expression is the most general case among such functional dependences describing the relation between the photovoltage and a set of physical and design factors:

$$\begin{aligned}
V = {} & \frac{I[1 - \exp(-\alpha d)]\alpha L}{(\alpha^2 L^2 - 1)[1 - \exp(-2\alpha d)]} \\
& \times [(S_0 + K)(S_d + K)\exp(d/L) \\
& - (S_0 - K)(S_d - K)\exp(-d/L)]^{-1} \\
& \times \{\alpha L[\exp(-\alpha x) + R\exp(-2\alpha d + \alpha x)] \\
& \times [(S_d + K)\exp(d/L) - (S_d - K)\exp(-d/L)] \\
& + 2\exp(-2\alpha d)[S_d(1 + R) - KL\alpha(1 + R)] \\
& - [\exp(-\alpha x) + R\exp(-2\alpha d + \alpha x)] \\
& \times [(S_d + K)\exp(d/L) + (S_d - K)\exp(-d/L)]\}.
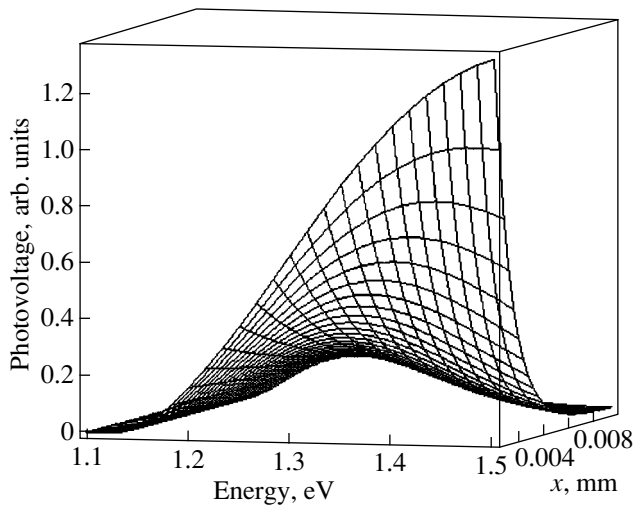\end{aligned} \tag{2}$$

Fig. 1. Dependences of the junction photovoltage on the photon energy and the emitter layer thickness x calculated at $D = 8$ cm^2/s, $R = 0.7$, $\tau = 1 \times 10^{-6}$ s, $S_0 = 10^3$ cm/s, $S_d = 10^3$ cm/s, and $d = 0.035$ cm.
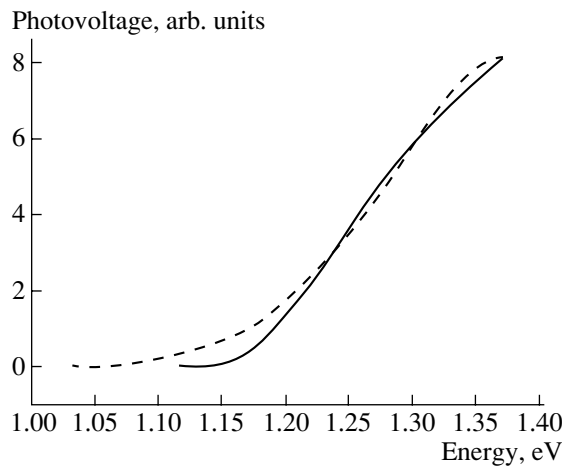

Fig. 2. Experimental dependence of the junction photovoltage of the type-*A* sample (dashed curve) and one of the curves in Fig. 1 at $\tau = 1.5 \times 10^{-6}$ s and $x = 1 \times 10^{-4}$ (solid curve).

Here, $L = \sqrt{D\tau}$; $K = D/L$; D is the electron diffusivity in the base, τ is the electron lifetime; S_0 and S_d are surface recombination rates on the front and rear sample surfaces, respectively; d is the base thickness; x is the emitter thickness; R is the light reflectance from the back surface; and I is the illumination intensity.

The set of dependences of the photovoltage on the photon energy of the excitation light calculated using Eq. (2) is shown in Fig. 1. Here, the analytical approximation $\alpha = (76.417 - 68.697E)^2$ [7] is used for the energy dependence of the silicon crystal absorbance. Figure 2 shows that the calculated (one of the depen-

dences in Fig. 1) and measured spectral characteristics of the photovoltage of the type-*A* sample are in good agreement, which gives grounds to further apply the formula to analysis of the spectral dependence of the anisotropy $\Delta\alpha = \alpha_\perp - \alpha_\parallel$. We note that the argument of the characteristics in this case is the photon energy (which is conventional in practice), although, as was mentioned above, the spectral dependences will be presented further on as functions of the absorbance.

As follows from [8], the states in direct-gap crystals are mixed in the valence band under the effect of a uniaxial strain. In particular, the bands V_+ and V_- change places in directions perpendicular to the deformation direction. This phenomenon results in the selection rules for interband transitions becoming dependent on the polarization state. When junctions are excited by linearly polarized light, these rules change as follows: transitions from the V_+ band are allowed under excitation by both polarization states, while transitions from the V_- band are allowed only for polarizations perpendicular to the compression direction. As a result, the spectral dependence of the absorbance, which is independent of polarization in an isotropic crystal, is split into two components, and one of them, specifically, $\alpha_\perp(\lambda)$, shifts in the energy scale.

Accordingly, two junction photovoltage components arise: $V_\perp$ and $V_\parallel$. Taking this factor into account, we can predict the result of their polarization difference measurement. It is evident that the spectral dependence of this difference is controlled by whether or not there is a maximum in the corresponding photovoltage characteristic of a nondeformed sample. If a maximum exists, the component $V_\perp$ is crossed by the unshifted dependence of $V_\parallel$, which results in a sign-alternating difference curve, as is the case for the photoconductivity [4]. In the second case, the characteristic should have a constant sign and resemble the characteristic of the polarization difference of the transmittance, which was studied in detail in [3].

In the crystal used in this study, optical transitions are indirect in the entire photon energy range under consideration. Nevertheless, the above considerations on the formation of the spectral difference characteristic are qualitatively confirmed by experiments. However, the experiments show that the actual situation is more complex and diverse, as is demonstrated in Fig. 3, where the spectral dependences of (a) the junction photovoltage and (b) the polarization difference characteristics of *p–n* junction samples of all types are shown. The absorbances (horizontal axis) are set identically for all three samples and are taken from [9]. We note that each of the three dependences in Fig. 3a is consistent (as shown in Fig. 2) with a corresponding theoretical curve in Fig. 1 if the photon energy is taken as their argument. The amplitude values of the spectra, controlled by various properties of the materials and technological parameters of the samples, differ, as in Fig. 1,
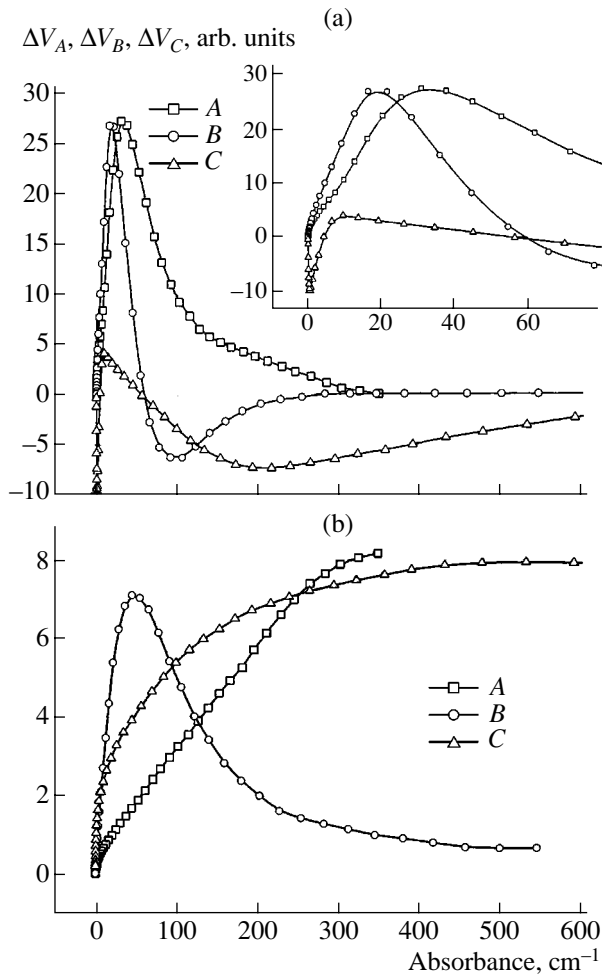
Fig. 3. Spectral dependences of (a) the polarization differences $\Delta V = V_\perp - V_\parallel$ of the type-*A*, -*B*, and *C* samples and (b) the junction photovoltage *V* of the same samples. The inset to panel (a) shows ΔV in the range of low absorbance.

Fig. 4. Spectral dependences of the polarization difference ΔV_B in the derivative of the junction photovoltage V_B on the absorbance of the type-*B* sample.

more than tenfold. For clarity, the curves in Fig. 3a are normalized to identical relative values. In this case, it should be kept in mind that the measured amplitudes of the polarization differences $\Delta V = V_\perp - V_\parallel$ are smaller than each of their components by two to three orders of magnitude in all three cases.

Comparing the curves in Figs. 3a and 3b in pairs, we can see that only in two of the three cases, specifically for the type-*A* and -*B* samples, the profile of the spectral characteristics ΔV agrees with the previously outlined argumentation of their formation. Namely, the spectral dependence of ΔV_B is actually sign-alternating in the case of a maximum in the spectral dependence of V_B and constant-sign ΔV_A in the case of the flattening characteristic V_A. However, the common origin of the curves ΔV_A and ΔV_B is only qualitative. For example, the polarization difference function ΔV_B agrees excellently with the derivative $dV_B(\alpha)/d\alpha$, at least in the range 50 cm^{-1} < α < 600 cm^{-1} (Fig. 4), while the shape of the depen-

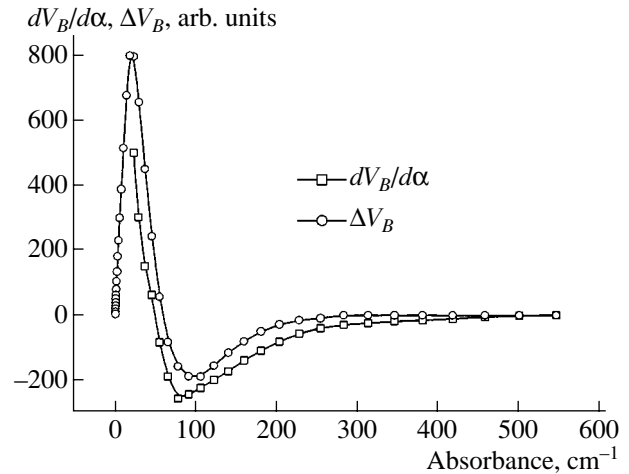dence $\Delta V_A(\alpha)$ in the type-*A* sample is quite different from the spectral characteristic of the derivative $dV_A(\alpha)/d\alpha$.

As for the type-*C* sample, the argumentation of the ΔV_C spectrum origin changes radically. Despite the fact that the characteristic $V_C(\alpha)$ is monotonic, the polarization difference ΔV_C is sign-alternating and twice crosses the horizontal axis. However, one of the intersections, at $\alpha \approx 5$ cm^{-1} (the inset in Fig. 3a), can be accounted for by the large reflectance from the specular back surface due to its metallization. Indeed, the high-intensity reflected light generates excess electron–hole pairs in the space-charge region adjacent to the *p–n* junction. These pairs give rise to a polarization difference of the same sign as strongly absorbed light.

An important conclusion can be drawn from Fig. 3b. The positive values of ΔV in all three cases are caused by the dichroism effect at a diffusion length comparable to the absorption length $1/\alpha$ for these characteristics. As for the dichroism at the space-charge region width *w*, it is so small in the case of the heavily doped type-*A* sample that is beyond the detectability of the used device. The situation is more favorable for the type-*B* and -*C* samples due to an increased Debye length, which allows observation of the anisotropy in the drift component of the junction photovoltage even for its monotonic characteristic. In the type-*C* sample (high-resistivity base), the magnitudes of the polarization difference of the spectral characteristic, as well as its extent, significantly exceed the corresponding values in the other cases. This circumstance is facilitated to a significant degree by the small thickness of the sample emitter region.

The conclusion concerning the dichroism drift component is based on an additional experiment aimed at measurement of the photovoltage spectral characteristics in the current mode at the two reverse bias voltages
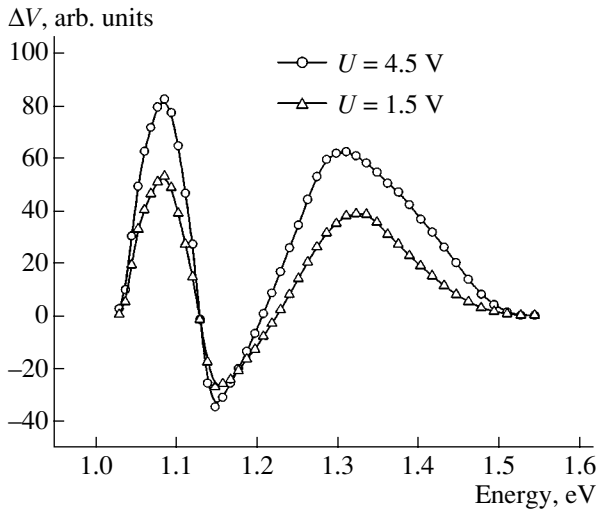
Fig. 5. Spectral dependences of the polarization difference ΔV_C at two reverse-bias voltages.

U = 1.5 and 4.5 V. The obtained characteristics ΔV_C, being versions of the curve ΔV_C in Fig. 3a, are shown, for convenience, in Fig. 5 in the form of the dependence on photon energy. We can see that one of the extrema, at $h\nu \approx 1.3$ eV, and one of the intersections of the curve with the energy axis are shifted to lower absorbances as the external voltage increases. However, this tendency can be expected, as the space-charge layer thickness increases due to a higher external voltage. In this case, the second intersection, at $E = 1.13$ eV, is independent of the bias voltage, since is caused by an unchanged diffusion length.

4. CONCLUSIONS

It is shown that a junction photovoltage spectral characteristic determined using polarization modulation of light in a weakly anisotropic *p–n* junction is a derivative of the spectrum with respect to the absorbance of an isotropic sample. Such a systematic feature is observed only in the type-*B* sample, in which the short electron lifetime τ, as follows from the characteristic shape in Fig. 3b, excludes the contribution of dichroism in the space-charge layer. This result is similar to the polarization difference of the photoconductivity (see Fig. 4 in [4]), and it can be understood by assuming that the contribution to the photopleochroism due to the space-charge layer does not manifest itself in this sample, as in the case of the photoconductivity. Expression (1), taking into account the dependence of the absorbance on the photon energy, is reduced to the expression

$$\Delta V = \frac{\partial V}{\partial \alpha}\frac{\partial \alpha}{\partial (h\nu)}\Delta \alpha, \qquad (3)$$

which, under the condition that $[\partial(h\nu)/\partial\alpha]\Delta\alpha \cong 1$, agrees with Fig. 4. Hence, it can be concluded that polarization modulation of light in the measurement of the junction photovoltage yields the spectral characteristic of the effect. This characteristic, as in the cases of transmission and photoconductivity, is the derivative of the spectral characteristic of an isotropic crystal with respect to the absorbance.

We note another methodical feature that manifests itself in this study. As was shown in [2], the polarization difference of the absorbances in a sample was determined indirectly using an external photodiode to measure the transmitted light intensity. In the case under consideration, the detecting element in the optical scheme was the *p–n* junction, i.e., a sample component, which immediately detected light-generated electron–hole pairs. At the same time, experience has shown that the contribution of the finite thickness x of the emitter to the measured value is negligible, as it should be under the condition $x < \lambda(2\pi n)$ (the Woltersdorff effect [10]). Furthermore, identification of the causes of such a variety of pleochroism characteristics was facilitated by the hierarchy of lengths employed in the used samples, i.e., $d > L > \omega > x$. Variation in the light wavelength and, hence, the absorbance when measuring the spectral characteristics allowed sequential exclusion of various causes of the pleochroism and their contribution to the resulting signal. It was found, at least in the case of the type-*C* sample, that there exist three pleochroism components related to the sample thickness, carrier diffusion length, and thickness of the region under the influence of the space-charge field of the *p–n* junction.

The last-mentioned observation is concerned with terminology. As we showed in [4], the pleochroism spectral characteristic $P = (V_\perp - V_\parallel)/(V_\perp + V_\parallel)$, at its small values $P \ll 1$ (which are found in the case under consideration), and the polarization difference characteristic $\Delta V = V_\perp - V_\parallel$ are absolutely identical. This circumstance means that the shape of $P(\alpha)$ is exclusively controlled by the properties of the numerator, which is referred to as the polarization difference. Therefore, the use (for brevity) of the term "pleochroism," along with the polarization difference, in this case should not cause objections.

REFERENCES

1. M. Cardona, *Modulation Spectroscopy* (Academic, New York, 1969; Mir, Moscow, 1972).

2. E. F. Venger, I. E. Matyash, and B. K. Serdega, Opt. Spektrosk. **94**, 38 (2003) [Opt. Spectrosc. **94**, 33 (2003)].

3. E. F. Venger, I. E. Matyash, and B. K. Serdega, Fiz. Tekh. Poluprovodn. (St. Petersburg) **37**, 1188 (2003) [Semiconductors **37**, 1160 (2003)].

4. I. E. Matyash and B. K. Serdega, Fiz. Tekh. Poluprovodn. (St. Petersburg) **38**, 684 (2004) [Semiconductors **38**, 657 (2004)].

5. F. P. Kesamanly, V. Yu. Rud', and Yu. V. Rud', Fiz. Tekh. Poluprovodn. (St. Petersburg) **33**, 513 (1999) [Semiconductors **33**, 483 (1999)].

6. A. P. Gorban', V. P. Kostylev, A. V. Sachenko, *et al.*, in *Optoelectronics and Semiconductor Engineering* (Naukova Dumka, Kiev, 2002), No. 37, p. 61 [in Russian].

7. *Annual Book of ASTM Standards* (1997), Sect. 10, Vol. 10.05.

8. F. T. Vas'ko and M. V. Strikha, Fiz. Tekh. Poluprovodn. (Leningrad) **24**, 1227 (1990) [Sov. Phys. Semicond. **24**, 773 (1990)].

9. W. C. Dash and F. Newman, Phys. Rev. **99**, 1151 (1955).

10. W. Woltersdorff, Z. Phys. **91**, 230 (1934).

Translated by A. Kazantsev

ELECTRONIC AND OPTICAL PROPERTIES
OF SEMICONDUCTORS

Mechanism of Radiative Recombination in the Region of Interband Transitions in Si–Ge Solid Solutions

A. M. Emel'yanov*^, N. A. Sobolev**^^, T. M. Mel'nikova**, and N. V. Abrosimov***

*Ioffe Physicotechnical Institute, Russian Academy of Sciences, St. Petersburg, 194021 Russia
^e-mail: Emelyanov@mail.ioffe.ru
**ORION Scientific and Industrial Corporation, Moscow, 111123 Russia
^^e-mail: nick@sobolev.ioffe.rssi.ru
***Institute for Crystal Growth, D-12489 Berlin, Germany
Submitted February 10, 2005; accepted for publication March 1, 2005

Abstract—The electroluminescence of Si–Ge diodes (with a Ge content of 5.2% in the corresponding solid solutions) in the region of interband transitions has been studied at the temperatures $T = 82$ K and 300 K. The emission spectra, the linear dependence of the electroluminescence intensity on current, and the exponential decay of the intensity suggest an exciton mechanism of radiative recombination with and without the involvement of phonons during radiative transitions. © 2005 Pleiades Publishing, Inc.

Studies of light-emitting structures based on single crystals of Si–Ge solid solutions have attracted considerable interest in the context of the opportunity to vary the radiation wavelength (λ) over a wide region of near-IR spectra by varying the content of the components in the solid solutions. Reasonably high internal efficiencies of electroluminescence (η) for such structures have already been achieved. According to [1], the maximum room-temperature efficiency $\eta = 0.1\%$ of Si- and Ge-based light-emitting diodes (including low-dimensional structures), which, for optical communication, typically emit at $\lambda \approx 1.3$ μm, has been attained precisely for diodes based on Si–Ge single crystals. It is worth noting that the maximal η indicated above is not a limiting value. The technology of Si–Ge light-emitting diodes can be included in the process of fabrication of integrated circuits based on silicon single crystal. The low-absorption waveguides for such optoelectronic devices can be manufactured from silicon. In this case, since the refractive indices of Si and Si–Ge are close to each other, the losses resulting from transfer of radiation from the emitting diode to the waveguide can be reduced to a minimum. An understanding of the mechanism of radiative recombination in Si–Ge solid solutions forms the physical grounds for accomplishment of the optimal characteristics of light-emitting structures based on Si–Ge and for successful applications of the structures.

Recent studies of the mechanism of indirect (phonon-assisted) radiative recombination occurring during interband transitions in Si single crystal [2] have led to a substantial shift away from earlier concepts. These studies have shown that the experimental results available can now be interpreted in the context of an exciton mechanism of radiative recombination in Si not only at low temperatures but also at comparatively high temperatures, including room temperature. The essential difference between the emission spectra of Si–Ge solid solutions and those of Si is that, in addition to emission due to phonon-assisted (PA) indirect transitions, there commonly exists, in the spectra of Si–Ge, a comparable emission due to transitions in which no phonons are involved (NP transitions) [1, 3–6]. The purpose of this study is to clarify the influence of such conditions on the characteristics of recombination emission in the region of interband transitions in Si–Ge single crystal and to identify the mechanism of radiative recombination in Si–Ge that accounts for these characteristics.

The diodes to be studied were prepared from a (122)-oriented polished wafer of boron-doped Si–Ge single crystal. The thickness of the wafer was about 350 μm, and its resistivity was 2.5 Ω cm. The Ge content was 5.2%. The *p–n* junctions were formed by planar technology, with a diffusion of phosphorus through the windows of 0.8 mm in diameter in a SiO_2 film. The phosphorus concentration in the n^+-type layer was $\sim 4 \times 10^{20}$ cm^{-3}. The rear side of the plate was doped by a diffusion of boron up to a concentration of $\sim 10^{19}$ cm^{-3}. Ohmic contacts were formed on the front and rear sides of the wafer by thermal sputtering of Au and Cr. Spectra for the emission from the front side were recorded. The minority-carrier lifetime, determined by the procedure used in [7], was ~ 11 μs at currents of 0.3–1.0 A.

In order to excite the electroluminescence (EL), a pulsed voltage was applied to the diodes at a pulse repetition frequency of 32 Hz and pulse duration of 0.1–0.2 ms. The EL spectra were recorded using a mono-
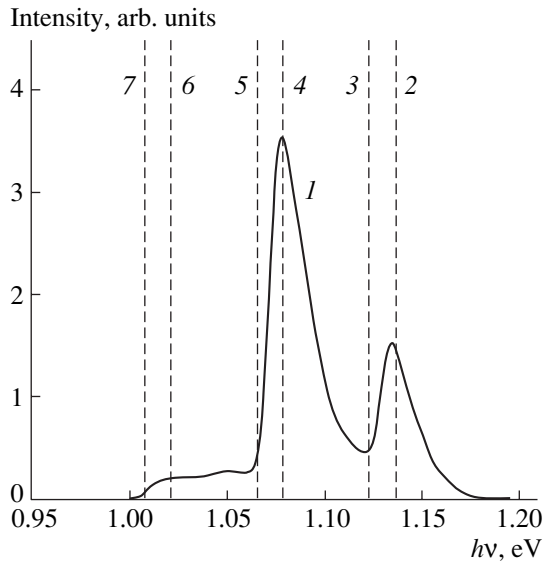
Fig. 1. Dependence of the electroluminescence intensity on the photon energy $h\nu$ at a current of 80 mA and temperature of 82 K (curve *1*). The dashed vertical lines refer to photon energies corresponding to (*2*) the band gap of the Si–Ge solid solution at $T \approx 82$ K ($E_g(82$ K$) \approx 1.137$ eV [8, 9]), (*3*) $E_g(82$ K$) - E_{ex}$, (*4*) $E_g(82$ K$) - E_{ph1}$, (*5*) $E_g(82$ K$) - E_{ph1} - E_{ex}$, (*6*) $E_g(82$ K$) - 2E_{ph1}$, and (*7*) $E_g(82$ K$) - 2E_{ph1} - E_{ex}$.
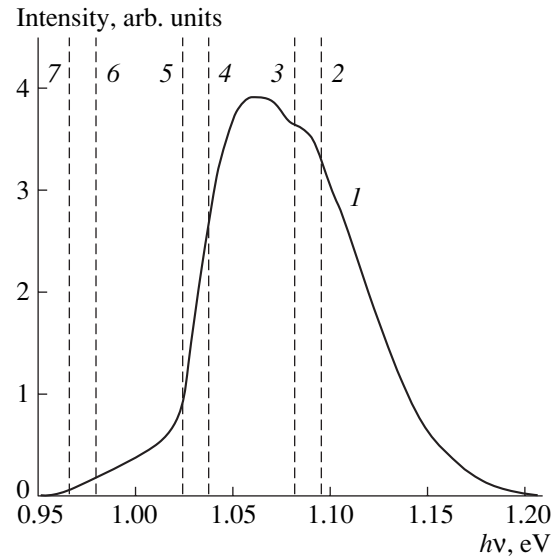

Fig. 2. Dependence of the electroluminescence intensity on the photon energy $h\nu$ at a current of 80 mA and temperature of 300 K (curve *1*). The dashed vertical lines refer to photon energies corresponding to (*2*) the band gap of the Si–Ge solid solution at $T \approx 300$ K ($E_g(300$ K$) \approx 1.096$ eV [8, 9]), (*3*) $E_g(300$ K$) - E_{ex}$, (*4*) $E_g(300$ K$) - E_{ph1}$, (*5*) $E_g(300$ K$) - E_{ph1} - E_{ex}$, (*6*) $E_g(300$ K$) - 2E_{ph1}$, and (*7*) $E_g(300$ K$) - 2E_{ph1} - E_{ex}$.

chromator (with the resolution 7 nm), an InGaAs-based photoelectric detector, and a selective nanovoltmeter. The spectra were corrected with regard to the spectral characteristics of the photodetector and the entire optical path.

Figures 1 and 2 show the emission spectra of an EL diode. The spectra were obtained with a current of 80 mA at temperatures of 82 K (Fig. 1) and 300 K (Fig. 2). Here, as in the spectra of previously studied Si–Ge diodes [1, 3–6], EL peaks related to PA and NP transitions can clearly be seen. At $T = 300$ K, a noticeable overlapping of these peaks is evident (Fig. 2). When analyzing the spectra, we used a method focusing on the vertical straight lines corresponding to the onset of an increase in the EL intensity in the long-wavelength part of the spectra for different mechanisms of radiative recombination in Si–Ge (see dashed vertical lines *2–7* in Figs. 1 and 2). The method was described in [2]. At a fixed temperature T, the band gap of a Si–Ge solid solution with a 5.2% Ge content $E_g(T)$ is narrower than the band gap of Si by ~24 meV [8], and the binding energy of the charge carriers in the exciton state (E_{ex}) is ~13.5 meV [3]. In this case, it follows from the results of [4] that the energy released in the recombination events involving transverse optical (TO) phonons defines the major EL peak and is equal to $E_{ph1} = 58$ meV. By analogy with Si, it is assumed that the energy of the phonons with the highest energy (E_{ph2}) is equal to $2E_{ph1}$, since two TO phonons of energy E_{ph1} are involved in a recombination event [9].

When analyzing the EL spectra, we used the following concept: at photon energies corresponding to the onset of each mechanism of radiative recombination (at the intersections of the spectral curves with the related vertical lines), bends in the spectral curves should be observed. These bends are accompanied by an increase in the derivatives of the dependences of the EL intensity on the photon energy $I(h\nu)$. It is obvious that such bends can be noticeable if the related contribution of a particular EL mechanism is sufficiently large. As can be seen from Figs. 1 and 2, the typical bends at 82 and 300 K are observed only for the exciton EL mechanisms. This circumstance allows us to argue that, in Si–Ge solid solutions, the predominant form of radiative recombination during PA and NP transitions is recombination via exciton states.

In the structures under study, linear dependences of the integrated EL intensity on the current were observed over a wide range of currents under the conditions of high-level injection (see Fig. 3). In addition, exponential decay of the EL was observed at as low as 300 K. The experimental procedure for studying EL decay has been described in [2]. As was shown in [2], the above two results can also be explained in the context of the exciton mechanism. It should be noted that no explanation for these results is provided by the model of radiative recombination of free charge carriers.

It was noted in [2] that, for predominance of the exciton mechanism of radiative recombination in Si at
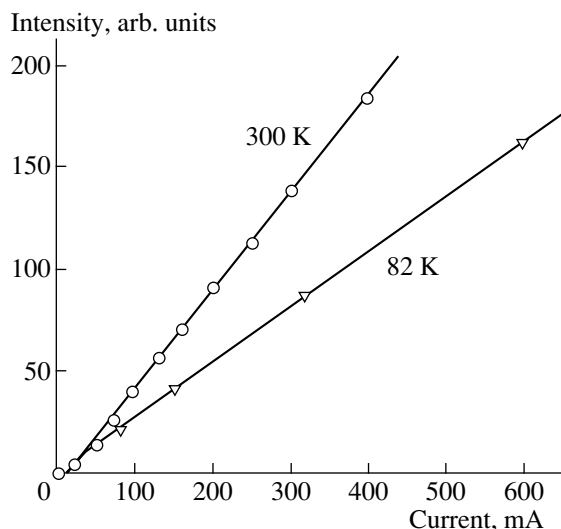
Intensity, arb. units

Fig. 3. Dependences of the electroluminescence integrated intensity on the current at 82 and 300 K.

300 K, it is necessary that the exciton radiative lifetime (τ_r) is several orders of magnitude shorter than the free-carrier radiative lifetime (τ_f). The same relationship between τ_r and τ_f is required for predominance of the exciton mechanism in Si–Ge at 300 K. As was noted in [2], this relationship is a consequence of two circumstances: first, the average spacing between free carriers is much larger than the exciton Bohr radius; second, radiative recombination necessitates a certain correlation between the positions of the electron, hole, and phonon emitted or absorbed in a recombination event. Such a correlation has a much higher probability of occurring in the case of recombination via excitons. According to the present concepts [4], radiative recombination with the participation of NP transitions in Si–Ge involves dopant atoms that allow compliance with the momentum conservation law in indirect transitions. Therefore, the second reason for the substantial difference between the times τ_r and τ_f for NP transitions

(the first reason being the substantial difference in the average spacing between the electron and hole) may be the necessity of a certain correlation between the positions of the electron, hole, and dopant atom. This correlation has a much higher probability of occurring in the case of recombination via excitons.

In conclusion, it should be noted that, at a current of 600 mA and temperature of 300K, the EL of the fabricated Si–Ge light-emitting diodes induced nearly the same photocurrent in the Ge photodiode as that induced by the EL of the previously studied Si light-emitting diode with $\eta \approx 0.6\%$ when focusing radiation onto the photodetector under similar conditions.

REFERENCES

1. T. Stoica and L. Vescan, Semicond. Sci. Technol. **18**, 409 (2003).
2. A. M. Emel'yanov, Pis'ma Zh. Tekh. Fiz. **30** (22), 75 (2004) [Tech. Phys. Lett. **30**, 964 (2004)].
3. D. J. Robbins, L. T. Canham, S. J. Barnett, *et al.*, J. Appl. Phys. **71**, 1407 (1992).
4. J. Weber and M. I. Alonso, Phys. Rev. B **40**, 5683 (1989).
5. T. Stoica, L. Vescan, and M. Goryll, J. Appl. Phys. **83**, 3367 (1998).
6. T. Stoica, L. Vescan, A. Mück, *et al.*, Physica E (Amsterdam) **16**, 359 (2003).
7. B. Lax and T. Neustadter, J. Appl. Phys. **25**, 1148 (1954).
8. R. Braunstein, A. R. Moor, and F. Herman, Phys. Rev. **109**, 695 (1958).
9. R. A. Smith, *Semiconductors*, 2nd ed. (Cambridge Univ. Press, Cambridge, 1978; Mir, Moscow, 1979).
10. A. M. Emel'yanov, Yu. A. Nikolaev, N. A. Sobolev, and T. M. Mel'nikova, Fiz. Tekh. Poluprovodn. (St. Petersburg) **38**, 634 (2004) [Semiconductors **38**, 610 (2004)].

Translated by É. Smorgonskaya

Magnetism of III–V Crystals Doped with Rare-Earth Elements

N. T. Bagraev*^ and V. V. Romanov**

Ioffe Physicotechnical Institute, Russian Academy of Sciences, St. Petersburg, 194021 Russia
^e-mail: impurity.dipole@mail.ioffe.ru
**St. Petersburg State Polytechnical University, St. Petersburg, 195251 Russia*
Submitted February 21, 2005; accepted for publication March 7, 2005

Abstract—The procedure of measuring static magnetic susceptibility is used for the study of local ordering in III–V crystals containing rare-earth dopants. The dependences of the static magnetic susceptibility on the temperature and magnetic field show a slight paramagnetism at high temperatures due to quasi-molecular Ln_2O_3-type centers present in the III–V(Ln) crystals. In such centers, the pairs of Ln^{3+} ions are antiferromagnetically ordered by an exchange interaction via the oxygen valence electrons. At low temperatures, the crucial role is played by localization of electrons at shallow donors. Due to the s–f exchange interaction, such localization results either in paramagnetism of the crystals, due to transformation of the Ln_2O_3 molecules from the antiferromagnetically ordered state to an ferromagnetically ordered state, or in superparamagnetism, due the formation of bound spin polarons. In this case, the constants of the s–f exchange interaction determined from the temperature dependences of the static magnetic susceptibility are anomalously large. This circumstance probably results from the efficient compensation of spin correlations by the electron–vibration interaction. © 2005 Pleiades Publishing, Inc.

1. INTRODUCTION

The development of solid-state devices for microelectronics and nanoelectronics is primarily based on the possibility of controlling the electrical characteristics of semiconductor materials. The electrical parameters of such materials are closely related to their magnetic and optical properties, which are defined by intrinsic and/or extrinsic defects [1–3]. In turn, point defects and extended-defect centers, which are varieties of extrinsic and intrinsic defects, are characterized by the interplay between charge (spin) correlations and the electron–vibration interaction (EVI). Such interplay conditions the two fundamental properties of the defects: their metastability, as a consequence of charge-transfer-induced changes in the position of the center in the crystal lattice, and compensation of the Coulomb repulsion of electrons at the center [4–6]. These two properties are most adequately represented in the behavior of the magnetic moment, which can be easily monitored by measuring the dependences of the static magnetic susceptibility on temperature and field. Such measurements can be performed without exposure of the samples to optical radiation as well as under exposure with the use of various sources of monochromatic or nonmonochromatic radiation [7–10].

In this study, the potential of the method of measuring the static magnetic susceptibility for understanding the interplay between the EVI and charge (spin) correlations is demonstrated using the example of the magnetic properties of III–V crystals containing rare-earth elements (REEs). The magnetic properties of these compounds are governed by the formation of point-type quasi-molecular rare-earth centers (QMRECs) and by magnetic ordering via the s–f exchange interaction in the domains in which there is a high local density of QMRECs [10, 11].

2. EXPERIMENTAL

2.1. REE Centers in III–V Crystals

There exist at least two basic reasons why semiconductor crystals containing REE dopants attract particular interest. The first reason is related to the electronic structure of the REE atoms, which considerably differentiates lanthanides from other magnetic dopants. The second reason is that it is possible to produce semiconductor materials that can be characterized by interplay between their electrical, magnetic, and optical properties.

The magnetic $4f$ electron shell of an REE atom is well screened by $5p$ and $5s$ electrons and, thus, can be only slightly distorted by the electric field of the ligands. This fact makes it possible to study the intracenter luminescence and absorption in virtually any matrix. The intracenter luminescence spectra of REE centers consist of a set of narrow lines (with a width smaller than 1 nm), since the ground states of the centers are barely hybridized with the band states of the crystal at all and the excited states are hybridized only slightly [3]. Moreover, the first studies of the electron spin resonance (ESR) and intracenter luminescence have shown that REE atoms, with the exception of gadolinium and europium, occupy cation sites in the III–V crystal lattice with a tetrahedral surrounding and bond via their two $6s$ and one $4f$ electrons [12, 13].
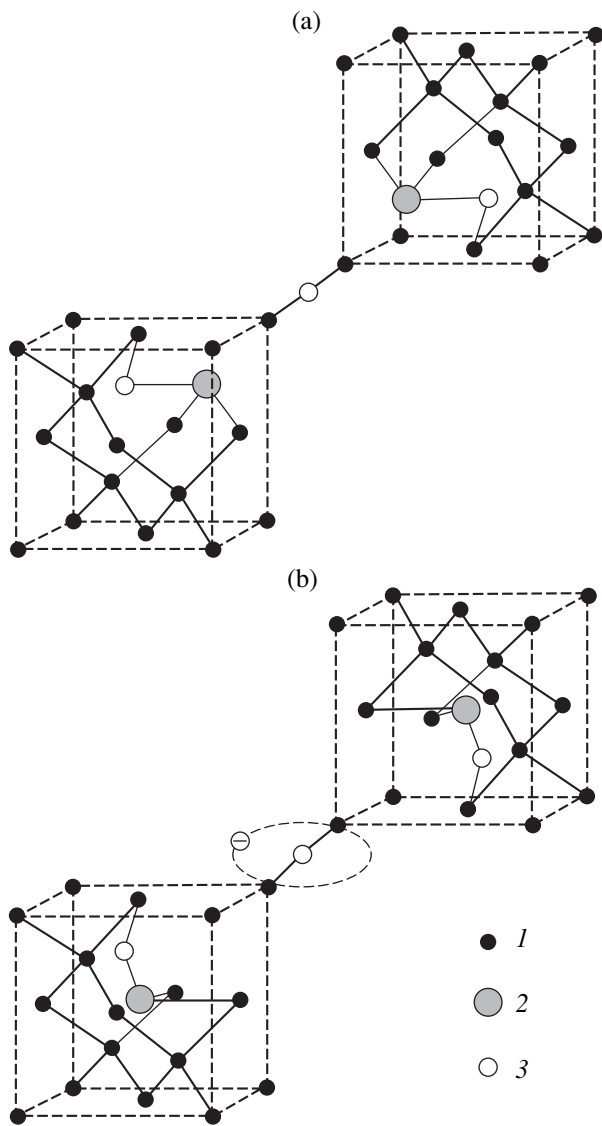
Fig. 1. Schematic representation of the trigonal quasi-molecular rare-earth center Ln_2O_3 in the (a) antiferromagnetically ordered and (b) ferromagnetically ordered states. The numbers refer to (*1*) the atoms of the basic lattice, (*2*) rare-earth atoms, and (*3*) oxygen atoms.

At first sight, therefore, it seems that the EVI should produce only a weak effect on the structure of the REE centers in III–V crystals. However, even the "smallest" lanthanide, ytterbium, when occupying the cation site, causes a profound "overstressing" of the lattice; as a result, the tetrahedral symmetry of the REE centers seems to be not the only possible symmetry in this case. In fact, further studies of the photoluminescence have revealed trigonal REE centers [14–16]. In addition, low-symmetry REE centers have been detected in III−V crystals from ESR measurements [17] and in studies of the Zeeman effect in high magnetic fields [18]. It should be noted that the tetrahedral centers were evident only in samples with a high content of REE

dopants, i.e., with an REE content much higher than the content of the residual carbon and oxygen impurities. At the same time, low-symmetry REE centers prevail in III–V crystals with a lower content of REE dopants [3, 12–18]. Thus, taking into account the high chemical activity of the REE, especially towards oxygen and carbon, we can assume that the low-symmetry REE centers in III–V crystals are Ln_2O_3-type quasi-molecular rare-earth centers (QMRECs) (Fig. 1a). Because of the weak paramagnetism, it is most reasonable to study the magnetic properties of QMRECs by recording the dependences of the magnetic susceptibility on temperature and magnetic fields.[1]

2.2. Experimental Procedure for Measurements of the Static Magnetic Susceptibility

The samples to be studied were grown from a molten solution and by the Bridgman–Stockbarger method. The samples were doped with the REEs from the melt. The concentration of REE dopants in the III–V crystals was determined, by spectral and neutron-activation analyses, to be at the level 10^{17}–10^{21} cm^{-3}.

The static magnetic susceptibility of the REE-doped III–V crystals was measured according to Faraday's procedure using an MGD 312 FG system. The magnetic fields ranged up to 15 kG.

The static magnetic susceptibility was determined from the relation

$$\chi(T, B) = \frac{F(T, B)}{mBdB/dz}, \tag{1}$$

where $\chi(T, B)$ has the dimension $[\chi] = $ cm^3/g and m is the sample mass (for the samples under study, $m = 0.1$–0.1 g). The value of the force acting on a sample in the strongly nonuniform field, $F(T, B)$, was measured using a precision electromechanical balance, which was involved in the setup. The magnetic field gradient was directed vertically upward along the fiber suspension (the z axis).

The setup was calibrated and the quantity BdB/dz was determined in an independent experiment at room temperature. In this experiment, an InP crystal with the known magnetic susceptibility $\chi_{dia} = -313 \times 10^{-9}$ cm^3/g was used as a reference sample. The value of BdB/dz measured when in this way was $\leq 2 \times 10^7$ cgsm.

The induction of the external magnetic field at the sample location was determined using a Hall detector or from the field dependence of the magnetic susceptibility χ_{para} of the CdF$_2$(Mn) samples at the temperature $T = 4.2$ K.

The MGD 312 FG setup allows measurements in the temperature range 3.2–300 K. The samples were placed in a quartz bowl suspended from the balance by a thin quartz fiber. The balance was encased, together with a

---

[1] Here and below, *Ln* is the general notation of any chemical element of the lanthanide Group.
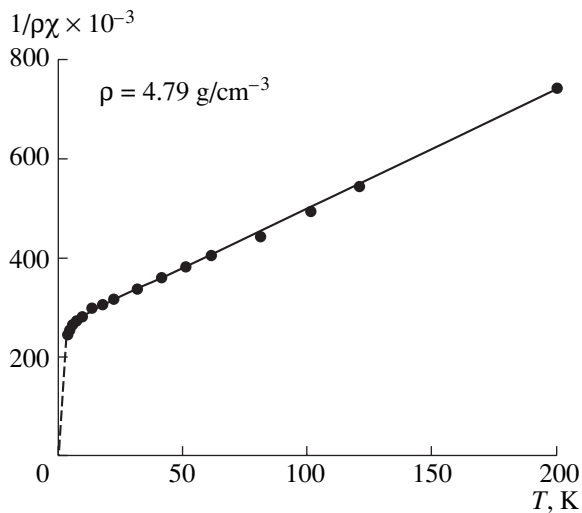
Fig. 2. Temperature dependence of the static magnetic susceptibility of the InP:Yb crystals with a statistically uniform distribution of rare-earth dopants over the bulk. The crystals were grown by the Bridgman–Stockbarger method; the Yb dopant was introduced when growing the crystal from the melt. The dependences calculated by Eq. (2) (solid line) and by Eq. (3) with regard to the contribution of the ferromagnetically ordered QMRECs (dashed line) are shown.

Fig. 3. Temperature dependence of the static magnetic susceptibility of the dendrite InP:Yb crystals doped with Yb during growth. The solid line corresponds to the dependence calculated by Eq. (4).

Fig. 4. Temperature dependence of the static magnetic susceptibility of the InP:Er crystals with a low Er concentration.

sample, in a hermetically sealed chamber. Before the measurements, the space inside the chamber was evacuated. Then, the chamber was filled with gaseous helium up to the pressure ~200 Torr to provide the necessary heat transfer between the sample and the chamber walls, whose temperature was kept constant. The walls of the chamber, where the sample was located, were cooled by a regulated flow of liquid helium vapors forcedly extracted from a Dewar vessel, with the temperature controlled to keep it at a fixed level. The temperature was measured by thermistors attached to the wall in the inner space of the cryostat. The thermistors were calibrated to within a hundredth of a Kelvin degree by a gas thermometer containing nitrogen, hydrogen, and helium.

The static magnetic susceptibility of the REE-doped III–V crystals was measured by a two-stage procedure. At the first stage, reference measurements for the empty quartz bowl were carried out at different temperatures over the entire range of magnetic fields. At the second stage, similar measurements were carried out with a sample in the bowl. The results of the reference measurements of the magnetic susceptibility were subtracted from the results of the second-stage measurements for the sample.

When measuring the static magnetic susceptibility, the sensitivity of the MGD 312 FG setup was no lower than 10^{-9} cm^{-3}/g. The errors in determining the value of $\chi(T, B)$ arise from errors generated by the balance (on the order of few micrograms) and from the inaccuracy involved in placing a sample in the same region of the nonuniform magnetic field when changing the sample
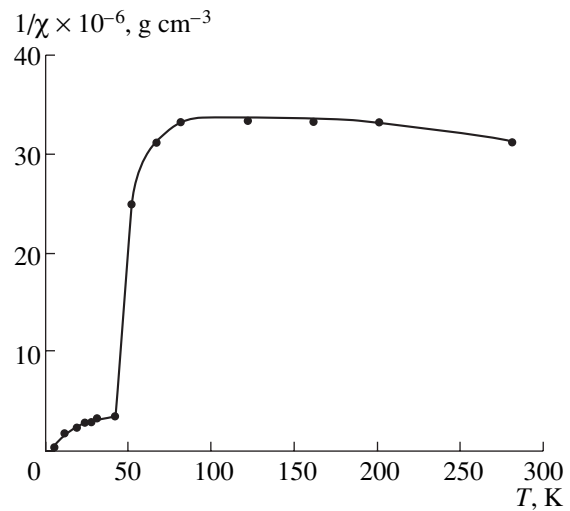
and partially disassembling the setup. The major error in the absolute value of the susceptibility was introduced by the measurement of the sample mass with the use of an ADV-200 analytic balance.

2.3. Temperature Dependences of the Static Magnetic Susceptibility

The experimental and calculated temperature dependences of the magnetic susceptibility of the REE-doped III–V crystals are shown in Figs. 2–10. It is clear that, over a wide temperature range, these dependences cannot be adequately described by the Langevin–Brillouin function that transforms into the Curie law at $kT \gg \mu H$.

Fig. 5. Temperature dependence of the static magnetic susceptibility of the GaP crystals doped with (*a*) gadolinium (the left-hand ordinate axis), (*b*) thulium, (*c*) terbium, and (*d*) erbium.

Fig. 6. Temperature dependence of the static magnetic susceptibility of the GaP crystals doped with (*a*) ytterbium, (*b*) neodymium, and (*c*) cerium.
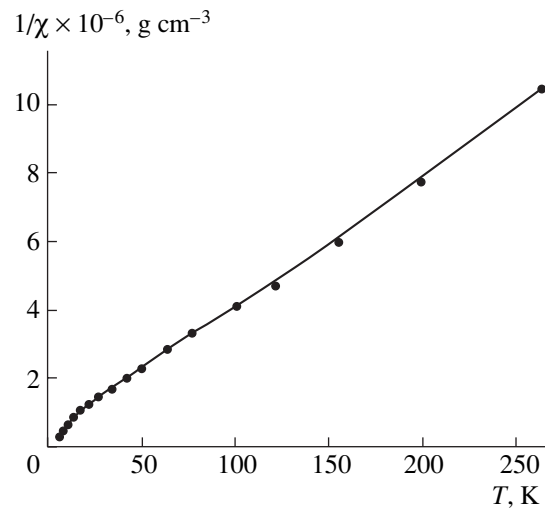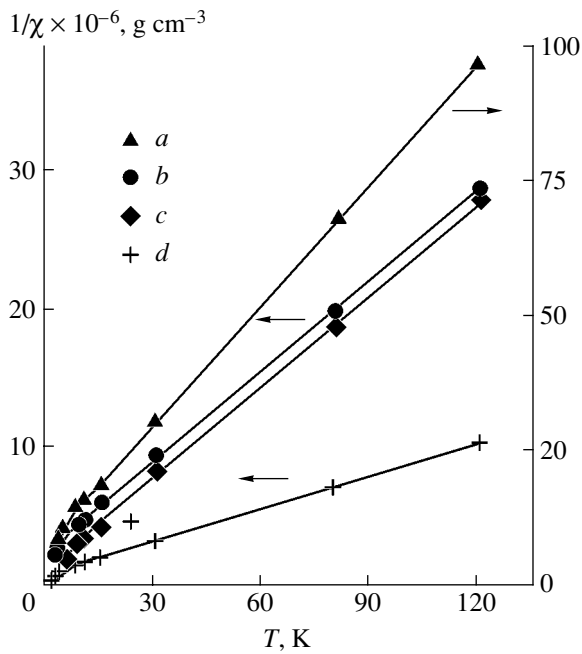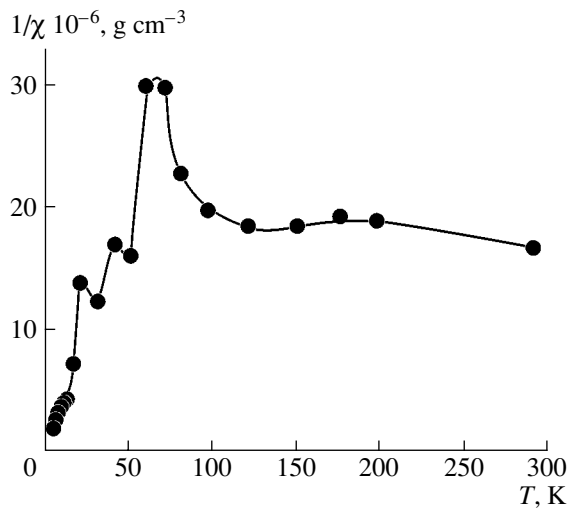

Fig. 7. Temperature dependence of the static magnetic susceptibility of the InP:Er crystals with a high Er concentration.

Fig. 8. Temperature dependence of the static magnetic susceptibility of the InP:Nd crystals containing "second-phase" inclusions.

Moreover, the magnetic susceptibility of the III–V crystals doped, e.g., with ytterbium, erbium, neodymium, or dysprosium is independent of temperature or monotonically varies with temperature. Thus, the REE dopants cannot be considered as a system of weakly interacting single-atom paramagnetic centers in III–V crystals.

In fact, the ESR spectra and the temperature dependences of the static magnetic susceptibility of the InP:Yb and InP:Gd crystals studied immediately after their synthesis and within a weak or a month after the synthesis show that the content of residual single-atom paramagnetic REE centers sharply decreases over time. These data suggest an intense "degradation" of the solid solution of the lanthanides in the III–V crystals doped with the REE in the melt. The degradation proceeds more intensively in solid solutions in which the difference in ionic radii between a lanthanide atom and a

substituted atom of the crystal lattice is more profound. This inference follows, in particular, from comparison of the data for samples doped with Gd and Yb [19].

The temperature-induced behavior of the static magnetic susceptibility and its essential independence of the external magnetic field confirm the assumption that the thermodynamically equilibrium state of the materials corresponds to a system of weakly interacting molecules of the Ln_2O_3 type, i.e., a system of QMRECs, in which the REE atoms are coupled via the exchange interaction. It should be emphasized that the paramagnetic centers involving single REE ions are probably observable in ESR measurements if the REE content is higher that the content of uncontrollable impurities in the III–V crystals.

2.4. The Ln_2O_3 Quasi-Molecules

In the range of relatively high temperatures, the REE atoms involved in quasi-molecules have the capability to order their magnetic moments in antiparallel directions, thus forming antiferromagnetically ordered pair centers. This behavior is due to a Bloembergen-type exchange interaction via the oxygen valence electrons [11, 20]. In this temperature range, variation in the magnetic susceptibility can be adequately described by the expression [10]

$$\chi = \frac{2N\mu_B^2 g^2}{3kT} \frac{\sum_I I(I+1)\exp\left[-\frac{a}{2kT}I(I+1)\right]}{\sum_I \exp\left[-\frac{a}{2kT}I(I+1)\right]}, \quad (2)$$

where a is the constant of the exchange interaction, and N and I are the density and the spin of the QMRECs, respectively.

The exchange interaction of the REE atoms in a quasi-molecule should be considered in close connection with the EVI, since the interaction of a center with the crystal lattice compensates, to a large degree, the spin and charge correlations. This compensation yields anomalously large values of the constant of the exchange interaction a (tenths of eV), thus making the antiferromagnetic ordering in the QMRECs observable at high temperatures [6, 10]. In the case of relatively small a, the exchange interaction in the QMRECs can degrade with an increase in temperature; then, the temperature dependence of the susceptibility will follow the Curie–Weiss law (Fig. 2).

At low temperatures, free electrons become localized at shallow donors. This effect results in an enhancement of the paramagnetism of the III–V crystals. It is clear, however, that the total contribution of shallow donor atoms to the increase in the magnetic susceptibility observed at low temperatures is negligible, since their concentration is, as a rule, no higher than $\sim 10^{18}$ cm^{-3}. At the same time, the electrons localized at shallow donors play a crucial role in the mag-
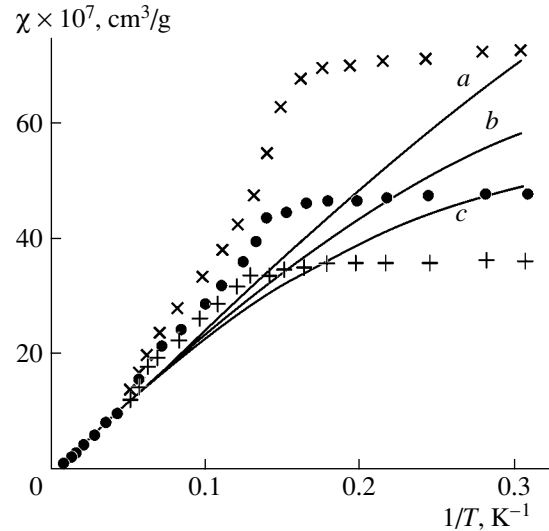
Fig. 9. Temperature dependence of the static magnetic susceptibility of the GaP:Dy crystals containing "second-phase" inclusions in different magnetic fields: (*a*) 0.5 T, (*b*) 1.0 T, and (*c*) 1.45 T.

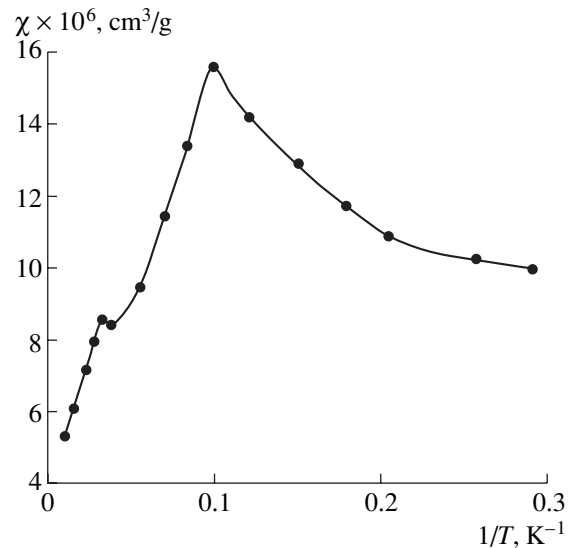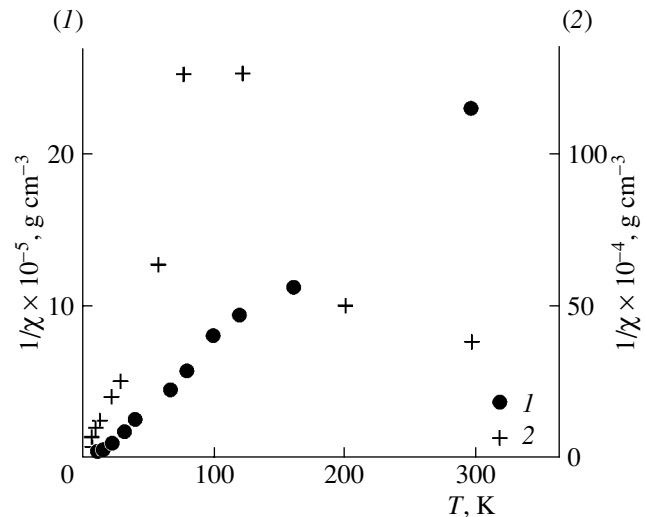**Fig. 10.** Temperature dependence of the static magnetic susceptibility of the InP:Eu crystals with the Eu concentrations (*1*) $N = 10^{18}$ cm^{-3} and (*2*) $N = 10^{20}$ cm^{-3}.

netic properties of the REE-doped III–V crystals. If a single QMREC falls on the orbit of an electron localized at a shallow donor, the REE ions involved in the antiferromagnetically ordered quasi-molecule transform into a ferromagneically ordered state due to the *s–f* exchange interaction via the donor electron [10, 11]. In the course of an exchange interaction event, an electron at a shallow donor is trapped by a QMREC. Such trapping is favorable particularly due to the large constant of the exchange interaction a, as follows from the above-mentioned interplay between the spin correlations and the EVI (Fig. 1b). In this case, the ferromagnetically

ordered QMRECs formed in the vicinity of shallow donors give rise to the paramagnetic component of the static magnetic susceptibility at low temperatures:

$$\chi = \frac{2N\mu_B^2 g^2}{3kT} \frac{\sum_I I(I+1)\exp\left[-\frac{a}{2kT}I(I+1)\right]}{\sum_I \exp\left[-\frac{a}{2kT}I(I+1)\right]}$$ (3)

$$+ \frac{\mu_B^2 g^2}{3kT}\{N[I(I+1)-I'(I'+1)]+N_d I'(I'+1)\}.$$

Here, N and I are the density and the spin of a QMREC, respectively; and N_d and I' are the density and the spin of a shallow donor involved in the formation of a ferromagnetically ordered QMREC.

Along with the formation of ferromagnetically ordered QMRECs, a competing process, namely, the formation of domains of spontaneous polarization (spin polarons) can be observed [10, 11]. Spin polarons can be produced if ten or more QMRECs are found within the orbit of a shallow donor. Such a situation can occur in regions of high local REE concentrations at relatively low temperatures [10]. Then, as a result of the s–f exchange via an electron at a shallow donor, several neighboring antiferromagnetic QMRECs transform into a ferromagnetic state and form a unified system that is referred to as a bound spin polaron. In this process, the energy of the donor electron involved in the exchange interaction is lowered depending on the constant of the s–f exchange interaction.

The temperature dependence of the static magnetic susceptibility of III–V crystals containing separated QMRECs and spin polarons localized at shallow donors (Fig. 3) can be described by the expression [10]

$$\chi = \frac{\mu_B^2 g^2 |J|^2 N_F}{3kT}$$

$$+ \frac{2N\mu_B^2 g^2}{3kT} \frac{\sum_I I(I+1)\exp\left[-\frac{a}{2kT}I(I+1)\right]}{\sum_I \exp\left[-\frac{a}{2kT}I(I+1)\right]}.$$ (4)

Here, N and I are the density and the spin of a QMREC, respectively; and N_F and J are the density and the moment of a spin polaron localized at a shallow donor. The moment J is calculated by solving the corresponding Schrödinger equation [21]

$$|J| = \int \langle L \rangle M d^3 r = 4\pi N \int_0^b \langle L \rangle r^2 dr,$$ (5)

where $\langle L \rangle$ is the average spin of an REE center and b is the Bohr radius of a shallow donor. It should be noted that the contribution of QMRECs to the static magnetic susceptibility becomes substantial only when their local concentrations are above 10^{20} cm^{-3}.

The temperature dependences of the static magnetic susceptibility calculated with expressions (3) and (4) are shown in Figs. 2 and 3. It is clear that, in the high-temperature region, a QMREC can exhibit paramagnetic properties if the energy of thermal motion of the constituent REE atoms is comparable to the constant of the exchange interaction a, which results in the thermal motion causing degradation of the interplay between the spin correlations and the EVI [6]. A decrease in temperature promotes antiferromagnetic ordering of the magnetic moments of the REE atoms in a QMREC via the oxygen valence electrons. At low temperatures, the major contribution to the magnetic susceptibility is made by the spin polarons localized at shallow donors, although their concentration is low, and by single ferromagnetically ordered QMRECs, as their moment increases sharply as the temperature decreases. It is worth noting that, with an increase in the concentration of shallow donors, the spin polarons can form a superparamagnetic system [22].

In what follows, we will analyze the characteristics of QMRECs formed from different REE atoms. These characteristics manifest themselves in the experimentally studied behavior of the static magnetic susceptibility of III–V crystals.

2.4.1. Ytterbium centers in indium phosphide. The QMREC model suggested above makes it possible to explain the weak paramagnetism of InP:Yb crystals, which is revealed by measuring the static magnetic susceptibility at high temperatures (Figs. 2 and 3). In this case, the ground state of ytterbium in indium phosphide, as in silicon [10], corresponds to an electrically inactive antiferromagnetically ordered QMREC that is a singlet with a zero magnetic moment. Due to overlap of the excited states of the neighboring QMRECs, however, the prohibition of temperature-induced transitions to the high-spin state is partially removed. This effect manifests itself in the high-temperature region (at $T > 20$ K) of the dependence of the magnetic susceptibility (Fig. 2). It also follows from the temperature dependence of the static magnetic susceptibility that, for the samples under study, the constant a exhibits a dispersion that is caused by a noticeable number of pairs of oxygen-based QMRECs, in addition to the single QMRECs, and by possibly formed quasi-molecular centers based on other chalcogenes.

As the temperature decreases, the effect of shallow donors with an activation energy of 6 meV becomes more pronounced. The electrons of these donors promote, via the s–f exchange interaction, transformation of the QMRECs into the ferromagnetically ordered state. As was noted above, a donor electron involved in the exchange interaction is trapped by a QMREC. In this case, the trapping of the donor electron at the "bridge" oxygen is accompanied by a change in the position of the ytterbium atoms to compensate for the

increase in the energy of the Coulomb repulsion and, hence, to stabilize the ferromagnetically ordered state of the QMREC (Fig. 1b). In the context of this mechanism of formation of ferromagnetically ordered QMRECs, in which the EVI plays the crucial role, the large values of the constants of the indirect exchange interaction can be explained. These large constants manifest themselves, among other things, in the temperature dependence of the static magnetic susceptibility, which follows the Curie law at low temperatures (Figs. 2 and 3).

In an InP:Yb crystal, for which the temperature dependence of the magnetic susceptibility is shown in Fig. 3, the average concentration of Yb dopants is $\sim 10^{17}$ cm^{-3}, as was shown by chemical spectral analysis. This concentration is two orders of magnitude lower than the Yb content in the InP:Yb crystal described above. The behavior of the magnetic susceptibility at temperatures above 80 K still suggests the major role of the QMRECs. At the temperatures between 80 and 40 K, however, the magnetic susceptibility of the sample varies exponentially, suggesting the formation of domains of high local REE concentration, where the REE density is several orders of magnitude higher than the average concentration in the sample bulk. The anomaly observed in the temperature dependence of the magnetic susceptibility can be explained if it is assumed that, as a result of the indirect s–f exchange interaction, a spin polaron localized at a shallow donor is formed.

The lowering of the energy of a donor electron involved in the formation of a spin polaron is then reflected in the "red" shift of the emission band of radiative recombination and in the spectrum of intracenter photoluminescence of an REE center. Indeed, the corresponding shift (1.35–1.40 eV) can be seen in the photoluminescence spectra of the InP:Yb crystals, in which the content of ytterbium introduced by ion implantation was as high as 10^{19} cm^{-3} [14–16]. The "red" shift of the photoluminescence band is in good agreement with the calculated results derived by solving the Schrödinger equation. Furthermore, this shift is consistent with the spin-polaron binding energy determined from the temperature dependence of the static magnetic susceptibility (Fig. 3).

Below 40 K, the InP:Yb sample exhibits the properties of a superparamagnetic crystal, since the interaction between spin polarons as well as between ferromagnetically ordered QMRECs is negligible. As a result, the temperature dependence of the static magnetic susceptibility of the InP:Yb samples can be described by the Langevin–Brillouin function. In this case, by the effective magnetic moment of the paramagnetic center, we mean the average effective moment of a spin polaron or ferromagnetically ordered pair (see expressions (3) and (5)).

2.4.2. Erbium centers in indium phosphide. Similarly to ytterbium, when erbium is introduced into InP

crystals, it can be detected not only in optical studies but also in ESR measurements [23]. Study of the ESR spectra has shown that the ground state of an Er^{3+} ion embedded in InP is the $\Gamma_{6(7)}$ doublet. The shape of the ESR lines suggests a slight axial distortion of the earlier assumed tetrahedral symmetry of the erbium centers. For Er-doped III–V compounds, intracenter luminescence at the wavelength $\lambda = 1.54$ μm (0.8 eV) has been observed in layers grown by deposition from the gas phase [24] and in crystals doped with erbium by ion implantation [14, 25]. As a result, it was established that erbium centers are noncubic. However, because of the specific features of the behavior of REEs discussed above, it is impossible to assess the interplay between the Er-controlled magnetic and optical properties of the crystals from these data.

Studies of the temperature dependence of the magnetic susceptibility of InP:Er crystals have shown that the behavior of erbium centers can be interpreted in the context of the formation of QMRECs. In the case of InP:Er, this dependence does not suggest that there exists a dispersion in the values of the constant of the exchange interaction a as in the above-considered case of InP:Yb (Fig. 4). This difference is probably due to the lower REE content in InP:Er compared to InP:Yb. As, in this case, there is a statistically uniform distribution of the lanthanides over the crystal bulk, the probability of the formation of REE centers containing more that two Er atoms is reduced. Thus, the vast majority of the REE centers in an InP:Er crystal consist of pairs of Er atoms. These pairs are, for the most part, responsible for the observed magnetic properties of the sample.

In addition, Fig. 4 shows the temperature range in which the exchange interaction between the Er ions in a QMREC is described by a smaller value of the constant a than in the case of Yb ion interaction. Therefore, the exchange interaction appears to be disrupted by thermal motion in this temperature range. As a consequence, the sample exhibits, at the temperatures above 40 K, paramagnetic properties that can be described by the Curie–Weiss law. Similar behavior is observed for the other REE centers in InP and GaP crystals (Figs. 5, 6). At the same time, at a higher dopant content in the InP:Er crystals, the magnetic anomalies appear against the background of spin polarons (Fig. 7). These anomalies are most likely due to the ferromagnetic ordering of the QMERCs.

With regard to the activity of REE atoms with respect to the formation of complexes, it can be expected that, when there is a high content of lanthanides, specific domains will appear in the III–V crystals. These domains exhibit very different properties from those considered above and, thus, can be referred to as "second-phase" inclusions. In this case, the lanthanide solid solutions cannot be considered as systems of weakly interacting point centers or as superparamagnetic systems consisting of spin polarons and ferromagnetically ordered QMERCs. The temperature

dependences of the magnetic susceptibility obtained for the crystals containing "second-phase" inclusions show some deviations from the Curie law, as indicated by phase transitions whose temperatures allow the identification of the chemical composition of the inclusions. It is well known that REE atoms can form, apart from the related oxides, stable compounds with phosphorus and nitrogen; the latter element is a residual impurity in III–V crystals. It seems likely that such "second-phase" inclusions are present in the samples doped with neodymium (Fig. 8) and dysprosium (Fig. 9).

2.4.3. Neodymium centers in gallium and indium phosphides. The photoluminescence spectrum of neodymium in gallium phosphide consists of two groups of lines at the wavelengths of 0.9 and 1.1 μm [26]. A similar spectrum has been observed in GaAs:Nd layers [26] fabricated by gas-phase epitaxy [27]. These groups of lines are produced by intracenter transitions between the $^4F_{3/2}$ multiplet of the ground state and the $^4I_{15/2}$ and $^4I_{11/2}$ multiplets of the exited states of an Nd^{3+} ion with noncubic symmetry. No ESR data are available regarding Nd centers in III–V crystals.

The temperature dependence of the static magnetic susceptibility of the GaP:Nd crystals reveals the same trends in the behavior of Nd centers as those observed in the QMRECs formed by Yb and Er. At the same time, studies of the solid solutions of neodymium in indium phosphide provide a clear confirmation of the fact that REE atoms are favorably disposed towards the formation of complexes with residual impurities and with Group V atoms, e.g., the phosphorus constituent of the basic lattice (Fig. 8). Thus, an increase in the local concentration of lanthanides in III–V crystals promotes the formation of "second phase" inclusions. This tendency manifests itself in the corresponding changes in the temperature dependences of the static magnetic susceptibility.

It should be noted that, in such crystals, centers formed by separate REE atoms are virtually nonexistent. This circumstance accounts for the unsuccessful attempts to detect the ESR spectra. However, if there exists an efficient channel for excitation, the lack of separate REE centers does not hinder the observation of intense intracenter recombination.

2.4.4. Dysprosium centers in gallium phosphide. Study of the temperature dependence of the static magnetic susceptibility has shown that the magnetic ordering observed at temperatures of 21 and 8 K can be related to microinclusions of dysprosium nitride and phosphide in the GaP:Dy crystals doped with REEs from the melt, since dysprosium can form compounds with phosphorus as well as with nitrogen and oxygen [28] (Fig. 9). This assumption is supported by two observations: (i) the nonuniform distribution of dysprosium over the GaP:Dy sample bulk, as established by secondary ion mass spectroscopy (SIMS), and (ii) the absence, in the optical absorption spectra of the crystals, of the substitutional-nitrogen line present in the

case of the undoped samples. Since, along with nitrogen, the major residual impurity in gallium phosphide is oxygen, it seems likely that the samples also contain Dy_2O_3 inclusions, which, however, were not detected because of the low temperature of the phase transition ($T_N = 1.2$ K).

2.4.5. Gadolinium centers in gallium and indium phosphides. The behavior of gadolinium presents an important argument in favor of the QMREC model suggested to account for the magnetic properties of III–V crystals. A neutral Gd atom has the electronic structure $4f^75s^25p^65d^16s^2$. Therefore, the ground state of a trivalent gadolinium center Gd^{3+} is the $^8S_{7/2}$ multiplet. It is obvious that the temperature dependence of the static magnetic susceptibility of the crystals containing Gd^{3+} ions in the S state will obey the Curie law. However, the experimental temperature dependence observed for the GaP:Gd sample shows a deviation from the Curie law. This deviation can be described by the Weiss constant $\vartheta = -11$ K (Fig. 5).

A microstructural analysis performed with the MS-46 spectrometer at a resolution of about 1 μm did not reveal any "second-phase" inclusions. This circumstance is most likely due to correlations in the distribution of gadolinium over the crystal, resulting in the formation of QMRECs. The lack of an ESR signal indicating gadolinium centers in the crystals under study provides additional evidence for the proposition that QMRECs are the major type of REE centers present in GaP:Gd crystals.

An ESR signal from cubic Gd centers was observed in the InP:Gd crystals fabricated by solution-melt technology (in addition, see [29]) and was related to separate Gd atoms in the crystals. Such individual Gd atoms may exist because the total gadolinium content in the crystals was considerably higher than the amount of chemically active uncontrollable impurities. However, further studies have shown that the previously detected cubic Gd centers are unstable. It was found that, within a time of 1–2 weeks, the ESR spectra of a sample kept at room temperature was spontaneously quenched: the ESR lines were distorted in shape and suppressed in intensity. After the above-indicated time, the ESR spectrum of separate Gd centers could not be detected. The disappearance of the ESR spectra can be explained if we assume that the diffusion of oxygen or other impurity atoms in the crystalline lattice brings about the formation of Gd_2O_3-type REE-based quasi-molecules that are stable REE centers in the crystals. This conclusion is confirmed by studies of the temperature dependence of the magnetic susceptibility that were performed at considerable time intervals.

2.4.6. Europium centers in indium phosphide. Europium is distinguished from the other REEs by its anomalously high solubility (above 10^{20} cm^{-3}) in indium phosphide. The dendrite crystals containing relatively small concentrations of europium (~10^{18} cm^{-3}) are not too different in their magnetic properties from

most of the samples doped with lanthanides (Fig. 10, curve *1*). In none of the InP:Eu crystals, regardless of the Eu dopant content, was an ESR signal from single Eu centers detected. Under these circumstances, the most thorough studies concern themselves with crystals possessing the highest Eu contents (~2×10^{20} cm^{-3}).

The structural uniformity of the dendrite InP:Eu crystals doped from the melt has been studied by SIMS and X-ray structural analysis. The sample surface has been qualitatively studied by local layer-by-layer Auger spectroscopy that provided, with a surface-area resolution of 5–10 μm, an energy resolution of ~0.5 eV. These studies have not revealed any "second-phase" inclusions [30–32].

An ESR signal from InP:Eu crystals was observed at temperatures ranging from 3.5 to 80 K [32]. At the temperature of 80 K, the ESR spectrum of InP:Eu crystals with an Eu concentration above 10^{20} cm^{-3} is an anomalously broad single isotropic line with a *g* factor equal to 1.90 ± 0.01. This permits us to interpret the spectrum as the spectrum of a europium ion in an *S* state. The data on the structure and composition of InP:Eu crystals show that europium is incorporated in the InP matrix in a bound state, which is most probably a EuO quasi-molecule.

Since these studies suggest the absence of "second-phase" inclusions in the crystals, the anomalously large width of the ESR line is most likely due to interactions between the electron spins of the dopant atoms. In this case, the best agreement of the calculated line width with the experimental value is attained under the condition that the Eu-based quasi-molecules are distributed in the crystal as pairs, in which paramagnetic Eu ions are spaced from each other at a distance on the order of the lattice constant.

The temperature dependences of the static magnetic susceptibility of the InP:Eu crystals (Fig. 10) are adequately interpreted in the context of exchange-coupled EuO quasi-molecules. In these quasi-molecules, at temperatures above 100 K, antiferromagnetic ordering of Eu^{2+} ions occurs via the valence electrons of the oxygen atoms. The high content of Eu dopants favors an increase in the probability of location of a pair of EuO quasi-molecules near shallow donors. Such donors can be formed, for example, by Group VI elements of the periodic system (S, Se, and Te) at a phosphorus site. As a result, with a decrease in temperature ($T < 100$ K), the *s–f* exchange interaction brings about the ferromagnetic ordering of Eu^{2+} ions, which is accompanied by trapping of the electrons from shallow donors at the pairs of EuO quasi-molecules (Fig. 10, curve *2*). The exchange interaction of REE ions via trapped electrons is most likely responsible for the shorter electron spin-lattice relaxation time and, as a consequence, for the above-mentioned considerable broadening of the ESR spectrum.

Undoubtedly, along with the pairs of Eu-based quasi-molecules, more complicated objects based on them can contribute to the magnetism of the samples under consideration as well. Among them, the domains of local magnetic ordering, namely, spin polarons, should be mentioned. Spin polarons manifest themselves in the superparamagnetism observed in the InP:Eu crystals at temperatures below 50 K. At the same time, analysis of the temperature dependence of the static magnetic susceptibility of InP:Eu compounds supports a conclusion that follows from structural studies: there are no "second-phase" inclusions in the crystals despite the high Eu content. The analysis shows that Eu dopants form a system of weakly interacting centers. At temperatures below 50 K, the InP:Eu crystals exhibit paramagnetic properties.

3. CONCLUSIONS

The study of the dependences of the static magnetic susceptibility on the temperature and magnetic field has allowed us to reveal local magnetic ordering in III–V crystals doped with REEs.

It is shown that the major contribution to the magnetism of III–V:*Ln* crystals is made by Ln_2O_3 quasi-molecules, in which pairs of Ln^{3+} ions are antiferromagnetically ordered due to a Blumbergen–Rowland exchange interaction via oxygen valence electrons. It is found that, at low temperatures, the Ln_2O_3 quasi-molecules trap electrons from shallow donors. Due to the *s–f* exchange interaction, these trapped electrons transform a pair of Ln^{3+} ions from an antiferromagnetically ordered state into a ferromagnetically ordered state. The competing process with respect to the formation of single ferromagnetically ordered quasi-molecular centers is the formation, in regions of high local concentrations of Ln_2O_3, of spin polarons localized at shallow donors. This process results in the superparamagnetism of III–V:(*Ln*) crystals at low temperatures.

It is shown that the separate ferromagnetically ordered Ln_2O_3 quasi-molecular centers and spin polarons localized at shallow donors in III–V:*Ln* crystals are characterized by large values of the constants of the *s–f* exchange interaction because of the efficient compensation of spin correlations by electron–vibration interaction.

REFERENCES

1. S. T. Pantelides, in *Deep Centers in Semiconductors*, Ed. by S. T. Pantelides (Gordon and Breach, New York, 1986), p. 3.

2. A. G. Milnes, *Deep Impurities in Semiconductors* (Wiley, New York, 1973; Mir, Moscow, 1977).

3. V. F. Masterov, Fiz. Tekh. Poluprovodn. (Leningrad) **18**, 3 (1984) [Sov. Phys. Semicond. **18**, 1 (1984)].

4. N. T. Bagraev and V. A. Mashkov, Mater. Sci. Forum **10–12**, 435 (1986).

5. N. T. Bagraev and V. A. Mashkov, Solid State Commun. **51**, 515 (1984).

6. N. T. Bagraev, A. I. Gusarov, and V. A. Mashkov, Zh. Éksp. Teor. Fiz. **92**, 968 (1987) [Sov. Phys. JETP **65**, 548 (1987)].

7. S. A. Kazanskii, A. I. Ryskin, and V. V. Romanov, Appl. Phys. Lett. **70**, 1272 (1997).

8. D. G. Andrianov, É. P. Bochkarev, V. P. Grishin, *et al.*, Fiz. Tekh. Poluprovodn. (Leningrad) **8**, 499 (1974) [Sov. Phys. Semicond. **8**, 320 (1974)].

9. D. G. Andrianov, É. P. Bochkarev, V. P. Grishin, *et al.*, Fiz. Tekh. Poluprovodn. (Leningrad) **12**, 511 (1978) [Sov. Phys. Semicond. **12**, 294 (1978)].

10. N. T. Bagraev, Izv. Akad. Nauk SSSR, Ser. Fiz. **47**, 2331 (1983).

11. É. L. Nagaev, *Physics of Magnetic Semiconductors* (Nauka, Moscow, 1979) [in Russian].

12. V. F. Masterov, V. V. Romanov, and K. F. Shtel'makh, Fiz. Tverd. Tela (Leningrad) **25**, 1435 (1983) [Sov. Phys. Solid State **25**, 824 (1983)].

13. V. A. Kasatkin, V. F. Masterov, V. V. Romanov, *et al.*, Fiz. Tekh. Poluprovodn. (Leningrad) **16**, 173 (1982) [Sov. Phys. Semicond. **16**, 106 (1982)].

14. H. Ennen, U. Kaufmann, G. Pomrenke, *et al.*, J. Cryst. Growth **64**, 165 (1983).

15. H. Ennen, G. Pomrenke, and A. Axmann, J. Appl. Phys. **57**, 2182 (1985).

16. G. Aszodi, J. Weber, Ch. Uihlein, *et al.*, Phys. Rev. B **31**, 7767 (1985).

17. V. F. Masterov, K. F. Shtel'makh, L. F. Zakharenkov, *et al.*, Fiz. Tekh. Poluprovodn. (Leningrad) **25**, 1375 (1991) [Sov. Phys. Semicond. **25**, 830 (1991)].

18. I. D. Maat-Gersdorf, T. Gregorkiewicz, C. A. J. Ammerlaan, *et al.*, in *Rare Earth Doped Semiconductors II*, Ed. by G. Pomrenke (Materials Research Society, San Francisco, 1996), MRS Symp. Proc., Vol. 422, p. 161.

19. V. V. Romanov and K. F. Shtel'makh, in *Abstracts of All-Union Conference on Physical Fundamentals of Reliability and Degradation of Semiconductor Devices* (Kishinev, 1986), p. 71.

20. S. V. Vonsovskiĭ, *Magnetism* (Nauka, Moscow, 1971; Wiley, New York, 1974).

21. N. T. Bagraev, L. S. Vlasenko, and I. A. Merkulov, Zh. Éksp. Teor. Fiz. **81**, 2160 (1981) [Sov. Phys. JETP **54**, 1147 (1981)].

22. C. P. Bean and J. D. Livingston, J. Appl. Phys. Suppl. **30**, 120S (1959).

23. V. F. Masterov, K. F. Shtel'makh, and L. F. Zakharenkov, Fiz. Tekh. Poluprovodn. (Leningrad) **21**, 365 (1987) [Sov. Phys. Semicond. **21**, 223 (1987)].

24. K. Uwai, H. Nakagome, and K. Takahei, J. Cryst. Growth **93**, 583 (1988).

25. H. Ennen, J. Schneider, G. Pomrenke, and A. Axmann, Appl. Phys. Lett. **43**, 943 (1983).

26. J. Wagner, H. Ennen, and H. D. Muller, J. Appl. Phys. **59**, 1202 (1986).

27. K. Uwai, H. Nakagome, and K. Takahei, Appl. Phys. Lett. **50**, 977 (1987).

28. K. N. R. Taylor and M. I. Darby, *Physics of Rare Earth Solids* (Chapman and Hall, London, 1972; Mir, Moscow, 1974).

29. V. F. Masterov, V. V. Romanov, B. E. Samorukov, and K. F. Shtel'makh, Fiz. Tekh. Poluprovodn. (Leningrad) **17**, 948 (1982) [Sov. Phys. Semicond. **17**, 596 (1982)].

30. K. F. Shtel'makh, L. F. Zakharenkov, V. V. Romanov, *et al.*, Fiz. Tekh. Poluprovodn. (Leningrad) **24**, 1482 (1990) [Sov. Phys. Semicond. **24**, 928 (1990)].

31. V. V. Romanov, I. A. Terletskiĭ, and K. F. Shtel'makh, Fiz. Tekh. Poluprovodn. (Leningrad) **24**, 1584 (1990) [Sov. Phys. Semicond. **24**, 989 (1990)].

32. L. F. Zakharenkov, S. I. Markov, V. F. Masterov, and K. F. Shtel'makh, Fiz. Tekh. Poluprovodn. (Leningrad) **19**, 1841 (1985) [Sov. Phys. Semicond. **19**, 1132 (1985)].

Translated by É. Smorgonskaya

SEMICONDUCTOR STRUCTURES, INTERFACES, AND SURFACES

Study of Certain Properties of Si–Si$_{1-x}$Ge$_x$ (0 ≤ x ≤ 1) Structures Grown from a Restricted Tin-Based Solution–Melt by Liquid-Phase Epitaxy

B. Sapaev^ and A. S. Saidov

Physicotechnical Institute of Physics–the Sun Scientific Association,
Academy of Sciences of Republic Uzbekistan, Tashkent, 700084 Uzbekistan
^e-mail: bayram@physic.uzsci.net
Submitted September 8, 2004; accepted for publication October 14, 2004

Abstract—The lattice parameters and band gap are experimentally determined for Si–Si$_{1-x}$Ge$_x$ structures in relation to the component ratio x (0 ≤ x ≤ 1). The distribution of components over the thickness of the Si$_{1-x}$Ge$_x$ alloys and certain photoelectric properties are studied. The experimental data indicate that the structures obtained are of high quality. Graded-gap Si$_{1-x}$Ge$_x$ alloys (0 ≤ x ≤ 1) can be used for the fabrication of photoelectric devices sensitive in the visible and near-IR regions. They can also be used as substrates for GaAs and GaAs-based layers. © 2005 Pleiades Publishing, Inc.

Study of epitaxial semiconductor materials with new properties and finding ways to improve the growth technology of alloys suitable for semiconductor devices remain topical problems in the field of the science and electronics of semiconductor materials. Si$_{1-x}$Ge$_x$ alloys can serve as a basis for semiconductor materials with the required control of properties. These properties are inherent in both Ge and Si. However, probably due to the complexity involved in obtaining single-crystal Si$_{1-x}$Ge$_x$ alloys over the entire composition range, they have received inadequate study. As the Si/Ge ratio varies in a Si$_{1-x}$Ge$_x$ epitaxial layer, the band gap, lattice parameters, band structure, carrier mobility, and spectral sensitivity also gradually vary. In an earlier study, we reported the possibility of growing Si$_{1-x}$Ge$_x$ alloys over the entire composition range (0 ≤ x ≤ 1) by liquid-phase epitaxy (LPE) from a tin-based solution–melt [1, 2]. Bolkhovityanov *et al.* [3] carried out a comparative analysis of various methods for obtaining artificial GeSi-based substrates for the further growth, for example, of a GeAs layer. In order to lower the misfit-dislocation density, they suggested the growth method of gradient buffer layers. Saidov *et al.* [4] showed that it was possible to grow Si$_{1-x}$Ge$_x$ epitaxial layers from a restricted Ga-based solution–melt. In this case, a Ge concentration of 100% was attained at the surface of the film at the epitaxial layer thickness d = 7–10 μm.

Bolkhovityanov *et al.* [5] made an attempt to optimize the plastic relaxation of mismatch strains in Si–Si$_{1-x}$Ge$_x$ heterostructures by growing a buffer layer with a gradual variation in the Ge content. It was shown that a thick buffer layer is undesirable because it leads to an increase in surface roughness and in the structure cost.

Certain photoelectric properties of epitaxial layers fabricated from Si$_{1-x}$Ge$_x$ alloys, which were grown from a gas phase, were reported in [6, 7]. The results of measurement of the current–voltage (*I–V*) characteristics and photoconductivity (PC) at x = 0.03, 0.22, and 0.60 are given therein. It was shown that an increase in the Ge content leads to an increase in the photoresponse of both short and long wavelengths. A further increase in the Ge content was found to decrease the PC. The authors of [6, 7] attribute this phenomenon to a decrease in the carrier lifetime in a film at a Ge content higher than 30%.

Atabaev [8] grew Si$_{1-x}$Ge$_x$ single crystals using a JEBZ-3B (Japan) installation for electron-beam floating-zone melting (FZM). After each experiment, the single crystallinity of the Si$_{1-x}$Ge$_x$ wafers was examined. It was shown that, at a Ge content ≥55%, the alloys were polycrystalline, and the ingot diameter was no larger than 6–8 mm. LPE-grown Si$_{1-x}$Ge$_x$ alloys have certain advantages over similar FZM-grown alloys (the bulk crystals obtained in [8] contained 45% Ge). These advantages include, for example, the substrate diameter D = 40–50 mm. Zabrodskiĭ *et al.* [9] carried out neutron-transmutation doping of Si$_{1-x}$Ge$_x$ alloys (0.8 at % ≤ x ≤ 18 at %) grown by electron-beam FZM. This transmutation-doped alloy, after being thermally treated in a mode similar to the initial alloy, yielded Si:P samples. The charges included Si:B with ρ ≈ 1000 Ω cm and Ge:Ga with ρ ≈ 30 Ω cm. The transmutation doping was performed for Si$_{1-x}$Ge$_x$ alloys in the composition region with low x, where the transmutations of both components were comparable. The temperature dependence of the resistivity of the transmutation-doped samples was studied. The concentrations of
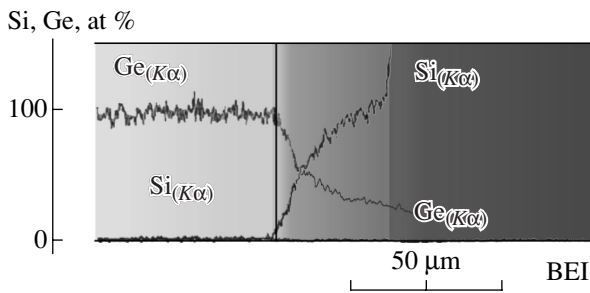
Si, Ge, at %

Fig. 1. Component distribution over the thickness of the $Si_{1-x}Ge_x$ graded-gap alloy.

free holes, which were generated by thermal ionization from the ground state of Ge into the valence band, were determined. The thermal energy of ionization was determined. This energy, which is a function of the doping level and degree of compensation, also depends on the alloy composition.

In this paper, we present the results of an examination of certain specific features of epitaxial growth of $Si_{1-x}Ge_x$ layers on Si substrates from a tin-based solution–melt restricted by two horizontal Si substrates. As the substrates, we used single-crystal Si [111] wafers of KEF (*n*-Si:P) or KDB (*p*-Si:B) grade with a resistivity of 5×10^{-3}–10^{-2} Ω cm. The volume of the solution–melt was controlled by the size of the gap between the substrates. The composition of the solution–melt was calculated from the phase diagram of a Si–Ge–Sn system [10, 11] and based on our preliminary experiments.

The optimal temperature growth modes were determined empirically. The alloys were grown in an ÉPOS installation in a Pd-purified hydrogen flow. Hydrogen was purified using a Pd-15*T* system. The specular layers of the $Si_{1-x}Ge_x$ alloys were grown on the Si substrates at a temperature corresponding to the onset of crystallization: $T_0 = 1050°C$. The optimal values of the cooling rate and the gap between the substrates were 1–1.5°C/min and 0.7–1.3 mm, respectively. The Ge content in the epitaxial $Si_{1-x}Ge_x$ alloy when grown under these conditions was found to increase monotonically in the growth direction of the film from zero at the film–substrate interface to ~100% at the surface. The presence of Sn was found at a depth of several μm in the substrate layers that were in contact with the liquid solution–melt and in the bulk of the grown epitaxial layers. The Sn content was low, and its distribution was uniform.

As a rule, Sn is not the main component. However, its presence in the epitaxial film is explained by the fact that Sn enters the alloy as an isovalent doping impurity during growth. There are numerous reports concerned with study of the diffusion mechanisms and defects present in Si:Sn crystals obtained by various methods [12–16]. The Sn impurity is electrically neutral and exerts almost no effect on the initial parameters of

semiconductor materials. It was shown that such isovalent impurities generate considerable elastic lattice stresses and can interact with point and impurity defects right up to the moment of their trapping.

The grown epitaxial films had *n*-type conductivity ($n \approx 10^{17}$ cm^{-3}). This result is explained by that the Sn dopant, which includes Ga, In, Sb, and As impurities at contents of 1×10^{-6}, 1×10^{-6}, 5×10^{-5}, and 1×10^{-5} at %, respectively, plays the role of a getter and removes acceptor impurities from the growing film [17].

The component distribution in the alloy (Si, Ge, and Sn) was determined using a Jeol JSM LV-1059 analyzer (Japan). The obtained scans indicated that their distribution over the surface of the epitaxial layer was almost uniform and that the alloy was of a graded-gap type throughout the thickness of the layer (Fig. 1). The fact that the epitaxial films grown were of a graded-gap type is illustrated by the film-thickness dependences of the composition of the $Si_{1-x}Ge_x$ alloy, which were obtained using a Cameca installation (Fig. 2a). It is noteworthy that no inclusions of macroscopic defects or second-phase inclusions were found in the film.

Under equal conditions, the thickness of the $Si_{1-x}Ge_x$ epitaxial layers depended on the gap d between the substrates, which varied in the range 0.5–3.0 mm.

Let us assume that a dissolved substance is completely crystallized on the substrate during the growth of $Si_{1-x}Ge_x$ layers from a solution–melt [18]. In this case, the thickness of the epitaxial layers h as a function of the gap can be calculated by formula

$$h_{Si_{1-x}Ge_x} = \frac{\delta\rho}{2A}\left[\frac{A_1}{\rho_1}x + \frac{A_2}{\rho_2}(1-x)\right](C_{Si} - C_{Ge}), \quad (1)$$

where A_1 and A_2 and ρ_1 and ρ_2 are the atomic weight and density of Si and Ge, respectively; ρ and A are the density and atomic weight of Sn; and C_{Si} and C_{Ge} are the atomic fraction of Si and Ge in the liquid phase.

Figure 2a shows that two characteristic regions exist in the dependences of the composition on the thickness of the epitaxial layers and the gap d.

(i) At $d < 1.0$ mm, the thicknesses of the epitaxial films deposited on the lower and upper substrates are equal to each other and coincide with the thickness calculated using formula (1), which is the solution to the diffusion equation. Therefore, it is possible to assume that, in this case, the mass transfer is performed via diffusion of the components of the $Si_{1-x}Ge_x$ alloy in the liquid phase to the solidification front.

(ii) At $d > 1$–1.2 mm, the film grown on the upper substrate is thicker than that grown on the lower substrate, and the thickness increases monotonically as d increases.

In addition, in the case of the $Si_{1-x}Ge_x$ alloy, the experimental value of the film thickness (Fig. 2b, curve *3*)

does not coincide with the calculated one (Fig. 2b, curve *1*), which indicates that the assumption that there is a complete crystallization of the dissolved substance on the substrates (see [11]) is incorrect. It seems likely that, in this case, the film thickness should be calculated based on the model suggested by Malinin and Nevsky [19, 20], who introduced the concept of the efficiency of crystallization with an allowance made for homogeneous nucleation in the bulk of the solution melt. They considered that the efficiency of crystallization depends on the temperature, the thickness of the solution–melt, and the cooling rate.

We were also able to identify the effect of mass transfer on the distribution of the components of the Si$_{1-x}$Ge$_x$ alloy over the thickness of the epitaxial layer.

At $d \approx 0.7$–1.0 mm, i.e., when the growth is limited by diffusion of components of the dissolved substance to the solidification front, the Ge distribution over the thickness of epitaxial layers is identical for upper and lower substrates. The Ge content increases monotonically in the growth direction and is as high as 100% at the film surface. As d increases, the films grown on the upper and lower substrates increasingly differ both in relation to the gradient of the Ge content over the alloy thickness and with respect to its absolute value on the surface (Fig. 3a). The film growth is mainly limited by the Si supply to the solidification front. The Si density is much lower than the density of the Sn solvent, while the Ge content in the alloy is determined by the distribution coefficient. Under nonequilibrium growth conditions, this leads to a situation in which the crystallizing substance floats to the upper substrate. Prior to floating, the substance is kept in a bulk of the liquid phase by intermolecular forces, which determine solubility at this temperature. This phenomenon increases the mass supply.

It is noteworthy that epitaxial layers of high structural quality grow at $d < 2$ mm. In this case, the roughness height S at the surface is no larger than 1 μm for the lower and upper substrates, while, at $d > 2$ mm, S attains 5 μm. Metal inclusions were found in the epitaxial layers grown from the solution–melt at $d > 2$ mm. The volume fraction of these inclusions increases as d increases (Fig. 3b).

Measurements of the lattice parameters for the Si$_{1-x}$Ge$_x$ layers grown on Si substrates were performed by an X-ray diffraction technique using a DRON-3M system (Fig. 4). It was also determined that the variation in the lattice parameter over the film thickness depends linearly on the alloy composition x. Diffraction spectra were obtained using filtered CuK_α radiation with a wavelength $\lambda = 1.5405$ Å for Cu$K_{\alpha1}$ and $\lambda = 1.5443$ Å for Cu$K_{\alpha2}$. Reflections from the same plane, specifically the (333) plane, were recorded separately, which allowed us to increase the accuracy when determining the interplanar spacings d_{hkl}, where hkl are the
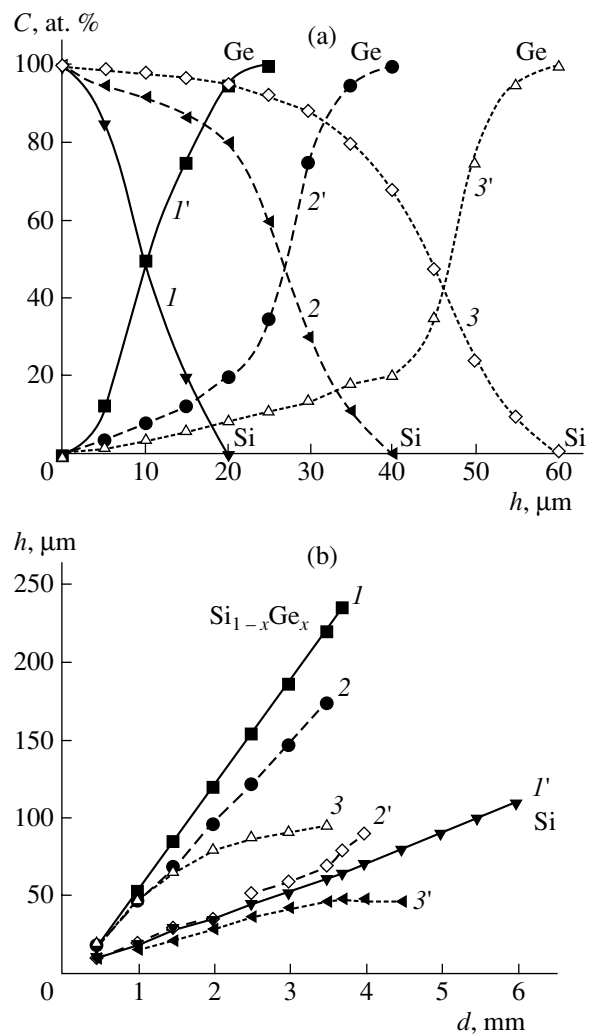

Fig. 2. (a) Composition of the Si$_{1-x}$Ge$_x$ alloy vs. the thickness h of epitaxial films obtained at the following temperatures corresponding to the onset of crystallization: $T_0 =$ (*1*, *1'*) 750, (*2*, *2'*) 850, and (*3*, *3'*) 1050°C. (*1*), (*2*), and (*3*) relate to Si, while (*1'*), (*2'*), and (*3'*) refer to Ge. (b) Thickness of epitaxial films h vs. the thickness of the solution–melt layer d: (*1*, *1'*) calculation, (*2*, *2'*) film on the upper substrate, and (*3*, *3'*) film on the lower substrate. The cooling rate was 1 K/min.

Miller indices. In order to determine the lattice parameters of the crystals, the selected reflections were recorded in a point-by-point scanning mode with the step $\Delta(2\theta) = 0.01°$ and scanning time $\tau = 5$ s. The calculated error of determining the interplanar spacings d_{hkl} in the angle region $2\theta = 93.5°$ for the reflection (333) was $\Delta d \approx 0.0001$ Å, which yields the value $\Delta a \approx 0.0004$ Å. The absence of other peaks in the X-ray diffraction pattern and the appearance of the doublet $K_{\alpha1}$ and $K_{\alpha2}$ additionally indicates that the obtained epitaxial layers were of high quality [21]. The general characteristic of variation in the lattice period depending on the composition of the epitaxial films gives grounds to
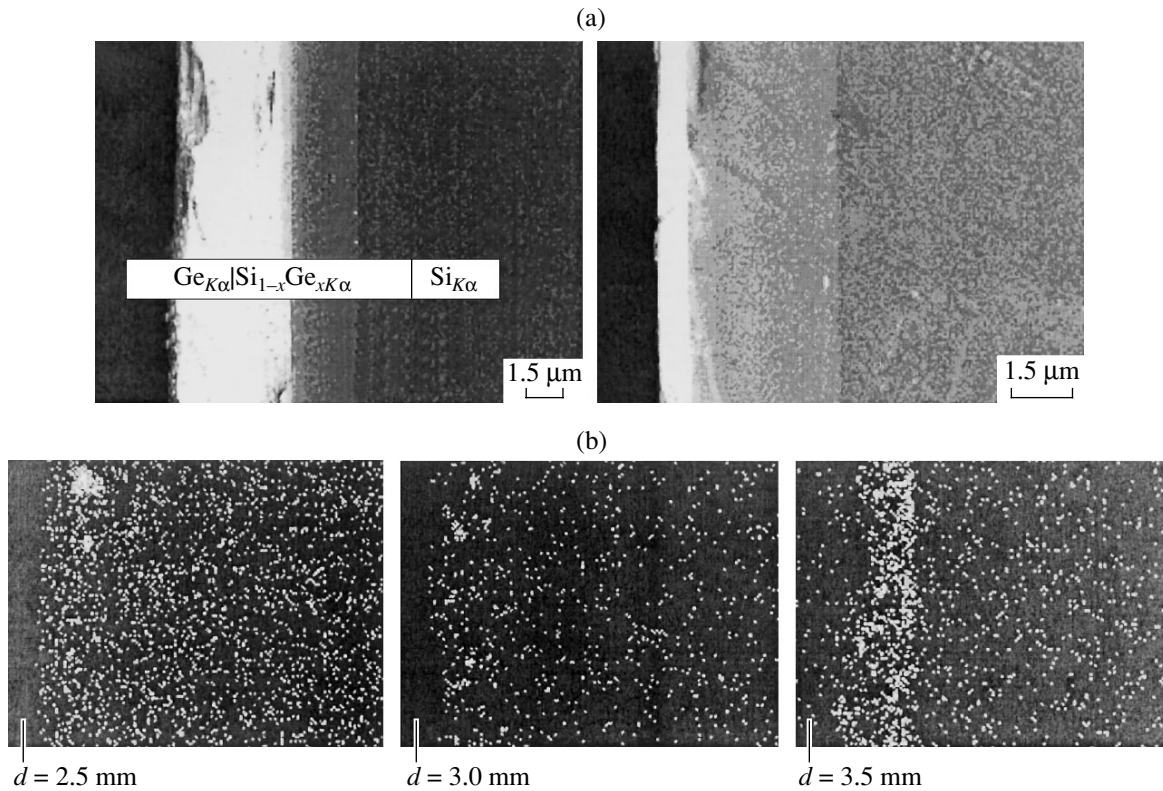
(a)

(b)

$d = 2.5$ mm $d = 3.0$ mm $d = 3.5$ mm

Fig. 3. (a) Epitaxial layers grown on the upper (on the left) and on the lower (on the right) substrates. (b) Photographs showing second-phase inclusions. As the gap between the substrates increases, the roughness and the fraction of the second phase increase.

consider that the alloys were actually obtained over the entire range $0 \leq x \leq 1$.

We also studied certain electrical parameters of the obtained $Si_{1-x}Ge_x$ epitaxial layers. The resistivity ρ, the carrier concentration n, and the Hall mobility μ were determined from Hall measurements. The dislocation

Fig. 4. X-ray diffraction patterns for the $Si–Si_{1-x}Ge_x$ heterostructures.

density N_D in the layers was determined by chemical etching. The measurements yielded the following values: $\rho = 0.1–10\ \Omega$ cm, $n = 10^{16}–10^{17}$ cm^{-3}, $\mu_n = 500–1000$ cm^2/(V s), and $N_D \approx 6 \times 10^5$ cm^{-2} at the heterointerfaces and $N_D \approx 4 \times 10^4$ cm^{-2} at the film surface.

We studied the composition dependence of the alloy band gap by measuring the photoluminescence (PL) spectrum and by layer-by-layer removal of the film in combination with the measurement of the long-wavelength edge. The results of measurements are given in the table.

The alloy band gap decreases from the Si substrate to the film surface. This observation is confirmed by the data given in the table. We also recorded the dependence of photosensitivity of the $Si–Si_{1-x}Ge_x$ heterostructures on the energy of incident photons using a ZMR-3 monochromator. The film surface was illuminated by an incandescent lamp. Figure 5 shows the spectral dependence of photoconductivity for one of the $Si–Si_{1-x}Ge_x$ structures with an epitaxial film 8–10 μm thick. The contacts were formed both to the substrate and the film. The measurement was carried out in a photodiode mode. It can be seen from Fig. 5 that the photoconductivity spectrum includes a broad band, which is typical of heterojunctions. This band encloses the regions of intrinsic photoconductivity of both Si and
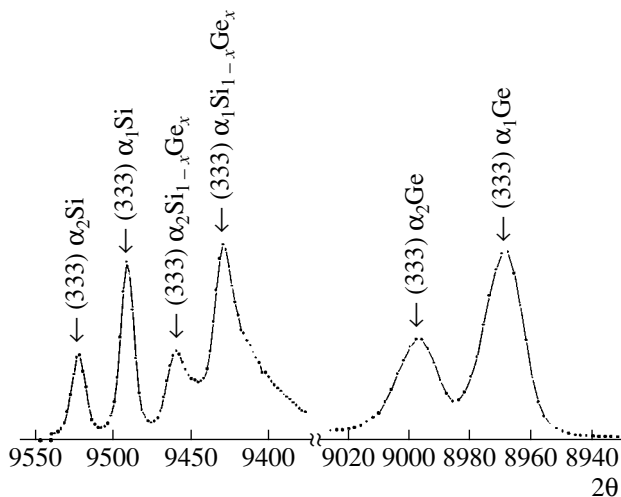
Data on the long-wavelength edge λ in relation to the composition of the Si$_{1-x}$Ge$_x$ graded-gap alloy

h, μm	x	E_g near the p–n junction, eV	Long-wavelength edge λ, μm
0	0	1.10	1.13
5	0.05	1.07	1.15
10	0.10	1.01	1.25
15	0.20	0.97	1.28
20	0.35	0.90	1.38
25	0.50	0.84	1.48
30	0.70	0.81	1.64
35	0.90	0.77	1.60
40	1.00	0.67	1.65

Ge. In addition, the spectrum includes a band that corresponds to the photoconductivity of the Si$_{1-x}$Ge$_x$ alloy. The photosensitivity in the short-wavelength region can be attributed to the weak absorption of the alloy in this region; i.e., high-energy photons are partially absorbed in the upper layers, while those that are not absorbed in the narrow-gap upper alloy layers penetrate into the substrate, where they are absorbed in Si. This conclusion is confirmed by the sensitivity in the intrinsic-absorption region of Si.

Thus, the studies carried out have shown that it is possible to obtain epitaxial films of high structural quality by selecting the growth temperature range, determining the best component ratios for the solution–melt, and by selecting the corresponding gap widths d between the horizontal substrates.

The obtained structures can be used to fabricate devices and to grow III–V semiconductor compounds and their alloys.
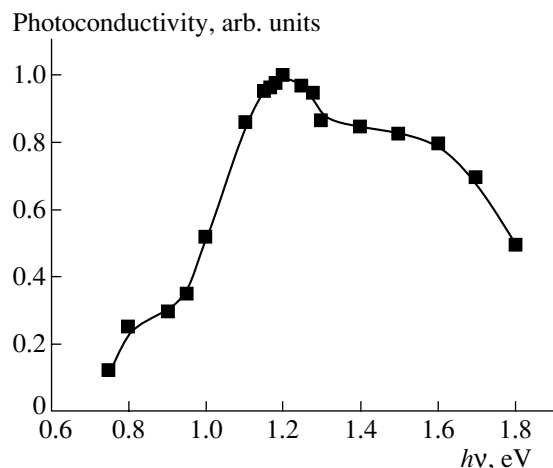
We can make the following conclusions.

(i) Si$_{1-x}$Ge$_x$ epitaxial layers with a controlled variation in the Ge content from 0 at % at the heterointerface up to 100 at % at the film surface can be grown.

(ii) It is shown that, at a thickness d of the solution–melt layer of about 0.7–1.0 mm, the epitaxial films on the upper and lower substrates grow identically, while, at d = 1.0–1.5 mm, the epitaxial films differ in terms of composition and graded-gap characteristics. In the former case, the films are of high structural quality. As d increases, the films grown on the upper and lower substrates increasingly differ and their structural quality worsens. This circumstance is probably associated with variation in the mass-transfer characteristics and with the emergence of homogenous nucleation in the liquid phase volume.

(iii) Study of the distribution of chemical components revealed that this distribution is graded by thickness and is uniform on the surface of the Si$_{1-x}$Ge$_x$ films.

(iv) In the case of study of the lattice parameters of the Si$_{1-x}$Ge$_x$ alloys, the experimental data indicate that the obtained Si$_{1-x}$Ge$_x$ epitaxial layers are of high structural quality.

Fig. 5. Spectral dependence of photoconductivity for the n-Si–p-Si$_{1-x}$Ge$_x$ structure. The film surface is illuminated.

REFERENCES

1. A. S. Saidov, B. I. Sushko, and A. M. Tuzovskiĭ, in *Abstracts of V Coordination Meeting on Investigation and Application of Silicon–Germanium Alloys* (Tashkent, 1981), p. 6.

2. M. S. Saidov, S. Dadamukhamedov, and A. S. Saidov, Dokl. Akad. Nauk UzSSR, No. 1, 29 (1984).

3. Yu. B. Bolkhovityanov, O. P. Pchelyakov, L. V. Sokolov, and S. I. Chikichev, Fiz. Tekh. Poluprovodn. (St. Petersburg) **37**, 513 (2003) [Semiconductors **37**, 493 (2003)].

4. A. S. Saidov, B. Sapaev, and É. A. Koshchanov, Dokl. Akad. Nauk Resp. Uzb., No. 11, 18 (1994).

5. Yu. B. Bolkhovityanov, A. S. Deryabin, A. K. Gutakovskiĭ, *et al.*, Pis'ma Zh. Tekh. Fiz. **30** (2), 61 (2004) [Tech. Phys. Lett. **30**, 68 (2004)].

6. K. L. Lyutovich, L. N. Strel'tsov, and A. S. Lyutovich, Fiz. Tekh. Poluprovodn. (Leningrad) **6**, 199 (1972) [Sov. Phys. Semicond. **6**, 169 (1972)].

7. Kh. T. Akramov, A. S. Lyutovich, and K. L. Lyutovich, Geliotekhnika, No. 6, 12 (1979).

8. I. G. Atabaev, Doctoral Dissertation (Tashkent, 2001).

9. A. G. Zabrodskiĭ, V. A. Evseev, and R. F. Konopleva, Fiz. Tekh. Poluprovodn. (Leningrad) **20**, 2042 (1986) [Sov. Phys. Semicond. **20**, 1278 (1986)].

10. V. M. Andreev, L. M. Dolginov, and D. N. Tret'yakov, *Liquid Epitaxy in Technology of Semiconductor Devices* (Sovetskoe Radio, Moscow, 1975) [in Russian].

11. M. Hansen and K. Anderko, *Constitution of Binary Alloys*, 2nd ed. (McGraw-Hill, New York, 1958; Metallurgizdat, Moscow, 1962), Vols. 1, 2.

12. J. Nielsen, K. B. Nielsen, and A. N. Larsen, in *Proceedings of 15th International Conference on Defects in Semiconductors* (Budapest, 1988), Mater. Sci. Forum, Vols. 38–41, Part 1, p. 439.

13. B. G. Svensson, J. Svensson, J. L. Lindstrom, *et al.*, Appl. Phys. Lett. **51**, 2257 (1987).

14. A. S. Oates, M. J. Binns, R. C. Newman, *et al.*, J. Phys. C **17**, 5695 (1984).

15. G. D. Watkins, Phys. Rev. B **12**, 4383 (1975).

16. A. Brelot, IEEE Trans. Nucl. Sci. **19**, 22 (1972).

17. B. Sapaev, Pis'ma Zh. Tekh. Fiz. **29** (20), 64 (2003) [Tech. Phys. Lett. **29**, 865 (2003)].

18. Yu. B. Bolkhovityanov, R. I. Bolkhovityanov, and P. L. Mel'nikov, in *Growth and Synthesis Processes of Semiconductor Crystals and Films* (Nauka, Novosibirsk, 1975) [in Russian].

19. A. Yu. Malinin and O. B. Nevsky, J. Electron. Mater. **7**, 757 (1978).

20. A. Yu. Malinin and O. B. Nevsky, J. Electron. Mater. **7**, 775 (1978).

21. E. F. Vegman, Yu. G. Rufanov, and I. N. Fedorchenko, *Crystallography, Mineralogy, Petrography, and X-ray Diffraction Analysis* (Metallurgiya, Moscow, 1990) [in Russian].

Translated by N. Korovin

SEMICONDUCTOR STRUCTURES, INTERFACES, AND SURFACES

Formation of Potential Barriers in Undoped Disordered Semiconductors

N. V. Vishnyakov*^, S. P. Vikhrov*, V. G. Mishustin*, A. P. Avachev*, I. G. Utochkin*, and A. A. Popov**

*Ryazan State Radio Engineering Academy, Ryazan, 391000 Russia
^e-mail: mel@rgrta.ryazan.ru
**Institute of Microelectronics and Informatics, Russian Academy of Sciences, ul. Universitetskaya 21, Yaroslavl, 150007 Russia
Submitted October 27, 2004; accepted for publication December 28, 2004

Abstract—The formation of potential barriers in undoped disordered semiconductors is considered. A generalized model of the potential barrier formation in such structures is examined using the example of a metal–amorphous hydrogenated silicon contact. It is shown that the properties of barriers in disordered semiconductors are determined by the energy distribution of the localized states in the mobility gap. An analytical expression for the electric field and potential in the space-charge region of a disordered semiconductor is obtained and a new method for the formation of surface quasi-ohmic contacts is suggested. © *2005 Pleiades Publishing, Inc.*

Contact phenomena in disordered semiconductors and, in particular, in amorphous hydrogenated silicon (a-Si:H) are of interest from both the theoretical and the practical standpoints, especially since, at present, there exists no adequate model describing the formation of potential barriers. The density of states (DoS) localized in the mobility gap near the Fermi level in such materials can be rather high (10^{15}–10^{19} cm^{-3} eV^{-1}). However, most electrical properties possessed by materials in this class are determined only by electrically active states, i.e., by the states that, under equilibrium conditions or under the effect of external factors, play the role of donors or acceptors [1]. Incorporated doping elements (for example, phosphorus or boron) can form donor or acceptor levels and create additional high-energy defects near the Fermi level E_F. The structural relaxation of a material in response to external factors (temperature, electromagnetic field, or ionizing radiation) can result in the breaking of weak chemical bonds and the formation of additional charged defects acting as donors or acceptors.

The classical approach to the problem of the appearance of potential barriers in disordered semiconductors [2, 3] does not account for their formation in the absence of a Schottky layer (at the contact of a metal with an undoped amorphous semiconductor) or in the case of low concentrations of "shallow" donors (for p–n junctions and heterojunctions). Earlier, Madan (see, e.g., [4]) took into account the DoS distribution in the mobility gap of a disordered semiconductor when solving the Poisson equation in the space-charge region (SCR). However, the DoS function has an integral character and includes states in band tails, which are not electrically active under equilibrium conditions [5].

Arkhipov *et al.* [6] have suggested a rather interesting model of an activation barrier at the contact between a metal (Me) and an amorphous semiconductor, where the current is limited by the space charge formed in the amorphous semiconductor in the presence of injection of electrons from the metal and their trapping. However, the results of these studies and our previous analysis of the current–voltage (*I–V*) characteristics [7, 8], as well as other known experimental results [4, 9, 10], show that the current across the barrier may be due to different mechanisms, mainly, over-the-barrier emission and, less often, space-charge-limited currents (SCLC). In the case of a Me–a-Si:H contact, the most detailed theoretical studies have been performed by Il'chenko and Strikha [10]. However, their analytical solution to the Poisson equation for the barrier under study could not be practically applied, since the function approximating the DoS near the Fermi level was inadequate.

The absence of a unified theory of the formation of potential barriers in systems with disordered semiconductors, similar to the theory that exists in the classical physics of crystalline semiconductors, means that it is not possible to suggest adequate mathematical models of the devices used in automated design systems. The aim of this study was to develop a generalized model of the formation of barriers in disordered semiconductors taking into account the shape of the distribution of the density of electrically active localized states in the mobility gap and their contribution to the charge density distribution in the SCR of the semiconductor.

For our analysis, we chose a Me–a-Si:H contact, since it is present in all a-Si:H-based devices and can play the role both of an ohmic contact and an active ele-

ment (in barrier structures). In addition, in the active mode, the currents passing through this contact can result from monopolar electron injection from the metal. Therefore, it is easier and more obvious to analyze the properties of such a barrier rather than the properties of *p–n* or *p–i–n* junctions. However, the nature of this potential barrier differs from that of a similar (Schottky) barrier between a metal and a crystalline semiconductor. The barrier considered has a number of specific features:

(i) The formation of the SCR directly involves charged localized states located near the Fermi level in the energy range from E_F to $E_F + e\varphi_0$, where φ_0 is the band bending at the semiconductor surface [5].

(ii) The process of SCR formation can be separated into two stages. The first stage, related to the diffusion of free charge carriers at the moment of contact, results in the establishment of an intermediate equilibrium; at this stage, the processes are similar to those at the contact of a metal with a crystalline semiconductor and can be mathematically described using the classical Schottky theory [2, 3]. The second stage, corresponding to longer times, is related to the ionization of electrically active localized states at the Fermi level. After the second stage, we may assume that the formation of the barrier between the metal and amorphous semiconductor is terminated [11]. Similar features should also be observed during the formation of the SCR in *p–n*, *p–i*, and *n–i* junctions.

The above processes are illustrated in Fig. 1 in more detail. In order to simplify the graphic representation, the spectra of deep localized acceptor- and donor-type states are represented by the local levels E_a and E_d, respectively. The time taken for complete formation of the barrier can be separated into two intervals: t_1 is the time interval during which the "fast" ionization processes of shallow levels occur, and t_2 is the time interval during which deep levels are ionized and the released carriers are swept out of the SCR. In other words, these times correspond to the establishment of complete thermodynamic equilibrium in the system and essentially determine the time τ_M of the relaxation of nonequilibrium charge (the Maxwell relaxation time). For crystalline semiconductors, $t_1 \leq 10^{-12}$ s; for amorphous semiconductors, $t_2 \leq 10^3$ s [4].

If we consider *a*-Si:H as a weakly compensated semiconductor, the dark conductivity is due to electrons with a concentration n_0 [10]:

$$n_0 = N_d^+ - N_a^-. \qquad (1)$$

Here, N_d^+ and N_a^- are the concentrations of the donor- and acceptor-like states ionized at a given temperature.

The space-charge density ρ is determined by the difference between the positive and negative charges in the traps. In the bulk of *a*-Si:H, this density is given by

$$\rho = e(n_0 + \Delta n), \qquad (2)$$

where e is the elementary charge; n_0 is determined by (1); and Δn appears because of the ionization of donorlike states near the Fermi level, which are initially occupied, at the instant of the contact of the metal with semiconductor.

It is also important that the charge carrier transport in *a*-Si:H is accompanied by multiple trapping and release of charge carriers involving both shallow and deep traps [12]. The trapping probability is determined by the capture cross section and the trap occupancy. The recombination of nonequilibrium carriers occurs in a time shorter than τ_M, and, therefore, a generated carrier can recombine before it leaves the SCR [6, 12]. We assume that, even in the presence of an external electric field, the currents in the SCR are so low that they do not perturb the static equilibrium of the charges. It should also be noted that this consideration does not take into account the effect of surface states and the Schottky effect.

At the initial instant ($t = 0$), the distance between the metal and *a*-Si:H is infinite (Fig. 1a). In the absence of surface states (or if they are "shunted" by the bulk states), the energy diagram of *a*-Si:H corresponds to "flat bands." The traps E_t and E_{ta} located between E_C and E_{F0} are unoccupied, while the levels E_{td} located between E_{F0} and E_V are, in contrast, occupied. Furthermore (Fig. 1c), at the instant of the contact of the metal and *a*-Si:H, due to the difference in the work functions of the semiconductor (φ_s) and metal (φ_m), the diffusion flow of free electrons (n) from the semiconductor to the metal appears during the time t_1, just as it does in crystalline semiconductors. Therefore, in this time interval, the distribution of the space-charge density and field in the SCR is established, as is shown in Fig. 1d. The formed field F affects the electron flow from the semiconductor and, at the instant t_1, the intermediate equilibrium is established. Thus, the width of the SCR is equal to the value W_1 that corresponds to the case of a crystalline semiconductor with a concentration of ionized donors $N_{td} = n$. The band bending in the SCR is

$$e\varphi_0 = e\varphi_m - e\varphi_s = e\varphi_m - \chi_s + (E_F - E_C), \qquad (3)$$

where χ_s is the electron affinity of *a*-Si:H.

The electric field at an instant $t \leq t_1$ is

$$F(x) = \frac{\varphi_t}{L_D^2}(W_1 - x), \qquad (4)$$

where $\varphi_t = kT/e$ is the thermal potential and L_D is the Debye length, which is determined by the screening properties of "free" electrons in an undoped *a*-Si:H film.

Using the approximation of the Fermi–Dirac function at absolute zero, we find that the band bending at the instant $t = t_1$ creates aninverse population of the E_{td} level; in turn, at $t \geq t_1$, this produces thermal activation of electrons from the traps. Thus, in the field F in the SCR, electrons drift into the depth of the semiconductor, but, having a low mobility (10^{-1}–10^{-2} cm^2/(V s) [4]
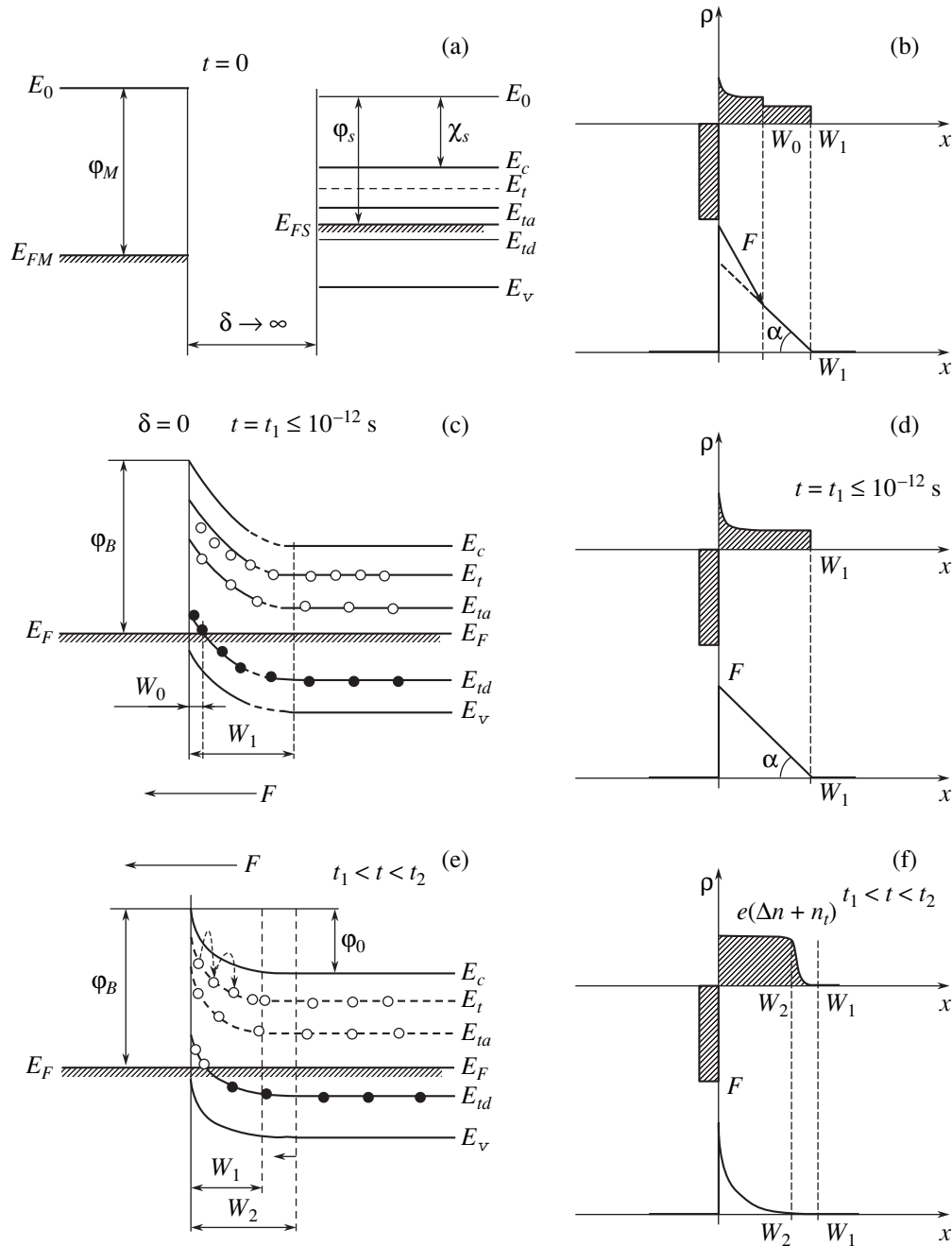
Fig. 1. Model of the formation of the barrier between a metal and an undoped disordered semiconductor. (a) The initial state of the system at $t = 0$; (c) the system at the instant of the contact $t = t_1$; (e) the system at an instant t such that $t_1 < t < t_2$; (b, d, f) the distribution of the charge density and electric field in the SCR of a crystalline semiconductor in the presence of a deep E_{td} level and a disordered semiconductor in cases (c) and (e), respectively; φ_s and φ_m are the work functions for the semiconductor and metal; φ_0 is the band bending in the SCR; δ is the spatial gap between the metal and a-Si:H; χ_s is the electron affinity; E_t is the energy level of shallow traps; E_{td} and E_{ta} is the energy region of donor- and acceptor-type deep traps; E_F is the Fermi level; F is the electric field; and W_1 and W_2 are the thicknesses of the space-charge layer at the instants $t = t_1$ and $t < t_2$.

and short diffusion length ($L < W_1$), they are immediately captured by shallow traps. Moving to the boundary of the SCR, where the electric field $F \longrightarrow 0$, the carriers, before reaching a deep trap, undergo several capture–activation events involving shallow traps (according to multiple trapping models [6, 12]). The spatial relaxation of the excess charge, which is formed due to the depletion of deep traps E_{td} in the SCR, occurs during the time t such that $t_1 \ll t \leq t_2$. This situation is an inherent property of all amorphous semiconductors with a continuous spectrum of localized states. The processes under study are illustrated in Figs. 1e and 1f.
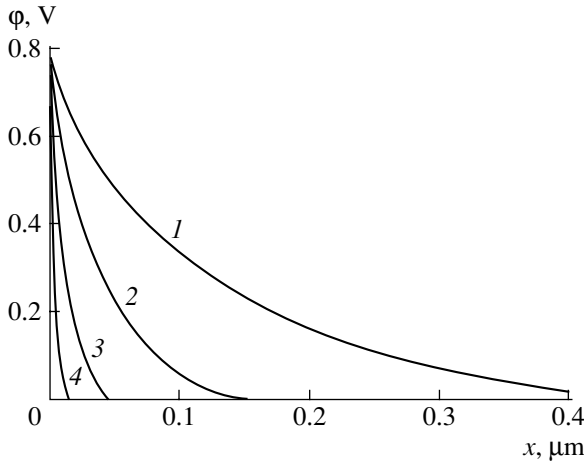
Fig. 2. Effect of the density of electrically active states at the Fermi level on the potential barrier profiles for the contact of a metal with an undoped amorphous semiconductor (from the calculations in [15, 20]): (*1*) $g_{F0} = 10^{16}$ cm^{-3} eV^{-1} and $\beta = 5.76$ eV^{-1}, (*2*) $g_{F0} = 10^{17}$ cm^{-3} eV^{-1} and $\beta = 5.18$ eV^{-1}, (*3*) $g_{F0} = 10^{18}$ cm^{-3} eV^{-1} and $\beta = 4.32$ eV^{-1}, and (*4*) $g_{F0} = 10^{19}$ cm^{-3} eV^{-1} and $\beta = 2.88$ eV^{-1}.

Due to these processes, the shape of the potential $\varphi(x)$ in the SCR is changed, the width of the SCR decreases to W_2, and the space-charge density increases to $e(n_0 + \Delta n)$ (Fig. 1f).

After the thermodynamic equilibrium is established ($t = t_2$), the space-charge density for the case of large band bending is [13]

$$\rho(\varphi) = \frac{e g_{F0}}{\beta} \exp(\beta e \varphi), \qquad (5)$$

where g_{F0} is the DoS near E_F and β is the slope of the approximating straight line $g_d(E)$ in semilog coordinates.

The electric field in the SCR is determined by the following analytical expression [14]:

$$F(x) = \sqrt{\frac{2 g_{F0}}{\beta^2 \varepsilon \varepsilon_0}} \tan\left(\sqrt{\frac{e^2 g_{F0}}{2 \varepsilon \varepsilon_0}} x\right)$$

$$= \sqrt{\frac{2 g_{F0}}{\beta^2 \varepsilon \varepsilon_0}} \tan\left(\frac{x}{\sqrt{2} L_D}\right). \qquad (6)$$

Here,

$$L_D = \sqrt{\frac{\varepsilon \varepsilon_0}{e^2 g_{F0}}}. \qquad (7)$$

The potential in the SCR is

$$\varphi(x) = -\frac{2}{\beta e} \ln\left|\cos\left(\frac{x}{\sqrt{2} L_D}\right)\right|, \qquad (8)$$

and the width of the SCR is

$$W = \sqrt{\frac{2 \varepsilon \varepsilon_0}{e^2 g_{F0}}} \arccos\left[\exp\left(-\frac{\beta e \varphi_0}{2}\right)\right]. \qquad (9)$$

Expressions (6)–(9) were obtained analytically in [14] and, from the point of view of practical application, considerably differ from earlier obtained expressions [10]. Similar expressions are also valid for crystalline semiconductors with deep traps E_{td} (the Saha–Reddi model for p^+–n junctions, Fig. 1b) [15].

If a reverse external bias is applied to a Me–*a*-Si:H system, the carriers are activated and, under a forward bias, captured by deep traps. Accordingly, the position of the electron quasi-Fermi level in the SCR changes. The duration of this process is determined by the same time $t = t_2$; i.e., the time taken for the formation of the barrier profile due to activation–drift processes in the SCR can be from several to tens of seconds. This conclusion can explain the results of measurement of the high-frequency capacitance–voltage characteristics (namely, the absence of the voltage dependence of the barrier capacitance at a frequency of the test signal equal to 1 MHz) [4, 7].

In the case of doped *a*-Si:H, the above scenario is retained. The difference is that, due to doping, the concentration of free charge carriers is higher, thus resulting in more significant band bending in the intermediate equilibrium. Therefore, a wider spectrum of "deep" donorlike states takes part in the final stage of barrier formation. In this case, the width of the SCR W_2 is smaller than in the case of undoped a-Si:H.

The effect of an increase in the DoS at the Fermi level is illustrated in Fig. 2. An analysis of expression (6) shows that the shape of the potential in the SCR depends on the DoS at the Fermi level: with an increase in the DoS, the barrier becomes thinner, and, therefore, the effective height becomes lower due to tunneling through a thin contact layer. Under an increase in the DoS at the midgap from 10^{15} to 10^{19} eV^{-1} cm^{-3}, the field concentrates near the contact and its magnitude increases. Thus, the width of the SCR decreases from several μm to several hundred nanometers [14]. The effective height of the barrier is thus reduced from 0.73 to 0.1 eV.

Thus, in disordered semiconductors with a high DoS at the Fermi level (of about 10^{19} eV^{-1} cm^{-3}), the potential barrier at the contact between a metal and a semiconductor limits the current very little, and its "blocking" properties disappear. Chalcogenide vitreous semiconductors and nonhydrogenated amorphous silicon (*a*-Si) are examples of such disordered semiconductors, where the DoS at the Fermi level can attain such values.

The above conclusions have led us to a new method for creating surface quasi-ohmic contacts to undoped *a*-Si:H [16]. The problem of the creation of an ohmic contact can be solved by introducing an additional annealing operation into the technological process of

fabrication of thin-film devices based on *a*-Si:H and other hydrogenated amorphous semiconductors. After deposition of a semiconductor film onto a substrate, instead of doping the film to be used for an ohmic contact, the amorphous semiconductor film is annealed for 20–30 min at a hydrogen effusion temperature. Annealing increases the near-surface DoS at the Fermi level and, therefore, reduces the effective height of the contact potential barrier, which is formed in the subsequent technological operations.

A similar approach can be extended to a contact between a doped and an intrinsic disordered semiconductor. Since the DoS in doped semiconductors exceeds the DoS in intrinsic semiconductors by one to two orders of magnitude, virtually the entire contact potential difference at the boundaries of the *p*–*i* and *i*–*n* regions falls on the undoped region [4]. Under such an assumption, the field in the *i* region of a *p*–*i*–*n* structure can be considered as a superposition of the contact fields at the boundaries of the *p*–*i* and *i*–*n* regions. The contact potential difference is determined by the shift of the Fermi level in the doped regions with respect to the position of the Fermi level in the intrinsic semiconductor, and the field profile is related to the magnitude and distribution of the DoS near the Fermi level in the mobility gap. In Fig. 3, the variation of the electrostatic potential and the field distribution in the *i* layer of a solar cell of an *a*-Si:H–based *p*–*i*–*n* structure are plotted at different values of the DoS; in the calculations, we took into account the effects of "deep" localized states on the formation of the contact barrier [13, 14]. For long illumination times, light-induced high-energy metastable states appear in the semiconductor. An increase in the DoS at the Fermi level produces a redistribution of the electric field in the structure: the SCR concentrates in the *i* region near the boundaries of the *p*–*i* and *i*–*n* regions. In turn, this redistribution results in the generation of additional defect-related states by the electric field, which leads to an even greater enhancement of the effect under study. The field at the middle of the *i* layer decreases, and, as a consequence, the carriers do not have time to be separated by the contact field and recombine, as they do not reach the contacts. As a result, the efficiency of the solar cell decreases [17]. Thus, an increase in the DoS due to photo-induced defects (and electrically induced defects near the interfaces) results not only in a decrease in the drift carrier displacement $\mu\tau$ but also in a redistribution of the field in the *i* layer of a solar cell based on a *p*–*i*–*n* structure. These processes increase the fraction of recombined carriers in the *i* region and reduce the collection factor of the photogenerated charge.

The suggested approach to the formation of potential barriers allowed us to apply it to the theory of *a*-Si:H–based thin-film field-effect transistors (TFFET) and to analytically obtain, for the first time, the current–voltage characteristics of TTFETs with an "inverted" structure, covering subthreshold and superthreshold transistor operation modes [18].
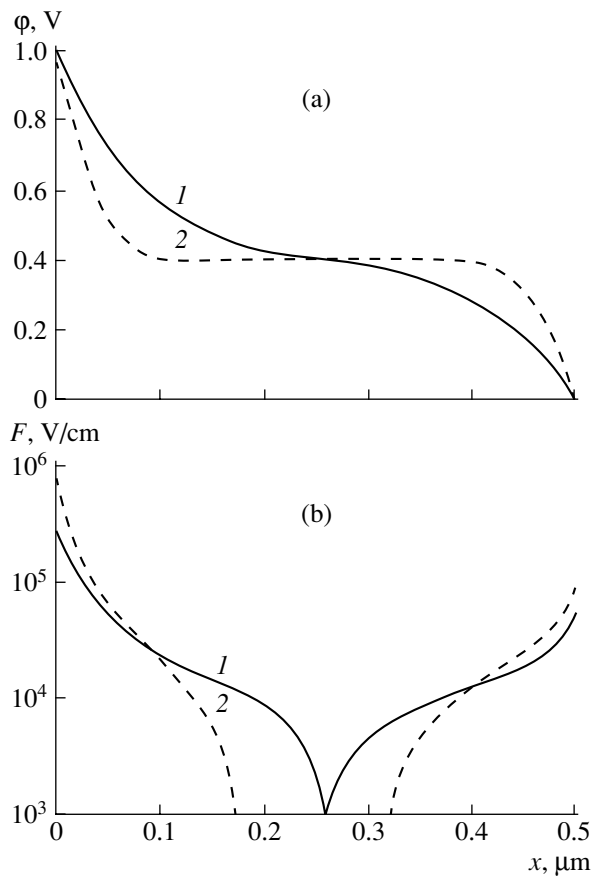

Fig. 3. (a) Electric potential profile and (b) distribution of the electric field in the *i* layer of an *a*-Si:H-based structure: $g_{F0} = $ (*1*) 10^{16} and (*2*) 10^{17} cm^{-3} eV^{-1}.

In closing, it should be noted that we have suggested a physical model of the formation of potential barriers in disordered semiconductors that takes into account the high midgap DoS characteristic of this class of semiconductor materials. These states are electrically active and contribute substantially to the magnitude, energy, and space distributions of the charge, electric field, and potential in the SCR of the semiconductor.

It is shown that the application of physical and mathematical models to classical Schottky barriers, as well as *p*–*n* and *p*–*i*–*n* junctions in the case of undoped amorphous semiconductors, is not quite correct and the barrier between the metal and amorphous semiconductor cannot be assumed to be a classical Schottky barrier. This statement is related to the fact that the SCR of a noncrystalline semiconductor is formed not only by donor- or acceptor-type impurity states but also by "deep" electrically active states near the Fermi level.

We have found that, in contrast to crystals, the process of formation of the barrier and SCR in disordered semiconductors may require times as long as 10^3 s. Therefore, studies of the capacitance–voltage characteristics of such structures cannot be performed using a

test-signal frequency of 1 MHz, typical of crystalline semiconductors.

We have shown that the increase in the DoS at the Fermi level changes the distribution of the potential and electric field in the SCR of a disordered semiconductor. As a consequence, the effective barrier height is lowered and the width of the SCR is decreased. Thus, for a contact of a metal with undoped *a*-Si:H, the width of the SCR decreases by a factor of 25 (from 500 to 20 nm) and effective barrier height decreases by a factor of 7 (from 0.73 to 0.1 eV) as the DoS at the Fermi level increases from 10^{16} to 10^{19} eV^{-1} cm^{-3}. For *p*–*i*–*n* diodes of *a*-Si:H-based solar cells, an increase in the DoS of the *a*-Si:H film makes the contact fields concentrate in the *i* layer near the boundaries of the *p*–*i* and *i*–*n* junctions. Accordingly, the field in the middle of the *i* layer decreases by one to two orders of magnitude. This effect results in a decrease in the drift displacement and collection factor of the photoinduced charge, i.e., in the degradation of the quality and efficiency of solar cells.

We have suggested a new method for the formation of quasi-ohmic contacts in hydrogenated disordered semiconductors, eliminating doping of the disordered semiconductor under the contact and, thus, making the technological process of fabrication of efficient devices with given characteristics substantially less expensive.

REFERENCES

1. N. F. Mott and E. A. Davis, *Electronic Processes in Non-Crystalline Materials* (Clarendon, Oxford, 1971; Nauka, Moscow, 1974).

2. V. I. Strikha, *Theoretical Foundations of Behavior of Metal–Semiconductor Contacts* (Naukova Dumka, Kiev, 1974) [in Russian].

3. E. H. Rhoderick, *Metal–Semiconductor Contacts* (Clarendon, Oxford, 1978; Radio i Svyaz', Moscow, 1982).

4. A. Madan and M. Shaw, *The Physics and Applications of Amorphous Semiconductors* (Academic, Boston, 1988; Mir, Moscow, 1991).

5. S. P. Vikhrov, N. V. Vishnyakov, A. A. Maslov, and V. G. Mishustin, in *Abstracts of IV International Conference on Physicotechnical Problems of Electrotechnical Materials and Components* (Mosk. Énerg. Inst., Moscow, 2001), p. 93.

6. V. I. Arkhipov, V. M. Login, A. I. Rudenko, *et al.*, Fiz. Tekh. Poluprovodn. (Leningrad) **22**, 276 (1988) [Sov. Phys. Semicond. **22**, 168 (1988)].

7. S. P. Vikhrov, V. A. Ligachev, and N. V. Vishnyakov, Proc. SPIE **1783**, 600 (1992).

8. N. V. Vishnyakov, Vestn. RGRTA **11**, 98 (2003).

9. A. A. Aĭvazov, B. G. Budagyan, S. P. Vikhrov, and A. I. Popov, *Disordered Semiconductors* (Mosk. Énerg. Inst., Moscow, 1995) [in Russian].

10. V. V. Il'chenko and V. I. Strikha, Fiz. Tekh. Poluprovodn. (Leningrad) **18**, 873 (1984) [Sov. Phys. Semicond. **18**, 544 (1984)].

11. S. P. Vikhrov, N. V. Vishnyakov, and D. N. Gusev, *The Schottky Barriers in Crystalline and Amorphous Semiconductors* (RGRTA, Ryazan, 1999) [in Russian].

12. S. P. Vikhrov, N. V. Vishnyakov, A. A. Maslov, *et al.*, in *Proceedings of III International Conference on Amorphous and Microcrystalline Semiconductors* (St. Petersburg, Russia, 2002), p. 31.

13. N. V. Vishnyakov, V. G. Mishustin, and I. G. Utochkin, Vestn. RGRTA **10**, 74 (2002).

14. S. P. Vikhrov, N. V. Vishnyakov, V. G. Mishustin, and A. A. Popov, J. Optoelectron. Adv. Mater. **5**, 1249 (2003).

15. A. G. Milnes, *Deep Impurities in Semiconductors* (Wiley, New York, 1973; Mir, Moscow, 1977).

16. S. P. Vikhrov, N. V. Vishnyakov, A. A. Maslov, *et al.*, RU Patent No. 2 229 755 (2004).

17. S. P. Vikhrov, N. V. Vishnyakov, V. G. Mishustin, *et al.*, in *Abstracts of IV International Conference on Amorphous and Microcrystalline Semiconductors* (St. Petersburg, Russia, 2004), p. 313.

18. A. P. Avachev, *The Physics of Semiconductors. Microelectronics. Radio-Engineering Devices* (RGRTA, Ryazan, 2003), p. 19 [in Russian].

Translated by I. Zvyagin

SEMICONDUCTOR STRUCTURES, INTERFACES, AND SURFACES

Stabilization of Charge at the Interface Between the Buried Insulator and Silicon in Silicon-on-Insulator Structures

I. V. Antonova

Institute of Semiconductor Physics, Siberian Division, Russian Academy of Sciences,
pr. Akademika Lavrent'eva 13, Novosibirsk, 630090 Russia

Submitted January 13, 2005; accepted for publication January 23, 2005

Abstract—The effect of additional implantation of hydrogen ions into the region of the interface between the split-off silicon layer and the buried insulator in silicon-on-insulator structures and subsequent high-temperature annealing on the parameters of the structures and their radiation resistance is studied. This modification of silicon-on-insulator structures gives rise to the following effects. The mobile charge present in the oxide of the initial structures becomes immobilized, which stabilizes the characteristics of silicon-on-insulator structures and simultaneously increases the fixed charge near the boundary with the split-off silicon layer. Furthermore, additional traps are introduced into the oxide; these are predominantly electron traps that accumulate negative charge during irradiation. As a result, the charge in the oxide of silicon-on-insulator structures is decreased somewhat at the initial stage of irradiation but then remains nearly unchanged up to doses of 10^7 rad. Conventional accumulation of positive charge occurs at the second boundary of the structure and is typical also of initial (unmodified) silicon-on-insulator structures. © *2005 Pleiades Publishing, Inc.*

1. INTRODUCTION

Development of the technology of silicon-on-insulator (SOI) structures is largely due to the progress that has been made regarding the radiation resistance of electronic devices by using SOIs instead of other structures. It is well known that irradiation of discrete devices and integrated circuits (ICs) leads to problems even at doses as low as 10^3–10^4 rad, in which case one observes an increase in generation currants, a decrease in the relaxation time of nonequilibrium depletion, and other processes that lead to a reduction in both the detectability of metal–insulator–semiconductor photodetectors and the efficiency of transport in charge-coupled devices [1]. The space charge increases in thick passivating oxides at doses ranging from 10^4 to 10^5 rad, which gives rise to a spurious coupling between IC components. Accumulation of charge in the gate insulator is observed only at the doses that exceed 10^5 rad. Location of the circuit components at separate islands in SOI structures brings about both a drastic decrease in the areas of *p–n* junctions and complete isolation of separate transistors from each other. As a result, problems with irradiation of SOI-based devices arise only at doses of 10^5 rad and higher. However, the charge in SOI-based devices is introduced not only into the gate oxide but also into the buried insulator. Accumulation of positive charge in the oxide brings about the formation of an *n*-type channel in the split-off silicon layer, an increase in the leakage current, and a shift of the threshold voltage in *n–p–n* transistors. This circumstance has aroused interest in study and modification of the properties of the buried insulator in SOI structures. The case where the charge at the Si/SiO$_2$ interface is constant and does not vary under the effect of irradiation seems to be optimal. A possible solution to the problem of charge accumulation may the introduction of electron traps into the oxide, as these can compensate for positive-charge accumulation. For example, excess silicon atoms are present in the oxide of SIMOX (separation by implantation of oxygen) wafers; it is believed that these atoms act as traps for electrons and ensure a smaller variation in the parameters of these wafers [2]. In addition, it is well known from both field- and radiation-related experiments that implantation of various impurities (for example, P, Si, Ge, As, etc.) into the oxide leads to the introduction of traps that capture negative charge [3]. It should be noted that the centers introduced by implantation of impurities capture, as a rule, not only electrons but also holes; moreover, the density of the introduced traps is typically quite high (higher than 10^{12} cm^{-2}). The presence of electron traps in the oxide after being subjected to an implantation of hydrogen ions and subsequent annealing at a high temperature is typical of the so-called UNIBOND structures, in which the implanted oxide serves as the buried insulator [4]. Implantation of hydrogen has been already used in the production of SOI wafers by the DeleCut method; however, the buried insulator was not subjected to ion implantation [5]. Nevertheless, the formation of a low-density negative charge was also observed in the vicinity of the bonding boundary [6]. In addition, the passivating effect of the properties of hydrogen on the states at the Si/SiO$_2$ interface and the traps in the oxide are well known.

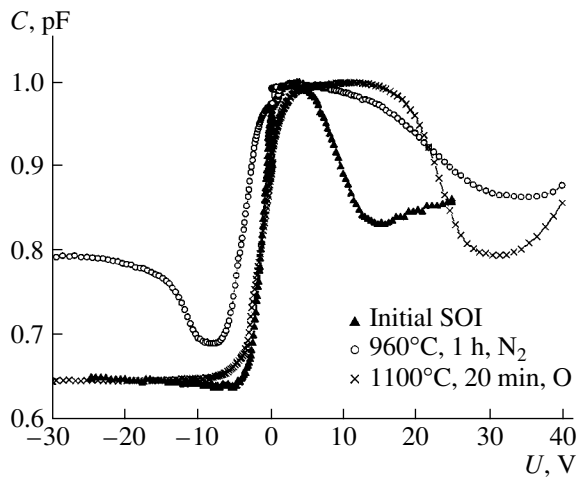In this paper, we report the results of studying the properties of SOI structures modified by additional

Fig. 1. Capacitance–voltage characteristics of the initial SOI structure and the SOI structures implanted with hydrogen and then annealed either for 1 h at 960°C or for 20 min at 1100°C.

hydrogen implantation into the boundary region and subsequent high-temperature annealing. It is established that this treatment of the structures somewhat increases the initial charge in the oxide at the interface between the split-off silicon layer and the buried insulator; however, this increase is balanced by stabilization of the mobile charge in the insulator of SOI structures and stabilization of the charge under irradiation at doses as high as 10^7 rad.

2. EXPERIMENTAL

As the initial material, we used SOI structures fabricated by the DeleCut method [5] and based on n-type silicon. The thickness of the split-off silicon layer was about 500 nm, and the thickness of the buried-insulator layer was 280 nm. Hydrogen ions with an energy of 130 keV were implanted into the structures at a dose of 4×10^{16} cm^{-2}. The projected range of ions with this energy nearly coincides with the depth of the Si/SiO$_2$

Table 1. Charge density at the Si/SiO$_2$ boundaries in the initial SOI structures and the structures implanted with hydrogen ions and then annealed at T_{ann} = 960°C in a nitrogen atmosphere and at T_{ann} = 1100°C in an oxygen atmosphere

Structure and T_{ann}	Determination based V_{FB}		Determination based V_{mg}	
	Q_f, cm^{-2}	Q_s, cm^{-2}	Q_f, cm^{-2}	Q_s, cm^{-2}
Initial	3.3×10^{11}	3.3×10^{10}	6×10^{11}	2.1×10^{11}
960°C	5×10^{11}	7.1×10^{10}	1.2×10^{12}	2.6×10^{11}
1100°C	8.8×10^{11}	7×10^{9}	1.2×10^{12}	2.3×10^{11}

Note: Q_s is the charge density at the oxide–substrate boundary and Q_f is the charge density at the interface between the split-off silicon layer and the oxide.

interface. The wafers were then annealed for 1 h at a temperature of 960°C in a nitrogen atmosphere or for 20 min at a temperature of 1100°C in an oxygen atmosphere. In order to study the SOI's properties, we fabricated Al/Si/SiO$_2$/Si/Al mesa structures with an area of 10^{-2}–10^{-3} cm^{-2}.

To determine the parameters of the structures, we measured and analyzed their high-frequency (1 MHz) capacitance–voltage (C–V) characteristics. Two distinct regions of capacitance modulation can be recognized in the C–V characteristics of the n-Si/SiO$_2$/n-Si structures (Fig. 1). We can assume the following:

(i) a decrease in the capacitance at negative voltages corresponds to the formation of a space-charge region (SCR) in the substrate if the split-off silicon layer is in a state of enhancement, and

(ii) a decrease in the capacitance at positive voltages is related to the SCR formation in the split-off silicon layer if the substrate is in a state of enhancement.

The value of the flat-band voltage V_{FB} in both regions of capacitance modulation was used to determine the charge in the insulator for two boundaries. This charge included the fixed charge in the insulator and the charge at the surface states. In order to separate the contribution of the surface states to the value of the fixed charge in the oxide, we also used the voltage corresponding to the Fermi level position at approximately the midgap V_{mg}; the fixed charge in the insulator was then calculated for each boundary on the basis of the value of V_{mg}. The traps present in the insulator were revealed by studying the field effect (accumulation of charge in the insulator when the structures were kept under the application of voltage). The radiation-related properties of the SOI structures modified by hydrogen implantation were studied using irradiation with 2-MeV electrons at doses ranging from 10^5 to 10^7 rad. Accumulation of charge in the insulator of the irradiated structures was also assessed from the C–V characteristics via the flat-band voltage.

3. RESULTS AND DISCUSSION

In Fig. 1, we show the C–V characteristics of the initial SOI structure and the structures modified by hydrogen implantation and annealing at different temperatures. In Table 1, we list the values of the charges, which were calculated using the flat-band voltage V_{FB} (case I) or the voltage V_{mg} (case II), at both boundaries of one of the SOI structures. In case I, the negative charge captured by the surface states in n-Si is subtracted from the fixed positive charge in the oxide. In case II, the calculated charge is related only to the fixed charge in the insulator. The surface-state density can be estimated from the difference $Q_f(V_{mg}) - Q_f(V_{FB})$. It can be seen that, as a result of the modification of the SOI structures by additional implantation, there is an increase in the positive-charge density at the interface between the split-off silicon layer and the oxide. It fol-
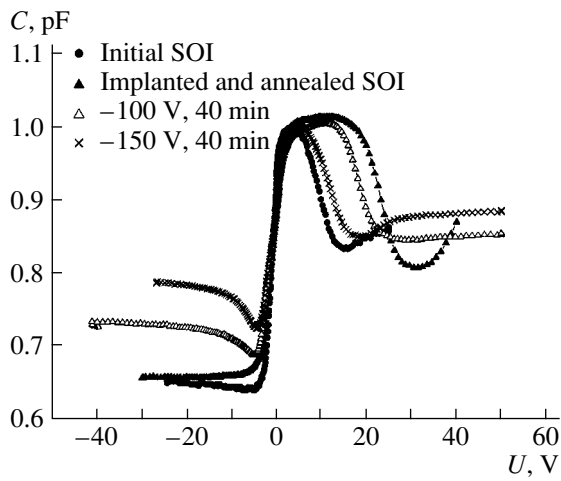
C, pF

Fig. 2. Capacitance–voltage characteristics of the initial SOI structure and the SOI structures implanted with hydrogen and then annealed at a temperature of 1100°C, before and after storage under negative voltages.
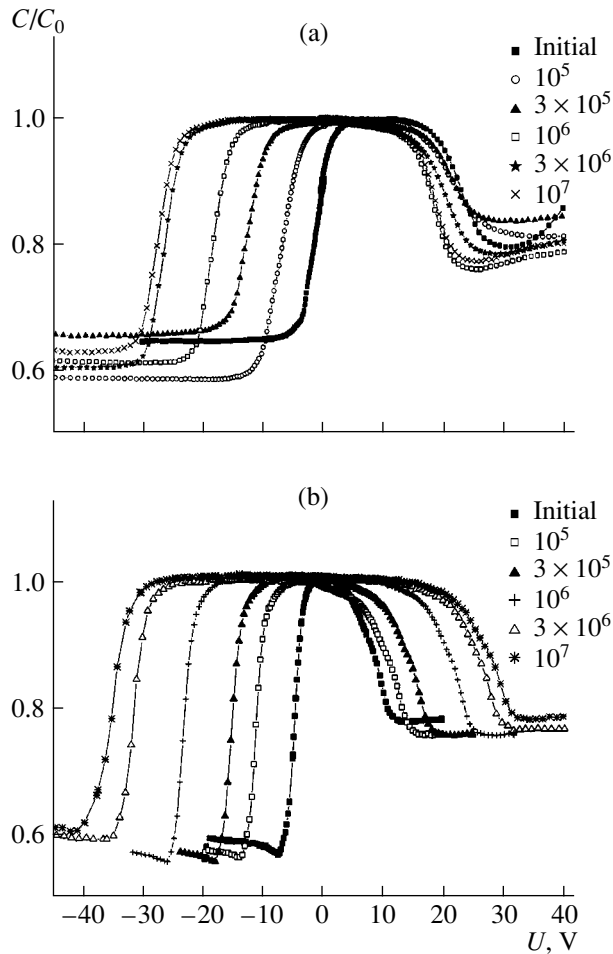
C/C_0

Fig. 3. Capacitance–voltage characteristics of the (a) initial and (b) modified SOI structures in relation to the dose of irradiation with 2-MeV electrons. The dose is indicated in the panel and is expressed in rads. $T_{ann} = 1100$°C for the modified structure.
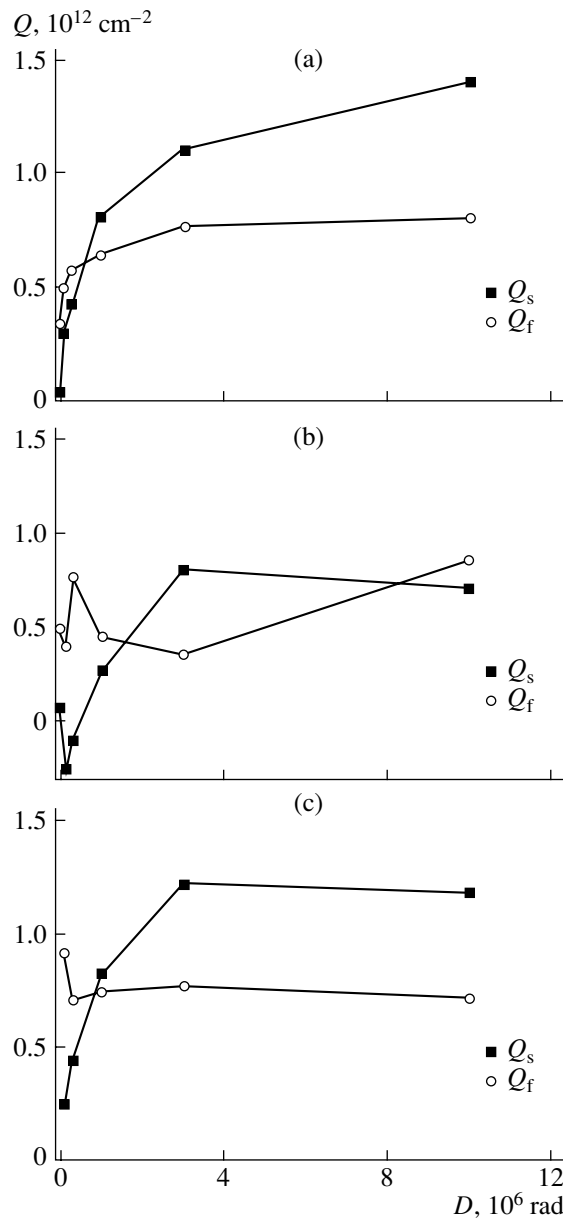
Q, 10^{12} cm^{-2}

Fig. 4. Dependences of the charge density in the buried oxide of (a) the initial SOI structure and the modified SOI structures annealed at (b) 960 and (c) 1100°C on the dose of irradiation with electrons. Q_s is the charge density at the oxide–substrate boundary and Q_f is the charge density at the interface between the split-off silicon layer and oxide.

lows from the data listed in Table 1 that the modified charge at the interface between the split-off silicon layer and the buried insulator is the same after annealing at 950 and 1100°C; however, the density of states at the boundary is much lower in the case of the higher annealing temperature (7×10^{11} and 3.2×10^{11} cm^{-2} after annealing at 950 and 1100°C, respectively). The charge at the second boundary remains nearly the same.

In Fig. 2, we show the C–V characteristics of the structures for which negative voltages of –100 and

Table 2. Charge density at the Si/SiO$_2$ boundaries in the SOI structures implanted with hydrogen ions and then annealed at 1100°C, both before and after storage under a voltage U for 40 min

U, V	Q_f, cm^{-2}	$Q_f - Q_{f0}$, cm^{-2}	Q_s, cm^{-2}	$Q_s - Q_{s0}$, cm^{-2}
0	8.8×10^{11}	0	6.8×10^{9}	0
−100	6.6×10^{11}	-2.2×10^{11}	3.9×10^{10}	3.2×10^{10}
−150	3.2×10^{11}	-5.6×10^{11}	3.9×10^{10}	3.2×10^{10}
−200	-7.6×10^{11}	-1.6×10^{12}	-1.3×10^{11}	-1.3×10^{11}
+100	9.3×10^{11}	5×10^{10}	10^{10}	3.2×10^{9}

−150 V were constantly applied to the split-off silicon layer for 40 min. In this case, electrons are injected from the split-off silicon into the oxide. It follows from Fig. 2 that the accumulation of negative charge occurs in the vicinity of the interface between the silicon layer and the oxide. In Table 2, we list the charge densities at both Si/SiO$_2$ interfaces in the structures under consideration; in addition, the variations in these densities are given in comparison to those in the initial structures. It can be seen that negative charge is accumulated at the interface between the split-off silicon layer and the oxide and that the density of this charge can be as high as ~2×10^{12} cm^{-2}. The introduction of a positive charge is observed in the SOI structures when a positive potential is applied to the split-off silicon layer; however, this charge has a much smaller magnitude than that of the negative charge (see Table 2). Measurements of the C−V characteristics of the structures within 5–20 min after the voltage was switched off showed that the introduced charge was stable and the structures under consideration did not involve a mobile charge at the bonding boundary.

The variations in the C–V characteristics of the initial and modified structures resulting from irradiation with electrons are illustrated in Fig. 3. It can be seen that the charge is mainly accumulated only at the interface with the substrate in the modified structures, whereas a shift of the modulation regions of the C–V characteristics to higher voltages is observed after irradiation of the initial structure. The slope of the C–V characteristics remains almost changed, which indicates that the density of states is constant at the boundaries (unaffected by irradiation). The charge density at the Si/SiO$_2$ interface (as calculated on the basis of the value of V_{FB}) is shown in Fig. 4 as a function of the electron dose for the initial and modified structures. The modified structure annealed at 1100°C is the most stable (from the standpoint of the charge at the interface between the split-off silicon layer and the insulator).

4. DISCUSSION

Maintenance of the initial SOI structures by applying voltage (without modification by hydrogen implan-

tation) made it possible to observe the motion of the mobile charge located in the oxide and localized near the interface with the split-off silicon layer but did not lead to accumulation of an additional charge [4]. The value of the mobile-charge density was typically equal to $(2–3) \times 10^{11}$ cm^{-2}.

An additional implantation of hydrogen into the SOI structures in combination with high-temperature annealing brings about significant changes in the structures. In this case, a mobile charge is not observed when studying the field effect in the structures. Apparently, the mobile charge is captured by the defects that arise in the course of irradiation. As a result, the modified SOI structures have more stable characteristics, which is important for optimization of the structure parameters. It can be also seen that, as a result of modification of the SOI structures, mainly electron traps are introduced (the hole-trap concentration is much lower).

Irradiation of the SOI structures typically leads to accumulation of a positive charge. The density of this charge at the interface between the split-off silicon layer and the buried oxide can be as high as $(7–12) \times 10^{11}$ cm^{-2}, whereas the initial value was 4×10^{11} cm^{-2}. As can be seen from Fig. 4a, the largest charge accumulated in the structure under consideration as a result of irradiation amounts to 7.5×10^{11} cm^{-2}. After modification of this structure (the temperature of the final annealing was 1100°C) the charge density at the given boundary becomes even higher (8.8×10^{11} cm^{-2}); a decrease in the charge density to 7.0×10^{11} cm^{-2} is observed in the course of irradiation (Fig. 4c). It is of interest that the densities of the positive charge accumulated in the initial and modified structures as a result of irradiation are in close agreement in spite of modification of the structures by additional irradiation. However, the structures do become more stable; i.e., the charge densities before and after irradiation differ from each other insignificantly. As a result of irradiation, a positive charge is conventionally accumulated at the second boundary. This behavior is also characteristic of the initial (unmodified) SOI structures.

The use of a lower temperature for the final annealing after SOI modification gives rise to more complex dose dependences of the charge density; in particular, an introduction of negative charge is observed at the initial stage. In this case, there is apparently loosely bonded hydrogen in the structure, which affects the charge accumulation at the second oxide–substrate interface. In addition, these structures also feature a high density of surface states (see Fig. 1 and Table 1). A higher temperature of final annealing for the modified SOI structures appears to be preferable from the standpoint of the stability of these structures.

In this study, the dose of the hydrogen implantation was not varied. It can be expected that the proper choice of implanted-hydrogen dose will make it possible to obtain SOI structures with a higher degree of optimization with respect to the parameters; however, it has

already been explicitly shown in this study that the SOI parameters can be stabilized.

5. CONCLUSIONS

Thus, additional implantation of hydrogen ions into SOI structures followed by high-temperature annealing gives rise to the following effects.

The mobile charge of protons in the oxide is fixed, which stabilizes the characteristics of SOI structures and simultaneously increases the fixed-charge density at one of the boundaries with the split-off silicon layer. Electron traps are predominantly introduced into the oxide in the course of the structures' modification; furthermore, these traps accumulate negative charge during irradiation. As a result, the charge density in the oxide of SOI structures decreases somewhat at the initial stage of irradiation with electrons and then remains almost constant up to doses as high as 10^7 rad. Positive charge is conventionally accumulated at the second boundary of the structure. This effect is also characteristic of the initial (unmodified) SOI structures.

REFERENCES

1. V. A. Gurtov, *Radiation-Induced Processes in Metal–Insulator–Semiconductor Structures* (Petrozavod. Gos. Univ., Petrozavodsk, 1988) [in Russian].
2. Y. E. Boesch, T. L. Taylor, L. R. Hite, and W. E. Bailey, IEEE Trans. Nucl. Sci. **37**, 1982 (1990).
3. A. N. Nazarov, T. Gebel, L. Rebohle, and W. Skorupa, J. Appl. Phys. **94**, 4440 (2003).
4. A. N. Nazarov, V. I. Kilchytska, I. P. Barchuk, and A. Tkachenko, in *Abstracts of Meeting of Electrochemical Society* (Washington, 2001), No. 502.
5. D. V. Nikolaev, I. V. Antonova, O. V. Naumova, *et al.*, Fiz. Tekh. Poluprovodn. (St. Petersburg) **36**, 855 (2002) [Semiconductors **36**, 800 (2002)].
6. V. P. Popov, I. V. Antonova, L. V. Mironova, and V. F. Stas', RU Patent No. 216719 (1999).

Translated by A. Spitsyn

LOW-DIMENSIONAL SYSTEMS

Radiative Recombination in GaN Nanocrystals at High Intensities of Optical Excitation

A. N. Gruzintsev*^, A. N. Red'kin*, and C. Barthou**

**Institute of Microelectronics Technology and High Purity Materials, Russian Academy of Sciences,
Chernogolovka, 142432 Russia*
^e-mail: gran@ipmt-hpm.ac.ru
**Université P. et M. Curie, Paris, France
Submitted January 11, 2005; accepted for publication January 26, 2005

Abstract—The spectra of spontaneous UV luminescence of GaN nanocrystals excited by optical pumping at power densities ranging from 50 W/cm² to 50 MW/cm² are studied. At room temperature, radiation peaks related to the emission of free excitons and recombination of electron–hole plasma are revealed. The spectral characteristics of the emission of the electron–hole plasma in GaN is studied in the wide temperature range of 77–550 K. © 2005 Pleiades Publishing, Inc.

1. INTRODUCTION

The contemporary approach in optoelectronics consists in the search for materials that can emit radiation in the blue and UV spectral regions [1]. At the present time, it is agreed that the compounds exhibiting the greatest potential with respect to developing light-emitting structures for these spectral regions are zinc oxide and gallium nitride, as well as GaN-based solid solutions. Of particular importance is the growth of these semiconductor materials and fabrication of the structures based on them and whether they can emit monochromatic radiation in the region corresponding to the exciton or optical absorption edge. To this end, it is necessary to fabricate high-quality thin films or crystals from ZnO and GaN wide-gap semiconductors, since intrinsic defects in the crystalline lattice or uncontrollable donor- or acceptor-type impurities may produce a long-wavelength shift of the luminescence line or new inhomogeneously broadened emission bands in the so-called impurity spectral region [2, 3].

Gallium nitride and zinc oxide are direct-band materials. The band gaps of their hexagonal modifications are 3.428 eV (GaN) and 3.37 eV (ZnO) at room temperature. UV emission can be caused by recombination of the free excitons present in the hexagonal phase. According to the data available earlier publications [4, 5], the binding energy of an electron and hole in the exciton state is 60 and 25 meV for ZnO and GaN, respectively. Therefore, in ZnO, excitons are thermally stable at room temperature, and it is possible to accomplish a laser effect on the basis of their recombination. The exciton mechanism of laser emission ("lasing") is reasonably efficient, allowing relatively low threshold intensities during optical pumping (from 24 kW/cm² and above) [6]. In GaN, excitons are unstable at room temperature, and stimulated near-edge emission is, as a rule, controlled by recombination of the electron–hole plasma (EHP). This circumstance leads to a sharp increase in the threshold pumping intensity up to 1.2 MW/cm² and, as a consequence, the use of micrometer-sized laser resonators [7]. As a result, quantum-well (QW) structures are commonly used in the development of GaN-based semiconductor lasers to increase the exciton binding energy and lower the lasing threshold.

At the same time, study of the mechanisms of radiative EHP recombination in GaN is of considerable interest in relation to developing high-power semiconductor lasers. In fact, if the intensity of optical or electron-beam pumping is much higher than the threshold intensity, the exciton mechanism of lasing is replaced by the EHP recombination mechanism. The purpose of this study was to investigate the spectral characteristics and intensity of EHP emission in GaN single crystals in relation to the temperature and optical excitation density.

2. EXPERIMENTAL

GaN single crystals were synthesized using a modified form of the chloride–hydride method of chemical transport reactions or the chemical vapor deposition (CVD) method [8]. In contrast to the conventional procedure, metallic gallium of 99.999% purity and extra-high-purity ammonium chloride of extra-pure grade were used as the initial components. High-purity nitrogen (PNG brand) served as a gas carrier. The process was carried out in a two-zone horizontal quartz reactor. In the first zone, gallium heated to a temperature of 400°C interacted with ammonium chloride. The vapors consisting of monoammoniate of gallium trichloride formed as a result of the reaction were transferred, by nitrogen flow, to the second zone, where they were

decomposed and the formation of gallium nitride occurred. The temperature of the pyrolysis was 950°C. Plates of (0001)-oriented sapphire served as substrates. According to electron microscopy data [8], GaN films consist of layers of fine single crystals (less than 1 μm in size), with the average size of separate crystallites being ~0.4 μm and each crystallite having well-pronounced crystalline facets. The crystallites showed *n*-type conductivity and a rather low resistivity (10 Ω cm). The regular hexagonal shape of the nanocrystals suggested the predominance of the hexagonal modification of GaN, as was confirmed by X-ray diffraction analysis.

The luminescence spectra were recorded during excitation with a Photonics LN 1000 nitrogen laser at the wavelength 337.1 nm (at a pulse duration of 0.6 ns and pulse energy of 1.4 mJ) or by a tunable xenon lamp whose radiation was transmitted through a monochromator. In the both cases, the excitation induced interband transitions. However, the xenon lamp provided a lower power density at the sample surface (50 W/cm^2), while the nitrogen laser, equipped with a set of absorbers, made it possible to attain power densities ranging from 50 kW/cm^2 to 50 MW/cm^2. The radiation emitted by a sample was collected along the direction orthogonal to the sample surface by an optical waveguide positioned at a distance of 10 mm from the sample surface. Then, the radiation was analyzed with the use of a spectrometer (Jobin–Yvon Spectrometer HR460) and a multichannel detector (PM Hamamatsu 5600U). The photoluminescence (PL) spectra of the GaN layers were studied in an optical cryostat at temperatures ranging from $T = 77$ to 550 K.

3. RESULTS AND DISCUSSION

Two typical room-temperature PL spectra for the GaN nanocrystals on sapphire substrates are shown in Fig. 1. The spectra were recorded under excitation of the samples by the xenon lamp (curve *1*) and nitrogen laser (curve *2*). As is evident from Fig. 1, the character of the PL spectra is strongly dependent on the optical-excitation power density (intensity). Under the low excitation intensity (50 W/cm^2) provided at the 300-nm line of the xenon lamp, two PL peaks at photon energies of 1.88 and 2.63 eV in the impurity spectral region and two PL peaks at 3.2 and 3.4 eV in the absorption-edge region are well resolved in the spectrum (Fig. 1, curve *1*). As the intensity of optical pumping increases to 50 kW/cm^2, a single intense line at 3.2 eV (curve *2*), controlled by EHP radiative recombination, becomes dominant in the spectrum. The red and blue emission lines of GaN are due to extended lattice defects and nitrogen vacancies, respectively [9, 10]. The shortest wavelength peak, at 3.4 eV, is related to recombination of free excitons in the hexagonal GaN phase. At room temperature, the intensity of this band is low because of thermal dissociation of the excitons.

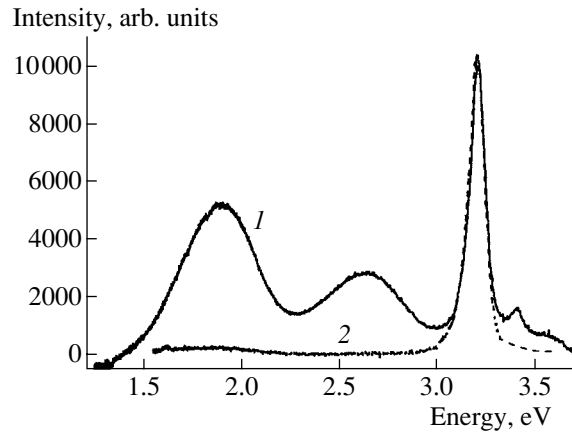In this study, we are particularly interested in the violet-region edge emission at 3.2 eV that is dominant

Fig. 1. Photoluminescence spectra of the GaN nanocrystals under excitation by (*1*) a xenon lamp at 300 nm and (*2*) a nitrogen laser at 337.1 nm. $T = 300$ K.
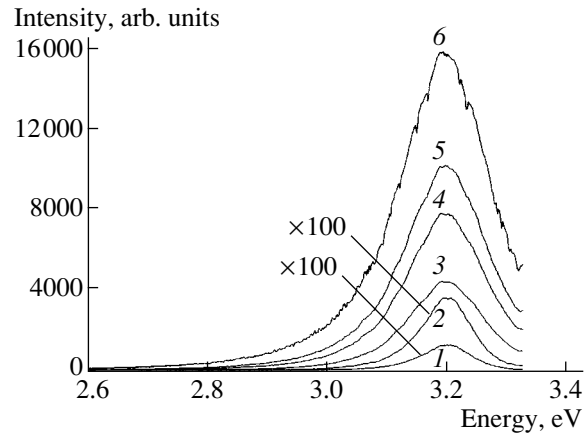

Fig. 2. Photoluminescence spectra of the GaN nanocrystals excited by a nitrogen laser at the intensities (*1*) 50 and (*2*) 122 kW/cm^2 and (*3*) 5.87, (*4*) 15.5, (*5*) 23.4, and (*6*) 50 MW/cm^2. $T = 300$ K.

in the PL spectrum of GaN at high levels of pulse pumping by the nitrogen laser. In order to accomplish lasing of the GaN nanocrystals in the absorption-edge region, we elevated the peak power of the laser excitation. Figure 2 shows the emission spectra of the samples at optical-pumping intensities ranging from 50 kW/cm^2 (curve *1*) to 50 MW/cm^2 (curve *6*). It is evident that, at very high pumping intensities, the EHP band is dominant in the PL of the nanocrystals. The peak of this band shifts slightly to longer wavelengths (from 3.2 to 3.19 eV) under a three orders of magnitude increase in the pumping intensity. The dependences of the area under the PL spectral curve and of the full width at half-maximum (FWHM) of the PL line on the laser excitation intensity suggest that emission is spontaneous over the entire intensity range. In fact, the area under the PL spectral curve increases almost linearly (dashed curve in Fig. 3) with excitation intensity, and the FWHM of the PL line
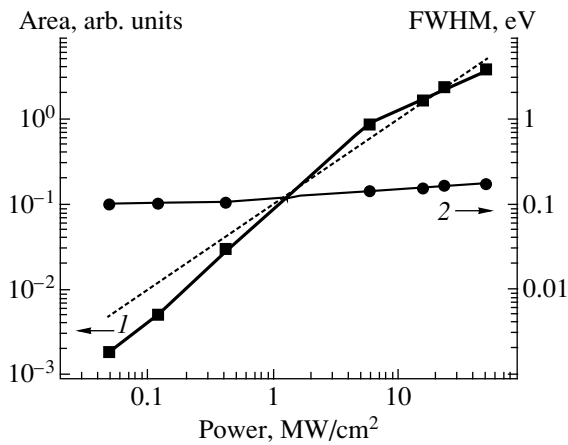
Fig. 3. Dependences of (*1*) the area under the emission spectral curve and (*2*) the FWHM of the PL band of the GaN nanocrystals on the excitation intensity of the nitrogen laser. *T* = 300K.

Fig. 4. Photoluminescence spectra of the GaN nanocrystals at *T* = (*1*) 77, (*2*) 100, (*3*) 132, (*4*) 165, (*5*) 200, (*6*) 232, (*7*) 262, (*8*) 300, (*9*) 302, (*10*) 332, (*11*) 360, (*12*) 398, (*13*) 433, (*14*) 460, (*15*) 501, (*16*) 532, and (*17*) 550 K. The power density of the nitrogen-laser excitation radiation was 50 MW/cm^2.

Fig. 5. Dependences of the (*1*) peak position in the emission curve and (*2*) width of the photoluminescence band at half-maximum in the GaN nanocrystals on the measurement temperature. The power density of the nitrogen-laser excitation radiation was 50 MW/cm^2.

increases gradually from 0.106 to 0.176 eV. In the case of stimulated PL emission, the increase in area would be superlinear and have a well-pronounced threshold; in contrast, the line width would decrease at above-threshold pumping intensities [7].

It can be assumed that the edge emission of the GaN nanocrystals becomes stimulated at lower temperatures. As the temperature decreases, the probability of nonradiative recombination of nonequilibrium electrons and holes decreases, and the probability of thermal dissociation of free or bound excitons in the material decreases as well. Figure 4 shows the PL spectra of the nanocrystals at temperatures in the range 77–550 K under the highest intensity of excitation pulses used (50 MW/cm^2). As the temperature increases, a gradual long-wavelength shift of the peak of the edge emission from the GaN nanocrystals from 3.26 to 3.07 eV is observed along with a simultaneous decrease in the PL intensity. Under these conditions, the FWHM of the PL band shows a considerable increase from 0.1 eV at 77 K to 0.33 eV at 550 K (Fig. 5). However, this increase is gradual, suggesting a lack of any changes in the PL mechanism in this temperature range. Therefore, under the maximal laser excitation intensity, spontaneous EHP luminescence is dominant in the GaN nanocrystals. A further increase in the pumping intensity resulted in complete degradation (laser-induced evaporation) of the samples. In this case, the samples were not thermally vaporized but exploded in the high electric field of the focused laser irradiation.

Thus, without special fabrication of QW structures or laser resonators, our attempts to achieve stimulated emission in GaN nanocrystals in the edge spectral region have been unsuccessful. Sometimes, the natural faces of the GaN microcrysals may serve as high-*Q* resonators for optical radiation [11]. A fraction of radiation is reflected from the crystal faces and passes back into the sample, providing the positive feedback of the
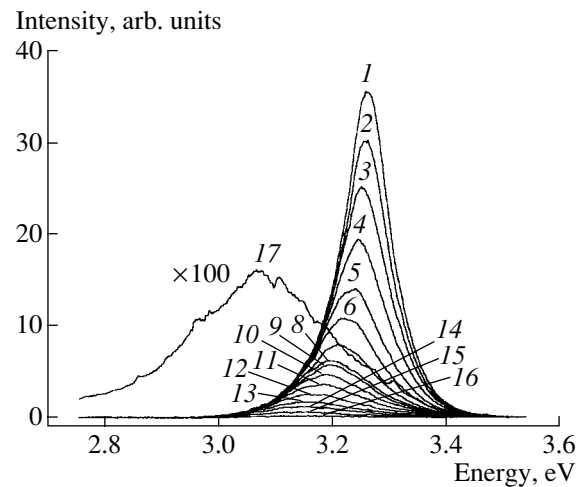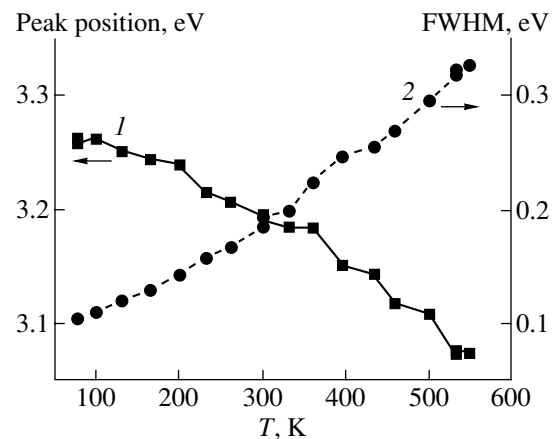
laser. In this case, the threshold pumping intensity was a few megawatts per unit area. The wavelength of lasing correlated with the peak of the EHP emission in GaN; as was shown above (Fig. 1), the position of this peak depends only slightly on the excitation intensity. In general, theoretical calculations of the density of excited states for the carriers in EHP are rather complicated. Such calculations should include the kinetic energy of electrons and holes, the energy of their exchange interaction, and the correlation energy [12]. A number of theoretical models currently in existence yield different results. For this reason, it is simpler to make use of the above data on the spectral dependences

of EHP radiative recombination in GaN in relation to temperature and pumping intensity to predict the parameters of GaN-based high-power semiconductor lasers. First of all, it can be seen that the peak position in the emission spectra demonstrates high stability over a wide range of pumping intensities, from 50 W/cm^2 to 50 MW/cm^2 (Fig. 1, 2). The temperature shift of the EHP emission peak for the GaN nanocrystals is rather large, exceeding the temperature change in the band gap of the material (Fig. 5). This circumstance is due to the considerable temperature broadening of the PL line resulting from the increase in the kinetic energy of electrons and holes in the plasma. In the general case, the large width of the EHP line is a disadvantage as compared to the narrow lines of the bound states of electrons and holes (excitons) in semiconductors. However, the intensity of exciton emission in GaN is low (the 3.4 eV peak in Fig. 1) at room temperature because of thermal disintegration of the excitons.

It should also be noted that a comparison of the efficiencies of the edge emission of GaN and ZnO [13] under the same level of optical pumping highlights the weakness of GaN in this context. For ZnO, the more efficient stimulated EHP emission is dominant in films and powders without laser resonators or QW structures. However, because low-resistivity p-type ZnO layers are unavailable at present, it is impossible to replace GaN with ZnO when developing UV semiconductor emission sources.

4. CONCLUSION

In summary, the intense UV emission observed in GaN nanocrystals exposed to high-intensity optical pumping can be attributed to spontaneous radiative recombination in the electron–hole plasma. As the pumping intensity increases, the EHP luminescence line becomes considerably broadened due to an increase in the kinetic energy of electrons and holes in the plasma. With an increase in temperature, the EHP band shifts to longer wavelengths and becomes broader and lower in intensity. The linear dependence of the intensity of this band on the excitation intensity is caused by the spontaneous character of the EHP emis-

sion of GaN over the entire range of pumping intensities from 50 W/cm^2 to 50 MW/cm^2. In order to attain stimulated EHP emission in GaN, optical resonators or quantum-confined structures have to be used to ensure the space localization of the excited carriers.

REFERENCES

1. S. Nakamura, T. Mukai, and M. Senoh, Jpn. J. Appl. Phys. **30**, L1998 (1991).
2. S. J. Xu, G. Li, and S. J. Chua, Appl. Phys. Lett. **72**, 2451 (1998).
3. E. R. Glaser, T. A. Kennedy, and K. Doverspike, Phys. Rev. B **51**, 13326 (1995).
4. M. H. Huang, S. Mao, H. Feiick, *et al.*, Science **292**, 1897 (2001).
5. J. W. Tomm, B. Ullrich, X. G. Qui, *et al.*, J. Appl. Phys. **87**, 1844 (2000).
6. P. Zu, Z. K. Tang, G. K. L. Wong, *et al.*, Solid State Commun. **103**, 459 (1997).
7. X. H. Yang, T. J. Schmidt, W. Shan, and J. J. Song, Appl. Phys. Lett. **66**, 1 (1995).
8. A. N. Red'kin, V. I. Tatsiĭ, Z. I. Makoveĭ, *et al.*, Neorg. Mater. **40**, 1197 (2004).
9. A. N. Gruzintsev, U. Kaĭzer, I. I. Khodos, and V. Rikhter, Neorg. Mater. **372**, 1 (2001).
10. U. Keiser, A. N. Gruzintsev, I. I. Khodos, and V. Richter, Neorg. Mater. **36**, 720 (2000).
11. S. Bidnyk, B. D. Little, Y. H. Cho, *et al.*, MRS Internet J. Nitride Semicond. Res. **4S1**, G6.48 (1999).
12. A. Yamamoto, T. Kido, T. Goto, *et al.*, Solid State Commun. **122**, 29 (2002).
13. A. N. Gruzintsev, V. T. Volkov, C. Barthou, *et al.*, Thin Solid Films **459**, 262 (2004).

Translated by É. Smorgonskaya

LOW-DIMENSIONAL
SYSTEMS

Spin Splitting of the *X*-valley Donor Impurity States in AlAs Barriers and the Spatial Distribution of the Probability Density of Their Wave Functions

E. E. Vdovin^ and Yu. N. Khanin

Institute of Microelectronic Technology and Ultra-High-Purity Materials, Russian Academy of Sciences,
Chernogolovka, Moscow oblast, 142432 Russia
^e-mail: vdovin@ipmt-hpm.ac.ru
Submitted December 22, 2004; accepted for publication January 27, 2005

Abstract—Using magnetotunneling spectroscopy, the spin splitting of the ground state of Si donors associated with the *X* valley in an AlAs barrier has been observed. The magnitude of the effective g_I factor in an AlAs barrier is found to be equal to 2.2 ± 0.1. It has also been found that the distribution of the probability density of electron wave functions of donor impurity states has a biaxial symmetry in the growth plane and axes corresponding to the principal crystalline directions in this plane. © 2005 Pleiades Publishing, Inc.

In recent times, the effect of spin on electronic transport has attracted profound interest from both applied and fundamental standpoints [1, 2]. Resonance tunneling via self-organized quantum dots (and localized impurity states physically similar to them) in semiconductor structures is a convenient tool for studying spin-dependent electron transport. Such tunneling experiments have made it possible not only to directly observe the spin splitting of zero-dimensional impurity states in GaAs quantum wells (QWs) [3–5] or isolated InAs quantum dots [6–8] and to directly measure the magnitude of the *g* factor of zero-dimensional states but, in addition, to study the mesoscopic fluctuations of spin splitting in such systems and to determine local variations in the *g* factor [9].

We studied electron transport through one-barrier GaAs/AlAs/GaAs heterostructures. Since AlAs is not a direct-gap semiconductor with the bottom of the conduction band at the *X* point of the Brillouin zone, while GaAs is a direct-gap semiconductor with the bottom of the conduction band at the center of the Brillouin zone (the Γ point), the tunneling current in such structures is controlled by resonance tunneling between two-dimensional states associated with the Γ valley of the GaAs conduction band and different (two-dimensional and zero-dimensional) donor states associated with the lower *X* valleys of the AlAs conduction band [10–23]. In this study, we report the first observation of spin splitting of *X*-valley donor impurity states in an AlAs barrier (*X* donors) using magnetotunneling spectroscopy. Such donor *X* states are formed in AlAs because silicon impurity atoms penetrate it from the adjacent δ-doped layers. We determined the magnitude of the *g* factor for different zero-dimensional donor *X* states to be equal to 2.2 ± 0.1. We also found that the distribution of the probability density of the electron wave functions

of donor impurity states has a biaxial symmetry in the growth plane, with the axes corresponding to the principal crystalline directions in this plane.

First, we consider tunneling via an isolated donor impurity in a GaAs QW in a large-area (AlGa)As/GaAs/(AlGa)As two-barrier resonance tunneling diode. An isolated donor impurity in the region of the QW forms a localized (~10 nm in size) hydrogen-like state related to a two-dimensional state in the QW [24]. Sharp resonance features in the current–voltage (*I–V*) characteristics of the tunneling structures are observed under the application of a bias voltage if the energy of each separate impurity state coincides with the Fermi energy of the emitter. The presence of many impurity levels with close energies results in numerous overlapping features in the *I–V* characteristic. By reducing the impurity concentration (or reducing the diameter of the tunneling structure to a submicrometer size), it becomes possible resolve the peaks in the resonance current corresponding to tunneling via separate impurities [22].

In a previous study, we found that resonance tunneling via separate *X* donors in a relatively thin (5 nm) AlAs barrier (representing a QW for the *X*-valley electrons) manifested itself as a fine structure of the main impurity resonance [21]. This fine structure represented a series of weak and relatively diffuse resonance features related to tunneling via donors localized at different positions inside the AlAs layer. In this case, the effect of random fluctuations in the electrostatic potential on the energies of donor impurities appeared to be small. In the situation described in this study, where the donors are located in a relatively thick (11.2 nm) barrier and the effect of random fluctuations in the electrostatic potential is large and governs the impurity state energies, tunneling via donors is seen as sharp well resolved

peaks in the *I–V* characteristic and each of the peaks corresponds to tunneling via an individual donor state. Due to this circumstance, we could observe the spin splitting of donor resonances and directly determine the *g* factor. In this case, the important role of random fluctuations in the electrostatic potential is related to the presence of δ-doped layers near the barrier [25] and to the weak dependence of the donor binding energy on the impurity position in this thick barrier [26].

In our samples, the active part was represented by an 11.2-nm-thick single AlAs barrier located between layers of a two-dimensional electron gas (2DEG). In order to form the 2DEG, we used δ-layers with a concentration of 3×10^{11} cm^{-2} located at distances of 2.8 nm from both sides of the barrier. The AlAs barrier was not doped during growth but donor *X* states were formed in AlAs because of diffusion of Si atoms from the adjacent δ-doped layers. Calculated profiles of the Γ and *X* bands of the active part of the device at a zero bias are shown in Fig. 1. Measurements of the Shubnikov–de Haas oscillations in the structures under study, which are similar to those of [27], have shown that the electron concentration in the 2DEG is $n_s = 3.27 \times 10^{11}$ cm^{-2} and approximately coincides with the technologically expected Si concentration in δ-doped layers.

Our samples were one-barrier heterodiodes grown by molecular-beam epitaxy on heavily doped *N⁺*-GaAs substrates with a (001) orientation at a temperature of 570°C. Silicon was used as the doping impurity and had a concentration in the substrates of 2×10^{18} cm^{-3}.

Symmetric heterostructures consisted of the following sequence of layers: a 2×10^{18} cm^{-3} *N⁺*-GaAs buffer layer 0.5 μm thick, a 3×10^{17} cm^{-3} *N⁺*-GaAs buffer layer 60 nm thick, an undoped GaAs layer 21.6 nm thick, an undoped Ga$_{0.9}$Al$_{0.1}$As layer 5.6 nm thick, an undoped GaAs layer 28 nm thick, a δ-doped layer with a Si concentration of 3×10^{11} cm^{-2}, an undoped GaAs layer 2.8 nm thick, an undoped AlAs barrier layer 11.2 nm thick, an undoped GaAs layer 2.8 nm thick, a δ-doped layer with a Si concentration of 3×10^{11} cm^{-2}, an undoped GaAs layer 28 nm thick, an undoped Ga$_{0.9}$Al$_{0.1}$As layer 5.6 nm thick, an undoped GaAs layer 21.6 nm thick, a 3×10^{17} cm^{-3} *N⁺*-GaAs layer 60 nm thick, and a 2×10^{18} cm^{-3} *N⁺*-GaAs contact layer 0.5 μm thick.

Ohmic contacts were formed by successive sputtering of AuGe/Ni/Au layers and annealing at $T = 400$°C. In order to form a mesa structure 50–200 μm in diameter, standard chemical etching technology was used. The *I–V* characteristics were measured using a standard dc technique at a noise current below 50 fA. The measurements were performed at a temperature of 4.2 K in magnetic fields up to 8 T.

Figure 2b shows the *I–V* characteristic of a typical experimental sample at the temperature 4.2 K, in which a series of sharp peaks appears in the bias range 10–50 mV. The positions and amplitudes of these peaks are different for different samples; however, they are com-
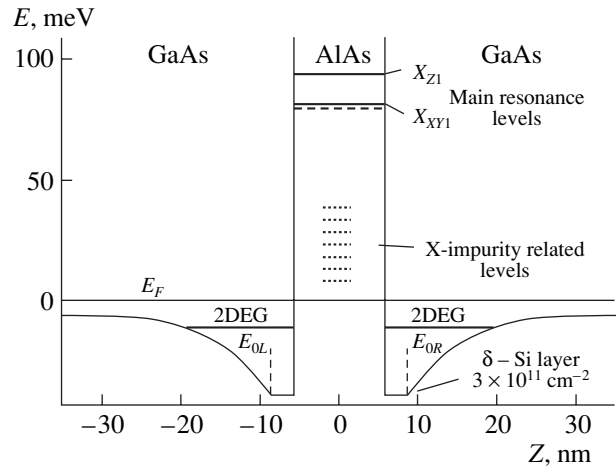

Fig. 1. Calculated potential profile in the active part of the experimental structure under a zero bias voltage. The positions of the Fermi level E_F, the quantum-confinement levels E_{0L} and E_{0R} in the GaAs emitter, the quantum confinement levels in the X_Z and X_{XY} subbands, and the levels of the *X* donors in AlAs are shown.

pletely reproducible for each peak, even after thermal cycling. We believe that these peaks indicate resonance tunneling of electrons via individual impurity states in the AlAs barrier. The observation of similar resonance features in the *I–V* characteristic of two-barrier heterostructures with GaAs QWs related to tunneling via separate zero-dimensional states has already been reported [3, 5, 28]. An increase in bias shifts the energies of donor states with respect to the Fermi level of the two-dimensional gas, which plays the role of the emitter for tunneling electrons. A sharp threshold increase in the tunneling current occurs at a bias at which the energy of a donor state coincides with the Fermi energy E_F of the emitter. Under a further increase in bias, the resonance current drops and vanishes when the energy of the donor state coincides with the bottom of the conduction band E_C in the emitter (see Fig. 2a). The temperature and existence of nonresonance tunneling processes broaden the observed features in the *I–V* characteristic and result in the appearance of a monotonic background current component.

At both directions of the magnetic field with respect to the direction of the current, the peaks corresponding to electron tunneling via impurity states are split. We believe that the observed splitting of the peaks is due to removal of the spin degeneracy of the impurity states by the applied magnetic field. In Fig. 2b, the *I–V* characteristics of an experimental sample are shown in the absence a magnetic field and in a perpendicular field of 8 T (the *I–V* characteristics in a field parallel to the current are similar). In a magnetic field, the energy of the ground state of a donor impurity is split according to the expression

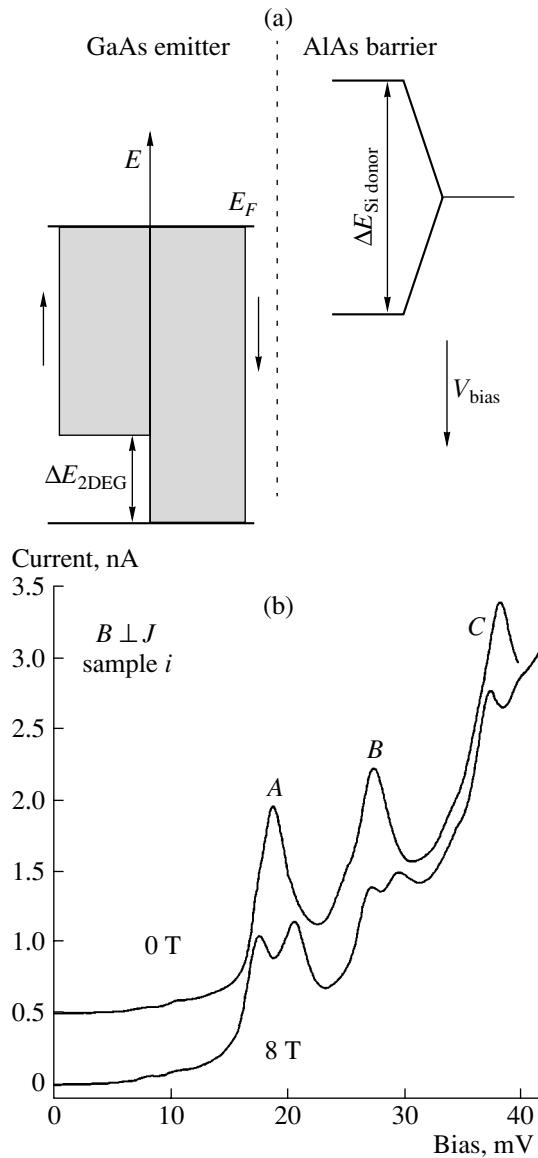$$E_{\text{Si donor}} = m_s g_I \mu_B B m_s \quad (m_s = \pm 1/2), \qquad (1)$$

Fig. 2. (a) Schematic representation of the spin splitting of an Si donor state in AlAs and partial spin polarization of the two-dimensional gas in the emitter in a magnetic field perpendicular to the current. The bias applied to the sample shifts the donor state energy with respect to the Fermi energy in the emitter. (b) Current–voltage characteristics of a sample at 0 T and 8 T in a magnetic field perpendicular to the tunneling current. The measurement temperature was 4.2 K.

where g_I is the g factor of the impurity and μ_B is the Bohr magneton. Accordingly, two separate tunneling channels are formed and we can see two peaks in the I–V characteristic corresponding to tunneling via these spin-split states. In a magnetic field perpendicular to the current (i.e., parallel to the plane of the two-dimensional gas), the 2D emitter is also spin-split by $g_{2D}\mu_B B$, where g_{2D} is the g factor of the GaAs emitter; however, since the two-dimensional gas is in thermal equilibrium, the chemical potentials of its two spin states are
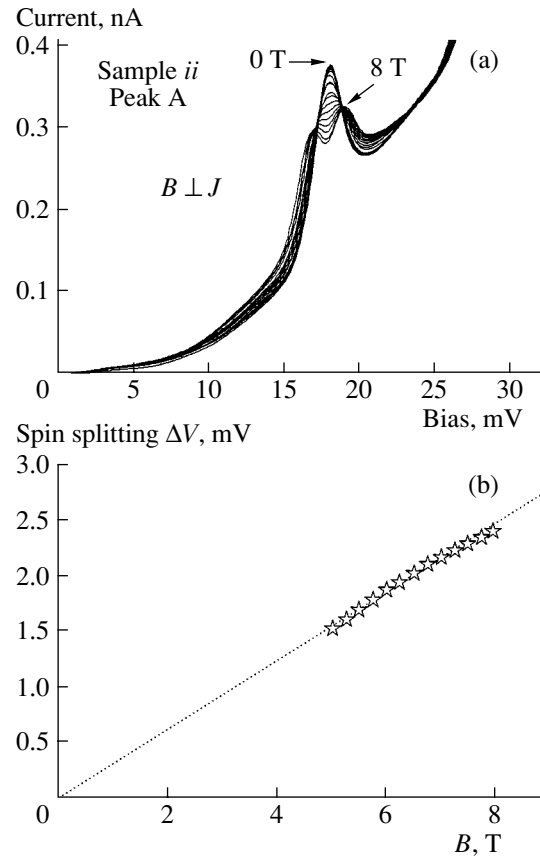

Fig. 3. (a) Details of the evolution of the resonance peak as the magnetic field perpendicular to the current increases to 8 T at a temperature of 4.2 K. The curves correspond to measurements performed at a 0.5-T step in the magnetic field. (b) The magnetic field dependence of the difference in the bias voltages corresponding to the split maxima in the current–voltage characteristic.

the same (see Fig. 2a). Since the threshold increase in the tunneling current occurs at a bias corresponding to the coincidence of the donor state energy with the Fermi energy E_F of the emitter and we assume that the spin is conserved during tunneling, we should observe a separate tunneling threshold for each spin; moreover, according to (1), the bias difference ΔV_{peak} between these thresholds must be proportional to the energy of the impurity spin splitting $\Delta E_{\text{Si donor}} = g_I\mu_B B$.

Figure 3a shows the detailed evolution of one of the resonance peaks as a magnetic field applied normally to the current increases to 8T at a temperature of 4.2 K. The experimental peaks in Fig. 3a are split starting at a magnetic field of about 5 T because of the finite width of the peaks caused by the temperature broadening. Figure 3b shows the magnetic field dependence of the difference in bias corresponding to the split peaks of the I–V characteristic. In Fig. 3b, we see that this dependence is linear, in agreement with the corresponding simple model of Zeeman splitting. The line approximating the experimental points passes through the ori-

gin $B = 0$, $\Delta V = 0$ and has a slope of $g_I\mu_B/f$, where g_I is the effective g factor in a magnetic field perpendicular to the current and f is the factor for the transformation of the measured bias into energy.

Additionally, studying the temperature broadening of the tunneling threshold allowed us to determine the coefficient f. Figure 4 shows typical *I–V* characteristics of our heterostructure near the tunneling threshold at three different temperatures. The broadening of the threshold of tunneling via a zero-dimensional state is caused by the temperature broadening of the Fermi distribution of electrons in the emitter. In accordance with [4, 6], by comparing the experimental curves at different temperatures, we were able to obtain the value $f \approx 0.44$. This value agrees with the value of f that we obtained from self-consistent calculations of the potential profile along the experimental structure in the bias range of interest (0–50 mV). Unfortunately, the accuracy for finding f affects the error in the g factor. We also note that it can be seen in Fig. 4 that the resonance peak becomes substantially sharper as the temperature decreases. This increase in the tunneling current seems to be related to the many-particle effect of the Fermi edge singularity [29].

The values of g_I, obtained by the procedure described above for the different observed peaks corresponding to tunneling via impurity states, lie in the range 2.10–2.22. These values of g_I for donor impurity states associated with the *X* valley in the AlAs barrier substantially exceed the value of g_I obtained in [20] and appear to be close to the g factor for bulk AlAs. Theoretical calculations and optical studies of the magnetic resonance in bulk AlAs layers show slight anisotropy of the g factor and yield the following sets of transverse and longitudinal components: 2.004 and 1.915; 1.976 and 1.917, respectively [30, 31]. Furthermore, in contrast to our experiment, the authors of [20] studied tunneling through two-barrier GaAs/AlAs heterostructures in which the impurities were located in thin (2 nm) AlAs layers. Thus, the value $g_I = 0.34$ obtained in [20] can probably be attributed to the penetration of the electron wave function into the neighboring GaAs layers, where the g factor is equal to 0.44 [4, 32, 33]. The calculations made in [34] and the experimental results given in [35] show that the value of the g factor in QWs in AlAs/GaAs heterostructures strongly depends on the width of the QWs. In our experiment, where the *X* donors were located in a relatively thick (11.2 nm) AlAs layer, the effect of nearby layers on the g factor appeared to be much weaker.

In what follows, we consider the dependence of the amplitude of the tunneling current via impurity states of the donors associated with the *X* valley in the AlAs barrier on the perpendicular magnetic field. A decrease in the amplitude of the tunneling resonance with an increase in B (see Fig. 5a) is related to a well-known effect that can be understood in terms of the one-particle model of electron tunneling in a magnetic field per-
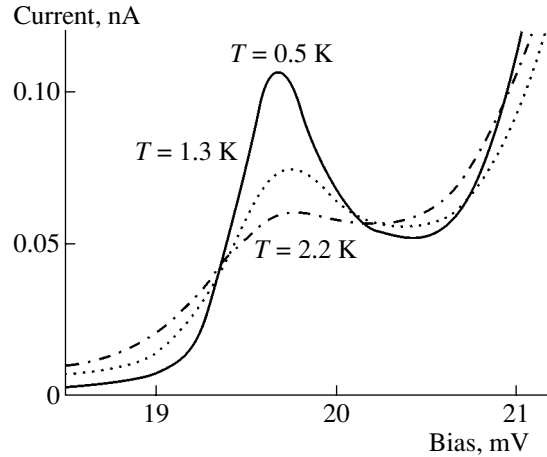

Fig. 4. Current–voltage characteristics of the sample under study in the region of the tunneling threshold at different temperatures.

pendicular to the current. This effect forms a basis for the method of visualization of electron wave functions of zero-dimensional states using magnetotunneling spectroscopy (MTS) and was considered in detail in [24, 36, 37].

The magnetic field dependence of the resonance amplitudes can be explained if we consider the effect of the magnetic field on a tunneling electron. Let α, β, and z denote the direction of B, the direction normal to B in the growth plane (X, Y), and the direction normal to the (X, Y) plane, respectively. An electron tunneling from the emitter to an impurity (to a zero-dimensional state) in a magnetic field acquires additional momentum $\Delta k_\beta = eB\Delta S/\hbar$, where ΔS is the effective tunneling length along z, since the momentum in the direction β changes under the effect of the Lorentz force on the tunneling electron. By measuring the variation in the tunneling current with B, we can determine the value of the matrix element that describes an electron transition from the emitter to the impurity state. It is convenient to express the matrix element for the tunneling transition in terms of Fourier transforms of the electron wave functions $\Phi_{i(f)}(k)$, where i and f correspond to the initial (emitter) and final (impurity) states between which the tunneling transition occurs. We note that the initial emitter states are weakly localized in real space, compared to strongly localized states of the impurity. Therefore, the function $\Phi_i(k)$ is delta-shaped in the k space, being nonzero only in the vicinity of the point $k = 0$. This circumstance means that, since the tunneling current is determined by the square of the matrix element containing $\Phi_i(k)$ and $\Phi_f(k)$, the delta-shaped form of $\Phi_i(k)$ makes it possible to determine the shape of $\Phi_f(k) = \Phi_{Si}(k)$ by varying B and, hence, k. In practice, by measuring the dependence $I(B)$ for a certain direction of B, we can determine the shape of $|\Phi_{Si}(k)|^2$ along the direction of k perpendicular to B. Then, by rotating B in the (X, Y) plane and performing successive measure-
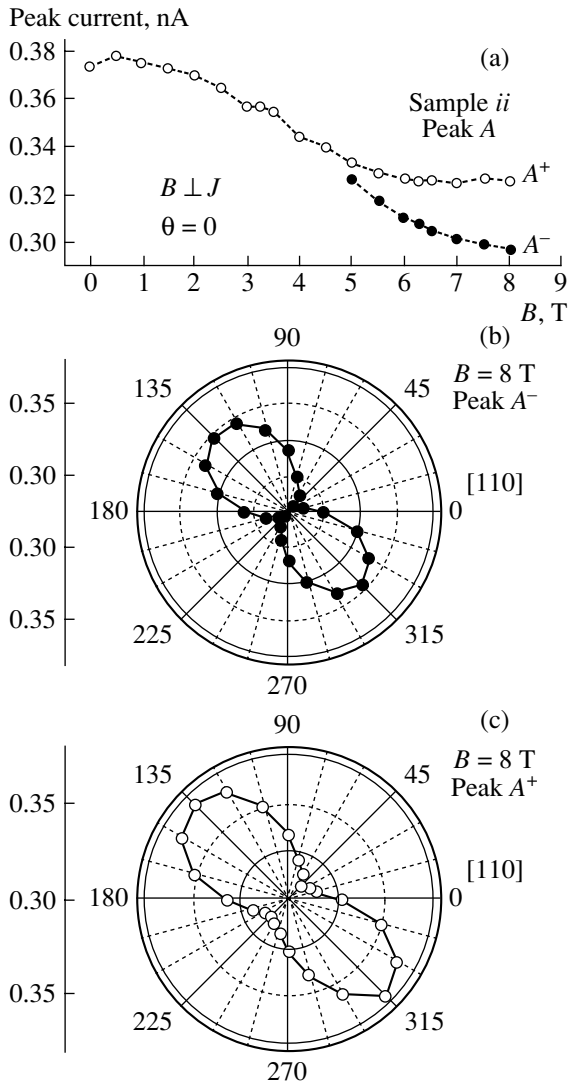
Fig. 5. (a) Dependence of the amplitude of peak *A* on the perpendicular magnetic field *B* ∥ [110]. The anisotropy corresponds to the dependence of the maximum tunneling current ((b) for peak A^+ and (c) for peak *A*) on the direction of the magnetic field *B* = 8 T in the plane perpendicular to the current.

5c, the direction 0° corresponds to the [110] direction, which means that the principal axes of the observed anisotropy correspond to the [100] and [010] directions. We believe that the observed anisotropy of the tunneling current can be related to the anisotropy of the effective mass of electrons in the *X* valleys of AlAs; nevertheless, in our opinion, this problem requires further study.

Thus, using magnetotunneling spectroscopy, we observed spin splitting of the ground state of Si donors associated with the *X* valley in an AlAs barrier. We found the magnitude of the effective *g* factor in the AlAs barrier to be equal to 2.2 ± 0.1. We also showed that the distribution of the probability density of electron wave functions of donor impurity states has a biaxial symmetry in the growth plane, with axes corresponding to the principal crystalline directions in this plane. We note that the possibility of observing the spin splitting of an impurity state at the relatively high temperature of 4.2 K is due to the relatively large *g* factor of AlAs, whereas, for an impurity in GaAs, where the value of the *g* factor is only 0.14–0.3, spin splitting can be observed only in the millikelvin temperature range [1–3].

REFERENCES

1. D. Loss and D. DiVincenzo, Phys. Rev. A **57**, 120 (1998).
2. R. Hanson, B. Witkamp, L. M. K. Vandersypen, *et al.*, Phys. Rev. Lett. **91**, 196 802 (2003).
3. J. W. Sakai, N. La Scala, Jr., P. C. Main, *et al.*, Solid-State Electron. **37**, 965 (1994).
4. M. R. Deshpande, J. W. Sleight, M. A. Reed, *et al.*, Phys. Rev. Lett. **76**, 1328 (1996).
5. J. Könemann, P. König, and R. J. Haug, Physica E (Amsterdam) **13**, 675 (2002).
6. A. S. G. Thornton, T. Ihn, P. C. Main, *et al.*, Appl. Phys. Lett. **73**, 354 (1998).
7. I. Hapke-Wurst, U. Zeitler, H. Frahm, *et al.*, Phys. Rev. B **62**, 12 621 (2000).
8. I. Hapke-Wurst, U. Zeitler, R. J. Haug, and K. Pierz, Physica E (Amsterdam) **13**, 802 (2002).
9. P. König, T. Schmidt, and R. J. Haug, Europhys. Lett. **54**, 495 (2001).
10. E. E. Mendez, W. I. Wang, E. Calleja, and C. E. T. Goncalves da Silva, Appl. Phys. Lett. **50**, 1263 (1987).
11. Y. Carbonneau, J. Beerens, L. A. Cury, *et al.*, Appl. Phys. Lett. **62**, 1955 (1993).
12. J. J. Finley, R. J. Teissier, M. S. Skolnick, *et al.*, Phys. Rev. B **54**, R5251 (1996).
13. R. Teissier, J. J. Finley, M. S. Skolnick, *et al.*, Phys. Rev. B **54**, R8329 (1996).

ments of *I(B)* at different orientations of *B*, we obtain a complete spatial profile of $|\Phi_{Si}(k_X, k_Y)|^2$ representing the projection of the probability density for a given zero-dimensional electron state in the *k* space onto the plane perpendicular to the current.

Typical experimental data on the dependence of the amplitude of the tunneling peak *A* on the direction of a magnetic field of 8 T perpendicular to the current in the growth plane (*X*, *Y*) are shown in polar coordinates in Figs. 5b and 5c. These data indicate that there is a pronounced biaxial anisotropy of the tunneling current, $\Delta I/I \approx 23\%$, for both split peaks A^+ and A^-. The anisotropy of all the peaks observed in the *I–V* characteristic has a similar amplitude and orientation. In Figs. 5b and

14. J. M. Smith, P. C. Klipstein, R. Grey, and G. Hill, Phys. Rev. B **58**, 4708 (1998).

15. H. Im, P. C. Klipstein, R. Grey, and G. Hill, Phys. Rev. Lett. **83**, 3693 (1999).

16. H. Im, P. C. Klipstein, R. Grey, and G. Hill, Phys. Rev. B **62**, 11076 (2000).

17. H. Fukuyama and T. Waho, Jpn. J. Appl. Phys. **34**, L342 (1995).

18. Yu. N. Khanin, E. E. Vdovin, K. S. Novoselov, *et al.*, Jpn. J. Appl. Phys., Part 1 **37**, 3245 (1998).

19. I. E. Itskevich, L. Eaves, P. C. Main, *et al.*, Phys. Rev. B **57**, 7214 (1998).

20. S. A. Vitusevich, A. Förster, K. M. Indelekofer, *et al.*, Phys. Rev. B **61**, 10898 (2000).

21. Yu. N. Khanin, E. E. Vdovin, Yu. V. Dubrovskii, *et al.*, Phys. Rev. B **66**, 073302 (2002).

22. M. Gryglas, M. Baj, B. Chenaud, *et al.*, Phys. Rev. B **69**, 165302 (2004).

23. Yu. N. Khanin, E. E. Vdovin, and Yu. V. Dubrovskiĭ, Fiz. Tekh. Poluprovodn. (St. Petersburg) **38**, 436 (2004) [Semiconductors **38**, 419 (2004)].

24. J. W. Sakai, T. M. Fromhold, P. H. Beton, *et al.*, Phys. Rev. B **48**, 5664 (1993).

25. P. McDonnell, T. J. Foster, P. C. Main, *et al.*, Solid-State Electron. **40**, 409 (1996).

26. G. Weber, Appl. Phys. Lett. **67**, 1447 (1995).

27. K. S. Chan, F. W. Sheard, G. A. Toombs, and L. Eaves, Phys. Rev. B **56**, 1447 (1997).

28. J. W. Sakai, P. C. Main, P. H. Beton, *et al.*, Appl. Phys. Lett. **64**, 2563 (1994).

29. A. K. Geim, P. C. Main, N. La Skala, Jr., *et al.*, Phys. Rev. Lett. **72**, 2061 (1994).

30. L. M. Roth, B. Lax, and S. Zwerdling, Phys. Rev. **114**, 90 (1959).

31. H. W. van Kesteren, E. C. Cosman, and W. A. J. A. van der Poel, Phys. Rev. B **41**, 5283 (1990).

32. M. J. Snelling, G. P. Flinn, A. S. Plaunt, *et al.*, Phys. Rev. B **44**, 11345 (1991).

33. E. L. Ivchenko and A. A. Kiselev, Fiz. Tekh. Poluprovodn. (St. Petersburg) **26**, 1471 (1992) [Sov. Phys. Semicond. **26**, 827 (1992)].

34. A. A. Kiselev and E. L. Ivchenko, Phys. Rev. B **58**, 16353 (1998).

35. P. Le Jeune, D. Robart, X. Marie, *et al.*, Semicond. Sci. Technol. **12**, 380 (1997).

36. E. E. Vdovin, A. Levin, A. Patane, *et al.*, Science **290**, 122 (2000).

37. A. Patane, R. J. A. Hill, L. Eaves, *et al.*, Phys. Rev. B **65**, 165308 (2002).

Translated by I. Zvyagin

Effect of Quantum Confinement on Optical Properties
of Ge Nanocrystals in GeO$_2$ Films

E. B. Gorokhov, V. A. Volodin^, D. V. Marin, D. A. Orekhov, A. G. Cherkov,
A. K. Gutakovskiĭ, V. A. Shvets, A. G. Borisov, and M. D. Efremov

Institute of Semiconductor Physics, Siberian Division, Russian Academy of Sciences, Novosibirsk, 630090 Russia
^e-mail: volodin@isp.nsc.ru
Submitted January 11, 2005; accepted for publication January 27, 2005

Abstract—Germanium dioxide films containing Ge nanocrystals are studied. The films have been prepared by two methods: (i) deposition from supersaturated GeO vapors with subsequent decomposition of metastable germanium monoxide into a heterophase Ge:GeO$_2$ system, and (ii) formation of anomalously thick native germanium oxides with a GeO$_2$(H$_2$O) chemical composition by a catalyst-accelerated oxidation of germanium. The films, which have been prepared on various substrates, are studied using the photoluminescence technique, Raman spectroscopy, spectral ellipsometry, and high-resolution electron microscopy. In the GeO$_2$ films with built-in Ge nanoclusters, intense photoluminescence is detected at room temperature. The nanocluster sizes are estimated from the position of the Raman peak related to localized optical phonons. The correlation between a decrease in the nanocluster size and the shift of the photoluminescence peaks to the blue spectral region as the relative Ge content decreases is revealed. The presence of nanoclusters is confirmed by the data obtained from high-resolution electron microscopy. The correlation of the optical gap calculated taking into account the quantum confinement of electrons and holes in the nanoclusters with the experimentally observed luminescence peak is established. It can be concluded from the data obtained that the Ge nanoclusters constructed in the GeO$_2$ matrix represent type I quantum dots. © 2005 Pleiades Publishing, Inc.

1. INTRODUCTION

Growing interest in Ge and Si nanoclusters constructed in dielectrics is motivated by the prospect of the application of such structures in optoelectronic devices and nonvolatile memory elements. The compatibility of the procedures involved in the formation of these structures with conventional silicon technology and the opportunity to modify their optical properties, which are controlled by quantum-confinement effects (band gap engineering), are very attractive features of these structures. The optical properties of the Ge and Si nanoclusters (NCs) produced by various techniques in silicon dioxide and silicon nitride were previously studied in [1–7]. Recently, photoluminescence (PL) was detected in GeO$_2$ films containing Ge NCs [8]. In this paper, we report data on the structural and optical properties of the Ge NCs produced in GeO$_2$ films by different technological procedures. The films were studied using the PL technique, Raman spectroscopy, spectral ellipsometry, and high-resolution transmission electron microscopy (HRTEM).

2. EXPERIMENTAL

2.1. Sample Preparation

In our experiments, we studied two types of Ge:GeO$_2$ films. For both types, the preparation procedure was based on the same technology of decomposi-

tion of thermodynamically unstable solid germanium monoxide:

$$2GeO \longrightarrow GeO_2 + Ge. \qquad (1)$$

For the preparation of these two types of experimental samples, we used two methods: (i) deposition from supersaturated GeO vapors onto different substrates and (ii) growth of anomalously thick native germanium oxides with a GeO$_x$(H$_2$O) chemical composition as a result of a catalyst-accelerated oxidation of germanium. Two series of samples, A and B, were fabricated by the first-mentioned method. The deposition of GeO was carried out in a gas-transport quartz reactor that had two zones: an evaporation zone and a deposition zone. In the evaporation zone, where the temperature was maintained at a level of 600–700°C, a number of pure Ge plates (20 plates) were mounted in parallel to an inert gas flow passing through the reactor. The inert gas, Ar or He, contained oxygen and water-vapor impurities (10^{-2}–10^{-3} Torr), which intensively reacted with germanium to form volatile germanium monoxide:

$$2Ge + O_2 \longrightarrow 2GeO(gas),$$
$$Ge + H_2O \longrightarrow GeO(gas) + H_2(gas). \qquad (2)$$
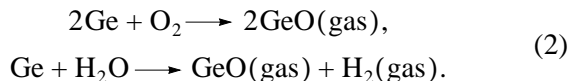
The inert gas saturated with GeO vapors was transferred to the deposition zone, where the excess GeO was deposited, from the cooled flow of the gas carrier, as a solid phase in the form of a thin transparent film. At a certain temperature, the metastable Ge monoxide

at the film surface decomposed into the Ge:GeO$_2$ heterophase system, as described by reaction (1). The lower the condensation temperature and the higher the condensation rate, the smaller the average sizes of the Ge nanoparticles and the volume of their crystallized fraction.

Ellipsometry, electron microscopy, infrared (IR) spectroscopy, and Raman spectroscopy have previously been used to show that such films are composed of a vitreous GeO$_2$ matrix containing built-in amorphous or crystalline germanium clusters (depending on the deposition conditions) [9]. In series A, the films were deposited on sapphire substrates. The substrate temperature was varied in the range 500–520°C. In series B, the films were deposited on silicon substrates whose temperature was varied from 540 to 580°C. The deposition technology was described in more detail in [10].

The samples of series C were anomalously thick films of native germanium oxide on a Ge (111) substrate. After etching of the Ge plates in HF, natural ~0.5-μm-thick oxide layers grew on these plates. The fabrication of such layers is based on the effect of chemical and mechanical treatment of the Ge plates on their oxidation rate during both heating and growth of the natural oxide. The mechanism of such growth is not yet adequately understood. According to data obtained by IR transmission spectroscopy [11], the chemical composition of the anomalously thick layers of native germanium oxide corresponds to a highly hydrated germanium monoxide of the GeO$_x$(H$_2$O) type, with $x \approx 1$. Some of the samples were subjected to a subsequent thermal treatment, namely, to thermal annealing in an He atmosphere for 15 min at a temperature of 630°C (sample C1) and 550°C (sample C2). Sample C3 was not annealed. The films of all types were kept open, i.e., not coated with special layers to protect from interaction with the atmosphere.

2.2. Experimental Procedures

The PL was excited at the radiation wavelength $\lambda = 337$ nm of a pulsed N$_2$ laser. The spectra were recorded using an SDL-1 spectrometer and an FÉU-79 photomultiplier as a detector. For the samples that were grown on transparent substrates (sapphire), the transmission spectra were recorded using a double-beam SF-20 spectrometer. For the samples that were grown on nontransparent substrates (germanium or silicon), the spectra of the ellipsometric parameters were recorded at the wavelengths $\lambda = 260$–650 nm. The measurements were carried out with the use of a spectral ellipsometer produced at the Institute of Semiconductor Physics, Siberian Division, Russian Academy of Sciences. The Raman spectra were obtained at room temperature under excitation with an Ar laser at 514.5 nm (2.41 eV). The Raman setup on the basis of a DFS-52 spectrometer was automated according to the CAMAC standard. The Raman signal was measured in the quasi-
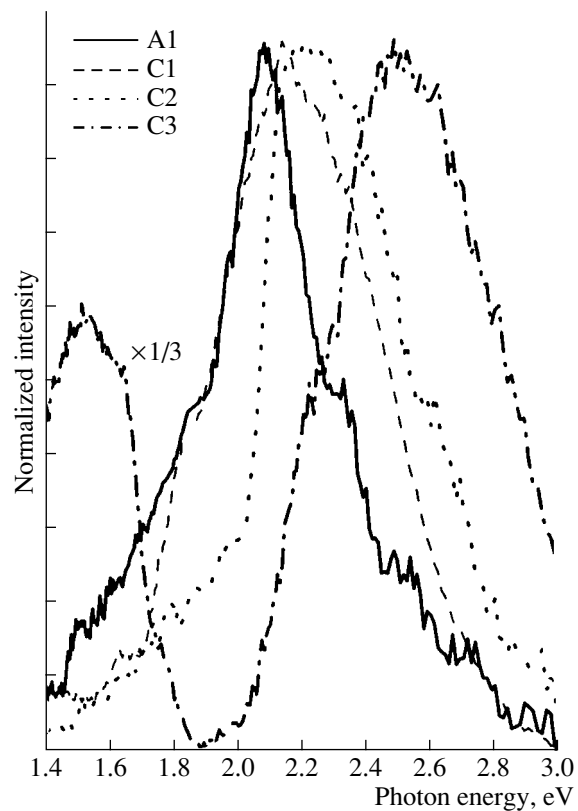

Fig. 1. Photoluminescence spectra of the GeO$_2$ films of series A and C with built-in Ge nanoclusters. The intensity is normalized to the peak amplitude.

backscattering mode of measurements $Z(XY)\bar{Z}$, in which case the polarization planes of incident and scattered light are orthogonal to each other. In addition, the layout of some of the experiments was such that the polarization of scattered light was not analyzed. Structural studies were carried out using a JEOL-4000EX high-resolution electron microscope, which provided, with the accelerating voltage 250 keV, a spatial resolution of 0.19 nm.

3. RESULTS AND DISCUSSION

Figure 1 shows the PL spectra of a sample of series A (sample A1, for which the temperature of the sapphire substrate was 500°C) and of three samples of series C. For the samples of series B, a PL signal was not observed in the visible spectral region. For convenience of presentation, the PL spectra are brought to the same amplitude. It is evident that, for the samples of series C, the PL peak is shifted to the blue spectral region. At the same time, the PL intensity became higher. In particular, the PL intensity for sample C3 was several times higher than the PL intensity for sample A1. Taking into account the light interference in the structure, the photon energy corresponding to the absorption edge was determined from an analysis of the transmission spectra
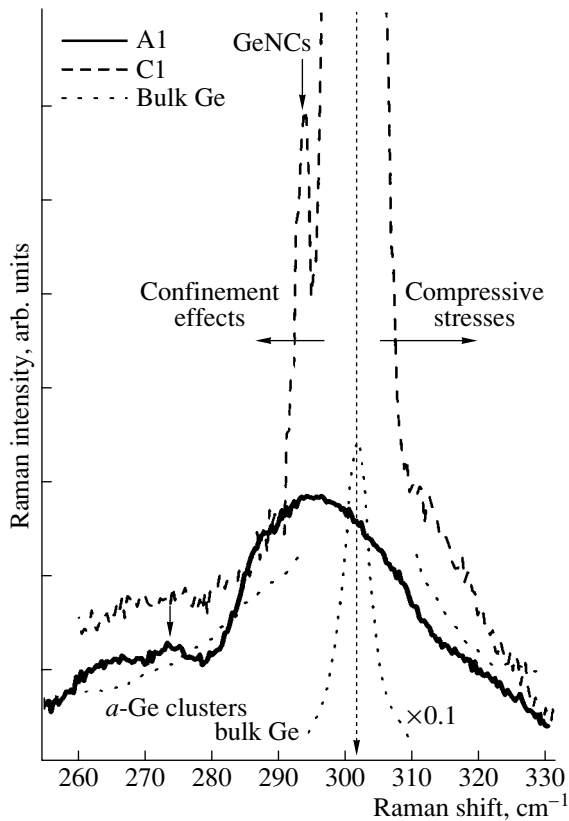
Fig. 2. Raman spectra of samples A1 and C1. The spectrum of the Ge bulk sample is shown for comparison.
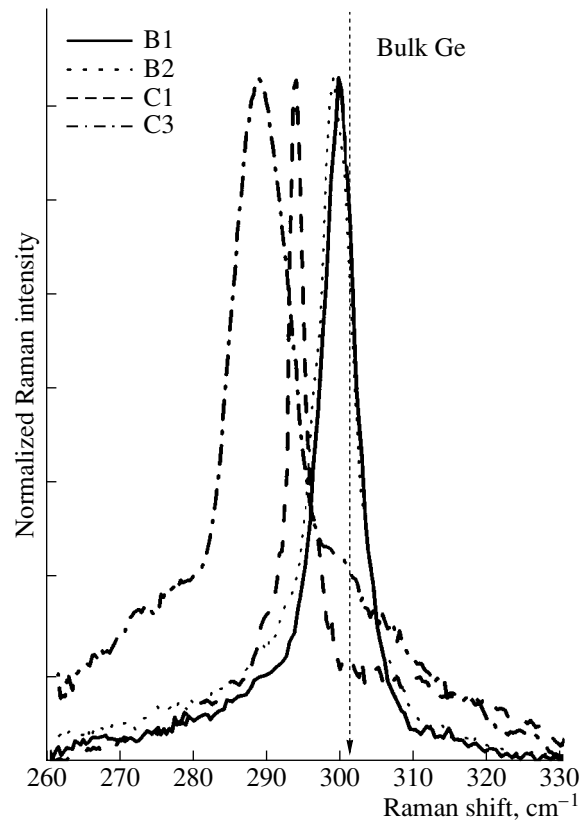

Fig. 3. Raman spectra of the samples of series B and C. The intensity is normalized to the peak amplitude.

of sample A1 [8]. The absorption edge (~1.8 eV) appeared to be shifted appreciably from the band gap of germanium (E_g = 0.67 eV) [12]. The optical gap of GeO_2 is ~5.5 eV [13]. It follows that the absorption is controlled by the germanium inclusions. The intense PL at room temperature and the substantial blue shift of the PL peak (Fig. 1) may be caused by quantum-confinement effects in the germanium nanocrystals. The large width and the asymmetry of the peaks are most likely due to the size dispersion of the nanocrystals. No PL signal from the sapphire, germanium, or silicon substrates was detected. One argument that counts in favor of the hypothesis that the PL signals from the films are controlled by the Ge nanocrystals rather that by some defects in GeO_2 is provided by the following experimental result: no PL signal was obseved when studying the GeO_2 films that were grown by thermal oxidation of germanium.

The structure of the germanium inclusions was studied using Raman spectroscopy. When combined with calculations, rapid and nondestructive Raman measurements can provide a considerable body of data on nanoobjects [14]. The position of the Raman peak related to scattering by optical phonons depends on the nanocrystal size, which means that the size can be determined by convolution of the effective density of

states [15]. The larger the shift of the Raman peak towards smaller wave numbers with respect to the peak for the germanium bulk, the smaller the Ge NC size. In contrast, compressive stresses promote a shift of the peak towards larger wave numbers. Figure 2 shows the Raman spectra of the A1, C1, and bulk Ge samples. In the spectrum of the A1 sample, a broad peak at ~297 cm^{-1} is evident. This peak is due to scattering by the optical phonons localized in the Ge nanocrystals. In addition, a low-intensity peak related to Raman processes in amorphous germanium (*a*-Ge) clusters is observed. In the Raman spectrum of the C1 sample, the peak at ~302 cm^{-1} related to the Ge substrate is dominant. Against the background of this peak, the peak of the Ge NCs can be seen at 294 cm^{-1}. The Raman spectrum of the Ge substrate is also shown in Fig. 2 for comparison. The peak resulting from scattering by the long-wavelength optical phonons of bulk germanium was subtracted from the Raman spectra of the samples of series C. These results and the Raman spectra of the samples of series B are shown in Fig. 3.

The shift of the Raman peak towards smaller wave numbers (Fig. 3) is a consequence of a decrease in the average Ge NC size, which results from a lowering of the substrate temperature when growing the samples from GeO vapors (series B) or from varying the anneal-

ing temperatures (series C). In the case of series B, the lowering of the substrate temperature suppresses the surface diffusion of germanium, which means that, at the same deposition rate, the Ge atoms have no time to segregate into large clusters. In the case of series C, the higher annealing temperatures yielded larger Ge cluster sizes, since thermal treatments stimulate segregation of Ge atoms into clusters. The temperature of these treatments was noticeably higher than the growth temperature of samples A and B. This observation suggests that the diffusion of Ge atoms inside the film is suppressed in comparison to the surface diffusion when growing the films. The broadened peaks in the region 275–280 cm^{-1} are also evident in the Raman spectra of the samples of series C. These peaks are related to amorphous Ge clusters. In fact, the above-indicated spectral region corresponds to the maximum in the density of optical-vibration states for amorphous germanium.

In order to ensure that Ge NCs do exist in GeO$_2$ films, HRTEM experiments were carried out for the purpose of direct observation of the NCs. The thin membranes required for the HRTEM measurements could be most easily prepared from the samples of series B (grown on the silicon substrate). Figure 4 shows an HRTEM image and the corresponding microdiffraction pattern of the sample grown under conditions close to those for sample B1. It is evident that the nanocrystalline inclusions embedded in the amorphous matrix are clearly visualized as darker regions in the image. The characteristic feature of the image of these inclusions is a regular system of interference bands that correspond to traces of the {111} atomic planes oriented orthogonal to the image plane. The electron diffraction in these inclusions yields a system of rings typical of polycrystalline materials. The interplane spacings calculated from the microdiffraction pattern for the first three rings are 0.32, 0.20, and 0.17 nm, which are consistent with the interplane spacings in the cubic crystalline Ge lattice. When calculating the interplane spacings in the nanocrystals, we used the diffraction pattern for the Si single crystal of the substrate as a reference pattern (see Fig. 4b). As can be seen from Fig. 4a, the NC size varies from 3 to 10 nm. In the case of samples B, the average NC size was ~10 nm.

The presence of Ge inclusions in the films of series C is confirmed by the data obtained using spectral ellipsometry. The spectra of the ellipsometric parameters of the samples, Ψ_λ and Δ_λ, were studied at the wavelengths λ = 260–650 nm. When interpreting the data, we used a model that involves a Ge substrate and a homogeneous film. In the first step of the calculation, we computed the optical constants of the film in the context of Bruggeman's model [16] for the mixture of GeO$_2$ and amorphous Ge, taking the reference data for these materials from the handbook. The adjustable parameters were the film thickness and the volume fractions of both phases. These parameters were chosen
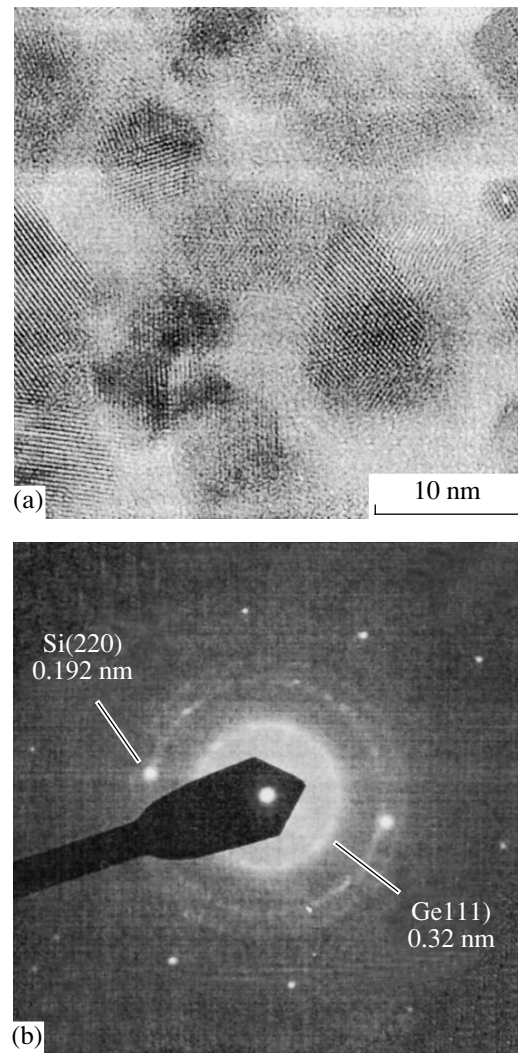

Fig. 4. (a) An HRTEM image and (b) the relevant microdiffraction pattern of the amorphous GeO film of series B with built-in Ge nanocrystals. The film was grown on an Si substrate.

from the best fit of the calculated spectral dependences of the ellipsometric parameters to the experimental spectra. For the three samples under study (C1–C3), the volume fraction of germanium in the clusters determined in such a way was 15, 14, and 9%, and the thickness of the films was in the range 80–90 nm.

With the approximately determined thickness of the films, it was possible to calculate the spectral dependences of the optical constants, the refractive index n, and the absorption index k. For this purpose, the nonlinear equation $\tan\Psi_\lambda \exp(i\Delta_\lambda) = f(\lambda, n, k)$ was numerically solved for each wavelength in succession. Figure 5 shows the results of this calculation, i.e., the dependences of the refractive index n (Fig. 5a) and the absorption index k (also referred to as the extinction coefficient) (Fig. 5b) on the photon energy for one of
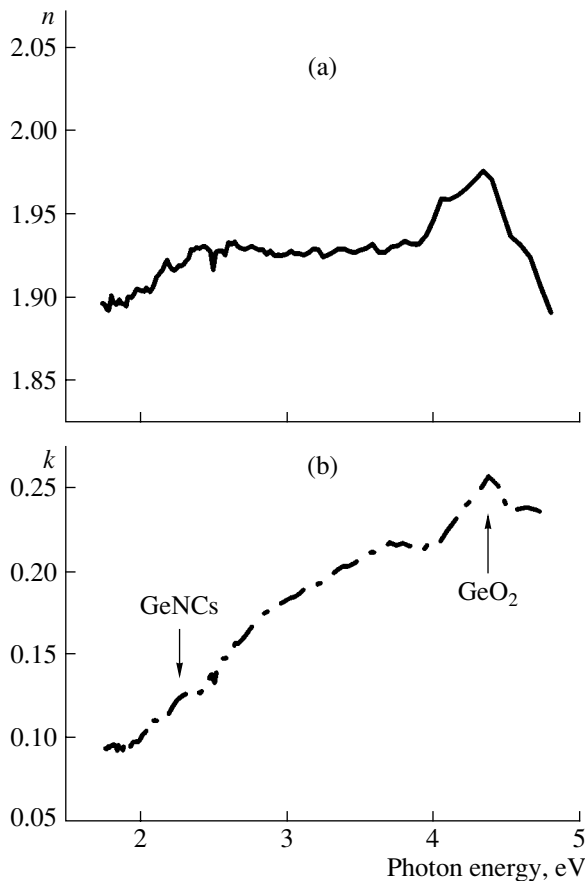
Fig. 5. Spectral dependences of (a) the refractive index and (b) the extinction coefficient of film C2. The dependences were obtained by processing the spectral ellipsometry data.

Fig. 6. Spectral positions of the Raman peak calculated according to a model of the folding of the effective density of states in relation to the Ge NC size (solid line). The open circles refer to the results given in [17].

the samples (C2). It is evident that the absorption in the film increases as the wavelengths decrease, with this dependence exhibiting several peaks. The broad peak at 3.7 eV is consistent with the absorption peak in amorphous Ge. As was mentioned above, the film actually contained amorphous clusters, as follows from the Raman data. The narrower peak at 4.37 eV is probably related to the absorption edge of GeO_2. In addition, a 2.28-eV absorption peak with a half-width of 0.12 eV is observed against the background of the smooth slope in the spectral dependence. This feature of the spectrum may be due to absorption in the quantum dots (QDs), i.e., the Ge nanocrystals. It should be noted that, for sample C2, the PL peak is also in the range 2.2–2.3 eV (Fig. 1).

We now proceed to the discussion of the results. The average size of the Ge NCs was estimated in the context of a model of the effective convolution of vibration modes [15, 8]. The model is briefly outlined below. Because of the relaxation of the momentum selection rules for finite-sized nanocrystals, the vibration modes with non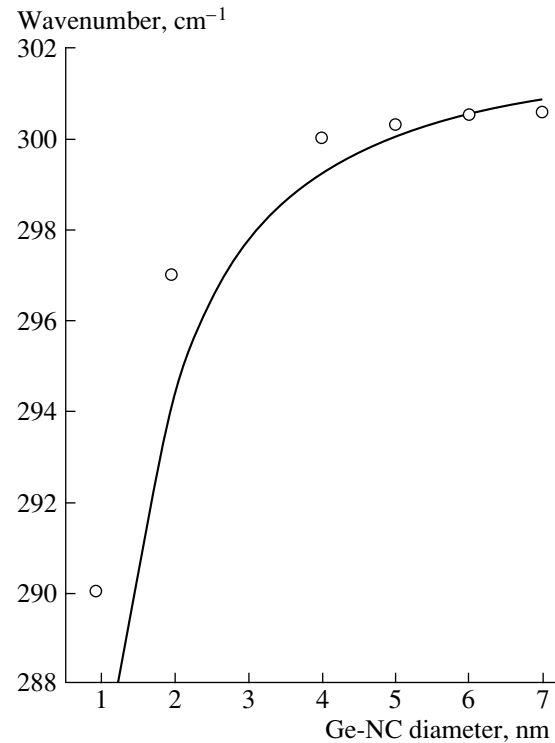zero wave vectors are involved in the Raman spectra. If the nanocrystals are nearly spherical in shape, the Raman scattering intensity can be written as [15]

$$I(\omega) = A \sum_{i=1}^{6} \int_{0}^{1} [n(\omega_i(q)) + 1]$$

$$\times \frac{4\pi q^2 \exp(-q^2 r_0^2/4)}{[\omega - \omega_i(q)]^2 + (\Gamma/2)^2} dq, \tag{3}$$

where $n(\omega)$ is the Bose–Einstein filling factor, $\omega_i(q)$ is the phonon dispersion in the ith phonon branch, Γ is the line width, r_0 is the nanocrystal radius, and q is the wave vector. The phonon dispersion curves $\omega_i(q)$ were represented as a set of harmonic functions, with the parameters found from the approximation of the experimental phonon-dispersion curves for germanium [17]. In this way, the Raman spectra of the Ge NCs were calculated in relation to the NC size. The calculated position of the Raman peak as a function of the nanocrystal size is shown in Fig. 6. The estimates presented in Fig. 6 are in agreement with the localized optical phonon frequencies calculated for the crystalline Ge clusters in the context of the microscopic model of valence forces [18]. The results of [18] are also shown in Fig. 6. Thus, the average size of the Ge NCs was determined for the films of series A, B, and C.

It should be noted that, in accordance with the molar relationship Ge : GeO$_2$ = 1 : 1 in the heterofilm, as follows from chemical considerations of its synthesis, the average distance between the spherical nanoparticles in the oxide is equal, with regard to the different densities of Ge and GeO$_2$, to ~1/2 of their diameter; i.e., it can be 1.5–2 nm. If the diameter is ~3 nm, the density of the NCs in the cross section of the layer is ~10^{13} cm^{-2}.

Since the barriers for electrons and holes in Ge surrounded by GeO$_2$ are 2 and ~3 eV, respectively [13], a Ge NC can be considered as a type I QD. Due to the strong localization of electrons and holes in the QDs and to the relaxation of the momentum selection rule, efficient radiative recombination is expected to be observable in the Ge:GeO$_2$ films.

The energy levels of the localized states of electrons and holes in the Ge nanocrystals were calculated. The maximum of the valence band of germanium is at the point Γ. For germanium, the effective masses of heavy holes m_{hh} and light holes m_{lh} are, correspondingly, 0.33m_0 and 0.042m_0, where m_0 is the free-electron effective mass [11]. The minimum of the conduction band is positioned in the (111) direction; the transverse and longitudinal electron effective masses are $m_{e\perp}$ = 0.082m_0 and $m_{e\parallel}$ = 1.58m_0, respectively.

The problem of finding the energies E of the levels in a spherically symmetric well of radius r_0 with a barrier height U_0 has been solved [19]. In this case, the separation of variables yields the following equation for the radial wave function:

$$\frac{1}{r^2}\frac{\partial^2}{\partial r^2}[r^2(\Psi(r))] - \frac{L(L+1)}{r^2}\Psi(r)$$
$$+ \frac{2m(r)}{\hbar^2}[E - U(r)]\Psi(r) = 0. \quad (4)$$

We are interested in the ground state, in which the orbital moment L is equal to zero and the equation is transformed into a one-dimensional equation with the potential well $U(r)$. In the case of an infinite potential, this equation can be solved exactly, and the finite solution inside the well at $r = 0$ is given by

$$\Psi = A\frac{\sin(\alpha r)}{r}, \quad (5)$$

where $\alpha = \sqrt{2mE}/\hbar = \pi/r_0$.

Being localized, the states with wave vectors parallel and orthogonal to the [111] direction are "mixed." Following the approach of [20], we take the effective electron mass as $m_e = 3m_{e\perp}m_{e\parallel}/(2m_{e\parallel} + m_{e\perp})$, so that $m_e = 0.123$. The "hole" level was calculated for heavy holes with $m_{hh} = 0.33$ [12]. Then, with the energy measured in eV and the radius of the well expressed in nanometers, the energy of the optical transition is

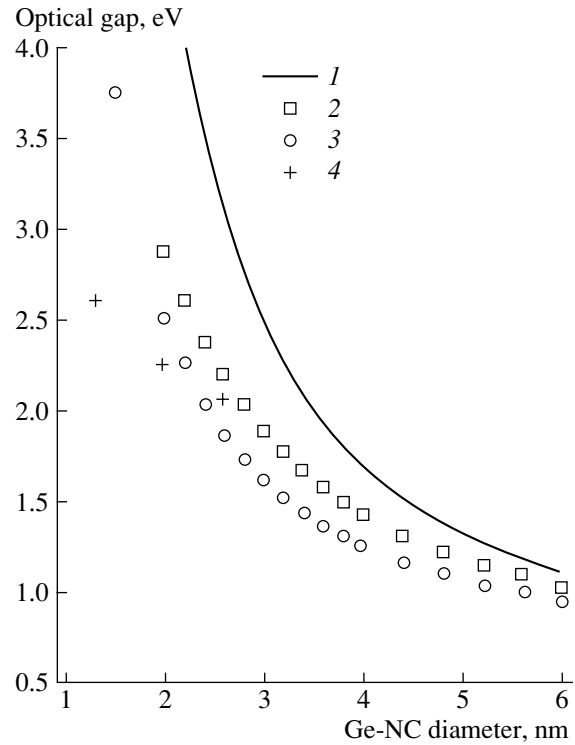$$E_{tr} = E_g + \frac{4.1}{r_0^2}. \quad (6)$$

Optical gap, eV

Ge-NC diameter, nm

Fig. 7. Optical gap of the spherical Ge nanocrystals in GeO$_2$ calculated (*1*, solid line) disregarding and (*2*, open squares) regarding the finiteness of the barrier height and (*3*, open circles) taking into account the finite barrier height and mass discontinuity. The experimental data (*4*, crosses) are shown for comparison.

In the case of a finite barrier, the solution can be found from joining the wave function and its derivative at the well–barrier interface:

$$\Psi_{well} = \Psi_{bar}, \quad \frac{\Psi'_{well}}{m_{well}} = \frac{\Psi'_{bar}}{m_{bar}}, \quad (7)$$

where m_{well} and m_{bar} are the effective masses in the well and barrier, respectively.

The corresponding equations were solved numerically, with the discontinuity of the electron and hole masses in the well and in the barrier either disregarded or taken into account. The masses of electrons and holes in GeO$_2$ are unknown. However, since GeO$_2$ is believed to be a wide-gap material, we assumed, by analogy with [20], that the carrier masses were close to the free-electron mass.

The results of the calculation are shown in Fig. 7. It is evident that, if the barriers for electrons and holes are assumed to be finite, the calculated energy of the optical transition for a Ge nanocrystal 2.6 nm in diameter (sample A1, Raman data) coincides with the PL peak position. In addition, Fig. 7 shows the experimental data for samples C1 and C3, for which the average nanocrystal size was, correspondingly, 2 and 1.2 nm, as followed from the Raman data. For these samples, a

noticeable discrepancy between the experimental and calculated data can be seen. Apparently, for such small Ge NCs, the effective mass approximation becomes invalid, and ab initio models should be used for the calculations. The narrower optical gaps found experimentally in the nanocrystal–dielectric heterosystem may be due to the following mechanism of radiative recombination: an excited electron localized in the nanocrystal moves to the level of a surface state at the nanocrystal–dielectric interface and, thus, emits a photon [21]. The level of the surface state no longer depends on the nanocrystal size. As a consequence, the quantum-confinement effect will be less pronounced. In addition, there exists another reason for the decrease in the experimental optical gap. In fact, the width of the barrier between neighboring NCs can be so small that tunneling of the carriers becomes more probable. The estimated distance between neighboring NCs can be as small as 1.3–2 nm [8]. With such barrier widths, the tunneling effects can bring about the transformation of the discrete energy level into a miniband. In this case, the lowest level in the miniband will be located deeper. In addition, it is possible that the barrier structure involves a transition layer of GeO_x ($0 < x < 2$). As a consequence, the well is found to be triangular rather than rectangular. This circumstance causes the experimental optical gap to be narrower.

As was mentioned above, the PL intensity for the samples of series C (small Ge NCs) is several times higher than the PL intensity for the samples of series A (relatively large Ge NCs). The efficient radiative recombination in the NCs of indirect-gap materials at room temperature is probably due to relaxation of the momentum selection rules in optical transitions [22]. The smaller the NC, the larger the uncertainty in the momentum and, hence, the higher the probability of radiative transitions [23]. We observed such a dependence experimentally. It should be noted that the very small sizes of the NCs formed at room temperature without thermal treatments are due to the metastability of the GeO films. It is well known that, because of the effect of the surface energy, the critical size of a crystalline Si nucleus in an amorphous medium is 2–3 nm. In the case considered here, the contribution of the Ge–GeO$_2$ interface to the free energy exists for both the amorphous Ge clusters and the crystalline ones. However, the crystalline state is energetically more favorable. Therefore, the amorphous clusters are crystallized.

For the samples of series B, the Ge NC sizes were 8 nm and above, as follows from the Raman and HRTEM studies. Thus, a PL signal was not observed for these samples in the visible spectral region. According to the calculations, the PL signal from such Ge NCs is expected to be observable in the IR region. In addition, it should be also noted that, in the PL spectra of samples C3 and C2, a substantial enhancement of the signal was observed in the longer wavelength region. For sample C3, an intense PL peak was observed even near 1.5 eV. This peak can be controlled by optical transitions that involve either surface states at the interface between an NC and the surrounding interface or defects inside the NCs. The additional PL peak revealed for sample C3 can be related to the nonground (excited) levels and allowed optical transitions from the exited level to the ground level in the NCs. Unfortunately, the spectral sensitivity of the photomultiplier was limited on the red-emission side, which prevented detection of a signal in the IR region.

4. CONCLUSIONS

In conclusion, we consider the possibility of controlling the electron level structure (band-gap engineering) in heterosystems of the form "QDs in a dielectric matrix." The technology of the Ge:GeO$_2$ film heterosystem is distinguished by the possibility of modifying the optical properties of the system using the following processes [8]:

(i) In situ modification of the Ge NC size by varying the temperature and rate of condensation of germanium monoxide when synthesizing the film.

(ii) Ex situ controllable increase in the Ge nanocrystal size and in the width of the barriers between the nanocrystals by annealing in an inert atmosphere (without changing the Ge:GeO$_2$ ratio in the film) to provide the diffusion-limited transformation of small Ge clusters into larger ones.

(iii) Controllable decrease in the Ge NC size by oxidation (with all of the treatments performed below 550°C).

(iv) Variations in the height of the potential barriers of quantum wells in the heterosystem using chemical and phase transformations of the constituent components [24]; in particular, the fraction x in germanium silicate glass $GeO_{2(x)}$:$SiO_{2(1-x)}$ can be changed in the range from unity to zero, simultaneously resulting in near-linear changes in the optical and electronic parameters of the dielectric [25–27]; in this case, the band gap E_g increases from ~5.5 to ~9 eV.

(v) The use of glasses of complex composition and their crystallization at low temperatures (below 650–700°C [28, 29]) to modify the properties of the dielectric barriers; it is worth noting that, on crystallization, the permittivity of the films increases by an average of ~20%, and this is favorable for quasi-nonvolatile MOS memory devices based on the trapping of charge carriers by QDs [24].

It should be noted that, in the GeO$_2$ films containing Ge nanocrystals, the PL signal was detected at room temperature. The shift of the PL peak was observed as the nanocrystal size decreased (quantum-confinement effect). The barriers for electrons and holes in the Ge:GeO$_2$ heterostructure is substantially lower than the barriers in the Ge:SiO$_2$ heterostructure, which has already been used in developing experimental optoelectronic devices [30]. For this reason, the Ge:GeO$_2$ het-

erostructure appears to be more efficient for the injection of electrons and holes and, hence, shows considerable promise with respect to use in various optoelectronic components.

REFERENCES

1. T. T. Shimizu-Iwayama, K. Fujita, S. Nakao, *et al.*, J. Appl. Phys. **75**, 7779 (1994).

2. V. Yu. Timoshenko, M. G. Lisachenko, B. V. Kamenev, *et al.*, Appl. Phys. Lett. **84**, 2512 (2002).

3. S. Takeoka, M. Fujii, S. Hayashi, and K. Yamamoto, Phys. Rev. B **58**, 7921 (1998).

4. I. E. Tyschenko, V. A. Volodin, L. Rebohle, *et al.*, Fiz. Tekh. Poluprovodn. **33**, 559 (1999) [Semiconductors **33**, 523 (1999)].

5. N.-M. Park, C.-J. Choi, T.-Y. Seong, and S.-J. Park, Phys. Rev. Lett. **86**, 1355 (2001).

6. D. Nesheva, C. Raptis, A. Perakis, *et al.*, J. Appl. Phys. **92**, 4678 (2002).

7. G. A. Kachurin, S. G. Yanovskaya, V. A. Volodin, *et al.*, Fiz. Tekh. Poluprovodn. (St. Petersburg) **36**, 685 (2002) [Semiconductors **36**, 647 (2002)].

8. V. A. Volodin, E. B. Gorokhov, M. D. Efremov, *et al.*, Pis'ma Zh. Éksp. Teor. Fiz. **77**, 485 (2003) [JETP Lett. **77**, 411 (2003)].

9. N. N. Ovsyuk, E. B. Gorokhov, V. V. Grishchenko, *et al.*, Pis'ma Zh. Éksp. Teor. Fiz. **47**, 248 (1988) [JETP Lett. **47**, 298 (1988)].

10. E. B. Gorokhov, V. V. Grishchenko, N. N. Ovsyuk, and L. I. Fedina, Poverkhnost, No. 10, 82 (1990).

11. E. B. Gorokhov and V. V. Grishchenko, in *Ellipsometry: Theory, Methods, and Applications*, Ed. by A. V. Rzhanov (Nauka, Novosibirsk, 1987), p. 147 [in Russian].

12. V. I. Gavrilenko, A. M. Grekhov, D. V. Korbutyak, and V. G. Litovchenko, *Optical Properties of Semiconductors* (Naukova Dumka, Kiev, 1987) [in Russian].

13. A. M. Mishchenko, Preprint, IFP SO RAN (Inst. of Semiconductor Physics, Siberian Division, Russian Academy of Sciences, Novosibirsk, 1979).

14. M. D. Efremov, V. A. Volodin, V. A. Sachkov, *et al.*, Pis'ma Zh. Éksp. Teor. Fiz. **70**, 73 (1999) [JETP Lett. **70**, 75 (1999)].

15. V. Pailard and P. Puech, J. Appl. Phys. **86**, 1921 (1999).

16. D. E. Aspnes, Thin Solid Films **89**, 249 (1982).

17. G. Nelin and G. Nilsson, Phys. Rev. B **5**, 3151 (1972).

18. Shang-Fen Ren and Wei Cheng, Phys. Rev. B **66**, 205 328 (2002).

19. L. D. Landau and E. M. Lifshitz, *Course of Theoretical Physics*, Vol. 3: *Quantum Mechanics: Non-Relativistic Theory*, 4th ed. (Nauka, Moscow, 1989; Pergamon, Oxford, 1977).

20. V. A. Burdov, Fiz. Tekh. Poluprovodn. (St. Petersburg) **36**, 1233 (2002) [Semiconductors **36**, 1154 (2002)].

21. T. V. Torchinska, A. Diaz Cano, M. Morales Rodrigues, and L. Yu. Khomenkova, Physica B (Amsterdam) **340–342**, 1113 (2003).

22. D. Kovalev, H. Heckler, M. Ben-Chorin, *et al.*, Phys. Rev. Lett. **81**, 2803 (1998).

23. M. Lannoo, C. Delerue, and G. Allan, J. Lumin. **70**, 170 (1996).

24. Y. C. King, T. J. King, and C. Hu, in *Technical Digest of International Electron Devices Meeting* (1998), p. 115.

25. E. B. Gorokhov, A. M. Mishchenko, I. G. Kovalenko, *et al.*, Poverkhnost, No. 5, 67 (1983).

26. E. B. Gorokhov, I. G. Kosulina, S. V. Pokrovskaya, and I. G. Neizvestny, Phys. Status Solidi A **101**, 451 (1987).

27. E. B. Gorokhov, S. V. Pokrovskaya, and I. G. Neizvestnyĭ, Poverkhnost, No. 4, 103 (1983).

28. E. B. Gorokhov and A. L. Aseev, in *Semiconductors*, Ed. by I. G. Neizvestnyĭ (Inst. Fiz. Poluprovodn. Sib. Otd. Ross. Akad. Nauk, Novosibirsk, 1995), p. 199 [in Russian].

29. E. B. Gorokhov, Poverkhnost, No. 9, 76 (1992).

30. L. Rebohle, J. von Borany, D. Borchert, *et al.*, Electrochem. Solid-State Lett. **4**, G57 (2001).

Translated by É. Smorgonskaya

LOW-DIMENSIONAL SYSTEMS

Electronic Structure and Spectral Properties of Si$_{46}$ and Na$_8$Si$_{46}$ Clathrates

S. I. Kurganskiĭ*^, N. A. Borshch*, and N. S. Pereslavtseva**

*Voronezh State University, Universitetskaya pl. 1, Voronezh, 394006 Russia
^e-mail: ssd18@phys.vsu.ru
**Voronezh State Technological Academy, pr. Revolyutsiĭ 19, Voronezh, 394000 Russia
Submitted February 2, 2005; accepted for publication February 3, 2005

Abstract—The electronic structure of Si$_{46}$ and Na$_8$Si$_{46}$ clathrates has been calculated using the linearized augmented plane wave method. The calculation yielded their band structure, total and partial electron densities of states, and Si$K_{\beta1,\,3}$ and Si$L_{2,\,3}$ X-ray emission spectra. The calculated and experimental spectra for the Na$_8$Si$_{46}$ clathrate were compared. © 2005 Pleiades Publishing, Inc.

1. INTRODUCTION

Silicon clathrates were synthesized for the first time in 1965 [1]. However, only recently have they become the subject of active experimental and theoretical studies [2–6]. Such interest is primarily due to the active search for new semiconductor materials. Since silicon is the most commonly used and available semiconductor, many studies are directed towards the production of new silicon nanoforms. From this standpoint, clathrates represent very promising compounds. Attempts to synthesize silicon clathrate compounds initially encountered the problem of stabilization of the silicon clathrate structure. This problem was solved by introducing alkali and (or) alkaline-earth metal atoms into voids in the semiconductor lattice [7, 8]. It was found that metal atoms strongly affect the properties of silicon clathrate compounds. For example, M$_8$Si$_{46}$ clathrates (M = Na or K) are thermoelectric materials and have extremely low thermal conductivity [6]. Partial substitution of Na atoms with Ba atoms results in superconducting properties. The Na$_x$Ba$_{8-x}$Si$_{46}$ clathrate becomes a superconductor at temperatures of 2–4 K, depending on the ratio of Na and Ba concentrations [9, 10]. If all the Na atoms are replaced with Ba atoms, the superconducting transition temperature increases to 8 K [8]. Thus, doping of a silicon clathrate structure with atoms of various metals makes it possible to produce compounds with the desired properties. However, study of the influence of various impurities on the properties of silicon clathrate compounds is impossible without a detailed analysis of the electronic structure of silicon and silicon–metal clathrates. In this paper, we present a calculation of the electronic structure of Si$_{46}$ and Na$_8$Si$_{46}$ clathrates. The calculation yielded such characteristics of the electronic structure as the total and partial electron densities of states and the Si$K_{\beta1,\,3}$ and Si$L_{2,\,3}$ X-ray emission

spectra. Furthermore, we also calculated the electronic structure of crystalline silicon (c-Si) and, as a result, obtained the related Si$K_{\beta1,\,3}$ and Si$L_{2,\,3}$ spectra. The calculated spectra of the Na$_8$Si$_{46}$ clathrate and crystalline silicon were compared with the relevant experimental data [11].

2. CALCULATION DETAILS

The electronic structure of the Si$_{46}$ and Na$_8$Si$_{46}$ clathrate compounds and crystalline silicon c-Si was calculated using the linearized augmented plane wave (LAPW) method [12] within the local density approximation of the density functional employing the exchange-correlation potential in the approximation applied in [13] and the scalar-relativistic approximation [14]. The latter takes into account all the relativistic effects except for spin–orbit splitting. The LAPW method was previously used with good results to calculate the electronic structure and spectral characteristics of transition metal silicides [15–17]. In order to calculate the electronic structure of the clathrates and crystalline silicon c-Si, bases of 1213 and 113 LAPWs were used. When expanding the basis function in spherical harmonics, contributions up to $l_{max} = 5$ were taken into account.

The eigenfunctions $\psi_{i,\,\mathbf{k}}(\mathbf{r})$ and eigenenergies $E_i(\mathbf{k})$ obtained by band calculation in the one-electron approximation were used to calculate the intensity of the X-ray emission spectra:

$$I(E) = \frac{2}{\Omega_{BZ}} \sum_i \int\limits_{\Omega_{BZ},\,E_i(\mathbf{k}) \le E_F} \{M_i^2(\mathbf{k})\delta(E - E_i(\mathbf{k}) + E_c)\} d\mathbf{k}.$$

Here, i is the energy band index; Ω_{BZ} is the Brillouin zone volume; E_c is the energy of the core state to which the transition occurs; and $M_i^2(\mathbf{k})$ is the matrix element of the X-ray transition probability, which was calculated using the dipole approximation.

Silicon and silicon–metal clathrates crystallize into a primitive cubic cell that has the $Pm3n$ space group [3, 18]. The lattice is composed of two Si_{20} dodecahedra and six Si_{24} tetra-kaidecahedra connected to each other. The cavities in Na_8Si_{46} polyhedra are filled with Na atoms. The structure contains two nonequivalent sites for sodium atoms ($2a$ and $6b$) and three nonequivalent sites for silicon atoms ($6c$, $16i$, and $24k$) with symmetries of $4m2$, 3, and m, respectively. The unit cell parameters and atomic coordinates are listed in Table 1.

3. BAND STRUCTURE

Figure 1 shows the band structures of the Si_{46} (Fig. 1a) and Na_8Si_{46} (Fig. 1b) clathrates in the region near the Fermi level. The energy band structures of these compounds are almost identical; only the relative positions of the Fermi level differ. This finding can be explained within the rigid-band model [13]. According to this model, the energy band structures for isostructural compounds such as Si_{46} and Na_8Si_{46} clathrates are similar. When a silicon structure is doped with Na atoms, the number of valence electrons increases (one valence electron is supplied by each metal atom); therefore, the band filling increases, thus shifting the Fermi level upwards.

In Si_{46}, 92 energy bands are completely filled and the Fermi level lies in the band gap. Thus, this compound is a semiconductor, and its band gap is 0.9 eV.

In Na_8Si_{46}, the Fermi level lies in the conduction band, i.e., this clathrate has metallic properties. In the conduction band, the Fermi level bounds an energy interval that attains a maximum width of 0.6 eV at the point X. This range is separated from the main part of the valence band by a gap of 0.7 eV.

The structure of the main part of the valence band for a Si_{46} clathrate is the same as for a Na_8Si_{46} clathrate. This band can be divided into two regions, each including 46 bands. In the Si_{46} and Na_8Si_{46} clathrates, these regions are separated by gaps of 2.0 and 1.8 eV, respectively. The width of the region near the bottom of the valence band is 7.4 eV in pure silicon clathrate and decreases to 7.2 eV in Na_8Si_{46}. The part lying closer to the Fermi level, although it also includes 46 subbands, is much narrower: 2.3 eV in Si_{46} and 2.5 eV in Na_8Si_{46} clathrates.

The calculated valence band structure of crystalline silicon c-Si is generally similar to that well known from

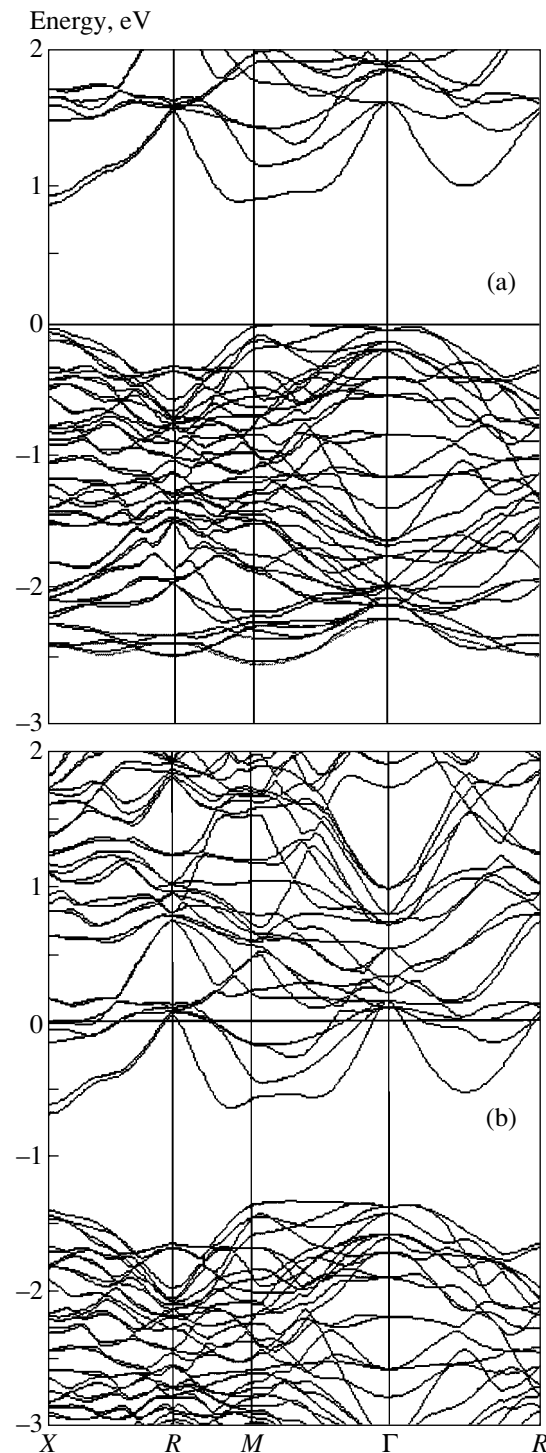**Fig. 1.** Band structure of (a) Si_{46} and (b) Na_8Si_{46} clathrates in the region near the Fermi level.

the available publications. In Table 2, we compare the energy gaps of the calculated valence band at a number of high-symmetry points of the Brillouin zone with the results of an (already classical) empirical calculation using the orthogonalized plane wave method [19].

Table 1. Coordinates of atoms in Si_{46} [11] and Na_8Si_{46} [12] clathrates measured in the unit cell parameter $a = 10.069$ Å for Si_{46} and $a = 10.196$ Å for Na_8Si_{46}

Atomic site	x		y		z	
	Si_{46}	Na_8Si_{46}	Si_{46}	Na_8Si_{46}	Si_{46}	Na_8Si_{46}
Si1(6*c*)	0.25	0.25	0	0	0.5	0.5
Si2(16*i*)	0.1840	0.1851	0.1840	0.1851	0.1840	0.1851
Si3(24*k*)	0	0	0.3160	0.3077	0.1170	0.1175
Na1(2*a*)	–	0	–	0	–	0
Na2(6*b*)	–	0.25	–	0.5	–	0

4. ELECTRON DENSITY OF STATES

Figure 2 shows the total and partial electron densities of states (DoS) in the Si_{46} and Na_8Si_{46} clathrates. The total DoS in these compounds are similar; however, doping the silicon structure with Na atoms results in a shift in the Fermi level to higher energies, with the result that it falls into the conduction band. This situation can be interpreted using the above-described rigid-band model. It has been shown that, when silicon-sodium clathrate is considered instead of silicon clathrate, the band structure remains almost unchanged, and only the Fermi level position changes. Hence, there should be no significant differences in the total DoS either.

In the Na_8Si_{46} clathrate, the contribution made by the states of metal atoms to the total DoS is insignificant. In the entire energy range under study, the main contribution is made by the electronic states of silicon atoms. As can be seen in Fig. 2, the contribution of silicon p states is predominant near the valence band top; however, when going into the depth of the valence band, the contribution of Si s states becomes predominant. The situation is the same for pure silicon clathrate. The region in which Si p states make the main contribution to the total DoS is separated from the region where the main contribution comes from Si s states by a gap of 1.4 in Si_{46} and 1.7 eV in the Na_8Si_{46} clathrates.

Table 2. Energy gaps (eV) of the valence band of crystalline silicon *c*-Si at the Γ, X, and L points of the Brillouin zone (directions are denoted according to [19])

Direction	This calculation	Data of [19]
$X_1–X_4$	5.4	5.0
$\Gamma'_{25}–\Gamma_1$	12.3	11.7
$L_1–L'_2$	2.9	2.7
$L_1–L'_3$	6.1	6.4

5. X-RAY EMISSION SPECTRA

Figures 3 and 4 show the calculated $SiK_{\beta 1,3}$ and $SiL_{2,3}$ spectra of the Si_{46} and Na_8Si_{46} clathrate compounds and crystalline silicon *c*-Si. Tables 3 and 4 list the energy positions of the main features in these spectra. For crystalline silicon and doped clathrate, the calculated spectra are compared with the experimental data [11]. The calculated and experimental spectra were superimposed according to the main maximum position.

The $SiK_{\beta 1,3}$ spectra correspond to $3p \longrightarrow 1s$ transitions, i.e., they map silicon valence p states. The $K_{\beta 1,3}$ spectrum of silicon clathrate has two features: a main peak (B) in the near-Fermi region and a much less intense peak at –5.2 eV. Peak B has a complex structure including an additional feature (B'). In the Na_8Si_{46} spectrum, the main peak shifts into the depth of the valence band, and a peak (C) appears near the Fermi level. This feature can be interpreted using Fig. 2 for the DoS. As was noted above, the Fermi level in doped clathrate
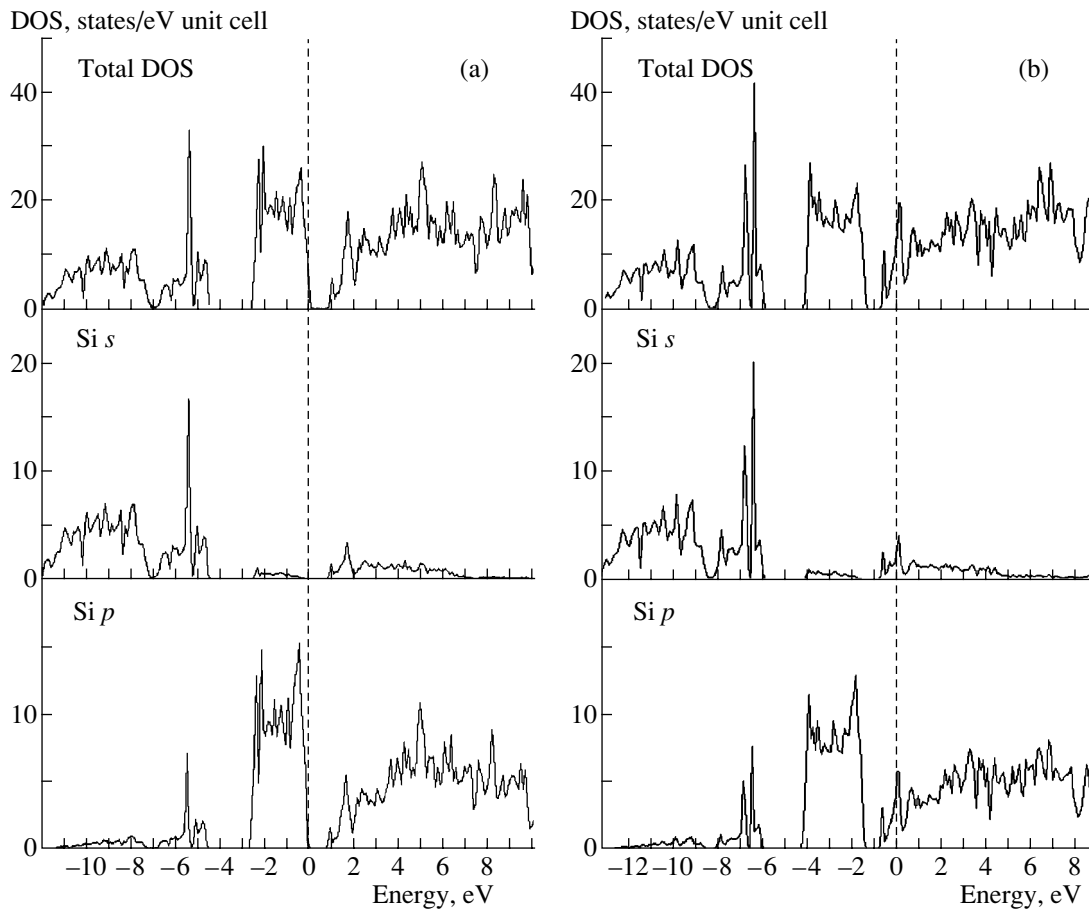
Table 3. Energy positions (in eV, measured from the Fermi level) of the features in the $SiK_{\beta 1,3}$ spectra of Si_{46} and Na_8Si_{46} clathrates and crystalline silicon *c*-Si

Feature	Si_{46}	Na_8Si_{46}		*c*-Si	
		Calculation	Experiment [11]	Calculation	Experiment [11]
A	–5.2	–6.5	–6.9	–6.8	–6.9
B	–0.6	–2.2	–2.2	–2.0	–2.0
B'	–1.3	–2.8	–3.0	–	–
C	–	–0.2	0.8	–	–

Table 4. Energy positions (in eV, with respect to the Fermi level) of the features in the $SiL_{2,3}$ spectra of Si_{46} and Na_8Si_{46} clathrates and crystalline silicon *c*-Si

Feature	Si_{46}	Na_8Si_{46}		*c*-Si	
		Calculation	Experiment [11]	Calculation	Experiment [11]
A	–8.4	–9.7	–9.7	–9.6	–9.5
B	–5.2	–6.7	–6.7	–7.0	–7.0
C	–1.3	–3.1	–4.0	–3.4	–3.5
D	–	–0.4	–0.7	–	–

Fig. 2. Total and partial electron densities of states of (a) Si_{46} and (b) Na_8Si_{46} clathrates.

shifts into the conduction band. This circumstance gives rise to an additional feature in the $SiK_{\beta1,3}$ spectra near E_F. Comparison of the spectra of $SiK_{\beta1,3}$ clathrates and crystalline silicon c-Si shows that the structures of the spectra are, for the most part, identical; however, some differences can be observed. Main peak B is symmetric in the spectrum of crystalline silicon, while this peak is split and asymmetric in the clathrate spectra.

The $SiL_{2,3}$ spectra correspond to $3s3d \longrightarrow 2p$ transitions and, hence, map the $Si3s$ and $Si3d$ states in the valence band. In the clathrate spectra, the main contribution comes from $Si3s$ states, with the contribution of $Si3d$ states being much smaller.

In the $SiL_{2,3}$ spectrum of the Si_{46} clathrate, as in the spectrum of crystalline silicon, three features, denoted by A, B, and C, may be distinguished in Fig. 4. In the Na_8Si_{46} spectrum, an additional peak (D) arises in the region near the Fermi level due to, as in the case of the $SiK_{\beta1,3}$ spectrum, a shift in the Fermi level into the conduction band.

In addition to this difference between the $L_{2,3}$ spectra of the clathrates, it should be noted that, in the $SiL_{2,3}$ spectrum of silicon–metal clathrate, the relative inten-

sity of peak B increases and this maximum becomes higher than maximum A. The comparison of experimental and calculated $SiL_{2,3}$ spectra presented in Fig. 4 shows that the shapes of the spectra and the energy positions of the features are identical. Certain differences are observed only in relation to the ratios of the intensities of the main maxima. This circumstance may be caused by the nonideal stoichiometry and crystalline structure of real Na_8Si_{46} clathrate, while, in the calculation, we studied a structure with an ideal stoichiometric composition and crystalline structure. This could also cause the difference in relative intensities of the features in the experimental and calculated spectra.

6. CONCLUSIONS

(i) The band structures of Si_{46} and Na_8Si_{46} clathrates are identical; only the Fermi level positions differ. The Si_{46} clathrate is a semiconductor, while Na_8Si_{46} has metallic properties.

(ii) In the total electron densities of states of clathrates, the contribution of Si s states is predominant in the depth of the valence band; near the Fermi level, the main contribution comes from silicon p states. The
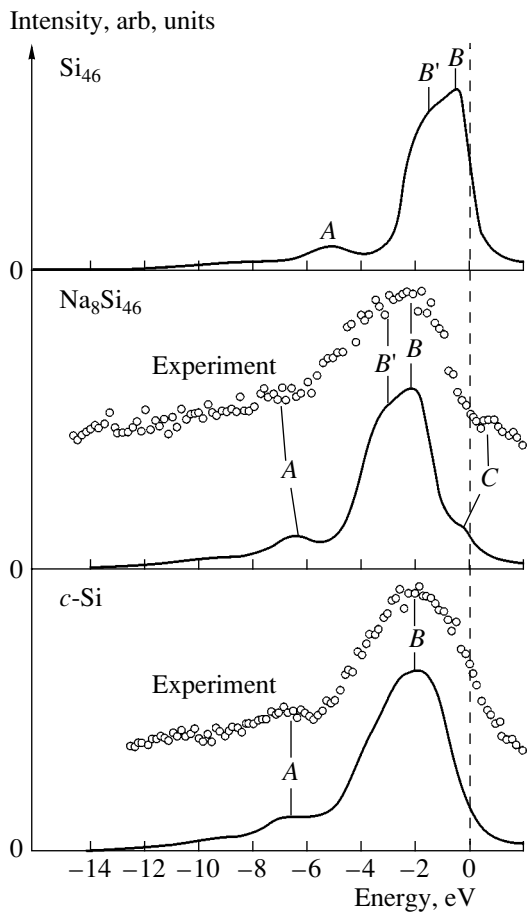
Fig. 3. Calculated and experimental [11] Si$K_{\beta1,3}$ X-ray emission spectra of Si$_{46}$ and Na$_8$Si$_{46}$ clathrates and crystalline silicon *c*-Si.
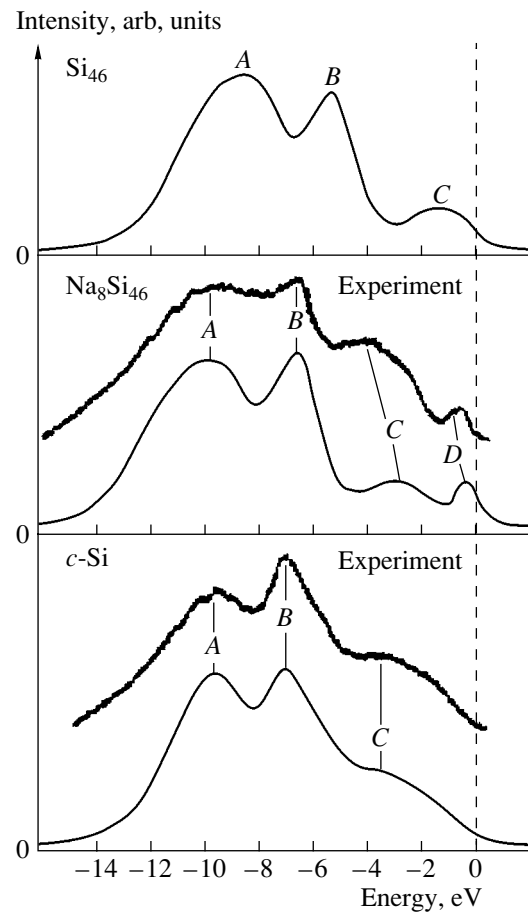

Fig. 4. Calculated and experimental [11] Si$L_{2,3}$ X-ray emission spectra of Si$_{46}$ and Na$_8$Si$_{46}$ clathrates and crystalline silicon *c*-Si.

influence of metal atom states in Na$_8$Si$_{46}$ on the total electron density of states is insignificant.

(iii) The Si$K_{\beta1,3}$ and Si$L_{2,3}$ spectra of the Si$_{46}$ clathrate exhibit two and three peaks, respectively. Doping of a silicon structure with Na atoms results in an additional maximum in the spectra near the Fermi level.

(iv) Comparison of the calculated Si$K_{\beta1,3}$ and Si$L_{2,3}$ spectra with the relevant experimental spectra [11] shows good agreement. A difference is observed only in the intensity ratios of the main maxima. We interpret this difference as resulting from the nonideal stoichiometry and crystalline structure of real clathrates.

ACKNOWLEDGMENTS

REFERENCES

1. J. S. Kasper, P. Hagenmuller, M. Pouchard, and C. Cros, Science **150**, 1713 (1965).

2. T. Yokoya, A. Fukushima, and T. Kiss, Phys. Rev. B **64**, 172504 (2001).

3. K. Moriguchi, M. Yonemura, A. Shintani, and S. Yamanaka, Phys. Rev. B **61**, 9859 (2000).

4. L. Qui, M. A. White, Z. Li, *et al.*, Phys. Rev. B **64**, 024303 (2001).

5. R. F. W. Herrmann, K. Tanigaki, T. Kawaguchi, *et al.*, Phys. Rev. B **60**, 13245 (1999).

6. J. S. Tse, K. Uehara, R. Rousseau, *et al.*, Phys. Rev. Lett. **85**, 114 (2000).

7. C. Cros, M. Pouchard, and P. Hagenmuller, J. Solid State Chem. **2**, 570 (1970).

8. S. Yamanaka, E. Enishi, H. Fukuoka, and M. Yasukawa, Inorg. Chem. **39**, 56 (2000).

9. H. Kawaji, H. Horie, S. Yamanaka, and M. Ishikawa, Phys. Rev. Lett. **74**, 1427 (1995).

10. S. Yamanaka, H. Horie, H. Nakano, and M. Ishikawa, Fullerene Sci. Technol. **3**, 21 (1995).

11. A. Moewes, E. Z. Kurmaev, J. S. Tse, *et al.*, Phys. Rev. B **65**, 153106 (2002).

12. S. N. Vosko, L. Wilk, and M. Nusair, Can. J. Phys. **58**, 1200 (1980).

13. D. D. Koelling and G. O. Arbman, J. Phys. F **5**, 2041 (1975).

14. A. H. MacDonald, W. E. Pickett, and D. D. Koelling, J. Phys. C **13**, 2675 (1980).

15. S. I. Kurganskiĭ, N. S. Pereslavtseva, and E. V. Levitskaya, Fiz. Tverd. Tela (St. Petersburg) **45**, 193 (2003) [Phys. Solid State **45**, 201 (2003)].

16. S. I. Kurganskii, N. S. Pereslavtseva, E. V. Levitskaya, and Yu. A. Yurakov, Phys. Status Solidi B **223**, 306 (2002).

17. S. I. Kurganskii, N. S. Pereslavtseva, E. V. Levitskaya, *et al.*, J. Phys.: Condens. Matter **14**, 6833 (2002).

18. G. K. Ramachandran, P. F. McMillan, J. Diefenbacher, *et al.*, Phys. Rev. B **60**, 12294 (1999).

19. F. Herman, R. Kortum, and C. Kuglin, Int. J. Quantum Chem. **IS**, 533 (1967).

Translated by A. Kazantsev

Terahertz Electroluminescence Originating from Spatially Indirect Intersubband Transitions in a GaAs/AlGaAs Quantum-Cascade Structure

G. F. Glinskiĭ*^, A. V. Andrianov**, O. M. Sreseli**^^, and N. N. Zinov'ev**

*St. Petersburg State Electrotechnical University (LETI), St. Petersburg, 197376 Russia
^e-mail: GFGlinskii@mail.eltech.ru
**Ioffe Physicotechnical Institute, Russian Academy of Sciences, St. Petersburg, 194021 Russia
^^e-mail: Olga.Sreseli@mail.ioffe.ru
Submitted February 2, 2005; accepted for publication February 16, 2005

Abstract—The terahertz electroluminescence of a GaAs/AlGaAs quantum-cascade structure in the range ~33–60 cm^{-1} (1–1.8 THz) is studied and an energy-level diagram of the structure is calculated. The strongest transitions in this system are analyzed and their dependence on the applied electric field is investigated. The analysis indicates that the observed line of terahertz radiation can be related to spatially indirect transitions of electrons between the states localized in neighboring quantum wells and corresponding to the minima in the quantum-confinement subbands. The results of numerical simulations satisfactorily describe the spectral position of the electroluminescence line and its shift as the bias voltage increases across the quantum-cascade structure. © 2005 Pleiades Publishing, Inc.

1. INTRODUCTION

Recently, electromagnetic waves in the terahertz (or far-infrared) range have become the subject of intensive study. The reason for this interest is related to the prospect of their widespread application in diverse areas of science and technology, in particular, their use in tomographic systems, intrascopy, microscopy, scanning imaging systems in medicine and biology, and control and communication systems. The absence of compact and wide-band sources of terahertz (0.1–10 THz) radiation has stimulated studies aimed at the development of emitters based on quantum-cascade structures (QCSs), which rely upon unipolar electron injection and intersubband radiative transitions with energies lower than the longitudinal-phonon energy (36 meV for GaAs). Structure designs with diagonal (interwell) transitions and those with vertical transitions (between the levels or minibands within the same well) have been investigated [1–3].

Vertical transitions have larger dipole moments and, consequently, higher radiative transition rates. However, the pronounced spatial overlap of the wave functions of the initial and final states also implies a high rate of nonradiative transitions due to phonon emission. In the case of spatially indirect transitions, both rates become lower. "Band-structure engineering" provides control over both the level energies and the probabilities of direct and indirect radiative transitions in QCSs. It is possible that, for spatially indirect transitions, the rate of radiative processes is higher than the rate of nonradiative ones; however, this issue requires detailed experimental and theoretical investigation. In addition, in structures with diagonal radiative transitions, it may be possible to tune the emission wavelength by varying the applied electric field. All these considerations determine the interest in the outlined problem.

The properties of two QCSs with a similar composition and design, one of them with diagonal and the other with vertical transitions, were experimentally compared in [4]. As was expected, the line of terahertz emission in the QCS with diagonal transitions exhibited a considerable Stark shift. In addition, spontaneous emission appeared at lower current densities than in the QCS with vertical transitions. The authors concluded that the nonradiative scattering rate is lower when the working levels of a QCS are spatially separated.

Here, we report on a study of a GaAs/GaAlAs QCS with sufficiently thin barriers (on the order of tens of angstroms) between the quantum wells (QWs) and between neighboring periods of the structure to provide a high probability of diagonal radiative transitions. Experimentally recorded spectra of the spontaneous terahertz emission of this GaAs/GaAlAs QCS are compared with a theoretical calculation of its energy-level diagram. The strongest transitions in this system and their dependence upon the applied electric field are theoretically analyzed.

2. EXPERIMENTAL TECHNIQUES AND RESULTS

The structures under study were grown by molecular-beam epitaxy (MBE) in the EPSRC MBE Center at
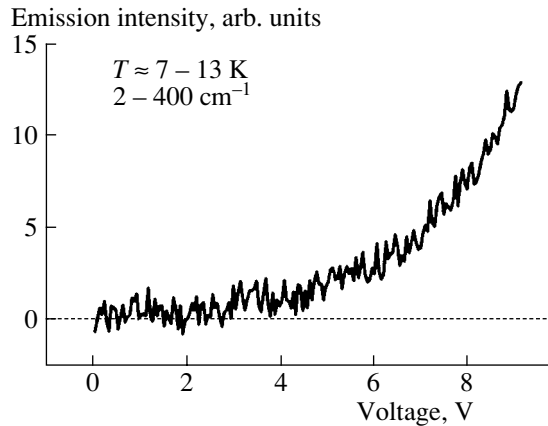
Emission intensity, arb. units

Fig. 1. Integrated intensity of the terahertz electroluminescence from a GaAlAs/GaAs QCS in the frequency range 5–325 cm^{-1} (0.15–9.75 THz) as a function of the bias voltage U.

Emission intensity, arb. units

Fig. 2. Spectra of the terahertz electroluminescence from a GaAlAs/GaAs QCS for the bias voltages $U = (1)$ 4, (2) 4.5, and (3) 5.5 V.

the University of Sheffield (UK). One structure consisted of 40 periods, each containing four GaAs QWs separated by $Al_{0.15}Ga_{0.85}As$ tunneling barriers. The layer sequence within a period was as follows: a 280-Å QW, a 25-Å barrier, a 180-Å QW, a 40-Å barrier, a 160-Å QW, a 25-Å barrier, a 150-Å QW, and a 40-Å barrier; the structure was then repeated. The structure was terminated on both sides with contact layers of n^+-GaAs ($n \approx 2 \times 10^{18}$ cm^{-3}; the upper and lower layer thicknesses were 2 and 0.1 μm, respectively) and 100-nm-thick spacer layers of undoped GaAs, which, in combination with the n^+-GaAs layers, provide for two-dimensional injection contacts. After their growth by MBE, the wafers were cut into samples with an area of 3×3 mm^2, and a number of independent mesa structures, with diameters from 200 to 400 μm, were formed on them. In order to guide the terahertz radiation out of the structure along the direction normal to its surface, a 20-μm-period coupling grating made of Cr/Au alloy was deposited onto the top contact layer of each mesa. Such a grating transforms the radiative modes of the QCS into a mode with the wave vector normal to the plane of the QWs.

The samples were mounted on a cold finger of a liquid-helium optical cryostat with windows made of a TPX material. A positive bias was applied to the samples (with the positive lead of the voltage source connected to the upper contact layer) in the form of a train of rectangular pulses with a duty cycle of 2 at a 500-kHz repetition rate, which was modulated by low-frequency rectangular pulses (with a repetition rate of 80 Hz, duty cycle of 2, and modulation coefficient of 1). Electroluminescence (EL) spectra were measured using a Fourier-transform (FT) spectrometer for the 5–400 cm^{-1} range, constructed on the basis of a Grubbs–Parsons instrument. A liquid-helium-cooled silicon bolometer (QMS Si detector) was used to detect terahertz radiation. The detector signal was recorded using a resonance amplifier with a phase-sensitive detector (PSD). Control of the step motor driving the
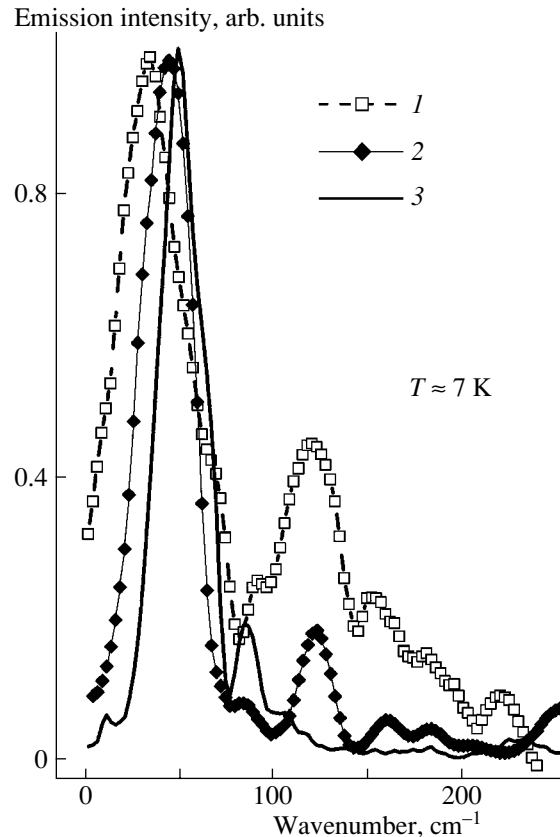
movable mirror of the FT spectrometer, measurements of the PSD signal, control of the amplitude of the bias-voltage pulses applied to the structure, as well as the fast Fourier transform of the interferograms obtained, were carried out on a PC. The emission spectra were taken with a ~10 cm^{-1} resolution.

Low-temperature (6–9 K) EL in the terahertz spectral range was observed in the QCSs under study [5]. The intensity of the terahertz emission grew sharply as the applied voltage was increased (Fig. 1). The emission spectra for several values of the bias voltage are shown in Fig. 2. It can be seen that a broad line (about 30 cm^{-1} FWHM) dominates in the EL spectra, and the peak of this line shifts to higher frequencies with an increase in the applied voltage. In the bias range 4 to ~7 V, the peak of the emission line appears between 33.7 and 59.4 cm^{-1} (4.14–7.37 meV or 1–1.78 THz) and shifts to higher frequencies nearly linearly with the applied voltage at a rate of ~8.9 cm^{-1}/V.

3. THEORETICAL CALCULATIONS AND DISCUSSION OF THE EXPERIMENTAL RESULTS

The energy spectrum and wave functions of electrons in the QCSs were determined in the context of the

Parameters of the $Al_xGa_{1-x}As$ alloy [6, 7]

$E_g^\Gamma(x)$	$1.5194 + 1.360x + 220x^2$ (eV)
m_e^Γ/m_0	$0.0665 + 0.0835x$
$\Delta E_v/\Delta E_c^\Gamma$	33/67
ΔE_c^Γ $(x = 0.15)$	0.140 (eV)

effective-mass approximation by solving a one-dimensional ($k_x = k_y = 0$) Schrödinger equation for a model structure containing an infinite number of periods:

$$\left[\frac{\hbar^2}{2}\frac{\partial}{\partial z}\frac{1}{m(z)}\frac{\partial}{\partial z} + V(z)\right]\Psi(z) = E\Psi(z).$$

Here, $V(z)$ is the periodic potential energy and $m(z)$ is the effective mass, which varies stepwise at the hetero-interfaces. Solutions satisfying the Bloch boundary conditions

$$\Psi_K(z + D) = \exp(iKD)\Psi_K(z)$$

(where D is the period of the structure (900 Å) and K, varying between $-\pi/D$ and π/D, is the electron wave vector in the z-axis direction) were sought for in the form of the expansion

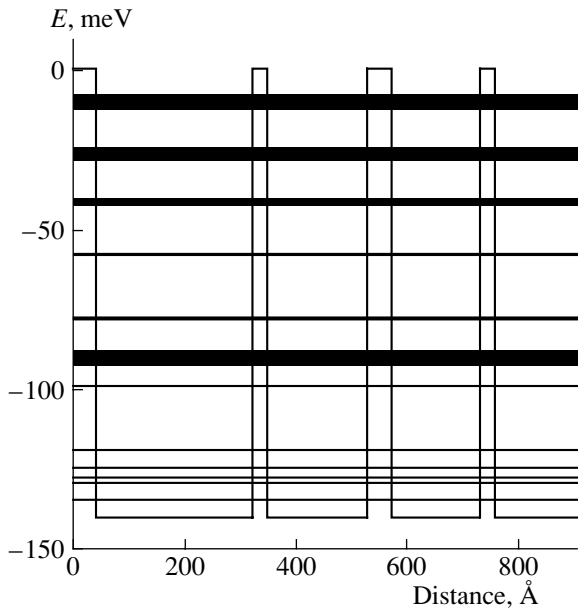$$\Psi_K(z) = \exp(iKz)\sum_{m=-\infty}^{\infty} A_m(K)\exp\left(i\frac{2\pi}{D}mz\right).$$

In this basis, the problem is reduced to finding eigenvalues and eigenvectors of the Hamiltonian matrix, which depends upon K as a parameter:

$$\sum_n H_{mn}(K)A_n(K) = E(K)A_m(K).$$

This procedure was implemented numerically on a PC. Carrying out calculations with a Hamiltonian matrix of dimensionality 300×300, we obtained the energies and wave functions with an error no larger than 0.01% for the 13 lowest quantum-confinement subbands. The parameters of the $Al_xGa_{1-x}As$ alloy used in the calculations are listed in the table.

Figure 3 shows a calculated electron energy diagram under zero bias for 13 levels located below the barrier in the $Al_{0.15}Ga_{0.85}As$/GaAs QCS under study (the structure parameters are specified in the previous section). The energy corresponds to the conduction band edge in the barrier layers. The calculation indicates that the widths of the quantum-confinement subbands for the five lowest levels are small in comparison with the energy spacing between them and does not exceed 0.1 meV; i.e., they may be considered as virtually discrete levels. In Fig. 4, we plotted the coordinate dependences of the squared moduli of the wave functions $|\Psi_i(z)|^2$ within a single period of the QCS for the 13 lowest states ($K = 0$). There is a certain correlation between the degree of localization of the electron wave function within a QCS period and the width of the corresponding quantum-confinement subband. Thus, the five lowest levels correspond to electron states localized within one or two QWs, while the other states are split into subbands as a result of the tunneling effects.
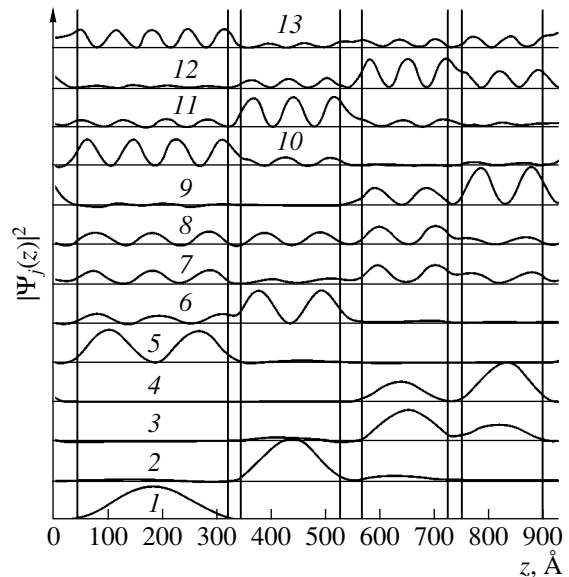

Fig. 3. Potential profile and the energy spectrum of a QCS under zero bias.

Fig. 4. Wave functions of the 13 lowest states within one period of a QCS. For clarity, the curves are shifted relative to each other along the vertical axis.
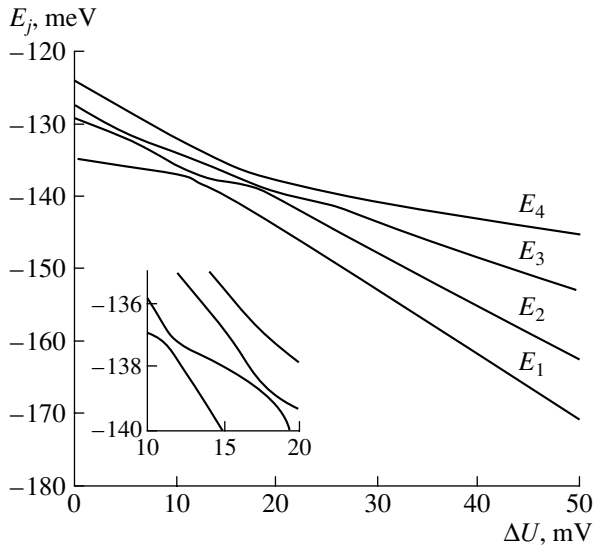
Fig. 5. Calculated dependences of the energies of the four lowest levels on the voltage ΔU across a single period of a QCS.

Fig. 6. Energy levels and wave functions of the four lowest states under the bias voltage $\Delta U = 45$ mV. For convenience, the wave-function curves are shifted vertically so that their baselines represent the corresponding energy levels.

Under the action of an external electric field applied to the QCS, electrons move in the z-axis direction and emit terahertz radiation due to radiative transitions to lower energy levels. If we assume that the electron coherent-motion length does not exceed the period of the QCS (900 Å), the analysis can be restricted to a single period of the structure in an external field. Thus, we performed calculations for a model structure whose "unit cell," repeated periodically, represents a single QCS period (four QWs) in a uniform external electric field oriented along the z axis. Figure 5 shows the dependences of the level energies in such a structure on the voltage ΔU across a structure period, which were calculated under the assumption of field uniformity. It can be seen that, along with a Stark shift of the levels towards lower energies, a considerable transformation of the entire energy spectrum takes place, which is caused by a mixing of the states in the electric field and their anticrossings. As an example, in Fig. 6, we show the wave functions and corresponding energy levels of the four lowest states for $\Delta U = 45$ mV. Obviously, as far as the wave-function localization is concerned, the ordering of the energy levels under the applied electric field is opposite to that existing in an unbiased QCS (Fig. 3).

On the basis of the data obtained, we calculated the matrix elements of optical transitions from state j to state i for $K = 0$,

$$M_{ij} \propto \int_{-D/2}^{D/2} \Psi_i^*(z)\frac{\partial}{\partial z}\Psi_j(z)dz,$$

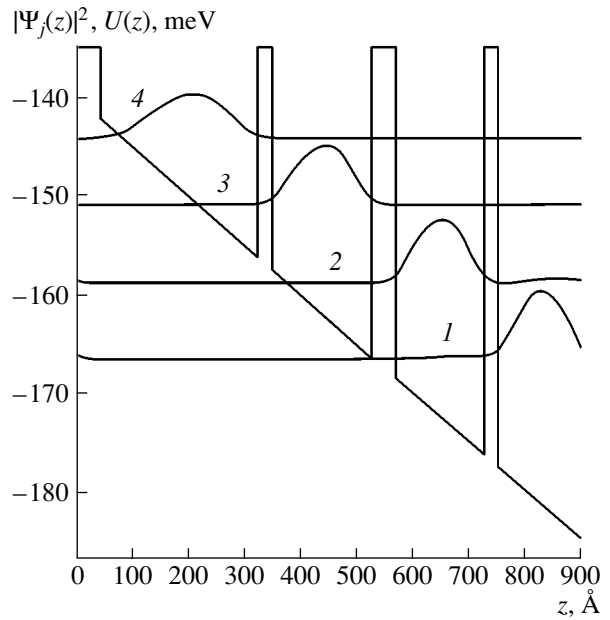and determined the bias-voltage dependences of the values of $|M_{ij}|^2$, which are proportional to the transition

probabilities. The corresponding curves are plotted in Fig. 7. It follows from these results that, for voltages $\Delta U > 20$ mV, the most intense transitions accompanied by photon emission are spatially indirect transitions between the ground states in QWs of width 160 and 150 Å, i.e., transitions from energy level E_2 to energy level E_1 (see Figs. 5, 6). It may be assumed that this transition is the main one and determines the emission spectrum of the structure under study in the terahertz range. In order to check this assumption, we calculated the electric-field dependences of the spectral positions of the EL lines for the most intense transitions: $E_4 \longrightarrow E_3$, $E_3 \longrightarrow E_2$, and $E_2 \longrightarrow E_1$. Comparison of these data with the experimentally observed shift of the EL line in the electric field unambiguously indicates that the main contribution to the emission spectrum comes from the $E_2 \longrightarrow E_1$ transitions. In Fig. 8, we show theoretically calculated EL spectra for several values of the voltage ΔU assuming Gaussian broadening. It can be seen that the calculated positions of the spectral lines are close to the experimentally observed ones (Fig. 2).

Theoretical and experimental dependences of the spectral position of the luminescence line peak upon the voltage U applied to the QCSs are compared in Fig. 9. Note that the theoretical data are represented taking into account the deviation of the actual field within a period of the structure from the average field. For this purpose, we introduce a factor f to account for the difference between the mean field in a sample $E_{av} = U/L$ (where L is the full length of the structure) and the
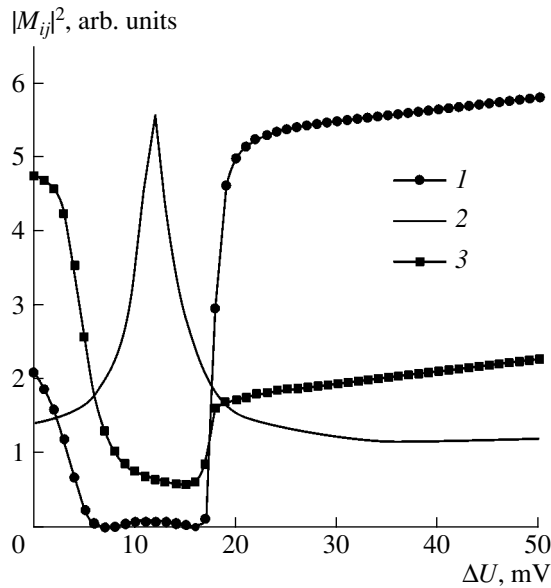
Fig. 7. Dependence of the squared absolute values of the optical transition matrix elements (*1*) $|M_{12}|^2$, (*2*) $|M_{23}|^2$, and (*3*) $|M_{34}|^2$ on the voltage ΔU.

Fig. 8. Calculated spectra of terahertz luminescence originating from $E_2 \longrightarrow E_1$ transitions under different voltages across a QCS period $\Delta U =$ (*1*) 20, (*2*) 30, (*3*) 40, and (*4*) 50 mV.

Fig. 9. Comparison of the calculated energy of the optical transition ΔE_{21} with the experimentally observed position of the peak of the terahertz electroluminescence line in a GaAlAs/GaAs QCS for different values of the bias voltage U applied to the structure. The closed circles represent experimental points, and the solid line shows the calculated photon energy of the terahertz emission at indirect intersubband transitions in the QCS (see text).

model field within a single period of the structure $E_{mod} = \Delta U/D$: $f = E_{av}/E_{mod}$. Such a difference can be caused by a voltage drop across the contacts and the spacer layers as well as by field screening due to an injection of electrons from the contact layer. Factor f was taken as an adjustable parameter. Such a kind of "electrostatic leverage factor" is usually introduced into analysis of the vertical transport in QW structures (see, e.g., [8–10]).

The best agreement of the calculation results with the experimental data was obtained for $f = 2.32$. It can be seen from Fig. 9 that, for this value of the parameter f, the calculated dependence $\Delta E_{21}(U)$ adequately describes the shift of the electroluminescence line occurring with an increase in the voltage across the structure.

It should be added that when the calculations were carried out with values of the band-structure parameters of the $Al_xGa_{1-x}As$ alloy taken from other sources (e.g., [11, 12]) and differing from the ones listed in the table, we obtained a somewhat different energy spectrum, but the energies of intersubband transitions did not change by more than 5–6%.

Thus, the results obtained made it possible to explain the energy position of the terahertz EL line and identify the optical transitions in QCSs as spatially indirect transitions of electrons between the states at the minima of the quantum-confinement subbands localized in neighboring QWs (160 Å and 150 Å wide). Furthermore, the shift of the terahertz radiation line when the bias voltage across a QCS was increased was also explained.
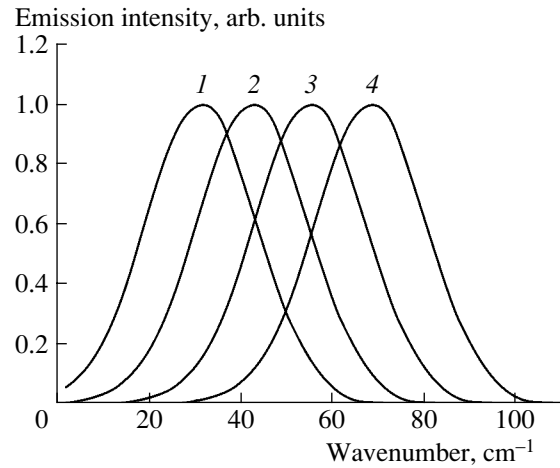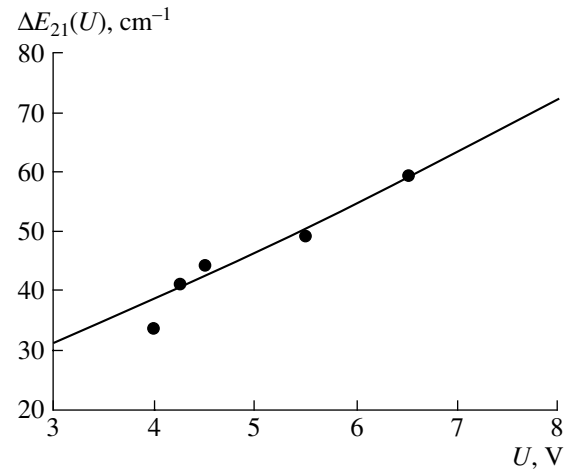
ACKNOWLEDGMENTS

REFERENCES

1. C. Sirtori, F. Capasso, J. Faist, *et al.*, Appl. Phys. Lett. **66**, 4 (1995).
2. M. Rochat, J. Faist, M. Beck, *et al.*, Appl. Phys. Lett. **73**, 3724 (1998).
3. M. Rochat, J. Faist, M. Beck, and U. Oesterle, Physica E (Amsterdam) **7**, 44 (2000).
4. J. Ulrich, R. Zobl, W. Schrenk, *et al.*, Appl. Phys. Lett. **77**, 1928 (2000).
5. N. N. Zinov'ev, A. V. Andrianov, V. Yu. Nekrasov, *et al.*, Pis'ma Zh. Éksp. Teor. Fiz. **74**, 105 (2001) [JETP Lett. **74**, 100 (2001)].
6. S. Adachi, *GaAs and Related Materials* (World Sci., Singapore, 1994).
7. K. Chang, Phys. Rev. B **61**, 4743 (2000).
8. J. Endicott, A. Patane, J. Ibanez, *et al.*, Phys. Rev. Lett. **91**, 126802 (2003).
9. R. J. A. Hill, A. Patene, P. C. Main, *et al.*, Appl. Phys. Lett. **79**, 3275 (2001).
10. B. R. A. Neves, T. J. Foster, L. Eaves, *et al.*, Phys. Rev. B **54**, R11106 (1996).
11. F. Vouilloz, D. Y. Oberli, M.-A. Dupertuis, *et al.*, Phys. Rev. B **57**, 12378 (1998).
12. F. Szmulowicz and G. J. Brown, Phys. Rev. B **51**, 13203 (1995).

Translated by M. Skorikov

LOW-DIMENSIONAL SYSTEMS

Nonequilibrium Room-Temperature Carrier Distribution in InAs Quantum Dots Overgrown with Thin AlAs/InAlAs Layers

N. V. Kryzhanovskaya*^, A. G. Gladyshev*, S. A. Blokhin*, M. V. Maksimov*, E. S. Semenova*, A. P. Vasil'ev*, A. E. Zhukov*, N. N. Ledentsov**, V. M. Ustinov*, and D. Bimberg**

*Ioffe Physicotechnical Institute, Russian Academy of Sciences, St. Petersburg, 194021 Russia
^e-mail: kryj@mail.ioffe.ru
**Institut für Festkörperphysik, Technische Universität, D-10623 Berlin, Germany
Submitted February 16, 2005; accepted for publication March 7, 2005

Abstract—The optical properties of quantum dots (QDs) formed in GaAs or $Al_{0.3}Ga_{0.7}As$ matrices by overgrowth of initial InAs islands formed in the Stranski–Krastanov mode with thin AlAs/InAlAs layers have been studied. It is shown that no transport of carriers between the QDs occurs in the temperature range 10–300 K, so the carrier distribution is of a nonequilibrium nature. The thermal excitation of carriers from the QDs is suppressed by an increase in the energy spacing between the ground and excited states, absence of the level related to the wetting layer, and higher carrier localization energy in the QDs with respect to the continuum states when the $Al_{0.3}Ga_{0.7}As$ matrix is used. © *2005 Pleiades Publishing, Inc.*

1. INTRODUCTION

Studies of methods for control over the formation of arrays of self-organized quantum dots (QD), which would make it possible to obtain QDs with a prescribed density, size, shape, and, correspondingly, energy spectrum, are of great importance both for a detailed investigation of self-organization processes in the course of growth and for the application of QDs in modern semiconductor devices, e.g., lasers. It is well known that one of the factors predetermining the poor temperature stability of QD lasers is the strong temperature dependence of the optical gain. This effect is related to thermal excitation of carriers from the ground to excited states of a QD, into the wetting layer, or into the matrix. At the same time, at low temperatures, the excitation of carriers from the QD states is suppressed, so a nonequilibrium distribution of carriers is formed over the states of the QD array [1], the threshold current is temperature-independent (the characteristic temperature $T_0 \longrightarrow \infty$), and the operation speed of QD lasers increases significantly [2]. For example, in [3], the modulation bandwidth $f(-3\text{ dB}) = 30$ GHz was obtained in a QD laser at 80 K, whereas, at room temperature, it did not exceed 8 GHz. An important factor for improving the temperature stability of laser characteristics is that the nonequilibrium distribution of carriers over the states of the QD array is maintained, in particular, via an increase in the energy spacing between the ground and first excited states. Therefore, the development of methods for controlling the QD energy spectrum is a constructive approach to improving the characteristics of QD-based devices. The majority of current publications are devoted to studies of MBE-grown QD arrays in an InAs/GaAs (001) system. The existing methods for

control of the QD shape and energy spectrum are direct variation of the principal technological parameters during QD deposition (the substrate temperature, growth rate, pressure of As in the growth chamber, and interruptions of growth) [4] and use of various sublayers and modes of QD overgrowth. For example, the possibility of independent control over the density and size of QDs in the top layer and an in-phase correlation with the QDs in the bottom layer has been demonstrated [5]. A method for increasing the volume of QDs while preserving their density, based on the effect of activated decomposition of the solid solution during the overgrowth of QDs with an InGaAlAs layer, was described in [6]. An effective technology allowing control of the volume and shape of InAs QDs is the overgrowth of QDs with a thin AlAs layer. During the deposition of AlAs onto the QDs, In atoms are displaced from the InAs wetting layer and migrate to the QDs, which leads to an increase in their height [7].

In this paper, we report a study of the optical properties of QDs produced by a combination of the above-described technologies [7–10]: InAs islands formed in the Stranski–Krastanov mode were successively overgrown with thin AlAs and InAlAs layers. QDs were formed in both the GaAs and the $Al_{0.3}Ga_{0.7}As$ matrices. The studied optical characteristics of the QDs are compared with the properties of conventional InAs QDs capped with an $In_{0.15}Ga_{0.85}As$ layer. Photoluminescence (PL) excitation spectroscopy and that of PL under resonance excitation are applied in order to study the mechanisms of carrier relaxation to the QD ground state and the temperature dependences of the optical properties in the range 10–300 K.

2. EXPERIMENTAL

The structures under study were MBE-grown on n-GaAs substrates in a Riber 32P machine with a solid-state As source. The structures comprised three QD layers placed in the middle of a GaAs (structures A, B, and C) or $Al_{0.3}Ga_{0.7}As$ (structure D) layer confined by barriers on the surface and substrate sides. Between the QD layers, 25-nm-thick layers of the matrix material were deposited. The substrate temperature was 485°C during deposition of the QD and capping layers and 600°C for all the other parts of the structure. The QD layers were formed by deposition of 2.3 monolayers (MLs) of InAs and different capping layers. In structure A, the QDs were capped with a GaAs layer; in structure B, the formation of QDs was followed by deposition of a 4-nm-thick $In_{0.15}Ga_{0.85}As$ layer; and, in structure C, 2 MLs of InAs and 4 nm of $In_xAl_{1-x}As$ with $x = 0.25$ were deposited. In structure D, layers with QDs and capping layers were formed in the same mode as in C but in the $Al_{0.3}Ga_{0.7}As$ matrix.

Photoluminescence was excited in the structures by a CW Ar$^+$ laser (the emission power $W = 1$–1500 W/cm^2 and the wavelength $\lambda = 514$ nm) or by the second harmonic of a YAG:Nd laser ($W = 10$ MW/cm^2 and $\lambda = 532$ nm) in a pulsed mode. Studies in the temperature range $T = 10$–300 K were performed in a closed-cycle helium cryostat. In the range 300–500 K, the samples were fixed onto a copper holder in a thermostat. The PL excitation and resonance PL spectra were recorded under excitation with light emitted by a halogen incandescent lamp and passed through a monochromator; the samples were mounted in a flow-through helium cryostat. The signal was detected using a monochromator and a cooled Ge photodiode.

3. RESULTS AND DISCUSSION

Figure 1 shows the PL spectra of the structures recorded under excitation with the second harmonic of the YAG:Nd laser in a pulsed mode (the pulse power density 10 MW/cm^2). The application of high-power optical pumping makes it possible to estimate the crystal perfection of the structure [11] and the energy spectrum of states. In all the structures, the observed PL spectra demonstrate a line related to recombination via the QD ground state as well as peaks corresponding to emission from excited states of the QDs and GaAs matrix. The spectra of structures A and B also show a peak: in the case of structure A, it corresponds to the wetting layer (WL); for structure B, it corresponds to the quantum well (QW) formed by the WL and $In_{0.15}Ga_{0.85}As$ layer. In the case of structure B, the ground-state line is red-shifted by 70 meV with respect to its position for structure A. The red shift of the QD PL upon deposition of an $In_{0.15}Ga_{0.85}As$ layer onto the QD layer (structure B) has been thoroughly studied [6, 8, 12] and is accounted for by several factors. It is believed that the principal reason for this shift is an acti-
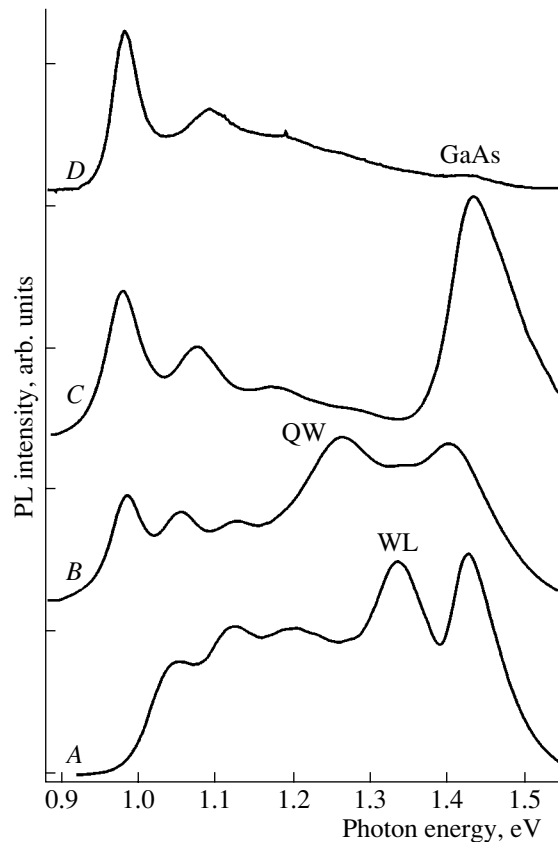

Fig. 1. PL spectra of the structures under excitation with a YAG:Nd laser ($W = 10$ MW/cm^2 and $T = 300$ K).

vated decomposition of the $In_xGa_{1-x}As$ solid solution over the QDs, which enlarges the volume of the QDs and reduces the stresses around them. During the overgrowth, it is energetically more favorable for In atoms to diffuse toward the QDs, whose lattice constant is close to that of InAs, and for Ga atoms to diffuse to regions in between the QDs, where the lattice constant is close to that of GaAs. This process results in the effective enlargement of the initial QD size and, accordingly, in a red shift of the PL line.

In the case of successive deposition of thin AlAs and InAlAs layers on top of InAs islands (structure C), the PL spectrum is also red-shifted with respect to initial structure A [7–10]. As was stated earlier, the deposition of a thin AlAs layer onto QDs enlarges their volume. As the QDs are further overgrown with $In_xAl_{1-x}As$, the $In_xAl_{1-x}As$ solid solution undergoes activated decomposition, similarly to the case of overgrowth with $In_xGa_{1-x}As$, which results in the region near and above a QD being enriched with In and depleted of Al [8]. This circumstance leads to an even more pronounced increase in the QD volume and to a corresponding increase in the energy spacing Δ_{ex} between the ground and first excited states. It is noteworthy that the broadening of the band gap of the matrix material in the case of the $Al_{0.3}Ga_{0.7}As$ matrix (structure D) does not induce a blue shift of the QD PL line. We believe that this fact
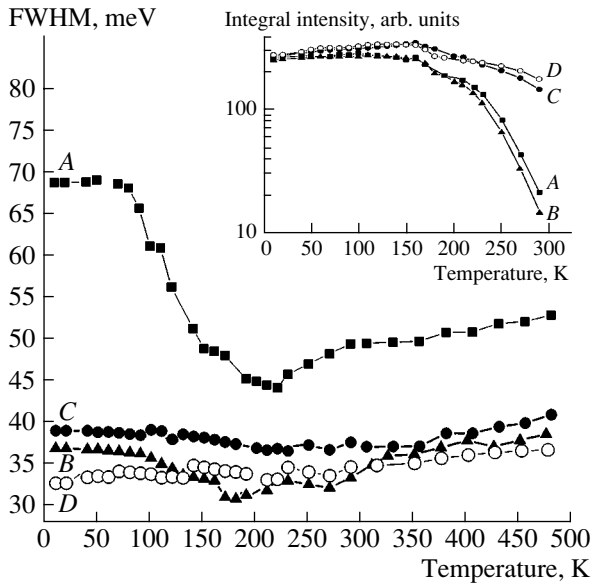
Fig. 2. FWHM of the spectral lines associated with the QD ground state for structures *A*, *B*, *C*, and *D*. The inset shows the temperature dependences of the integral intensity for these structures. Excitation was carried out using an Ar$^+$ laser with $W = 1$ W/cm^2.

can be attributed to strong localization of the electron and hole wave functions of the QD ground state, which results in their weak penetration into the matrix material and low "sensitivity" to the matrix band gap.

The optical properties of the structures were studied in the temperature range $T = 10$–500 K under excitation by an Ar$^+$ laser ($W = 1$ W/cm^2). Figure 2 shows temperature dependences of the FWHM of the QD ground-state lines. Structures *A* and *B* demonstrate standard temperature dependences, which can be accounted for by the redistribution of carriers between the QDs [13]. At low temperatures, carriers are randomly distributed over the states of the QD array; at a sufficiently low excitation density, the PL spectrum reflects the energy spectrum of the ground states in the QD array [14]. At temperatures <50 K, the FWHM remains virtually constant. As the temperature increases, carriers can be excited from small QDs with relatively weak carrier localization and captured in larger QDs via the level related to the WL or matrix. This process depresses luminescence from the small QDs and reduces the PL linewidth. Such a reduction is observed at temperatures up to 200 K. A further increase in temperature leads to a completely equilibrium distribution of carriers among the QDs and to gradual thermal filling of small-sized QDs.

For structures *C* and *D*, the PL linewidth remains virtually unchanged in the entire temperature range studied. In these structures, the reduction in the integral intensity as the temperature increases to 300 K is an order of magnitude weaker than in structures *A* and *B* (see the inset in Fig. 2). Evidently, this fact is related to depression of the thermal redistribution of carriers

among the QDs and of their excitation into the matrix. It necessary to note that the localization energy, which is defined as the difference between the band gap of the matrix and the energy of the ground-state transition in a QD, is the same in structures *B* and *C*. Therefore, the temperature stability of the linewidth in structures *C* and *D* is related to the existence of AlAs/InAlAs barriers, absence of a WL level, and increased energy spacing between the levels of the ground and excited states.

Figure 3 shows the PL spectra (Ar$^+$ laser with $W = 1.5$ kW cm^2) and PL excitation spectra of structures *B*, *C*, and *D* at $T = 7$ K. The arrows indicate the energies of signal detection E_{DET} used in the study of the PL excitation spectra. Spectral lines related to absorption in the WL and in the QW are observed only in structure *B*. At excitation energies below 1.35 eV, the PL excitation spectra of all the structures demonstrate sets of resonance lines related to absorption on the excited states in QDs and to LO-phonon relaxation of carriers into the ground state [15]. The lines equidistant from the detection energy for the PL excitation spectra, whose relative positions remain unchanged when the point E_{DET} moves along the PL line, correspond to 1LO, 2LO, and 3LO phonon resonances. All the structures demonstrate phonon lines spaced by ~32 meV, which corresponds to the phonon energy in InAs QDs. The phonon energy in a QD may differ slightly from 32 meV because it is affected by the distribution of stresses within a QD [16]. It can be seen that, when QDs are overgrown with a thin In$_{0.15}$Ga$_{0.85}$As layer (structure *B*), Δ_{ex} is 82 meV, whereas, when QDs are capped with AlAs/In$_{0.25}$Al$_{0.75}$As layers, Δ_{ex} increases to 105 and 115 meV (structures *C* and *D*). Along with the LO lines associated with InAs QDs, structures *C* and *D* demonstrate phonon resonances spaced by ~40 meV, which corresponds to the LO phonon mode of the In$_x$Al$_{1-x}$As layer (LO*).

Figure 4 shows PL excitation spectra recorded at different temperatures for structures *B*, *C*, and *D*. In these measurements, the detection energy corresponded to the peak energy of the PL spectrum at the given temperature. For convenience, all the spectra were shifted along the energy scale by the detection energy E_{DET}. The PL excitation spectra of structure *B* exhibit a gradual decrease in the intensity of resonance lines as the temperature increases, with nearly complete quenching at $T = 270$ K. No specific features are observed in the excitation spectra at room temperature. This circumstance means that thermal excitation of electrons and holes and their lateral transport become so efficient that carriers photoexcited from QDs with a certain energy are redistributed over the entire ensemble and excitation is no longer selective for QDs with a ground-transition energy corresponding to E_{DET}. The same conclusion can be drawn in an analysis of the PL spectra recorded under resonant excitation of this structure (Figs. 5a, 5b). The PL spectra recorded at low temperatures under excitation with a monochromatic light
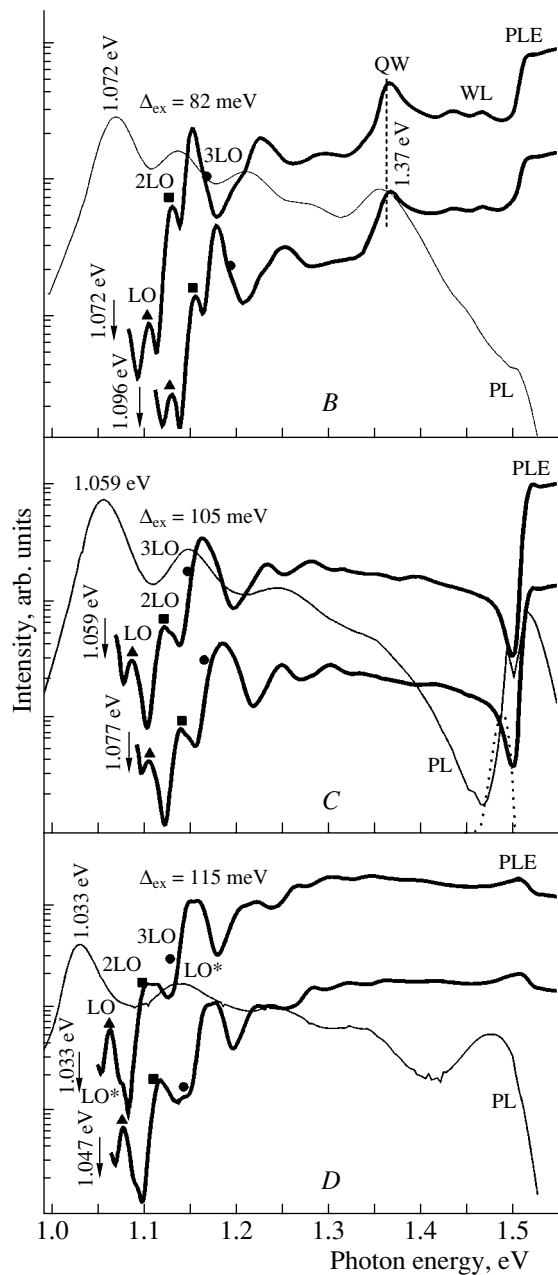
Fig. 3. PL (thin lines) and PL excitation (PLE, thick lines) spectra for structures *B*, *C*, and *D*. $T = 7$ K. Excitation was performed with an Ar$^+$ laser.

Fig. 4. PL excitation spectra for structures *B*, *C*, and *D* at different temperatures. The spectra are shifted along the *E* scale by the detection energy E_{DET}.

at an energy close to the energy of the QD ground state (Fig. 5a) demonstrate phonon lines that correspond to phonon replicas in the excitation spectrum (Fig. 4). The presence of LO-phonon resonances, which define the shape of the QD PL resonance spectrum, is indicative of selective excitation of QDs in which the energy spacing between the ground state and the excitation line is a multiple of the LO phonon energy [15]. In the spectra recorded at room temperature (Fig. 5b), increasing the excitation energy results only in a broadening of the PL lines, whereas the peak position remains unchanged
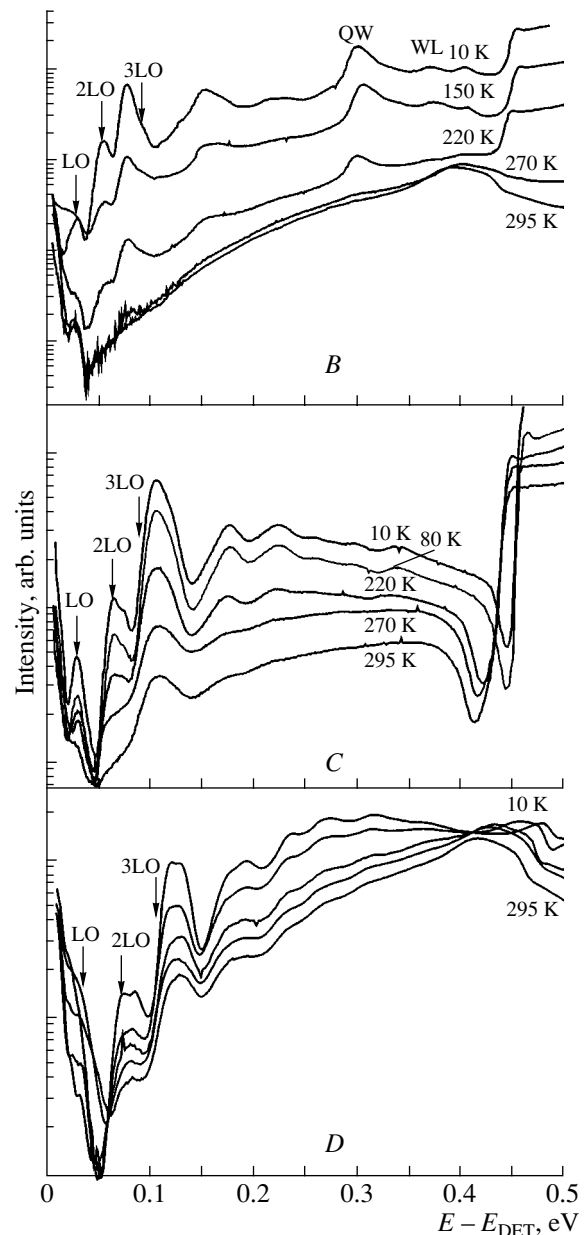
and no LO-phonon replicas are observed. It is noteworthy that, in the room-temperature PL excitation spectra of this structure, the absorption in the matrix is suppressed, which indicates that nonradiative recombination of carriers occurs in the GaAs matrix.

In the PL excitation spectra of structure *C* (Fig. 4b), a resonance line corresponding to absorption in the excited state is observed up to room temperature. The modification of the resonance PL spectra at $T = 300$ K (Fig. 5d) as the excitation energy is varied and the presence of LO phonon lines indicate that thermal excitation of carriers from QDs, as well as subsequent lateral
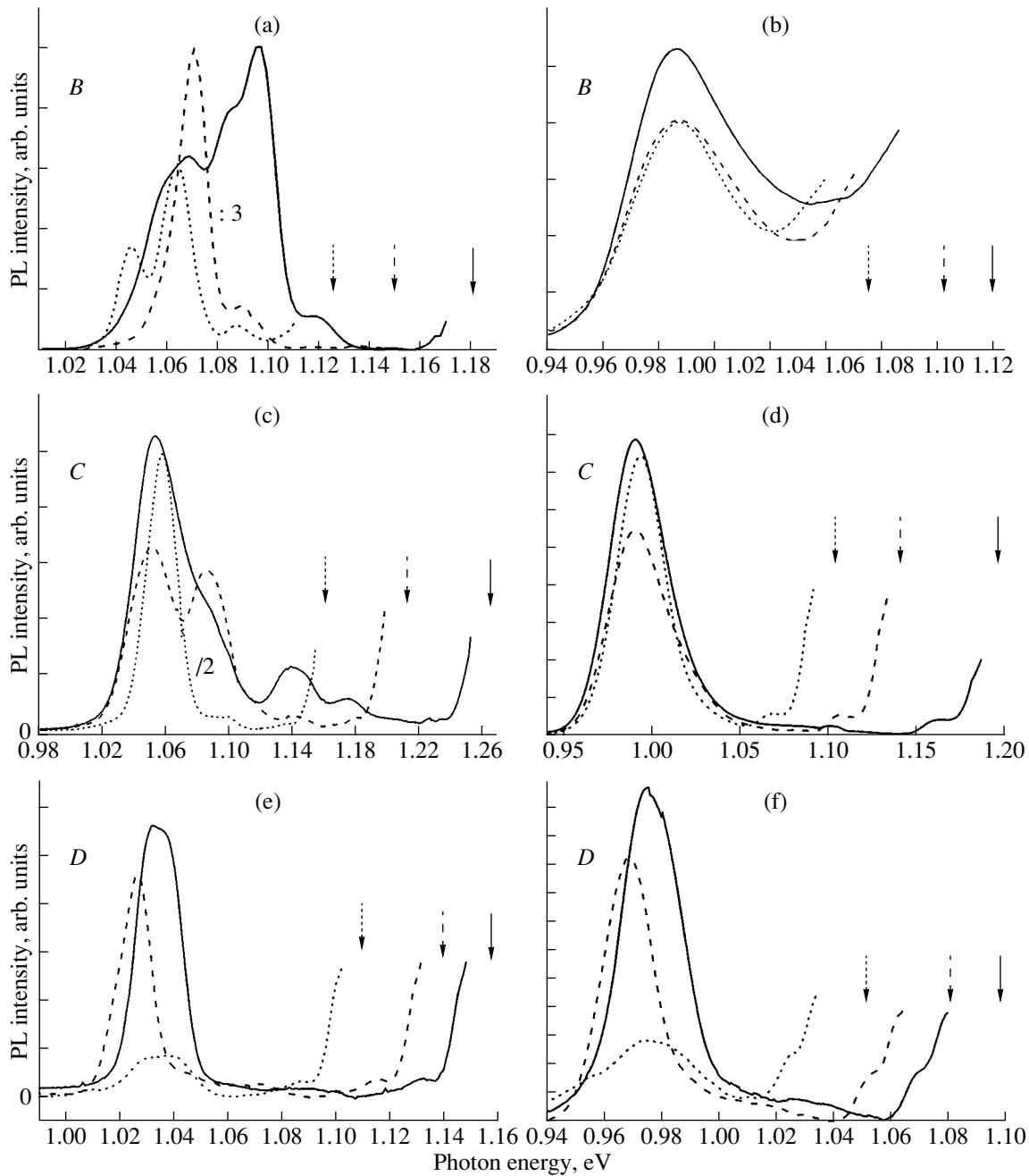
Fig. 5. Resonance excitation spectra recorded at (a, c, e) 10 K and (b, d, f) 295 K for (a, b) structure *B*, (c, d) structure *C*, and (e, f) structure *D*. The arrows indicate the energy of PL excitation.

transport and capture into another QD, is suppressed and the conditions of selective excitation of QDs are preserved.

The increase in the localization energy occurring in the case of the $Al_xGa_{1-x}As$ matrix used in structure *D* results in the effects typical of structure *C* becoming more pronounced. The resonance lines in the PL excitation spectrum are observed up to room temperature over the entire energy range. In addition, the strong modulation of resonance PL spectra is preserved at

300 K (Fig. 5f). Thus, at room temperature, all the carriers captured in QDs in structure *D* are completely isolated; moreover, the distribution of the carriers over states is of a nonequilibrium nature, since thermal excitation of the carriers from the QDs and their subsequent lateral transport are lacking.

4. CONCLUSIONS

InAs QDs formed in GaAs or $Al_{0.3}Ga_{0.7}As$ matrices and overgrown with thin AlAs/InAlAs layers have been

studied by means of PL and PL excitation spectroscopy. The wavelength of QD emission at $T = 300$ K is 1.27 μm. The FWHM of the PL line associated with the ground state remains virtually constant in the temperature range 10–400 K. As the temperature increases, the decrease in the PL integral intensity is significantly less than in the case of InAs QDs capped with a thin $In_{0.15}Ga_{0.85}As$ layer. The spectra of resonance PL demonstrate peaks corresponding to phonon relaxation at temperatures up to room temperature, which indicates the absence of thermal distribution of carriers among the states in the QDs. Thermal redistribution of carriers among different QDs at 300 K is suppressed due to the presence of AlAs/InAlAs barriers, increased energy spacing between the ground and excited states in the QDs, absence of a level related to the wetting layer, and an increase in the carrier localization energy in the QDs when the $Al_{0.3}Ga_{0.7}As$ matrix is used.

ACKNOWLEDGMENTS

REFERENCES

1. M. V. Maximov, I. L. Krestnukov, Yu. M. Shernyakov, *et al.*, J. Electron. Mater. **29**, 487 (2000).

2. S. Ghosh, S. Pradhan, and P. Bhattacharya, Appl. Phys. Lett. **81**, 3055 (2002).

3. D. Klotzkin, K. Kamath, K. Vineberg, *et al.*, IEEE Photonics Technol. Lett. **10**, 932 (1998).

4. N. N. Ledentsov, M. Grundmann, N. Kirstaedter, *et al.*, Solid-State Electron. **40**, 785 (1996).

5. I. Mukhametzhanov, R. Heitz, J. Zeng, *et al.*, Appl. Phys. Lett. **73**, 1841 (1998).

6. M. V. Maximov, A. F. Tsatsul'nikov, B. V. Volovik, *et al.*, Phys. Rev. B **62**, 16671 (2000).

7. A. F. Tsatsul'nikov, A. R. Kovsh, A. E. Zhukov, *et al.*, J. Appl. Phys. **88**, 6272 (2000).

8. B. V. Volovik, A. F. Tsatsul'nikov, D. A. Bedarev, *et al.*, Fiz. Tekh. Poluprovodn. (St. Petersburg) **33**, 990 (1999) [Semiconductors **33**, 901 (1999)].

9. Z. Y. Zhang, B. Xu, P. Jin, *et al.*, J. Cryst. Growth **241**, 304 (2002).

10. I. R. Sellers, H. Y. Liu, M. Hopkinson, *et al.*, Appl. Phys. Lett. **83**, 4710 (2003).

11. M. V. Maksimov, D. S. Sizov, A. G. Makarov, *et al.*, Fiz. Tekh. Poluprovodn. (St. Petersburg) **38**, 1245 (2004) [Semiconductors **38**, 1207 (2004)].

12. Kenichi Nishi, Hideaki Saito, Shigeo Sugou, and Jeong-Sik Lee, Appl. Phys. Lett. **74**, 1111 (1999).

13. D. P. Popescu, P. G. Eliseev, A. Stintz, and K. J. Malloy, Semicond. Sci. Technol. **19**, 33 (2004).

14. R. Heitz, M. Grundmann, N. N. Ledentsov, *et al.*, Appl. Phys. Lett. **68**, 361 (1996).

15. R. Heitz, M. Veit, N. N. Ledentsov, *et al.*, Phys. Rev. B **56**, 10 435 (1997).

16. B. Jusserand and M. Cardona, Top. Appl. Phys. **66**, 49 (1994).

Translated by D. Mashovets

LOW-DIMENSIONAL
SYSTEMS

Study of the Properties of a Two-Dimensional Electron Gas in p^--3*C*-SiC/n^+-6*H*-SiC Heterostructures at Low Temperatures

A. A. Lebedev^, D. K. Nel'son, B. S. Razbirin, I. I. Saĭdashev,
A. N. Kuznetsov, and A. E. Cherenkov

Ioffe Physicotechnical Institute, Russian Academy of Sciences, ul. Politekhnicheskaya 26, St. Petersburg, 194021 Russia
^e-mail: Shura.Lebe@mail.ioffe.ru
Submitted March 3, 2005; accepted for publication March 14, 2005

Abstract—The photoluminescence and magnetoresistance spectra of p^--3*C*-SiC/n^+-6*H*-SiC heterostructures are studied at temperatures ranging from 6 to 80 K. These studies show that the heterojunction affects both the photoluminescence spectrum and the magnetoresistance. However, the rather poor structural quality of the epitaxial structures has so far prevented the classical effects for structures with a two-dimensional electron gas from being observed. Presumably, a refinement of the experimental technique and, also, optimization of the growth and postgrowth technologies for SiC will make it possible to observe these effects in the near future. © 2005 Pleiades Publishing, Inc.

1. INTRODUCTION

Recently, a number of publications concerned with fabrication and study of heterostructures formed from various SiC polytypes have appeared [1–7]. For example, Lebedev *et al.* [1] were the first to study the electrical characteristics of p-3*C*-SiC/n-6*H*-SiC heterostructures and used the experimental data obtained to construct an energy-band diagram that was found to be close to the theoretical diagram. In particular, this diagram indicated that it is basically possible to obtain a two-dimensional electron gas (2DEG) at the heteroboundary of the above pair of semiconductors. In order to realize the 2DEG by the method of sublimation in vacuum, structures with modulated doping were fabricated; in these structures, the wide-gap semiconductor with n-type conductivity (6*H*-SiC) was heavily doped, whereas the narrow-gap semiconductor (3*C*-SiC) had conductivity close to the intrinsic state [8]. In the emission spectra of diodes fabricated on the basis of these structures, a shift of the luminescence band related to recombination of free excitons in 3*C*-SiC to shorter wavelengths was observed. The experimentally observed shift was in good agreement with the calculated value obtained for the shift of a localized state in a two-dimensional quantum well [8, 9].

In this paper, we report the results of studying the photoluminescence spectra and galvanomagnetic effects (transport phenomena) in initial p^--3*C*-SiC/n^+-6*H*-SiC epitaxial structures before the formation of mesas on them.

2. PHOTOLUMINESCENCE

The structures under study were obtained by sublimational epitaxy in vacuum. Similarly to [5, 8], a lightly doped ($N_a - N_d \approx 1 \times 10^{16}$ cm^{-3}) p-3*C*-SiC layer was grown directly on a heavily doped ($N_d - N_a \approx 3 \times 10^{18}$ cm^{-3}) 6*H*-SiC substrate.

The photoluminescence (PL) spectra were measured at liquid-helium ($T = 6$ K) and liquid-nitrogen ($T = 80$ K) temperatures. The PL was excited with radiation from an LGI-505 pulsed nitrogen laser (the radiation wavelength was 337.1 nm; the pulse width, 10 ns; the repetition frequency, 1 kHz; and the power in a pulse, 5 kW). The laser radiation was focused onto the sample in the form of a spot with a diameter of ~1 mm. The excitation density could be varied in the range from 1 to 100 kW/cm^2 using preliminarily calibrated filters. The spectral sensitivity curve of the setup was measured before carrying out the studies; the PL spectra were then corrected according to this curve.

The well-known band peaked at 2.64 eV was prevalent in the PL spectrum of the studied heterostructures. This band is related to recombination at the N–Al donor–acceptor pairs in 6*H*-SiC. In addition to this band, another band, in which four features located at 1.95, 2.02, 2.06, and 2.13 eV could be recognized, was observed in the long-wavelength portion of the spectrum (1.9–2.2 eV). It is worth noting that this band is located at an energy lower than the 3*C*-SiC band gap (2.39 eV) (3*C*-SiC is the narrow-gap semiconductor in the heterostructure) and, correspondingly, at an energy lower than the energy position of the characteristic structure in the PL spectrum of the bulk 3*C*-SiC sample (Fig. 1).

We also studied the PL spectra of an isotype n-3*C*-SiC/n^+-6*H*-SiC heterostructure, at whose heteroboundary a potential well for electrons should not be formed. The PL spectrum of this sample differed radically from that considered above; i.e., although the band peaked at

2.64 eV was still observed, the structure observed in the long-wavelength region of the spectrum was different and was characteristic of the bulk 3*C*-SiC samples (Fig. 2).

3. CONDUCTANCE IN A MAGNETIC FIELD

We used similar heterostructures to fabricate samples for the Hall measurements. These samples had the shape of $2 \times 0.5 \times 0.5$ mm rectangular parallelepipeds, with six ohmic contacts arranged in the form of a double Hall cross. The measurements were carried out at a constant current in a magnetic field with an induction as high as 1.2 T.

We studied the two-dimensional motion of charge carriers in the structures under consideration by measuring the conductance anisotropy in magnetic fields that were either perpendicular ($H_\perp$) or parallel ($H_\parallel$) to the interface. In order to establish the presence of conductance anisotropy in the magnetic fields applied to the structures under study, we rotated the rod with the sample attached about the vertical axis, thus changing the angle between the magnetic-field vector and the sample plane.

The low charge-carrier mobility, as well as the fairly high contact resistance at low temperatures, led to serious difficulties with the measurements and prevented precise identification of the experimental dependences. However, we managed to establish that the structures' conductivity ($\sim 8.7 \times 10^{-4}$ Ω^{-1} cm^{-1} at $T \approx 80$ K) is almost two orders of magnitude higher than the conductivity of a 6*H*-SiC substrate with the same geometric parameters and the same doping level but without the p^--3*C*-SiC epitaxial layer. This observation suggests that there is a two-dimensional conducting layer at the heteroboundary; however, possibly, this layer does not exist over the entire area of the heterostructure.

4. DISCUSSION

The absence of the PL spectrum (observed in the p^--3*C*-SiC/n^+-6*H*-SiC samples) in the structures without modulated doping shows that this PL is related to the presence of a triangular quantum well at the 3*C*-SiC/6*H*-SiC heteroboundary. In the absence of a quantum well at the heteroboundary, radiative recombination proceeds according to the conventional mechanisms characteristic of hexagonal and cubic polytypes of silicon carbide. At the same time, the PL spectrum observed in this study is located in a different energy region from the electroluminescence (EL) spectrum of heterodiodes formed on the basis of a similar heterostructure.

In order to explain the origin of the observed PL spectrum, let us consider the energy-band diagram of the heterostructure. The wide-gap semiconductor with n-type conductivity is heavily doped, whereas the p-type narrow-gap semiconductor is lightly doped. A potential well for electrons is formed at the heteroboundary, and the bottom of this well is located below the Fermi level. This circumstance gives rise to transi-
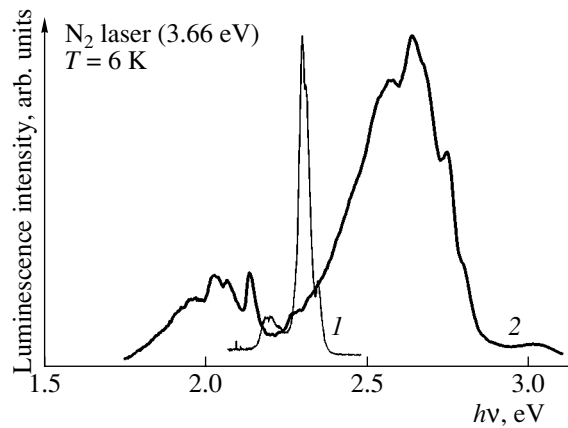

Fig. 1. PL spectra of the samples at $T = 6$ K. Spectrum *1* corresponds to a 3*C*-SiC single crystal and spectrum *2* corresponds to the p^--3*C*-SiC/n^+-6*H*-SiC heterostructure.
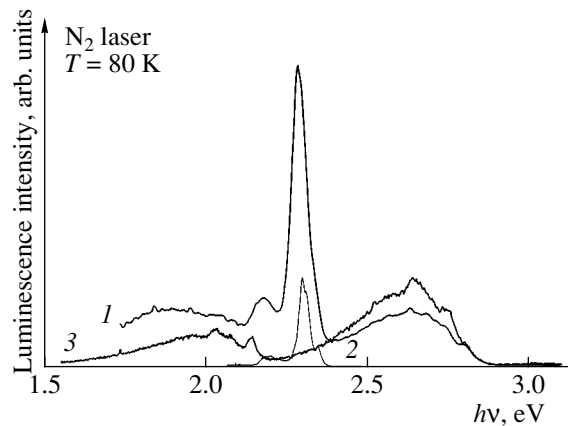

Fig. 2. PL spectra of the samples at $T = 80$ K. Spectrum *1* corresponds to the n-3*C*-SiC/n^+-6*H*-SiC heterostructure (without modulated doping), spectrum *2* corresponds to a 3*C*-SiC single crystal, and spectrum *3* corresponds to the p^--3*C*-SiC/n^+-6*H*-SiC heterostructure.

tions of electrons from the wide-gap semiconductor to the potential well, with the resulting formation of a 2DEG (Fig. 3). When the PL is excited, electron–hole pairs are formed. It is important that, as a result of the band bending in the vicinity of the heteroboundary, photogenerated holes drift from the boundary into the depth of the narrow-gap semiconductor. Correspondingly, in the course of radiative recombination, the transition under consideration is found to be indirect in real space; moreover, the energy of this transition can be smaller (in relation to the magnitude of band bending) than the band gap of the narrow-gap semiconductor with dimensional-quantization energy added. This mechanism of recombination has previously been suggested by Bergman *et al.* [10] for GaAs/Al$_x$Ga$_{1-x}$As heterostructures. The fact that a shift of the free-exciton line to shorter wavelengths was observed in the EL spectrum of heterodiodes formed on the basis of a sim-
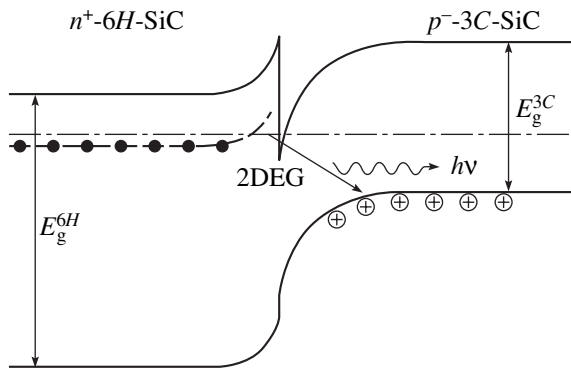
Fig. 3. Energy-band diagram and schematic representation of radiative transitions in the studied p^--3C-SiC/n^+-6H-SiC heterostructure.

ilar 3C-SiC heterostructure was apparently related to a decrease in the band bending as a result of the applied voltage and, also, a higher charge-carrier concentration (injection) in the vicinity of the heteroboundary.

5. CONCLUSION

Our studies show that the heterojunction affects both the PL spectrum and the resistivity. However, specific features of the SiC semiconductor (difficulties encountered with the formation of high-conductance contacts at low temperatures), as well as the inadequate structural quality of epitaxial the structures (the absence of a heavily doped spacer and the possibility of the heterojunction forming over part of the structure area, see [8]) has so far precluded observation of effects that are considered classical for structures with a two-dimensional electron gas. Presumably, a refinement of the experimental techniques (for example, application of an external field when measuring the PL spectra) and

optimization of the growth and postgrowth technologies will make it possible to observe the above effects in the near future.

REFERENCES

1. A. A. Lebedev, A. M. Strel'chuk, D. V. Davydov, *et al.*, Appl. Surf. Sci. **184**, 419 (2001).
2. A. Fissel, U. Kaiser, B. Schroter, *et al.*, Appl. Surf. Sci. **184**, 37 (2001).
3. R. S. Okojie, M. Xhang, P. Pirouz, *et al.*, Appl. Phys. Lett. **79**, 3056 (2001).
4. A. A. Lebedev, G. N. Mosina, I. P. Nikitina, *et al.*, Pis'ma Zh. Tekh. Fiz. **27** (24), 57 (2001) [Tech. Phys. Lett. **27**, 1052 (2001)].
5. A. A. Lebedev, A. M. Strel'chuk, N. S. Savkina, *et al.*, Pis'ma Zh. Tekh. Fiz. **28** (23), 78 (2002) [Tech. Phys. Lett. **28**, 1011 (2002)].
6. A. A. Lebedev, A. M. Strel'chuk, N. S. Savkina, *et al.*, Mater. Sci. Forum **433–466**, 169 (2003).
7. S. Juillaquet and J. Camassel, Mater. Sci. Forum **483–485**, 335 (2004).
8. A. A. Lebedev, A. M. Strel'chuk, N. S. Savkina, and A. N. Kuznetsov, Mater. Sci. Forum **457–460**, 597 (2004).
9. S. Yu. Davydov, A. A. Lebedev, and O. V. Posrednik, Fiz. Tekh. Poluprovodn. (St. Petersburg) **39** (2005) (in press).
10. J. P. Bergman, Q. X. Zhao, P. O. Holtz, *et al.*, Phys. Rev. B **43**, 4771 (1991).

Translated by A. Spitsyn

Kinetics of Structural and Phase Transformations in Thin SiO_x Films in the Course of a Rapid Thermal Annealing

V. A. Dan'ko, I. Z. Indutnyĭ^, V. S. Lysenko, I. Yu. Maĭdanchuk, V. I. Min'ko, A. N. Nazarov, A. S. Tkachenko, and P. E. Shepelyavyĭ

Lashkarev Institute of Semiconductor Physics, National Academy of Sciences of Ukraine, Kiev, 03028 Ukraine
*^e-mail: indutnyy@isp.kiev.ua*
Submitted January 18, 2005; accepted for publication February 28, 2005

Abstract—Infrared spectroscopy and analysis of photoluminescence spectra have been used to study variations in the composition of the oxide phase in a SiO_x film and the precipitation of the Si phase in the course of a rapid thermal annealing for 1–40 s at temperatures of 500–1000°C. Kinetics of phase segregation has been observed for the first time at temperatures of 600–700°C: an increase in the amount of precipitated silicon as the annealing duration increases followed by an eventual leveling off. The phase separation is brought to completion in a time as short as 1 s at temperatures higher than 900°C. The diffusion coefficient is estimated in the context of a model of the diffusion-controlled formation of Si nanoparticles. The obtained values of the diffusion coefficient exceed, by five to ten orders of magnitude, those of the silicon diffusion coefficients in SiO_2 and Si and are comparable to the diffusion coefficients of the oxygen contained in these structures. It is assumed that oxygen mobility forms the basis for the mechanism of structural and phase transformations in the SiO_x layers and for the formation of Si nanoparticles in the course of annealing. © *2005 Pleiades Publishing, Inc.*

1. INTRODUCTION

Recently, increasing interest has been displayed in films of silicon suboxide (SiO_x) in their role as a possible initial material for the fabrication of silicon light-emitting structures under the condition of formation of silicon nanoparticles in the oxide matrix. These nanoparticles (amorphous or crystalline) are formed in the course of thermally stimulated decomposition of amorphous SiO_x into silicon and SiO_2 phases. The process of incomplete decomposition is often described by the reaction

$$y\,SiO_x \longrightarrow x\,SiO_y + (y - x)\,Si, \quad (0 < x < y \leq 2). \quad (1)$$
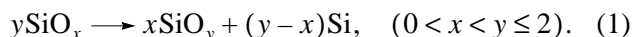
The annealing temperature controls the nanoparticles' structure: annealing at temperatures below 800°C gives rise to amorphous inclusions, whereas Si nanocrystals (nc-Si) are formed at higher temperatures; moreover, the electronic structure of these nanocrystals is modified owing to the quantum-dimensional effect [1–3]. The photoluminescence (PL) observed in annealed SiO_x layers in the spectral region 700–900 nm is related to the presence of Si nanoparticles.

In order to gain insight into the PL origin and to accomplish controlled variations in the PL spectra, we have to study the processes that lead to the formation of silicon nanoparticles. The diffusion-related phenomena observed in the course of annealing have been studied in many publications; however, there is, as yet, no satisfactory model or quantitative estimates that can be used to describe these phenomena. Estimates of the diffusion coefficient reported in various publications differ by orders of magnitude.

The effect of the duration of annealing of silicon-oxide layers on the PL spectra was studied in [4–6]. It was shown [4] that complete decomposition of SiO_x into Si and SiO_2 phases occurs as a result of annealing for 1 min at a temperature of 1250°C. Further annealing leads to a slow increase in the luminescence intensity; the annealing duration insignificantly affects the shape of the PL band. The position of the PL peak remains virtually unchanged in the course of annealing.

Annealing for less than 1 min involves certain difficulties. Gallas *et al.* [6] applied laser annealing using pulses with a duration of tens of nanoseconds. It was shown that SiO_x was partially decomposed into silicon and silicon dioxide and that the process had a threshold character. It was admitted [6] that pulsed-laser annealing makes it impossible to both control the film temperature and study the temperature distribution in depth of the film. The results show that the temperature at the surface is equal to approximately 1550°C and decreases to 1000°C at a depth of 100 nm. It was also shown [6] that evaporation (ablation) of the material occurs as a result of irradiation with laser pulses.

Daigil *et al.* [7] annealed oxide layers using short pulses generated by an excimer laser (with a pulse width of 30 ns and wavelength of 308 nm). It was shown that such annealing did not give rise to silicon nanoparticles even at high heating temperatures (as high as those corresponding to melting of the silicon-oxide layer).

Recently, a large number of publications concerned with thermally stimulated transformations in SiO_2 films implanted with Si ions, some of which were also concerned with the effect of pulsed annealing, have appeared [8–10]. A specific feature of this method consists in the fact that a large number of defects are formed as a result of ion implantation, and PL is often observed even in unannealed samples. Kachurin *et al.* [8] used two types of pulsed annealing procedures: either with a pulse width of 1 s at temperatures of 900–1200°C in an Ar atmosphere or with a pulse width of 20 ms at temperatures of 1050–1350°C (with a constant component of 600°C) in a N_2 atmosphere. The kinetics of the formation of silicon nanocrystals in the course of annealing was not studied in [8]; however, the results made it possible to conclude that silicon nanoparticles were formed at a high rate in the implanted films. These results cannot be explained in the context of the mechanism of silicon diffusion in the SiO_2 matrix.

In this paper, we report the results of a more detailed study of the kinetics of silicon-nanocluster formation in SiO_x films in the course of rapid thermal annealing. The studies were carried out using the methods of photoluminescence and infrared (IR) spectroscopy.

2. EXPERIMENTAL

Samples in the form of thin SiO_x films were obtained by thermal evaporation in vacuum (at a residual pressure of 1×10^{-3} Pa) of silicon monoxide with a purity of 99.9% (Cerac Inc.). As substrates, we used either silicon wafers polished on both sides or wafers of fused quartz for optical measurements in the visible region of the spectrum. The deposition rate for the samples was measured using a quartz oscillator and was kept constant and equal to 1.5 nm/s for all the samples. The thickness of the films was measured using an MII-4 microinterferometer with an accuracy of ±5 nm and was equal to 350–450 nm. This thickness was chosen in order to avoid interference effects in the PL spectra.

Annealing at temperatures of 500, 600, 650, 700, 900, and 1000°C was carried out using an Impuls-3 semiautomatic system of pulsed annealing. This system makes it possible to control the sample temperature at an annealing duration longer than 1 s. The time taken for heating from 0 to 1000°C was 4 s, and the duration of cooling to a temperature of 500°C was 9 s. The annealing was performed in a nitrogen atmosphere. Some of the samples were also annealed in vacuum for 1–4 min at temperatures of 600 and 700°C.

The IR transmission spectra were measured in the wave-number range ν = 800–1200 cm^{-1} using a Specord 80 spectrometer, and a silicon substrate without a deposited film was used as the reference sample. Photoluminescence was excited with an argon laser at a wavelength of 488 nm. The PL spectra were measured in the wavelength range 600–1100 nm at room temperature.

The transmission and reflection spectra of the samples in the visible region of the spectrum were measured at room temperature using an MDR-23 spectrometer. We calculated the absorption-coefficient spectrum of the deposited SiO_x layer using the obtained values of transmittance and reflectance, the film thickness, and the refractive index of the quartz substrate.

The ratio between the atomic contents of oxygen and silicon (the value of x) in the deposited samples was determined using two methods. In the first method, we used the experimental dependence of the position of the band of the interband-absorption edge on the composition of the SiO_x film. This dependence was tabulated at a level of the absorption coefficient equal to 10^4 cm^{-1} by Zuther [11]. This method makes it possible to determine x for freshly deposited homogeneous samples in which, as has previously been shown [12], there are no silicon inclusions. The silicon phase is additionally segregated in the film as a result of high-temperature annealing, and the dependence of the absorption edge on the averaged composition becomes nonmonotonic [2].

The second method (see [13]) is based on the dependence of the position of the absorption band in the IR spectra of SiO_x films in the range 1000–1100 cm^{-1} on the film composition. The position of the peak of the band under consideration shifts monotonically from 980 cm^{-1} for SiO to higher frequencies as the oxygen content in the oxide increases. This band is caused by stretching vibrations in the bridge oxygen (the stretching Si–O–Si mode). Since only vibrations of the silicon–oxygen phase manifest themselves in this region and Si–Si bonds are not detected, this method can be used to determine the composition of the oxide matrix both in the as-prepared and in the annealed samples that contain the silicon phase.

Thus, the position of the IR absorption band under consideration is sensitive to a variation in the oxide-matrix composition and makes it possible to determine the ratio between the content of atomic oxygen and silicon before and after annealing (the values of x and y in expression (1)). In turn, measurements of the stoichiometric coefficient of the matrix make it possible to find the amount of silicon that precipitated in the form of nanoparticles and to determine the specific volume of nanoparticles in the matrix.

For all the freshly deposited samples, the value of x was equal to 1.32 if determined from the interband-absorption edge and to 1.27 if determined from the IR spectra.

3. RESULTS AND DISCUSSION

In Fig. 1, we show the IR transmission spectra of the SiO_x films immediately after deposition (curve *1*) and after annealing in a nitrogen atmosphere at T = 650°C for 1 s (curve *2*) and 38 s (curve *3*). It can be seen that the IR absorption band shifts to higher frequencies as the annealing duration increases: the position of the
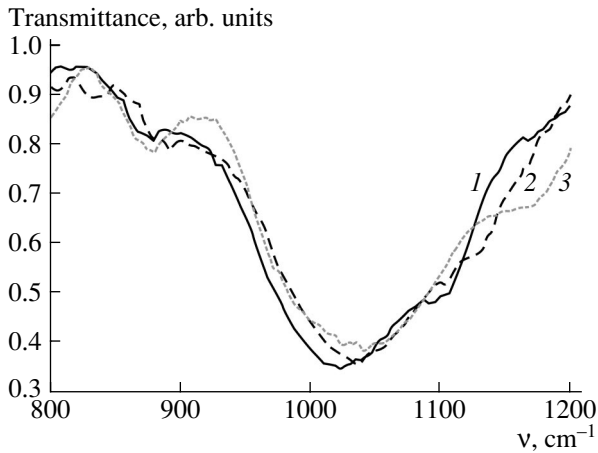
Transmittance, arb. units

Fig. 1. IR transmission spectra for (*1*) an unannealed sample and samples annealed for (*2*) 1 s and (*3*) 38 s at 650°C.
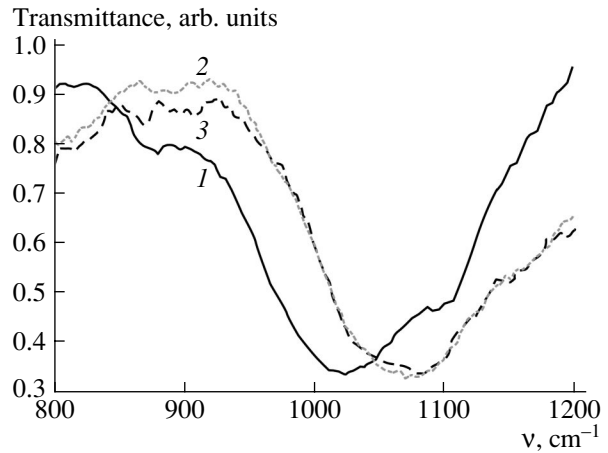
Transmittance, arb. units

Fig. 2. IR transmission spectra for (*1*) an unannealed sample and samples annealed for (*2*) 1 s and (*3*) 30 s at 900°C.

peak of this band was 1023 cm⁻¹ for an unannealed film and became 1030 cm⁻¹ after annealing for 1 s and 1040 cm⁻¹ after annealing for 38 s; simultaneously, the shape of the band somewhat changes. Similar dependences were obtained at the annealing temperatures of 600 and 700°C.

At higher annealing temperatures ($T = 900$ and 1000°C), the shift of the band to higher frequencies is virtually the same for all the annealing durations, from 1 s upwards (the results for the annealing temperature of 900°C are shown in Fig. 2).

An annealing carried out at a temperature of 500°C did not lead to a detectable change in the IR spectra of the SiO$_x$ layers in the region 1000–1100 cm⁻¹ in the range of annealing durations under study (1–40 s).

In Figs. 3a and 3b, we show the dependences of the high-frequency shift for the IR band ($\Delta\nu$) on the duration of the rapid thermal annealing. Since the value of $\Delta\nu$ characterizes the variation in the composition of the oxide matrix (i.e., the amount of excess silicon precipitated in the form of nanoclusters), the dependences shown in Fig. 3 describe the kinetics of thermally stimulated phase decomposition in SiO$_x$. It can be seen from Fig. 3 that, at annealing temperatures higher than 900°C, the process of phase separation is complete after even 1 s of annealing. This observation is consistent with the results reported by Kachurin *et al.* [9], according to which nanocrystals were formed in implanted SiO$_2$ layers even after 1 s and 20 ms of annealing at temperatures of 1200 and 1350°C, respectively. A slower kinetics of the process is observed at lower annealing temperatures (Fig. 3a): a gradual increase in the amount of precipitated silicon as the annealing duration increases and ultimate flattening out of the dependence on the annealing duration. The time required for the process to attain saturation decreases as the temperature increases. This time is equal to ~40 s for annealing at 600°C, 10 s at 650°C, and 4 s at 700°C.

It is worth noting that the degree of decomposition of the oxide matrix at the stage of process saturation, i.e., the difference $y - x$ in Eq. (1), depends on temperature. In Table 1, we list the values of the stoichiometric coefficients for the oxide phase of the SiO$_x$ layers annealed at different temperatures for a time that exceeds the time required for the process of thermally stimulated decomposition to come to saturation. We recall that the layer composition before annealing corresponds to $x = 1.27$.

It follows from Table 1 that almost complete decomposition of the suboxide into Si and SiO$_2$ occurs only at temperatures higher than 900°C, in which case crystalline silicon nanoinclusions are formed. At lower temperatures, the decomposition process attains saturation under an incomplete decomposition of the oxide, and the atomic fraction of the precipitated silicon phase (ΔSi) decreases as the temperature decreases.

The PL in the freshly deposited films has a low intensity, which makes it difficult to separate a pronounced band; this low intensity can be attributed to the presence of defects in the deposited films. It is also impossible to recognize a separate PL band in the samples annealed at 500°C, which is caused by the absence of the silicon phase in the samples.

Broad PL bands in the red and near-IR regions of the spectrum were observed for the samples annealed at

Table 1. Composition of the annealed SiO$_x$ layers

T, °C	500	600	650	700	900	1000
y	1.27	1.4	1.5	1.52	1.92	2.0
ΔSi, at %	0	4.09	6.75	7.25	14.9	16.1

Note: T is the annealing temperature, y is the stoichiometric coefficient that corresponds to the annealed oxide matrix and is determined from the position of the IR absorption band, and ΔSi = $[(y - x)/y(1 + x)] \times 100\%$ is the atomic fraction of the silicon phase.
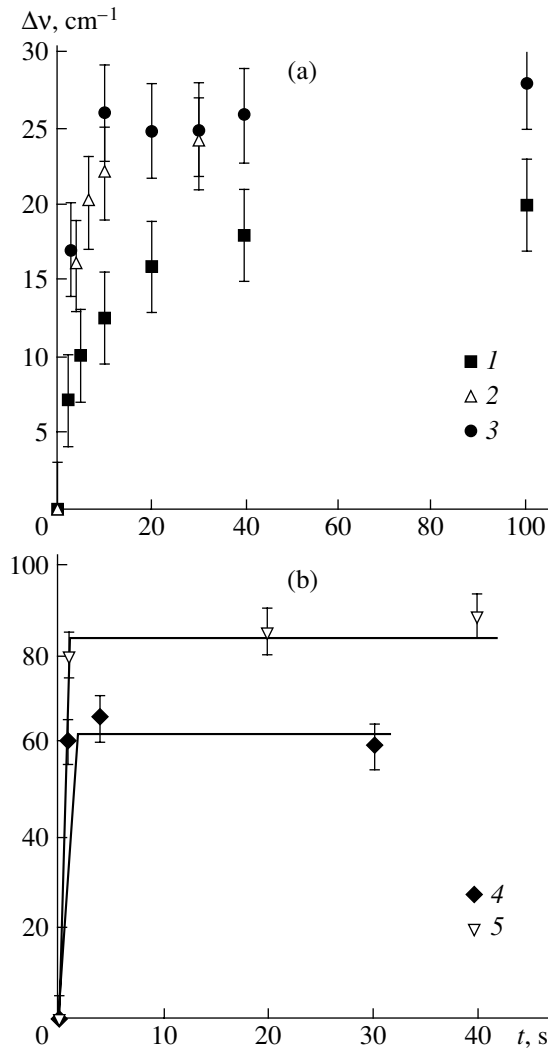
Fig. 3. Dependence of the shift of the peak of the IR absorption band on the annealing duration. The annealing temperature T = (a) (*1*) 600, (*2*) 650, and (*3*) 700°C, and (b) (*4*) 900 and (*5*) 1000°C.

Fig. 4. PL spectra of the samples annealed at a temperature of 700°C. The annealing duration was (*1*) 3, (*2*) 5, and (*3*) 20 s.

higher temperatures (Figs. 4, 5). For the annealing temperatures of 600 and 650°C, the peak of the band corresponds to the wavelength $\lambda = 800 \pm 20$ nm; this peak is located at $\lambda = 900 \pm 20$ nm at a temperature of 1000°C. Both bands can be separated in the PL spectra obtained after annealing at intermediate temperatures.

As was shown in [12, 14], the PL with its peak at a wavelength of 900 nm can be related to the emission from crystalline silicon nanoparticles or from the recombination centers located at the nanocrystal–oxide interface, whereas the band at shorter wavelengths corresponds to radiative recombination of electron–hole pairs in amorphous silicon nanoparticles. However, this interpretation is incorrect for the annealing temperature of 700°C, since the crystalline silicon phase has not yet been formed. Such a two-mode PL structure has been observed in the PL spectrum of silicon-implanted and,
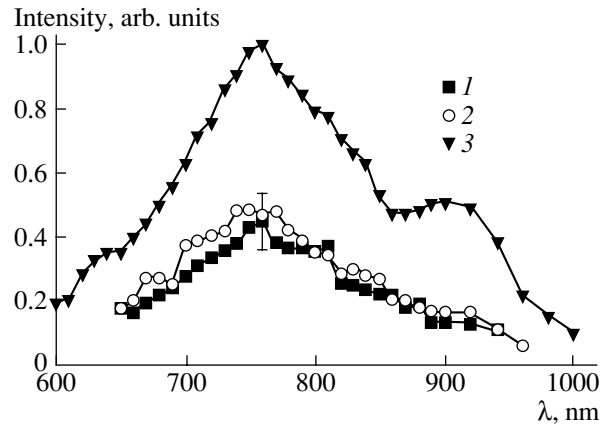
then, annealed silicon oxide grown in a water-vapor atmosphere [15]. It was assumed [15] that the long-wavelength band is caused by interfacial states; however, reliable identification of the origin of the two-mode PL structure requires additional study.

The PL intensity depends on the annealing duration of the structures studied. In the annealing-temperature range 600–700°C, the PL intensity increases as the annealing duration increases and attains a maximum after several tens of seconds. This increase in intensity correlates with the kinetics of precipitation of the silicon phase in the course of annealing, which confirms the assumption that the short-wavelength PL band is related to the amorphous silicon nanoinclusions.

For the annealing temperatures of 900 and 1000°C, the highest PL intensity was observed for the shortest annealing duration (1 s). As the annealing duration increases, the PL intensity decreases drastically and then begins to increase gradually at an annealing duration in excess of 16 s. The increase in the PL intensity continues as the annealing duration increases to 30 min [14], which is in good agreement with the results of other studies [4, 5], where an increase in the PL intensity was observed over 4 h of annealing. This behavior is accounted for by annealing-stimulated passivation of the centers that give rise to nonradiative recombination at the boundary between the Si and SiO$_y$ phases.

Using the obtained data on the kinetics of precipitation of the silicon phase in the course of annealing (Fig. 3), we can estimate the parameters of the diffusion process that controls the formation of silicon nanoparticles. In order to perform this estimation, we have to know the sizes and shape of the nanoparticles that are formed. Expressions that relate the optical-gap width E_g and the position of the PL-band peak to the sizes of silicon nanocrystals have been derived in a number of theoretical studies. As an example, we can cite the following expression derived by Delerue *et al.* [16]: $E_g =$

$1.12 + 3.73/d^{1.39}$, where E_g is the energy corresponding to the peak in the PL spectrum expressed in eV and d is the nanoparticle diameter expressed in nanometers. In the case under consideration, the nanoparticles in the samples annealed at temperatures of 600–700°C are amorphous; therefore, the above expression cannot be used for a quantitative analysis. In turn, as shown by Nesheva *et al.* [12], the sizes of the amorphous nanoparticles that act as centers involved in PL are approximately equal to the sizes of crystallites. Therefore, the use of the above dependence for approximate estimation of the nanoparticle sizes is justified. According to the above expression, the nanoparticle diameter is equal to 4.7 nm for an emission wavelength of 800 nm.

We earlier employed high-resolution electron microscopy to determine the sizes of the silicon nanocrystals in samples that were similar to those used in this study ($x = 1.3$, and a thermal deposition of SiO) and annealed at a temperature of 1000°C [12]. We found that the Si nanocrystals were distributed uniformly in the oxide matrix and their average diameter was equal to 4.3 nm.

Thus, we can assume that the diameter of the nanoparticles is equal to 4–5 nm in the case under consideration in order to approximately estimate the diffusion coefficient. It was assumed in earlier studies concerned with nc-Si–SiO$_x$ structures that nc-Si nanocrystals are formed as a result of diffusion of silicon atoms from the environment to the nuclei [17]. It has been assumed in a number of recent publications, on the basis of experimental data and the results of theoretical simulations, that the formation of nanoclusters and chains of silicon atoms at temperatures below 700°C is related to percolation phenomena [8–10]. As the annealing temperature is increased, the percolation-induced precipitates are transformed into nanodimensional particles of a silicon amorphous phase. The diffusion coefficient of Si in SiO$_2$ becomes sufficiently large for the diffusion-controlled growth of silicon precipitates only at temperatures higher than 1000°C. However, this model was suggested for layers obtained by implantation of Si into SiO$_2$, in which case small silicon clusters can be formed even in the course of implantation and luminescence is observed even before annealing. A model of the diffusion-controlled formation of nanoparticles appears to be preferable for the more homogeneous amorphous layers obtained by thermal deposition.

Let us assume that silicon nanoparticles grow in the form of spherical particles with a radius of 2.5 nm; furthermore, the growth occurs owing to diffusion of silicon atoms into these particles from the surrounding region (the so-called diffusion sphere), which has a radius of 2.5 nm + $\sqrt{Dt}$, where $\sqrt{Dt}$ is the diffusion length, D is the diffusion coefficient, and t is the diffusion time. We assume that the diffusion time is equal to the time required for leveling off of the kinetic curve that describes the thermally stimulated precipitation of the silicon phase. This time is unknown for annealing
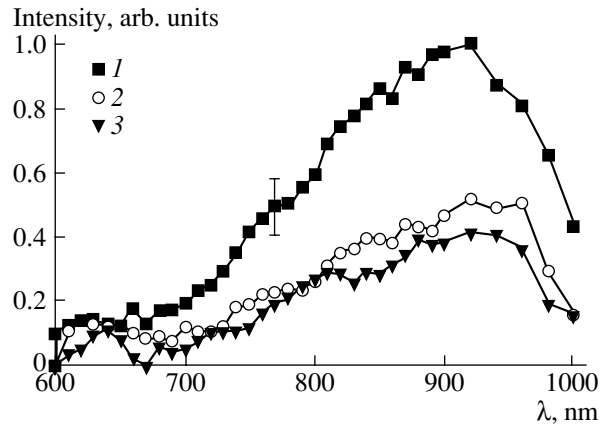

Fig. 5. PL spectra of the samples annealed for (*1*) 1, (*2*) 6, and (*3*) 36 s at a temperature of 1000°C.

temperatures higher than 900°C; we can only state that it is shorter than 1 s. Knowing the initial composition of the film and the matrix composition in the region of the diffusion sphere after the silicon phase has precipitated, we can determine first the diffusion-sphere radius for each temperature and, then, the value of D. For temperatures higher than 900°C, in which case almost complete decomposition of SiO$_x$ into SiO$_2$ and Si occurs, the oxide composition within the diffusion-sphere region corresponds to SiO$_2$. For lower annealing temperatures, the experimental value of y represents an averaged composition of the oxide matrix after annealing. If the oxide matrix is homogeneous after annealing, we can use the value of y to estimate the diffusion coefficient D. Otherwise, each nanoparticle is surrounded by a shell with an increased content of oxygen, whereas the medium in the space between the particles has the composition of SiO$_x$. It is noteworthy that the averaged composition of the oxide matrix corresponds to the value of y. We estimate the value of D for temperatures 600–700°C in two limiting cases: (i) the oxide matrix is homogeneous after annealing (the maximum value of D) and (ii) the diffusion spheres with a SiO$_2$ composition overlap (the minimum value of D). The results obtained are listed in the first row of Table 2 (D_{exp}).

Let us compare the data obtained with the results of measurements of the diffusion coefficients for silicon in similar structures. Data on the diffusion coefficient for thermally deposited oxide SiO$_x$ layers are lacking in the available publications. The diffusion of silicon atoms implanted into SiO$_2$ has been studied using secondary-ion mass spectrometry [18]. It was shown that the obtained experimental data can be adequately approximated by the expression $D_{\text{Si–SiO}_2}$ [cm^2/s] $= 33.2\exp(-5.34$ eV/$kT)$, where $D_{\text{Si–SiO}_2}$ is the diffusion coefficient for silicon in SiO$_2$; T is temperature, which was varied in the range 1000–1200°C; and k is the Boltzmann constant. The values of $D_{\text{Si–SiO}_2}$ obtained using this expression are

Table 2. Values of the diffusion coefficient

T, °C	600	650	700	900	1000
D_{exp}	4.6×10^{-15}–7.3×10^{-16}	9.6×10^{-15}–2.9×10^{-15}	2.1×10^{-14}–7.3×10^{-15}	$>3 \times 10^{-14}$	$>3 \times 10^{-14}$
$D_{Si–SiO_2}$	3.2×10^{-30}	2.5×10^{-28}	7.7×10^{-27}	3.9×10^{-22}	2.5×10^{-20}
$D_{Si–Si}$	1.4×10^{-26}	5.9×10^{-25}	1.7×10^{-23}	6.0×10^{-19}	3.2×10^{-17}
$D_{O–SiO_2}$	5.5×10^{-11}	1.3×10^{-10}	2.7×10^{-10}	2.8×10^{-9}	7.0×10^{-9}
$D_{O–Si}$	5.9×10^{-16}	3.5×10^{-15}	1.6×10^{-14}	2.3×10^{-12}	1.6×10^{-11}

Note: All the values of the diffusion coefficient are expressed in cm^2/s.

listed in the second row of Table 2. It can be seen that the diffusion coefficient that controls the process of formation of silicon nanoparticles in the layers studied is ten or more orders of magnitude larger than the diffusion coefficient for silicon atoms in SiO$_2$. It is conceivable that the diffusion coefficient would be larger in the oxide matrix enriched with silicon. Therefore, in the third row of Table 2, we list the values of the self-diffusion coefficient for silicon atoms in crystalline silicon $D_{Si–Si}$ from [19] (extrapolation to the temperatures of 600–700°C was carried out using the expression $D_{Si–Si}$ [cm^2/s] $= 9.0 \times 10^3 \exp(-5.17$ eV$/kT)$, which was reported in [19] for the temperature range 1100–1300°C). It can be seen that these values are also no less than five orders of magnitude smaller than those we obtained for the diffusion coefficient D.

Thus, the assumption that silicon nanoparticles are formed owing to a diffusion-related drain of excess Si atoms is in conflict with the results obtained. However, the nanoparticles in the silicon phase can be also formed as a result of a thermally stimulated diffusive drain of oxygen atoms from the localization region of a silicon nanoparticle under formation into the diffusion sphere. The assumption that this process is possible was advanced in one of our previous publications [20]. This assumption was based on a detailed analysis of the phase and structural transformations in SiO$_x$ films in the course of heat treatments in vacuum. In that particular study, we used IR spectroscopy [20]. It was shown that slightly oxidized molecular clusters in the initial SiO$_x$ layer (mainly, SiOSi$_3$) lose oxygen and transform into SiSi$_4$ tetrahedra. Oxygen diffuses, interacts with highly oxidized clusters (for example, SiO$_3$Si), and transforms them into SiO$_4$. As a result, local precipitation of the silicon phase and enrichment of the oxide phase with oxygen occur.

In the fourth and fifth row of Table 2, we list the values of the diffusion coefficients for oxygen in SiO$_2$ ($D_{O–SiO_2}$) and silicon ($D_{O–Si}$). The data for the temperature range under consideration were taken from a reference book [21].

It can be seen from Table 2 that the diffusion coefficient for oxygen atoms in both oxide and silicon exceeds, by many orders of magnitude, the diffusion coefficient for silicon atoms and is consistent with the values obtained in this study at temperatures of 600–700°C. The estimate of the lower value of D at 900 and 1000°C is also closer to the values of the diffusion coefficient for oxygen. This observation favors the hypothesis that it is oxygen mobility that forms the basis for the mechanism of phase separation in SiO$_x$ layers.

4. CONCLUSIONS

The rapid thermal annealing of SiO$_x$ vacuum-deposited layers for 1–40 s in the temperature range 600–1000°C leads to a change in the composition of the layers' oxide phase, precipitation of the silicon phase, and the appearance of an absorption band in the near-IR region of the spectrum. The amount of silicon that forms the clusters and, also, the matrix composition after annealing (SiO$_y$) depend on the temperature and duration of annealing. The process of phase separation is complete after even 1 s of annealing at temperatures higher than 900°C. At lower annealing temperatures, we observed, for the first time, the kinetics of the phase separation in silicon oxide. We observed both an increase in the amount of precipitated silicon as the annealing duration increased and a leveling off of the duration dependence. The time required for the leveling off of the duration dependence of silicon precipitation decreases as the temperature increases. This time is equal to ~40 s for annealing at 600°C, 10 s at 650°C, and 4 s at 700°C.

The peak of the photoluminescence (PL) band corresponds to a wavelength of 800 ± 20 nm for annealing temperatures of 600 and 650°C and to 900 ± 20 nm for 1000°C. Both bands can be recognized in the PL spectra of the samples annealed at intermediate temperatures.

We used a model of the diffusion-controlled formation of silicon nanoparticles to estimate the value of the diffusion coefficient. The obtained values of the diffusion coefficient D that controls the process of formation of silicon nanoparticles in the layers studied exceeds, by almost ten orders of magnitude, the value of the diffusion coefficient for silicon atoms in SiO$_2$ and exceeds, by five orders of magnitude, the self-diffusion coefficient for silicon atoms in crystalline silicon. At the same time, the experimental values of D are compa-

rable to the diffusion coefficients for oxygen in SiO_2 and silicon.

The results reported validate the assumption that oxygen diffusion plays the determining role in the process of structural and phase transformations in SiO_x layers and in the formation of Si nanoparticles.

REFERENCES

1. M. Molinari, H. Rinnert, and H. Vergnat, Appl. Phys. Lett. **82**, 3877 (2003).

2. V. Ya. Bratus', V. A. Yukhimchuk, L. I. Berezhinskiĭ, *et al.*, Fiz. Tekh. Poluprovodn. (St. Petersburg) **35**, 854 (2001) [Semiconductors **35**, 821 (2001)].

3. I. P. Lisovskiĭ, I. Z. Indutnyĭ, B. N. Gnennyĭ, *et al.*, Fiz. Tekh. Poluprovodn. (St. Petersburg) **37**, 98 (2003) [Semiconductors **37**, 97 (2003)].

4. B. Garrido Fernandez, M. Lopez, C. Garcia, *et al.*, Appl. Phys. Lett. **81**, 798 (2002).

5. M. Lopez, B. Garrido, C. Garcia, *et al.*, Appl. Phys. Lett. **80**, 1637 (2002).

6. B. Gallas, C.-C. Kao, S. Fission, *et al.*, Appl. Surf. Sci. **185**, 317 (2002).

7. Daigil Cha, Jung H. Shin, In-Hyuk Song, and Min-Koo Han, Appl. Phys. Lett. **84**, 1287 (2004).

8. G. A. Kachurin, I. E. Tyschenko, V. Skorupa, *et al.*, Fiz. Tekh. Poluprovodn. (St. Petersburg) **31**, 730 (1997) [Semiconductors **31**, 626 (1997)].

9. G. A. Kachurin, A. F. Leĭer, K. S. Zhuravlev, *et al.*, Fiz. Tekh. Poluprovodn. (St. Petersburg) **32**, 1371 (1998) [Semiconductors **32**, 1222 (1998)].

10. G. A. Kachurin, S. G. Yanovskaya, V. A. Volodin, *et al.*, Fiz. Tekh. Poluprovodn. (St. Petersburg) **36**, 685 (2002) [Semiconductors **36**, 647 (2002)].

11. G. Zuther, Phys. Status Solidi A **59**, K109 (1980).

12. D. Nesheva, C. Raptis, A. Perakis, *et al.*, J. Appl. Phys. **92**, 4678 (2002).

13. M. Nakamura, V. Mochizuki, K. Usami, *et al.*, Solid State Commun. **50**, 1079 (1984).

14. I. Z. Indutnyy, I. P. Lisovskyy, D. O. Mazunov, *et al.*, Semicond. Phys. Quantum Electron. Optoelectron. **7**, 161 (2004).

15. D. I. Tetel'baum, O. N. Gorshkov, A. P. Kasatkin, *et al.*, Fiz. Tverd. Tela (St. Petersburg) **47**, 17 (2005) [Phys. Solid State **47**, 13 (2005)].

16. C. Delerue, G. Allan, and M. Lannoo, Phys. Rev. B **48**, 11024 (1993).

17. L. A. Nesbit, Appl. Phys. Lett. **46**, 38 (1985).

18. D. Mathiot, J. P. Schunck, M. Perego, *et al.*, J. Appl. Phys. **94**, 2136 (2003).

19. *Physical Properties. Properties of Elements: Handbook*, Ed. by V. Samsonov (Metallurgiya, Moscow, 1976), Part 1 [in Russian].

20. I. P. Lisovskiĭ, I. Z. Indutnyĭ, V. G. Litovchenko, *et al.*, Ukr. Fiz. Zh. **48**, 250 (2003).

21. *VLSI Technology*, Ed. by S. M. Sze (McGraw-Hill, New York, 1983; Mir, Moscow, 1986), Vol. 1.

Translated by A. Spitsyn

A Quasi-hydrodynamic Modification of the Uniform-Channel Approximation in MOS-Transistor Theory

V. A. Gergel' and M. N. Yakupov^

Institute of Radio Engineering and Electronics, Russian Academy of Sciences, ul. Mokhovaya 18, Moscow, 125009 Russia
^e-mail: yamt@mail.ru
Submitted September 14, 2004; accepted for publication November 15, 2004

Abstract—A new method for calculating the characteristics of the ultrasubmicrometer field-effect transistors used in modern microelectronics is suggested. This model combines the traditionally simplified quasi-one-dimensional representation of the electric-field distribution in the transistor channel (the approximation of a uniform channel and charged layers) and an advanced quasi-hydrodynamic description of the high-field electron drift (the energy-balance equation) and adequately describes the situations in which there are high temperature gradients in the electron gas. A detailed mathematical formulation of the model; the method of its numerical implementation; the calculated current–voltage characteristics of test transistor structures; and a physical analysis of the electrical characteristics of ultrasubmicrometer transistors with an allowance made for specific features of the distributions of mobile-charge concentrations, electric fields, and temperature in the transistor channel are presented. © 2005 Pleiades Publishing, Inc.

1. INTRODUCTION

The phenomenal progress made in relation to microelectronic metal-oxide-semiconductor (MOS) technology leading to successful implementation of the production of integrated circuits with a characteristic transistor channel length of ~10^{-5} cm gave rise to a certain crisis in the understanding of the physics involved in the operation of devices with the aforementioned very short channels. The reason is that nonlocal electric heating largely governs the electrical characteristics of ultrasubmicrometer MOS transistors, and this heating is further aggravated by the two-dimensional spatial distribution of high electric fields (10^5–10^6 V/cm) in the device structure. Therefore, the transistor models that are used in contemporary computer systems of circuitry-engineering design [1, 2], are based on the drift–diffusion variant of the so-called uniform-channel approximation, and include as many as a hundred adjustable parameters should be considered as no more than methods for analytical approximation of the corresponding experimental dependences.

At the same time, the available elaborate software packages intended for two-dimensional simulation of transistor characteristics and based on the so-called energy-transport model [3, 4] are not only rather time consuming but also unconvincing from the standpoint of verification of the electron-drift mechanisms and parameters that are included in the software, which makes physical interpretation of the results of any simulation difficult. In our opinion, it is the above circumstance that limits the use of two-dimensional quasi-hydrodynamic transistor models for design in practice.

Taking into account the above-described insight into the current situation in the field of simulation of the characteristics of ultrasubmicrometer MOS transistors, we decided to develop an intermediate-level transistor model; this model combines the traditionally simplified quasi-one-dimensional representation of the distribution of electric fields in the transistor channel (the approximation of a uniform channel and charged layers) with an advanced quasi-hydrodynamic electron-drift description that is adequate in situations in which there are high temperature gradients in the electron gas. This paper is devoted to presentation of the model under consideration. We describe the mathematical formulation of the model and methods for its numerical implementation. We also calculate the electrical characteristics of a test transistor structure and physically analyze the electrical properties of the transistor taking into account specific features of the distributions of concentrations, fields, and temperature in the channel.

2. THE UNIFORM-CHANNEL APPROXIMATION

As is well known, the term "uniform-channel approximation" [5, 6] implies (i) disregard of the divergence of the electric-field lateral component E_x in the Poisson equation for a semiconductor-substrate region near an insulator; and (ii) the assumption that the distribution of the inversion-layer density along the normal coordinate z corresponds to a quasi-equilibrium state (the Boltzmann distribution). These assumptions make it possible to write the first integral of the Poisson equation, express the z electric-field component that exists in the oxide and is induced by charges in the semicon-

ductor, determine the voltage drop across the oxide, and derive, as a result, the well-known formula

$$V_G = \phi + \frac{d}{\varepsilon_i \varepsilon_0} \sqrt{2\varepsilon_s \varepsilon_0 q N} \sqrt{\phi + T \exp\frac{\phi - 2\phi_B - V(x)}{T}}, \quad (1)$$

which is written with relevant simplifications that correspond to the state of inversion. Here, as is conventional, V_G is the gate potential minus the flat-band voltage, $\phi = \phi(x)$ is the surface potential, T is the electron temperature expressed in volts, N is the acceptor concentration, $\varepsilon_i \varepsilon_0 / d = C_0$ is the specific oxide capacitance, d is the oxide thickness, ε_i and ε_s are relative permittivities of the oxide and semiconductor, ε_0 is the permittivity of free space, and q is the elementary charge. We call attention to the fact that the exponential function in (1) incorporates, along with the so-called inversion potential $2\phi_B = 2T\ln(N/n_i)$, the local Fermi potential $V(x)$, which is a priori unknown. As a result, formula (1) makes it possible to find the desired relation between the gate voltage and the surface potential only at the channel boundaries where the Fermi potential is specified by the neighboring heavily doped regions of the source ($V(0) = 0$) and drain $V(L) = V_D$ (V_D is the drain voltage). In order to consider the channel region $0 < x < L$ itself, we use the following specific change of variables:

$$\sqrt{2\varepsilon_0 \varepsilon_s q N} \sqrt{\phi + T \exp\frac{\phi - 2\phi_B - V(x)}{T}}$$
$$= Q_{inv} + \sqrt{2\varepsilon_0 \varepsilon_s q N \phi}. \quad (2)$$

Here, Q_{inv} is the surface charge density in the electron inversion layer and $\sqrt{2\varepsilon_0 \varepsilon_s q N \phi}$ is the surface charge density in the acceptor depletion region. Formulas (1) and (2) allow us to express the surface charge density in the inversion layer in terms of the current value of the surface potential:

$$Q_{inv} = C_0(V_G - \phi - \sqrt{\phi_1 \phi}),$$
$$\phi_1 = 2\varepsilon_0 \varepsilon_s q N C_0^{-2}. \quad (3)$$

We now define the drift surface current by the formula

$$I = Q_{inv} \mu \frac{d\phi}{dx} \quad (4)$$

and, then, use the continuity condition for this current, $dI/dx = 0$, to establish the following relation between the surface potentials at the channel boundaries:

$$I = \frac{\mu C_0}{L}\left(V_G \phi - \frac{\phi^2}{2} - \frac{2}{3}\phi\sqrt{\phi_1 \phi}\right)\Bigg|_{\phi(0)}^{\phi(L)}. \quad (5)$$

We substitute the boundary values of the surface potential into (5); these values are determined to within a certain accuracy from (1). As a result, (5) is transformed into a formula for the current–voltage (I–V) characteristics of a transistor. It is worth noting that the very

crude approximation $\phi(0) = 2\phi_B$ and $\phi(L) = 2\phi_B + V_D$ is typically appropriate for the conducting states of the transistor.

3. QUASI-HYDRODYNAMIC MODIFICATION

Thus, we have expounded, in sufficient detail, the essence of the uniform-channel approximation, which is sometimes referred to as the model of charged layers [7]. We now consider a quasi-hydrodynamic modification of this approximation while retaining formula (3) for the surface charge density in the inversion layer as the starting expression.

First, we introduce the temperature dependence of mobility into the consideration in the form

$$\mu_\alpha(T) = \mu_0\left(\frac{T_0}{T}\right)^\alpha, \quad (6)$$

restricting the analysis to the simplest power law ($\alpha = 1$ or 0.5). Here, $\mu_0 = 1500\ \text{cm}^2/(\text{V s})$ is the initial low-field mobility of electrons in silicon and $T_0 = 0.025\ \text{V}$ is the equilibrium lattice temperature. We then write the following formula for lateral electron current taking into account all its components (drift, diffusion, and thermal diffusion):

$$j_n = \mu_\alpha Q_{inv}\frac{d}{dx}(\phi - T) - Q_{inv}\frac{d}{dx}(\mu_\alpha T) - \mu_\alpha T\frac{dQ_{inv}}{dx}. \quad (7)$$

We note that the derivative of the potential at the centroid of the inversion charge is written in formula (7) in the form of the effective lateral electric field; this charge is smaller than the surface charge by exactly the value of the temperature. We then, as is standard, write the following expression for the flux of the electron-gas temperature:

$$j_T = q^{-1}\left(\frac{5}{2} - \alpha\right)\left(-\mu_\alpha Q_{inv} T\frac{dT}{dx} + j_n T\right). \quad (8)$$

Here, $(5/2 - \alpha)$ is the Peltier coefficient and the terms in the second bracket describe the thermal conductivity and convection. Finally, the so-called energy-balance equation is written as

$$q\frac{dj_T}{dx} = j_n\frac{d}{dx}(\phi - T) - \frac{Q_{inv}(T - T_0)}{\tau_e(T)}. \quad (9)$$

It should be remembered [8] that the law of variation in energy-relaxation time involving the temperature $\tau_e(T)$ can be made consistent with the formula for the mobility:

$$\tau_e(T) = \tau_0\left(\frac{T}{T_0}\right)^{1-\alpha}, \quad \tau_0 = \frac{\mu_0 T_0}{v_s^2}. \quad (10)$$

Here, $v_s \approx 10^7\ \text{cm s}^{-1}$ is the saturation velocity.

Now, in order to lend a certain "elegance" to the final mathematical formulation of the model, we introduce the dimensionless variables

$$\phi = \frac{\phi}{T_0}, \quad T = \frac{T}{T_0}, \quad x = \frac{x}{L}, \quad (11)$$

where L is the distance between the drain and source, i.e., the channel length. Then, instead of (7), we obtain the following expression for the current:

$$j_n = \frac{\mu_0 C_0}{L} T_0^2 i_n. \quad (12)$$

Here, in accordance with (3), a dimensionless current is given by

$$i_n = T^{-\alpha}\left[\frac{d\phi}{dx} - (2-\alpha)\frac{dT}{dx} - T\frac{d}{dx}\right](V_G - \phi - \sqrt{\phi\phi_1}). \quad (13)$$

Correspondingly, we have

$$j_T = \frac{\mu_0 C_0}{qL} T_0^3 i_T, \quad (14)$$

$$i_T = \left(\frac{5}{2} - \alpha\right)\left[-T^{1-\alpha}\frac{dT}{dx}(V_G - \phi - \sqrt{\phi\phi_1}) + i_n T\right]. \quad (15)$$

The energy-balance equation that in fact forms the model in combination with the condition for the conservation of current (13), $di_n/dx = 0$, takes the form

$$\frac{di_T}{dx} = i_n\frac{d}{dx}(\phi - T)$$
$$- (V_G - \phi - \sqrt{\phi\phi_1})(T-1)T^{\alpha-1}\left(\frac{L}{l_T}\right)^2. \quad (16)$$

It is worth noting that the squared ratio between the so-called thermal length $l_T = \sqrt{\mu_0\tau_0 T_0} \approx 30$ nm and the channel length of a transistor is incorporated in the relaxation term in (16) and, in fact, represents the most important parameter of the model.

4. THE BOUNDARY CONDITIONS

We now consider the boundary conditions for energy-balance Eq. (16). Evidently, we cannot formulate these conditions on the boundaries between the channel and the heavily doped regions of the source and drain in a traditional way since we do not know, a priori, the electron-gas temperature at these boundaries, which cannot be physically defined with confidence. Our experience with simulation of a high-field drift in $n^+–n–n^+$ structures [8] shows that the boundary conditions in the problem under consideration should be effected at the exterior boundaries between the drain and source and the corresponding metal contacts, where the electron-gas temperature can be considered as corresponding to the equilibrium state with a higher degree of confidence. To this end, we formulate a new quasi-one-dimensional

representation of the electron drift in the drain and source regions of a transistor. By following the tendency of modern MOS technology towards a decrease in the thickness of the source and drain regions to its limits, we position the implanted donor centers virtually at the interface with the oxide and, thus, transform these centers into a built-in charge screened by the corresponding inversion layer of mobile electrons. As a result, a surface potential is formed; the relation of this potential to the inversion-layer density can be described by the same formula (1) if V_G in this formula is replaced by the corresponding flat-band voltage $V_{FBS} = C_0^{-1} D_S \approx 100$ V, where D_S [C cm^{-2}] is the implantation dose. It is clear that, by adding the term $V_{FBS}f(x)$, where $f(x)$ is a fairly sharp auxiliary function whose values are close to zero in the channel and to unity in the drain and source regions, to the terms in the corresponding brackets in Eqs. (13) and (16) we correspondingly widen the range of the simulation and specify the necessary boundary conditions at the exterior boundaries as

$$\phi_S = 2\left(\phi_B + T_S\ln\frac{V_{FBS}}{\sqrt{\phi_1 T_S}}\right) \approx 1 \text{ V}, \quad (17)$$

$$\phi_D = V_D + \phi_S, \quad T_S = T_D = T_0. \quad (18)$$

5. THE ALGORITHM FOR CALCULATIONS

Finally, the system of model equations consists of the continuity and heat-balance equations given by

$$\begin{cases} \dfrac{di_n}{dx} = 0, \\[2mm] \dfrac{di_T}{dx} = i_n\dfrac{d}{dx}(\phi - T) \\[2mm] \quad - (V_G' - \phi - \sqrt{\phi\phi_1})(T-1)T^{\alpha-1}\left(\dfrac{L}{l_T}\right)^2, \end{cases} \quad (19)$$

where $V_G' = V_G f(x) + V_{FBS}[1 - f(x)]$,

$$f(x) = \begin{cases} 1/(1 + e^{20}), & 0.0 < x < 0.5, \\ 1/(1 + e^{20\cos[\pi(x-0.5)]}), & 0.5 < x < 2.5, \\ 1/(1 + e^{20}), & 2.5 < x < 3.0, \end{cases} \quad (20)$$

and i_n and i_T are defined by formulas (13) and (15) with V_G replaced by V_G'. Correspondingly, the conditions at the drain and source exterior boundaries are written as

$$\phi(0) = \phi_S, \quad \phi(3) = \phi_D, \quad T(0) = T(3) = T_0, \quad (21)$$

where ϕ_S and ϕ_D are the surface potentials determined from (17) and (18). It is worth noting that the values of the dimensionless coordinates $1 \le x \le 2$ correspond to the channel region proper.
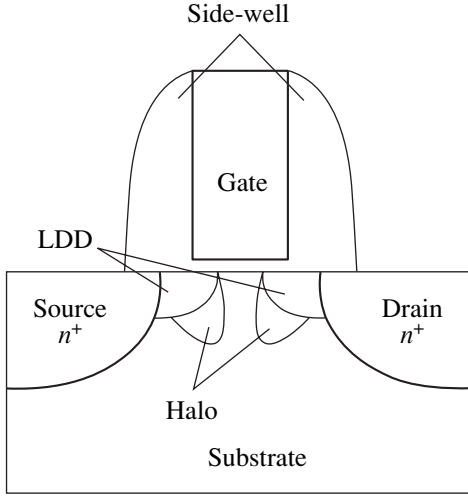
Fig. 1. Typical spatial structure of an ultrasubmicrometer MOS transistor.

Fig. 2. Calculated current–voltage characteristics of a test transistor structure with $L = 0.5$ μm and $d = 10$ nm at $\alpha = 0.5$ (solid lines) and $\alpha = 1.0$ (dashed lines). $V_G = 3$, 4, 5, and 6 V.

In order to discretize system (19), we use the method of integral identities; as a result, we obtain

$$
\begin{cases}
i_n^{i+1} - i_n^i = 0; \\[2mm]
i_T^{i+1} - i_T^i = \left\{ i_n^i \dfrac{d}{dx}(\phi - T)^i - (V_G^{'i} - \phi_i - \sqrt{\phi_i \phi_1}) \right. \\[4mm]
\left. \times (T_i - 1) T_i^{\alpha - 1}(L/l_T)^2 \right\} 0.5(a_i + a_{i+1}).
\end{cases}
\tag{22}
$$

Here, $a_i = x_i - x_{i-1}$, and the densities of the electron current and heat flux are given by

$$
i_n^i = T_i^{-\alpha}\left[\frac{d\phi^i}{dx} - (2 - \alpha)\frac{dT^i}{dx} - T_i\frac{d}{dx}\right](V_G^{'i} - \phi_i - \sqrt{\phi_i \phi_1}),
\tag{23}
$$

$$
i_T^i = \left(\frac{5}{2} - \alpha\right)\left[-T_i^{1-\alpha}\frac{dT^i}{dx}(V_G^{'i} - \phi_i - \sqrt{\phi_i \phi_1}) + i_n^i T_i\right],
$$

where $dn^i/dx = (n_i - n_{i-1})/a_i$ and $dT^i/dx = (T_i - T_{i-1})/a_i$.

System of Eqs. (22) with boundary conditions (21) was solved by a modified form of the Newton method. As the initial approximation, we used a uniform distribution of impurity with a gradual transition to abrupt $n-n^+$ boundaries. In particular, the properly corrected final approximation for the previous step was used as the initial approximation for the potential at each current value of the voltage. This procedure ensured a fairly rapid convergence of the iterative process; specifically, we had to carry out no more than five to six Newton iterations for each new value of the applied voltage V_D.
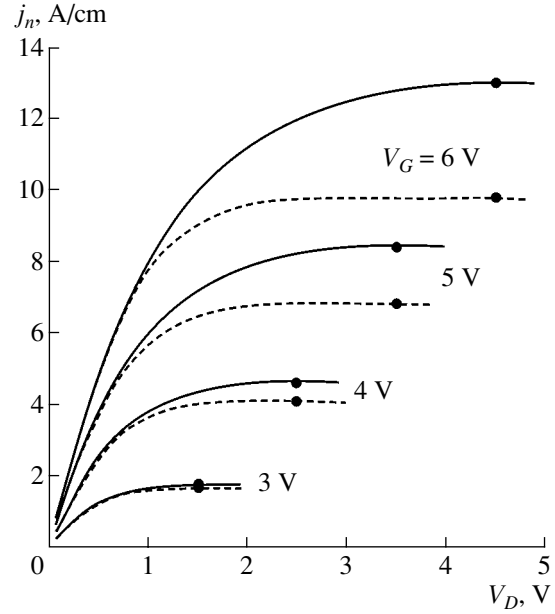
6. VERIFICATION OF THE MODEL

In order to test the applicability of the developed model of high-field electron drift in the inversion layer of a submicrometer MOS transistor and try to reveal some fine physical features of the drift process that are impossible to understand in the context of the conventional drift–diffusion approach, we used the traditional simplified concept of a spatial–technological device structure; i.e., we assumed that the substrate of the test transistor is uniformly doped and the boundaries of the drain and source regions are abrupt and disregarded (temporarily) the specific features of the LDD, halo, and side well found in real ultrasubmicrometer structures (Fig. 1).

In Fig. 2, we show the resulting output I–V characteristics of a transistor with the parameters $N = 10^{17}$ cm^{-3}, $d = 10$ nm, and $L = 0.5$ μm. The characteristics were calculated for two values of the parameter α in the temperature dependence of mobility: $\alpha = 0.5$ and 1.0. As expected, the slope of the initial portion (slight heating) of the curves is the same for different values of α; in contrast, the I–V characteristics with $\alpha = 0.5$ and 1.0 differ significantly at high currents, which indicates that the effect of the character of mobility thermal degradation on the shape of the I–V characteristics is profound. Since a priori data on a specific value of α are lacking, this quantity should be considered as an important adjustable parameter of the model.

It is worth noting that we did not hope to observe the so-called pinch-off of the channel when we were still relying on the uniform-channel approximation. Therefore, while increasing the drain voltage V_D, we termi-
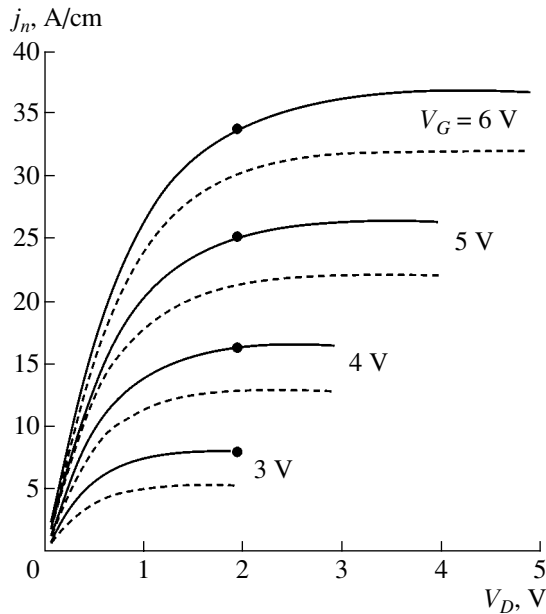
Fig. 3. Calculated current–voltage characteristics of test transistor structures with $L = 0.25$ μm, $d = 5$ nm, and $N = 10^{17}$ cm^{-3} (solid lines) or $N = 4 \times 10^{17}$ cm^{-3} (dashed lines) at $\alpha = 0.75$. $V_G = 3$, 4, 5, and 6 V.

Fig. 4. Calculated distributions of the temperature and heat-flux density (in arbitrary units) that correspond to the regimes indicated by circles in Fig. 3 ($V_D = 2$ V; $V_G = 4$, 5, and 6 V).

Fig. 5. Typical distributions of the electron velocity v and surface potential under the conditions $V_D = 2$ V and $V_G = 4$, 5, and 6 V.

nated calculations just at the point where the convergence degraded. For clarity, we indicated values of the saturation voltage that corresponded to the elementary transistor theory, $V_{Dsat} = V_G - V_{th}$ (see the circles in the I–V characteristics); as is conventional, we determined $V_{th} = 1.5$ V from the intersection of the gate-voltage dependence of the channel conductance at small values of V_D with the horizontal axis.

In order to illustrate the sensitivity of the model to variations in the structural parameters, we show, in Fig. 3, a series of calculated I–V characteristics that correspond to $\alpha = 0.75$ for transistor structures with $L = 0.25$ μm, $d = 5$ nm, and $N = 10^{17}$ or 4×10^{17} cm^{-3}.

Internal distributions of the temperature, potential, and local electron velocity over the channel length and in the neighboring regions of the drain and source, which were obtained in the course of calculating the I−V characteristics, are of great physical interest. As an example, Figs. 4 and 5 show the distributions of the above quantities for a number of typical points in the I−V characteristic represented in Fig. 3; these points correspond to the drain voltage $V_D = 2$ V and the gate voltages $V_G = 4$, 5, and 6 V.

Particular attention should be given to the temperature distributions in Fig. 4, where dashed curves represent the heat-flux density in arbitrary units. These distributions illustrate the main specific feature of electric heating in ultrasubmicrometer transistor structures: spacial separation of heating (in the channel) and cooling (in the drain region). In this case, the differential rigidity of the process (the continuity of the first deriv-
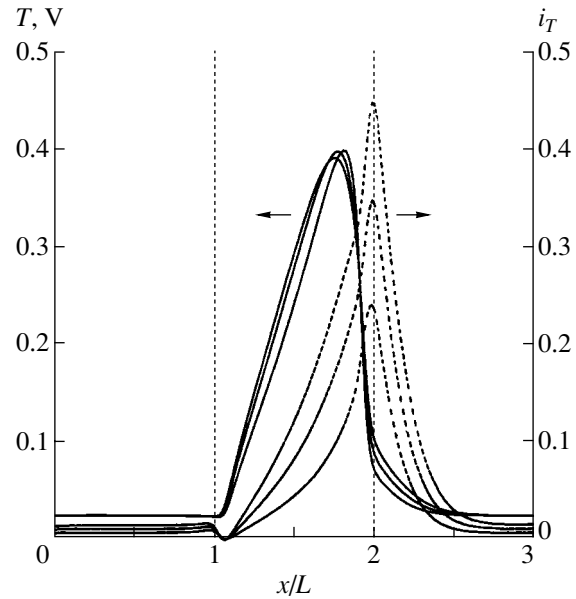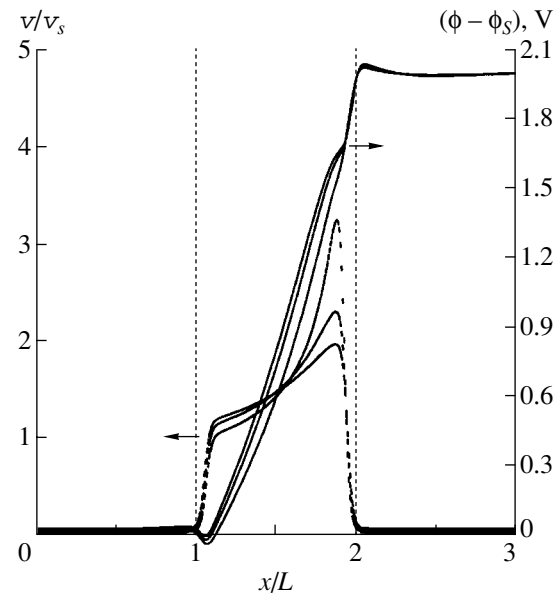
ative of temperature) brings about an appreciable drop in temperature even in the near-drain part of the channel, where the thermal current changes its sign and is added to the drift and diffusion currents. The latter effect, in combination with the corresponding jump in mobility, gives rise to a specific peak in the electron velocity in the near-drain region of the channel (Fig. 5).

It is worth noting that the absolute values of the velocity in this case appreciably exceed the saturation velocity. In addition, it should be emphasized that, in the near-drain region of the channel under consideration (and also in other regions of the channel), the intensity of Joule heating significantly exceeds the thermal-relaxation intensity. Intensive cooling of the charge carriers in this region is mainly caused by divergence of the heat flux that transfers the excess electron-related heat to the drain region with a low electric field, where thermal relaxation becomes dominant and thermal conductivity becomes the main component of the heat flux.

It is noteworthy that the above-described process of local cooling of the charge carriers in the near-drain region of the channel becomes more abrupt and pronounced in regimes that are close to the pinch-off state of the channel.

7. CONCLUSION

In summary, we can state that this study and the corresponding new approach to simulation of the high-field drift in submicrometer transistor structures are based on the suggested model representation of the drain regions as ultradense inversion layers. As a result, it becomes possible to consider the complete transistor structure in the quasi-one-dimensional approximation. Thus, we could use a powerful tool such as the quasi-hydrodynamic approach [9], which describes, with exceptional completeness, the high-field drift in its most illustrative (one-dimensional) variant.

We also note the relative simplicity of mathematical implementation of the developed intermediate-level model, which can appropriately be referred to in future as MESOMOS by analogy with the well-known MINIMOS model of Selbercher [10].

We believe that it would be highly beneficial to introduce the MESOMOS model into the practical research and development being carried out in microelectronics, since the transistor characteristics obtained as a result of test calculations are consistent with the typical characteristics of real transistor structures and exhibit a fairly high sensitivity (controllability) to numerical values of the relevant parameters. It is clear, however, that a certain modification of the model is required in order make its implementation feasible; this modification should include both the physics of the drift process and an adequate consideration of the structural–technological features of the device design.

In the next more advanced MESOMOS version, we will use the following more general expression for the mobility instead of elementary formula (6):

$$\mu_\alpha(T) = \mu_0 \left[\frac{\mu_0^2}{\mu_S^2} - 1 + \frac{N_A}{10^{17}} + \left(\frac{T}{T_0} \right)^{2\alpha} \right]^{-1/2}. \quad (24)$$

This expression makes it possible to take into account electron scattering by the interface roughness and Coulomb centers in the surface region of the semiconductor. We also plan to replace formula (3) by a somewhat more cumbersome expression that takes into account the depletion of the polysilicon-gate edge. In addition, we are going to use a pair of auxiliary coordinate functions in order to introduce into the consideration a lateral nonuniformity of doping of both the drain and source regions (LDD) and the substrate (halo). Finally, knowing the electron-temperature profile, we could, without much difficulty, introduce the impact ionization (the hole current in the substrate) and the above-barrier injection into the oxide (the gate current and the initial stage of degradation) into the model.

REFERENCES

1. BSIM3 User's Manual (Department of Electrical Engineering and Computer Science, Univ. of California, Berkeley, CA, 1996).

2. HiSIM1.1.1 User's Manual (STARC, 2002).

3. Taurus-Medici™, Synopsys Data Sheet (California, 2003).

4. Dessis™, ISE Data Sheet (Switzerland, 2003).

5. S. Sze, *Physics of Semiconductor Devices*, 2nd ed. (Wiley, New York, 1981; Mir, Moscow, 1984).

6. Y. P. Tsividis, *Operation and Modeling of the MOS Transistor*, 2nd ed. (McGraw-Hill, New York, 1999).

7. H. C. Pao and C. T. Sah, Solid-State Electron. **9**, 927 (1966).

8. V. A. Gergel', Yu. V. Gulyaev, V. A. Kurbatov, and M. N. Yakupov, Fiz. Tekh. Poluprovodn. (St. Petersburg) **39**, 453 (2005) [Semiconductors **39**, 429 (2005)].

9. R. Stratton, Phys. Rev. **126**, 2002 (1962).

10. MINIMOS-NT 2.0 User's Guide (Inst. for Microelectronics Technical Univ., Vienna, 2002).

Translated by A. Spitsyn

Temperature Dependence of the Threshold Current
of QW Lasers

N. L. Bazhenov^, K. D. Mynbaev, V. I. Ivanov-Omskiĭ, V. A. Smirnov,
V. P. Evtikhiev, N. A. Pikhtin, M. G. Rastegaeva, A. L. Stankevich,
I. S. Tarasov, A. S. Shkol'nik, and G. G. Zegrya

Ioffe Physicotechnical Institute, Russian Academy of Sciences, St. Petersburg, 194021 Russia
^e-mail: bazhnil.ivom@mail.ioffe.ru
Submitted November 29, 2004; accepted for publication December 14, 2004

Abstract—The temperature dependence of the threshold current in GaInAs-based laser structures has been studied in a wide temperature range ($4.2 \leq T \leq 290$ K). It is shown that this dependence is monotonic in the entire temperature interval studied. Theoretical expressions for the threshold carrier density are derived and it is demonstrated that this density depends on temperature linearly. It is shown that the main contribution to the threshold current comes from monomolecular (Shockley–Read) recombination at low temperatures. At $T > 77$ K, the threshold current is determined by radiative recombination. At higher temperatures, close to room temperature, Auger recombination also makes a contribution. The threshold current grows with temperature linearly in the case of radiative recombination and in accordance with T^3 in the case of Auger recombination. © *2005 Pleiades Publishing, Inc.*

1. INTRODUCTION

An important parameter of semiconductor lasers is their threshold current. It is known that, as the temperature (T) becomes higher, the threshold current in heterolasers and, in particular, quantum-well (QW) lasers increases. The temperature dependence of the threshold current density J_{th} is frequently described in publications by the following expression:

$$J_{th} = A \exp(T/T_0). \tag{1}$$

Here, A and T_0 are parameters, with T_0 being a characteristic temperature. Several linear portions are frequently distinguished in the $\ln J_{th}(T)$ dependence, with each portion having its own values of A and T_0; i.e., A and T_0 are themselves temperature-dependent. The temperature dependence of the threshold current density has been extensively studied [1–7]. However, the influence of temperature on the threshold current has been examined in sufficient detail only in a narrow temperature interval.

In this study, GaInAs-based laser structures were experimentally examined in a wide temperature range,

$4.2 \leq T \leq 290$ K, and it was shown that the threshold current density has a monotonic temperature dependence in structures of this kind in the entire temperature range considered. In addition, the influence exerted by the main processes of carrier recombination on the threshold current density in QW lasers in the studied temperature interval was analyzed.

2. EXPERIMENTAL

Semiconductor lasers based on strained InGaAs–AlGaAs heterostructures with QWs and with an emission wavelength λ of 0.95–1.54 μm at room temperature were chosen for experimental study. The sample parameters are listed in the table (where a stands for QW width).

The threshold current was measured in the temperature range $4.2 \leq T \leq 290$ K, with the structures excited by 1-μs pulses. The threshold current was found from the cutoff of the light–current characteristic. Figure 1 shows the temperature dependences of the threshold current for the samples studied. A monotonic tempera-

Parameters of the samples studied

Sample no.	Composition	Number of QWs	a, Å	λ, μm ($T = 300$ K)	λ, μm ($T = 4.2$ K)
1	$Ga_{0.2}In_{0.8}P_{0.25}As_{0.75}$ in $In_{0.1}Ga_{0.9}As_{0.7}P_{0.3}$	2	65	1.54	1.42
2	$In_{0.28}Ga_{0.72}As$ in GaAs	1	90	1.06	0.99
3	$In_{0.22}Ga_{0.78}As$ in GaAs	2	80	1.03	0.92
4	$In_{0.2}Ga_{0.8}As$ in $Al_{0.125}Ga_{0.875}As$	1	70	0.95	0.89

ture dependence of the threshold current is observed for all the laser structures.

It can be seen that the threshold current is virtually temperature-independent at $T < 60$ K and a linear dependence $J_{th}(T)$ is observed at $T > 60$ K. For sample nos. 1 and 3, the linear dependence gives way to a steep rise in J_{th} at $T > 170$, whereas, for sample nos. 2 and 4, the linear dependence $J_{th}(T)$ is preserved up to room temperature. In the following sections, we consider mechanisms that may lead to this temperature dependence of the threshold current density.

3. THRESHOLD CONCENTRATION

In order to calculate the threshold current density in a laser structure with QWs, it is primarily necessary to know the threshold concentration n_{th} of 2D carriers and its temperature dependence. The threshold concentration can be obtained as follows. Under strong injection conditions, the electron–hole plasma in a QW is quasi-neutral and the electron and hole concentrations are equal:

$$n = p. \qquad (2)$$

This condition can be supplemented by the lasing threshold condition

$$\Gamma g(\omega) = \alpha_i + \frac{1}{L}\ln\frac{1}{R}. \qquad (3)$$

Here, $g(\omega)$ is the gain of a QW laser, Γ is the optical confinement factor, α_i is the internal loss, R is the mirror loss, and L is the cavity length. For large L, such that $L^{-1}\ln R^{-1} \sim \alpha_i$, the lasing threshold virtually coincides with the inversion threshold [8, 9]. Then, condition (3) takes the form

$$g(\omega) = G(\omega)\left[\frac{1}{1 + \exp[(-F_e + \varepsilon_e)/T]}\right.$$
$$\left. + \frac{1}{1 + \exp[(-F_h + \varepsilon_h)/T]} - 1\right] \approx 0,$$

and we obtain

$$F_e - \varepsilon_e + F_h - \varepsilon_h = 0, \qquad (4)$$

where F_e and F_h are the quasi-Fermi energies for electrons and holes and ε_e and ε_h are the energies of the first quantum-well levels for electrons and holes, calculated from the conduction and valence band edges, and $G(\omega)$ is the absorption coefficient in the absence of injection [9]. Substituting the dependences of the electron and hole concentrations on the quasi-Fermi energies into (2) in the explicit form

$$n = N_c\ln\left[1 + \exp\frac{F_e - \varepsilon_e}{T}\right],$$
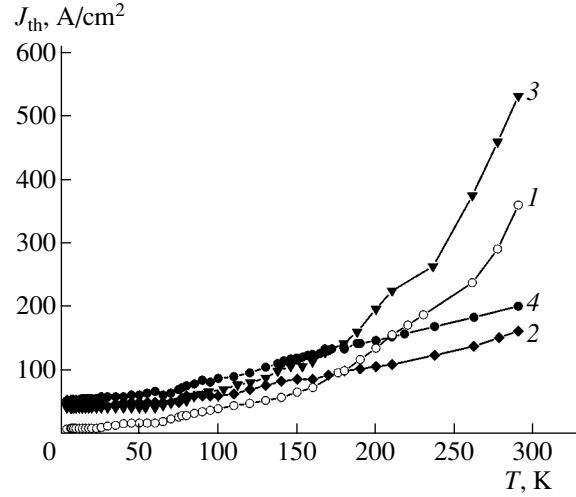$$p = N_v\ln\left[1 + \exp\frac{F_h - \varepsilon_h}{T}\right], \qquad (5)$$

Fig. 1. Experimental temperature dependences of the threshold current density for samples with the following room-temperature emission wavelengths λ: (*1*) 1.54, (*2*) 1.06, (*3*) 1.03, and (*4*) 0.95 μm. The curve numbers correspond to the sample numbers in the table.

as well as expressing F_h and ε_h in terms of F_e and ε_e with the use of (4), we obtain an expression for $\tilde{F}_e = (F_e - \varepsilon_e)/T$:

$$N_c\ln[1 + \exp(\tilde{F}_e)] = N_v\ln[1 + \exp(-\tilde{F}_e)], \qquad (6)$$

which leads to the following equation for $x = \exp(\tilde{F}_e)$:

$$(1 + x)^{m_e/(m_{hh} + m_{hl})} - \frac{1}{x} - 1 = 0. \qquad (7)$$

Here, m_e, m_{hh}, and m_{hl} are the effective masses of electrons and heavy and light holes, respectively. Expression (7) was derived under the assumption that electrons occupy the ground quantum-well level. This expression leads to the following conclusion: the ratio of the difference between the quasi-Fermi energy and that of a quantum level to temperature, i.e., $\tilde{F}_e$, is a constant dependent only on the ratio of the effective masses of carriers. A similar result was obtained for the 3D case in [10]. For the 2D case, an approximate expression for $\tilde{F}_e$ was derived in [9].

According to (5), the threshold concentration of 2D electrons (or an equal concentration of holes) is given by

$$n_{th} = \frac{m_e T}{\pi\hbar^2}\ln[1 + \exp\tilde{F}_e]. \qquad (8)$$

Thus, the threshold concentration is a linear function of temperature. This result is important because it is precisely this fact that largely determines the temperature dependence of the threshold current. It is noteworthy that, in the 3D case, the concentration would be propor-

tional to $T^{1.5}$, as demonstrated in the above-cited reference [10].

4. THRESHOLD CURRENT OF A LASER

The expression for the threshold current density J_{th} of a QW laser can be written as follows:

$$J_{\text{th}} = e[R_{\text{ph}} + R_A + R_m], \qquad (9)$$

where R_{ph}, R_A, and R_m are the rates of radiative recombination, Auger recombination, and monomolecular recombination involving local centers, respectively. The relative efficiency of these recombination mechanisms varies with temperature. Let us consider the role of each of these recombination mechanisms.

4.1. Radiative Recombination

In the limiting case, when electrons and holes are on the ground quantum-well levels, and in the absence of a spin–orbit interaction, the following analytical expression can be obtained for the rate of radiative recombination (see [11], chapter 7):

$$R_{\text{ph}} \approx \gamma(T) n_{\text{th}}^2. \qquad (10)$$

Here, the coefficient of bimolecular recombination $\gamma(T) \propto 1/T$. Consequently, according to (8)–(10), the current due to radiative recombination linearly depends on temperature.

In the case of a single QW, the exact expression for the threshold current associated with radiative recombination has the form [12]:

$$J_{\text{th}} = I_{cv}^2 e \frac{2}{3\pi} \alpha \frac{M}{1+M} \frac{E_g(E_g + \Delta_0)}{E_g + (2/3)\Delta_0} \frac{\sqrt{\kappa_0}}{\hbar^2 c^2} I_1, \qquad (11)$$

$$I_1 = \int_{E_0}^{\infty} E \left\{ \exp\left[\frac{[M/(1+M)](E-E_0) + \varepsilon_e - F_e}{T} \right] + 1 \right\}^{-1}$$

$$\times \left\{ \exp\left[\frac{[1/(1+M)](E-E_0) + \varepsilon_h - F_h}{T} \right] + 1 \right\}^{-1} dE. \qquad (12)$$

Here, $\alpha = e^2/\hbar c$ is the fine structure constant, E_g is the band gap of the active region, κ_0 is a low-frequency dielectric constant, Δ_0 is the energy of the spin–orbit interaction, $M = m_{hh}/m_e$, $E_0 = E_g + \varepsilon_e + \varepsilon_h$, and I_{cv} is the overlap integral between the wave functions of electrons and holes in the QW in the direction perpendicular to its plane.

The temperature dependence of expression (11) is contained in integral (12), which can be evaluated if we use expression (4) and assume that $\tilde{F}_e \gg 1$ (this corresponds to a situation in which electrons are degenerate

and holes are not). In this case, the integral can be taken analytically:

$$I_1 = T^2(1+M)^2 \exp(-\tilde{F}_e)\left[(1+M) + \frac{E_0}{T}\right] \qquad (13)$$

$$\approx TE_0(1+M)\exp(-\tilde{F}_e).$$

Here, we take into account that $E_0/T \gg (1+M)$ in the temperature range under consideration. If we take into account (13), expression (11) also yields a linear temperature dependence of the threshold current.

4.2. Auger Recombination

The expression for the rate of Auger recombination has the form

$$R_A = C_{\text{CHCC}} n^2 p + C_{\text{CHHS}} n p^2, \qquad (14)$$

where the subscripts CHCC and CHHS refer to recombination involving an electron and a heavy hole, with the energy transferred to, respectively, an electron or a heavy hole that passes into a split-off band. Expressions for C_{CHCC} and C_{CHHS} were reported in [11–14]. Here, we emphasize that, in the case of relatively narrow QWs, both Auger recombination coefficients show a weak, rather than exponential, temperature dependence; therefore, it should be expected, taking into account (8), that the corresponding threshold current shows a power-law dependence on temperature in the form T^β, where β is close to 3.

4.3. Monomolecular Recombination

At low temperatures (i.e., at low threshold concentrations), recombination should be strongly affected by irradiative recombination via local centers. In this case, the type of temperature dependence of J_{th} can be determined as follows. Let us write the expression for the current resulting from monomolecular recombination in terms of the carrier lifetime τ:

$$J_{\text{th}} = \frac{e n_{\text{th}}}{\tau}. \qquad (15)$$

It was shown in [15] that, in the case of a cascade mechanism of carrier capture in 2D systems, the time of capture by attracting centers changes from $\tau \propto T^3$ at $T > T_0$ to $\tau = \text{const}(T)$ at $T < T_0$, where T_0 is a certain characteristic temperature estimated, in the case under consideration, to fall within the range 20–60 K. It is clear that we have, in this transition region, a certain intermediate dependence and, taking into account the temperature dependence of n_{th}, which is again defined by expression (8), we find that J_{th} may be temperature-independent or even increase as the temperature is lowered. Consequently, this mechanism may also be important for the temperature dependence of J_{th} at low temperatures.

5. DISCUSSION OF RESULTS

Figure 2 shows a theoretical curve for sample no. 4 that was calculated using expression (11) for the threshold current governed by radiative recombination (curve *2*). The structure parameters were taken from [16]. The best agreement between the theoretical and experimental results was obtained at a value of the overlap integral I_{cv} equal to 0.73, which is quite reasonable. The calculated curve describes the experimental dependence at temperatures exceeding 70 K well.

At temperatures close to liquid-helium temperature, J_{th} tends to a constant value. In [17], the assumption was made that one of the reasons for such behavior is recombination of electrons and holes via the density-of-states tails of the conduction and valence bands. However, the possible degree of disorder for the structures studied, which could give rise to density-of-states tails, is low. At the same time, recombination processes should be strongly affected at low temperatures by nonradiative recombination via local centers. As the temperature dependence of the threshold concentration $n_{th}(T)$ is known and described by (8) at any temperature, we can determine the type of temperature dependence of the carrier lifetime, corresponding to experimentally observed $J_{th}(T)$, by fitting the calculated temperature dependence of the current generated by monomolecular recombination to the experimental dependence. For sample no. 4, it has the form

$$\tau = (1.07 \times 10^{-11} T - 3.22 \times 10^{-14} T^2), \qquad (16)$$

where τ is given in seconds and T is in degrees Kelvin. The corresponding threshold current is represented by curve *1* in Fig. 2. This expression for the temperature dependence of the time of monomolecular recombination is valid in the temperature range $4.2 \leq T \leq 60$ K.

Deviations from the linear dependence $J_{th}(T)$ for sample nos. 1 and 3 at $T > 170$ K may be due to the initiation of nonradiative Auger recombination mechanisms. For example, for long-wavelength lasers ($\lambda \approx 15$ μm), the key role is played by Auger recombination processes at room temperature [11]. As was demonstrated in [14], Auger recombination in QW structures is a zero-threshold process that largely depends on the number of heterointerfaces in a structure, i.e., on the number of QWs. Comparison of the data in the table and Fig. 1 shows that a deviation from linearity is observed for the dependence J_{th} in samples with two QWs, whereas the structure with a single QW exhibits linear behavior of $J_{th}(T)$ up to room temperature. In addition, approximation of the experimental curve for $J_{th}(T)$ for sample nos. 1 and 3 at $T > 170$ K with the dependence $J_{th}(T) = \alpha T^\beta$ gives a value $\beta \approx 2.7$, which, as was mentioned in the preceding section, is close to the theoretically predicted value $\beta = 3$. These facts indicate that Auger recombination predominates at $T > 170$ K. A detailed analysis of the behavior of J_{th} for this temperature range will be given elsewhere. Here, we focus our attention on those fundamental recombination mechanisms that
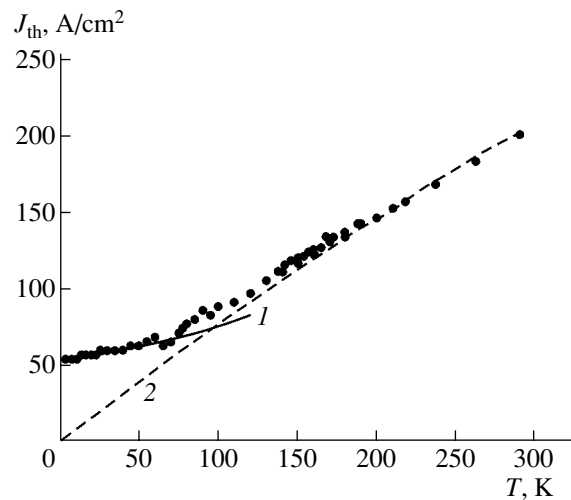

Fig. 2. Experimental (points) and calculated (lines) temperature dependences of the threshold current density for sample no. 4: (*1*) calculation by (15) and (16); (*2*) calculation by (11).

make a major contribution to the threshold current in the semiconductor QW lasers under consideration.

6. CONCLUSION

The temperature dependences of the threshold current density were studied in the range $T = 4$–300 K. The analysis performed demonstrated that the threshold current density is determined in different portions of the dependence by different recombination mechanisms. For example, the main contribution to the threshold current at low temperatures is made by monomolecular recombination (the Shockley–Read mechanism). At $T > 77$ K, the threshold is determined by radiative recombination. At higher temperatures, close to room temperature, a contribution to the threshold current is also made by Auger recombination.

7. ACKNOWLEDGMENTS

REFERENCES

1. D. Z. Garbuzov, A. V. Chudinov, V. V. Agaev, *et al.*, Fiz. Tekh. Poluprovodn. (Leningrad) **18**, 102 (1984) [Sov. Phys. Semicond. **18**, 61 (1984)]; D. Z. Garbuzov, V. V. Agaev, Z. N. Sokolova, *et al.*, Fiz. Tekh. Poluprovodn. (Leningrad) **18**, 1069 (1984) [Sov. Phys. Semicond. **18**, 665 (1984)]; I. S. Tarasov, D. Z. Garbuzov, V. P. Evtikhiev, *et al.*, Fiz. Tekh. Poluprovodn. (Leningrad) **19**, 1496 (1985) [Sov. Phys. Semicond. **19**, 920 (1985)].

2. H. C. Casey, Jr. and M. B. Panish, *Heterostructure Lasers* (Academic, New York, 1978; Mir, Moscow, 1981), Vol. 1.

3. G. P. Aggrawal and N. X. Dutta, *Long-Wavelength Semiconductor Lasers* (Van Nostrand Reinhold, New York, 1986), Chaps. 3, 9.

4. V. P. Duraev and G. I. Ryabtsev, Obz. Élektron. Tekh., Ser. 2: Lazer. Tekh. Optoélektron., No. 5[1376], 1 (1988).

5. B. Zhao, T. R. Chen, L. E. Eng, *et al.*, Appl. Phys. Lett. **65**, 1805 (1994).

6. K. D. Moiseev, M. P. Mikhaĭlova, O. G. Ershov, and Yu. P. Yakovlev, Pis'ma Zh. Tekh. Fiz. **24** (4), 55 (1997) [Tech. Phys. Lett. **23**, 151 (1997)].

7. E. G. Golikova, V. A. Kureshov, A. Yu. Leshko, *et al.*, Fiz. Tekh. Poluprovodn. (St. Petersburg) **34**, 886 (2000) [Semiconductors **34**, 853 (2000)].

8. N. A. Pikhtin, S. O. Slipchenko, Z. N. Sokolova, and I. S. Tarasov, Fiz. Tekh. Poluprovodn. (St. Petersburg) **36**, 364 (2002) [Semiconductors **36**, 344 (2002)].

9. G. G. Zegrya, A. D. Andreev, N. A. Gun'ko, and E. V. Frolushkina, Proc. SPIE **2399**, 307 (1995).

10. B. L. Gel'mont and G. G. Zegrya, Fiz. Tekh. Poluprovodn. (Leningrad) **25**, 2019 (1991) [Sov. Phys. Semicond. **25**, 1216 (1991)].

11. L. E. Vorob'ev, S. N. Danilov, G. G. Zegrya, *et al.*, in *Photoelectric Phenomena in Semiconductors and Quantum-Dimensional Structures*, Ed. by V. I. Il'in and A. Ya. Shik (Nauka, St. Petersburg, 2001), Chaps. 6, 7 [in Russian].

12. L. V. Asryan, N. A. Cun'ko, A. S. Polkovnikov, *et al.*, Semicond. Sci. Technol. **15**, 1131 (2000).

13. L. V. Asryan, N. A. Gun'ko, A. S. Polkovnikov, *et al.*, Semicond. Sci. Technol. **14**, 1069 (1999).

14. G. G. Zegrya and A. S. Polkovnikov, Zh. Éksp. Teor. Fiz. **113**, 1491 (1998) [JETP **86**, 815 (1998)].

15. V. Karpus, Fiz. Tekh. Poluprovodn. (Leningrad) **20**, 559 (1986) [Sov. Phys. Semicond. **20**, 353 (1986)].

16. *Handbook Series on Semiconductor Parameters*, Ed. by M. Levinshtein, S. Rumyantsev, and M. Shur (World Sci., Singapore, 1999), Vol. 2.

17. V. P. Gribkovskiĭ, *The Theory of Emission and Absorption of Light in Semiconductors* (Nauka i Tekhnika, Minsk, 1975) [in Russian].

Translated by M. Tagirdzhanov

===== **PHYSICS OF SEMICONDUCTOR DEVICES** =====

Mid- and Far-IR Focal Plane Arrays Based on $Hg_{1-x}Cd_x$Te Photodiodes

V. I. Stafeev^, K. O. Boltar', I. D. Burlakov, V. M. Akimov, E. A. Klimanov, L. D. Saginov, V. N. Solyakov, N. G. Mansvetov, V. P. Ponomarenko, A. A. Timofeev, and A. M. Filachev

ORION RD&P Center, State Scientific Center of the Russian Federation, Moscow, 111123 Russia
^e-mail: root@orion.extech.ru
Submitted November 2, 2004; accepted for publication January 13, 2005

Abstract—This review presents the results of the research and development work carried out at the ORION RD&P Center (Federal State Unitary Enterprise) on HgCdTe photodiodes and focal plane arrays based on solid solutions of mercury and cadmium tellurides for the 3–5 and 8–12 μm spectral ranges. The structure, topology, and parameters of the photodiodes and staring and time-delay-integration focal plane arrays, as well as the structure and circuitry of silicon multiplexers developed for the focal plane arrays, are discussed. The parameters of photodiode arrays of various formats and of a prototype thermal imager based on a 128×128 staring focal plane array are presented. © 2005 Pleiades Publishing, Inc.

The overwhelming majority of modern IR optoelectronic devices use photodetectors based on a mercury cadmium telluride (MCT) solid solution in spite of the complicated technology and high price of this material. The main reasons are the following unique physical properties of $Hg_{1-x}Cd_x$Te [1–5]:

(i) MCT possessing optimal characteristics for the detection of IR radiation within the main spectral windows of the Earth's atmosphere can be obtained by simply varying the relative content of Hg and Cd in the solid solution: the range 1–2.5 μm at $x \approx 0.4$, 3–5 μm at $x \approx 0.3$, and 8–12 μm at $x \approx 0.2$ (Fig. 1).

(ii) MCT detectors for all the spectral ranges can be fabricated using the same planar technology.

(iii) MCT can be produced both as an *n*-type material with a low carrier density and as a *p*-type material with high structural perfection. This circumstance

makes it possible to produce high-performance photoresistors for a range up to 15 μm, as well as high-speed photodiodes.

(iv) MCT-based transistors can be created [6, 7].

(v) MCT can be grown in the form of both single crystals and thin epitaxial layers on substrates that are transparent in the desired spectral range, which makes it possible to form large focal plane diode arrays.
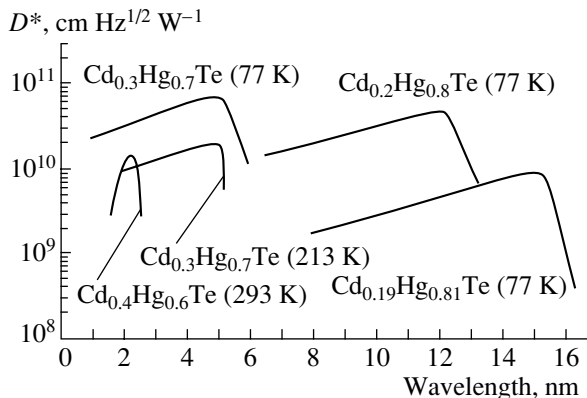

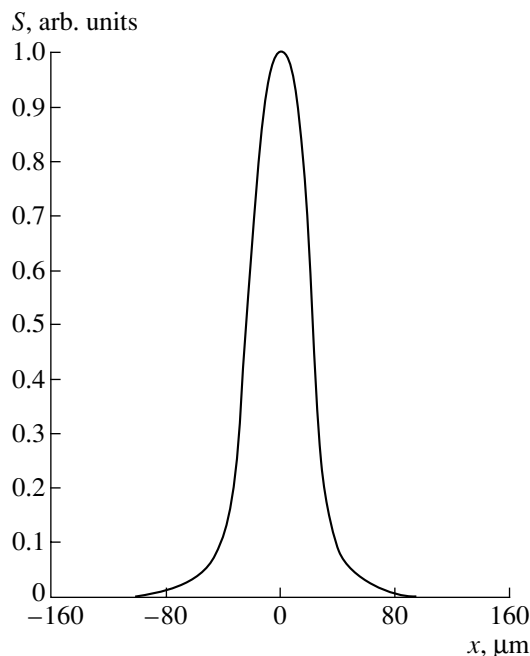**Fig. 1.** Spectra of the detectivity of MCT photodetectors.

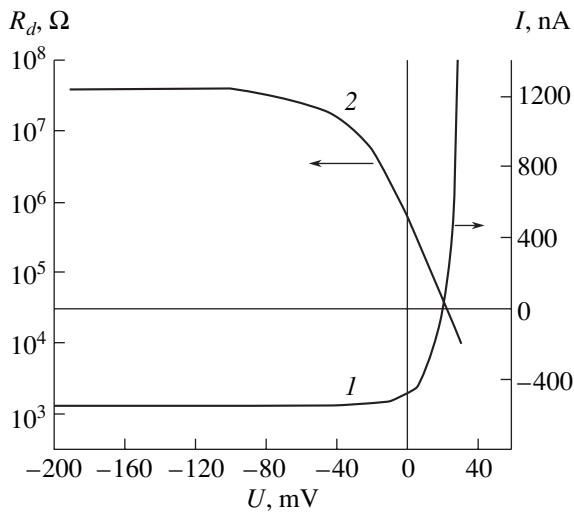**Fig. 2.** Distribution of the photosensitivity of an MCT photodiode.

Fig. 3. (*1*) Current–voltage characteristic and (*2*) differential resistance R_d of a photodiode fabricated from bulk MCT single crystal.
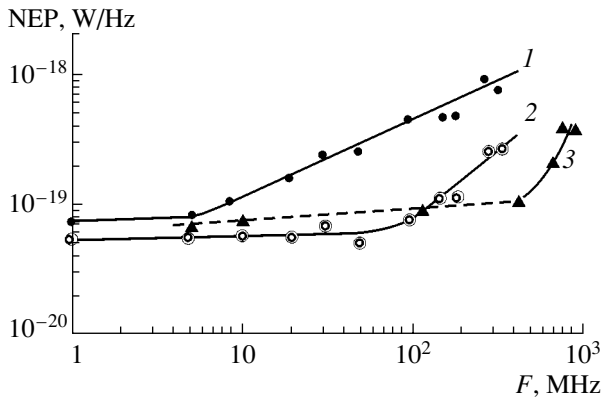

Fig. 4. Frequency characteristics of photodiodes in the heterodyne mode. Heterodyne emission power P_b: (*1*, *2*) 0.5 and (*3*) 1 mW. Photodiode current I: (*1*) 0.5; (*2*) 5; and (*3*) 10 mA.

(vi) Owing to the high density of structural defects, MCT photodetectors are much more resistant to penetrating radiation than devices based on InSb, Si, and other semiconductors.

The diodes were developed on the basis of p-MCT with a hole density of about 10^{16} cm^{-3} by either implantation of ~160-keV boron ions or double-charged Al or by treatment in Ar plasma with an ion energy on the order of several hundreds of electronvolts [4, 5]. In the latter case, microscopic regions of MCT are fused under the impact of the Ar ions. This process results in a sharp increase in the local concentration of "free" Hg atoms, which quickly diffuse via interstices into the crystal bulk and compensate the existing vacancies. Under fast cooling, the introduced excess of interstitial Hg leads to inversion of the conduction type [8].
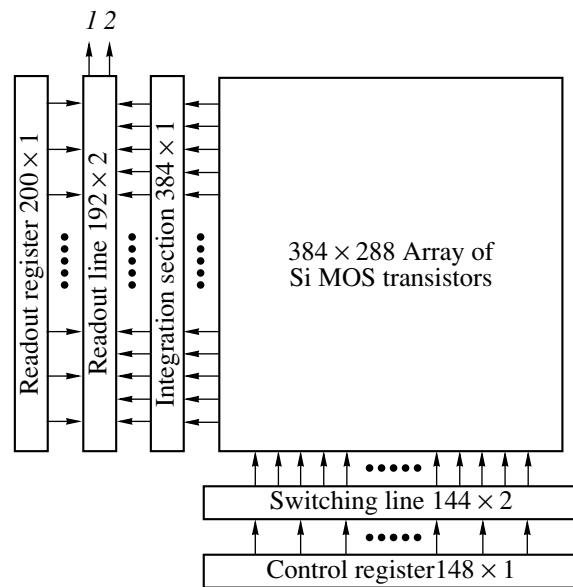

Fig. 5. Block diagram of a Si MOS multiplexer.

At liquid-nitrogen temperature, the electron mobility in MCT is high, $(3–5) \times 10^5$ cm^2/(V s), so the diffusion length can reach several hundred micrometers. When a forward current is passed through a diode, minority carriers injected from the p–n junction are transferred a rather long distance. These carriers are generated in an n^+-type region, and the absorption of an energy slightly exceeding the band gap occurs; this energy is then released in the recombination taking place at the second contact. Therefore, the n^+-type region is cooled, and the region of the second contact is heated. This injection-related heat transport was predicted by one of the authors in 1960 [9]. This effect was discovered and studied experimentally in 1974 [10], in which case additional cooling to 5 K below liquid-nitrogen temperature was obtained.

Schottky diodes were also produced. In order to improve the quality of the interface between the metal and semiconductor, a tunnel-transparent 3- to 5-nm-thick dielectric Al_2O_3 layer was deposited [6, 7]. In this structure, the density of surface states near the midgap was $(2–3) \times 10^{11}$ cm^{-2} eV^{-1}, the density of slow surface states was $\sim10^{10}$ cm^{-2}, and the density of the built-in positive charge was $\sim(3–5) \times 10^{10}$ cm^{-2} [7].

The photodiodes in focal plane arrays and in photodetectors with a small number of elements had p–n junctions ranging in size from 15×15 to 300×300 μm, and, in single-element detectors, they were as large as 2×2 mm or even more. The effective area of a photosensitive element exceeds that of a p–n junction because the carriers generated by light are collected by the p–n junction from within an adjacent region limited by the diffusion length or by the distance to the second contact. Figure 2 shows a typical distribution for the diode photosensitiv-
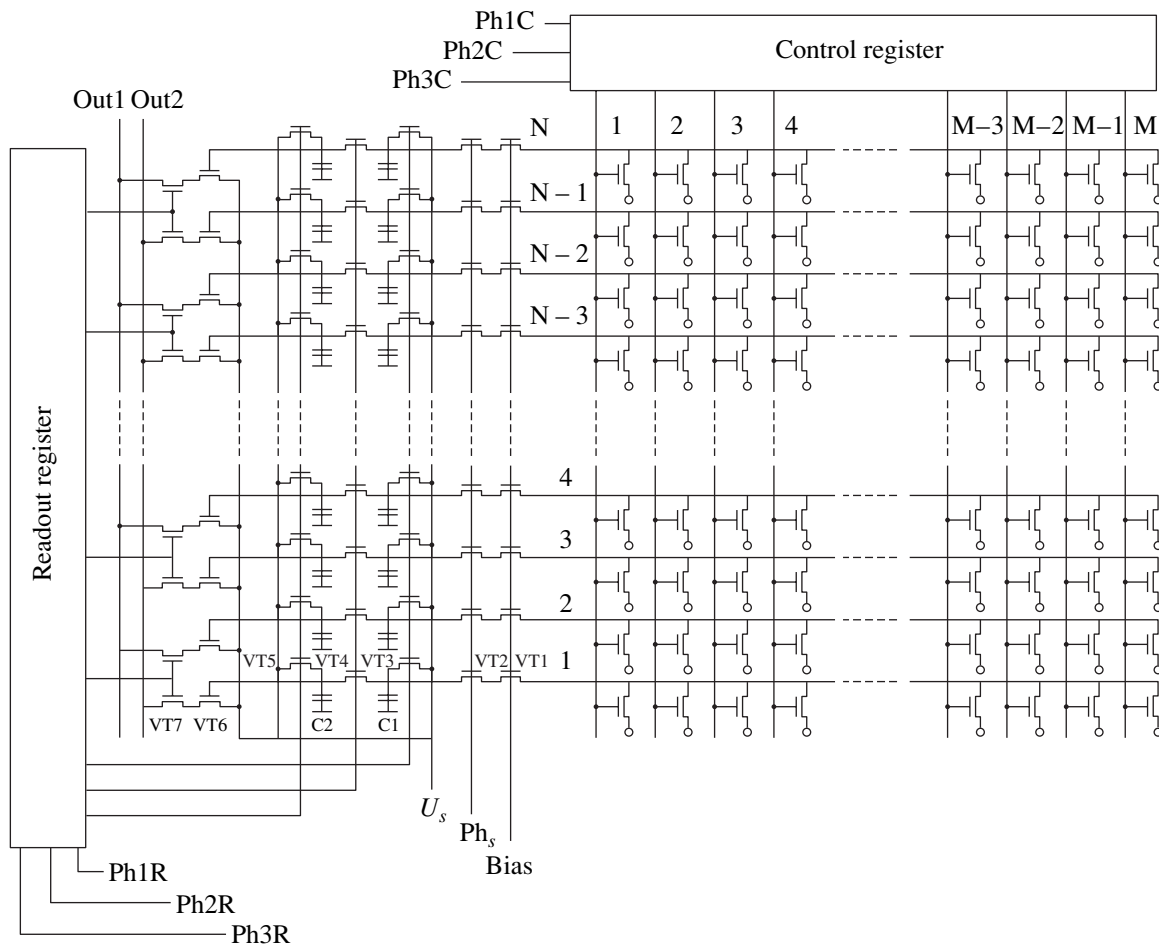
Fig. 6. Electric circuit of a MOS multiplexer. Ph1C–Ph3C represent the control phases; Ph1R–Ph3R, the readout phases; and Ph$_s$, the store phase.

ity. For a p–n junction ~20 μm in size, the real size of the photosensitive area at a 0.5 level is 35–40 μm [11].

The detectivity D^* and the current photosensitivity S_i are somewhat higher and the reverse current is smaller in photodiodes produced in LPE-grown MCT layers, as compared with diodes fabricated in layers grown by other epitaxial techniques [12].

Figure 1 shows the detectivity spectra of MCT detectors. Figure 3 shows the current–voltage characteristic of a photodiode fabricated on bulk MCT single crystal. The operation speed of the photodiodes reaches several tens of megahertz in the direct detection mode and 1 GHz in the heterodyne mode. At liquid-nitrogen temperature, the noise equivalent power (NEP) at a 10.6-μm wavelength is below 10^{-19} W/Hz [4, 5, 13]. Figure 4 shows the frequency characteristics of photodiodes in the heterodyne mode.

The currently existing concepts concerning the instability of MCT and devices based on MCT (see, e.g., [14]) are associated, in our opinion, with the insta-

Table 1

Number of elements	Format	Element dimensions, μm	Pitch, μm	λ_{co}, μm	Field of view	$D^*_{\lambda max}$, cm W^{-1} Hz$^{1/2}$
32×32	$N \times N$	40×40	70	10.5–11.5	60°	$(3–4) \times 10^{10}$
128×128	$N \times N$	30×30	35	10.5–11.5	60°	$(4–5) \times 10^{10}$
384×288	$M \times N$	25×25	28	10.3–11.2	60°	$(3–4) \times 10^{10}$
256×256	$N \times N$	25×25	30	10.8	>40°	4×10^{10}

Note: λ_{co} is the cutoff wavelength, and $D^*_{\lambda max}$ is the detectivity at the maximum spectral sensitivity.

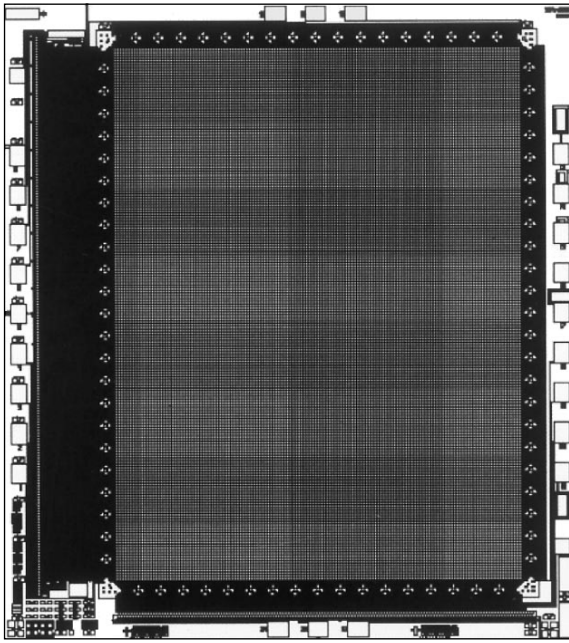**Fig. 7.** Topology of a 384 × 288 MOS multiplexer with an FPA element pitch of 28 μm.
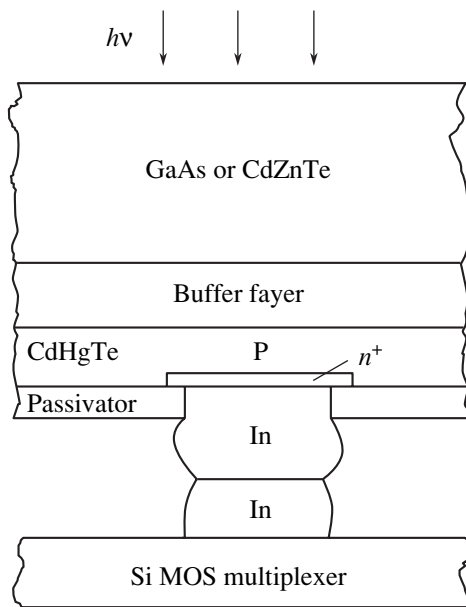

Fig. 8. Structure of a photosensitive element.

bility of the sample surface, caused by its poor pretreatment and protection. The techniques developed by the authors for pretreatment of the MCT surface and deposition of a protective dielectric coating provided for the fabrication of high-stability temperature-resistant photodiodes. A prolonged (up to 10 years) storage at temperatures up to 80°C did not impair the photodiode parameters. The admissible temperature of long-term storage is +70°C [15, 16]. These data have been con-

firmed by recent studies [17] performed at the Institute of Semiconductor Physics, Siberian Division, Russian Academy of Sciences.

Focal plane arrays (FPAs) based on MCT best satisfy the requirements of modern thermal imaging instruments as regards radically decreasing their weight and size, increasing the range of vision, etc. Two-dimensional FPAs are designed in a configuration with $M \times N$ elements, where M and N are the number of elements in the rows and columns, respectively. Two types of FPAs have been developed: staring and time-delay-integration (TDI) types.

Staring FPAs contain tens or hundreds of thousands of elements, and, usually, $M \geq N$. Systems for the IR range containing staring FPAs for obtaining thermal images of objects do not require mechanooptical scanning, which simplifies a thermal imager and reduces its price.

Multiple-row TDI FPAs are intended for systems using time delay and integration of photosignals. The time-delay-integration mode consists in the integration (accumulation) of signals from all the M elements in each row, with the delay in the readout of signals from each element in the row synchronized with the speed of the image scanning along this row. The extension of a thermal imaging system by introduction of a mechanooptical scanning device is rewarded by an increase in the signal-to-noise ratio by a factor of $M^{1/2}$, since the signal is multiplied by M and the noise, by $M^{1/2}$. Additionally, M-fold redundancy improves the temporal stability and reliability of the FPA.

FPAs include an array of MCT photodetectors and Si integrated circuits (ICs), which are placed in the focal plane of an evacuated case, for readout and front-end processing of a photosignal. The case serves as device protection and connection with the system for cooling to the necessary operation temperature.

Arrays of photosensitive elements were fabricated on the basis of p-type epitaxial MCT layers with a hole density of about 10^{16} cm^{-3}, in which photodiode arrays were formed using a planar batch process. Epitaxial layers were grown by different techniques: an LPE layer of ~15 μm in thickness was grown on a $Cd_{0.96}Zn_{0.04}Te$ substrate (developed by "Giredmet" Federal State Unitary Enterprise); a 7- to 10-μm MBE layer was grown on a GaAs substrate possessing a CdZnTe sublayer (developed by the Institute of Semiconductor Physics, Siberian Division, Russian Academy of Sciences), or an MOCVD epitaxial layer was grown on a GaAs substrate possessing a CdZnTe sublayer (developed by the Institute of Chemistry of High-Purity Substances, Russian Academy of Sciences, and Lobachevski State University, Nizhni Novgorod).

The MCT surface was protected with a dielectric layer. p–n junctions were formed in the windows of the protective passivating layer, and ohmic contacts to the p-type layer common to all the diodes were fabricated on the peripheral areas of the epitaxial layer that were
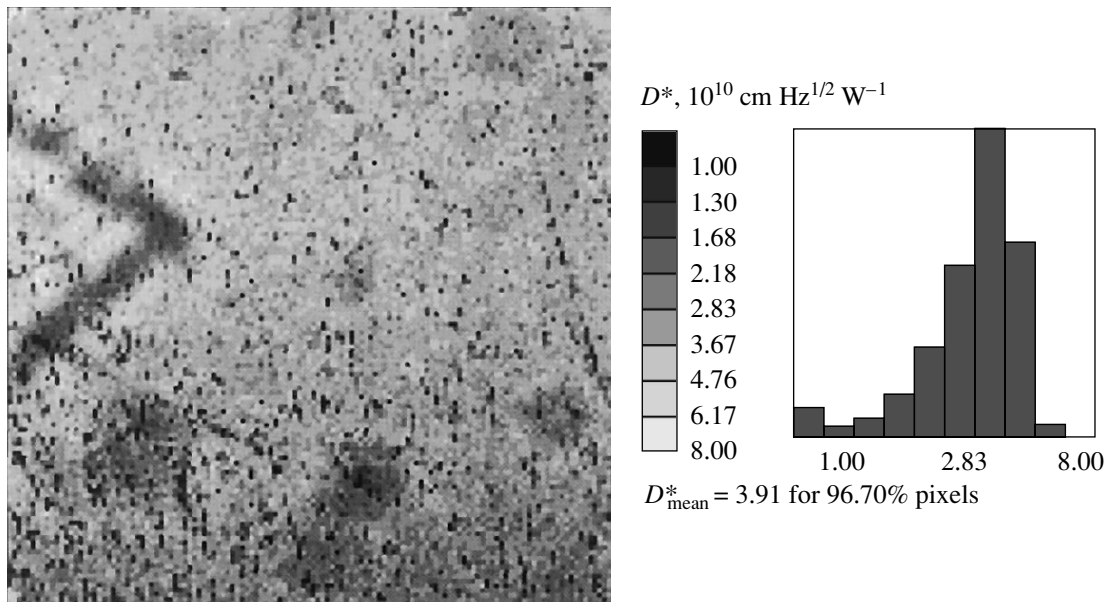
Fig. 9. Histogram of the distribution of the detectivity D^* for a 128×128 FPA.

free of p–n junctions. Indium bump microcontacts to the n-type region of the diodes were fabricated with a 20×20 μm base and height of ~12 μm. They provided a connection to the similar microcontacts of the arrays formed on a sapphire substrate or on a Si MOS multiplexer IC. Mechanical and electrical bonding of the indium microcontacts were performed using the flip-chip technique. Several thousand In microcontacts were aligned on the photodiode array and the Si crystal of the IC using a specially developed IR microscope, with the microcontacts being joined and visualized through the Si crystal of the IC.

An important parameter of an FPA is the element crosstalk. A strong crosstalk may lead to significant smearing of the thermal image. Three types of crosstalk are possible: optical, electric, and photoelectric. Optical crosstalk is defined by the quality of the optical path of a thermal imaging device. Photoelectric crosstalk is related to diffusion of photogenerated carriers within the common semiconductor layer of the photodiode array. Electric crosstalk is defined by the voltage drop in the charge transport from the p–n junctions to inactive contacts and by the coupling between the input channels of the cooled silicon IC.

In order to monitor the crosstalk between the elements in the working mode of an FPA, the spot of the optical probe or a band of IR light formed by an optical slit is focused onto an element of the array and the signal from neighboring elements is measured. As the optical probe is shifted across the illuminated element, the effective size of the photosensitive area is measured from the dependence of the photosignal on the beam coordinate (Fig. 2). In the wavelength range 2–14 μm, the width of the optical probe at a 0.5 level was about

15 μm and the minimum displacement was 3 μm. For a p–n junction area of 20×20 μm and pitch of 35 μm, the crosstalk in an FPA, determined by processing the photosignal, was within 5% [11]. The presence of an additional layer with an inverse type of conduction on the MCT surface can enhance the electric coupling.

Silicon ICs for readout and preprocessing of photosignals can be fabricated by MOS or complementary MOS (CMOS) technology, which are more promising than CCD (charge-coupled device) technology. This approach yields a higher capacitance of MOS integration capacitors, which is important for wavelengths longer than 5 μm, at which the background illumination is strong. Furthermore, a higher coefficient of filling of the cell area by the integration capacitor, denser packing, higher and more uniform electrical parameters at 77 K, lower control voltage, and wider dynamic range are reached.

In the developed FPAs, an Si MOS multiplexer is responsible for the integration of signals from separate photodiodes on the corresponding capacitors, amplification, parallel transfer of the accumulated charge from integration capacitors to storage capacitors, and successive readout of information from hold capacitors to outputs from the cold zone for further processing. Figure 5 shows a block diagram of a Si MOS multiplexer. Thus, accumulation and readout of information are spatially separated. Two-phase dynamic shift registers are used in the multiplexers. The photocurrent input in the multiplexers is attained by direct injection. The coefficient of current transfer to the integration capacitors is over 0.95, with the noise characteristics of a photodiode remaining satisfactory even under rather lax requirements on the noise level of the input transistor (up to
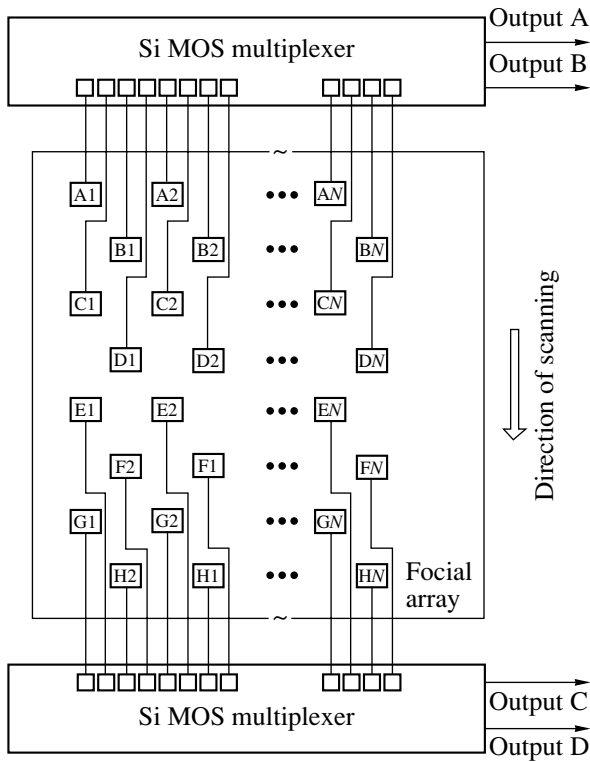
Fig. 10. Block diagram of a cooled 2 × 256 unit.

Fig. 11. Block diagram of a 4 × 288 FPA.

100 nV/Hz$^{1/2}$). A multiplexer IC contains a comparatively small number of elements, it does not consume power during the integration cycle, and provides good control of the voltage applied to the photodiodes. Similar multiplexers are used both in TDI FPAs and in staring FPAs with the due regard for their specific features [18, 19]. Figure 6 shows the electric circuit of a MOS multiplexer. The topology of a 384 × 288 multiplexer with a 28-μm pitch is shown in Fig. 7.

The multiplexers were fabricated by *n*-channel technology and had polysilicon gates and a thickness of the subgate insulator equal to ~50 nm. Polysilicon was also used in the first-level wiring. For insulation of the elements, either local oxidation of silicon (LOCOS) technology or p^+-type stop-diffusion regions was used. The source–drain regions were formed by implantation of phosphorus or arsenic ions at a dose of 400 μC. The threshold voltage of the channel region was adjusted by
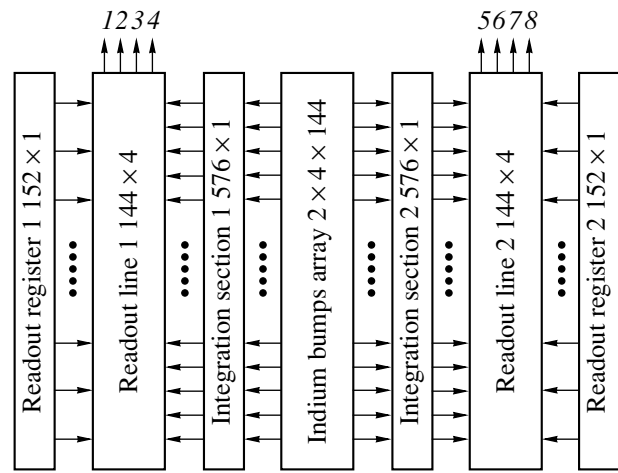
boron ion doping at a dose up to 0.05 μC. The interlayer insulation and surface planarization were achieved using deposition of a 0.45-μm-thick SiO_2 layer by decomposition of tetraethoxysilane.

Studies of the spectral density of the noise of input transistors operating in the subthreshold mode at 77 and 300 K have shown that, at low frequencies, the noise may increase by a factor of 1.5–2. The level of this noise was reduced by fabrication of dielectric layers and annealing of the ion-implanted regions at temperatures no higher than 950°C.

Staring FPAs for the spectral ranges 3–5 and 8–12 μm have been developed in formats of 32 × 32, 128 × 128, and 384 × 288 elements [12, 20, 21]. Figure 8 shows the structure of a photosensitive element for the example of an element of a 384 × 288 FPA with a 28-μm pitch and *p–n* junction area of $16 × 16$ μm^2. The incident radiation falls through the epitaxial layer substrate, which is transparent and antireflection-coated in the required spectral range, and then enters the active photosensitive MCT layer. The array of photosensitive elements is connected by indium microcontacts with the Si multiplexer IC. The height of the In contacts on both crystals is ~12 μm, and their area is 20 × 20 μm. The thus hybridized assembly is cemented, with the Si microchip side, onto the surface of the supporting sapphire substrate. Photosignal readout, feeding, and con-

Table 2

Number of elements	Format	Element dimensions, μm	Pitch, μm	λ_{co}, μm	Field of view	$D^*_{\lambda\max}$, cm W^{-1} Hz$^{1/2}$
4 × 48	4 × *N*	30 × 30	60	≥10.5	30°	≥7 × 10^{10}
2 × 96	2 × 2*N*	30 × 30	60	≥10.5	30°	≥5 × 10^{10}
2 × 256	2 × 2*N*	35 × 35	70	≥10.5	≥32°	≥5 × 10^{10}
4 × 288	4 × *N*	28 × 28	56	≥10.5	≥32°	≥10^{11}

D^*, cm Hz$^{1/2}$/W
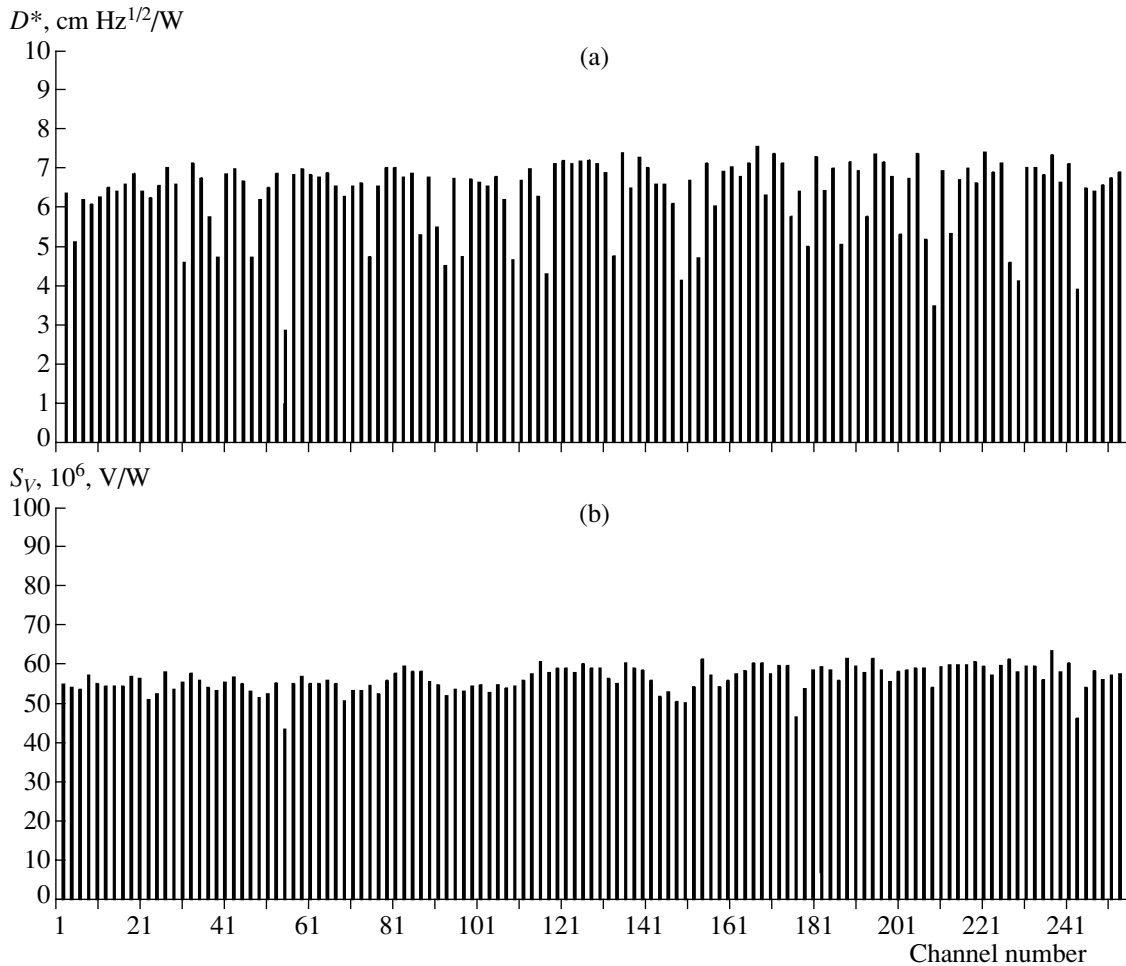
(a)

S_V, 10^6, V/W

(b)

Channel number

Fig. 12. Distribution of the (a) detectivity and (b) voltage sensitivity of a 2×256 FPA at a photocurrent integration time of 25 μs.

trol leads are wire-bonded to contact pads on the substrate. The cooling diaphragm and heat sensors are mounted on the same substrate. The obtained photoreceiver unit is mounted onto its place in the evacuated cryostated case. The heat emission from the unit does not exceed 60 mW. The total number of signal, control, and auxiliary leads is 24. Photosignals are output via two channels.

The detectivity D^* and voltage photosensitivity S_V of the developed and studied FPAs based on LPE-grown MCT epitaxial layers are higher than in FPAs based on layers produced by other epitaxial techniques. However, FPAs based on MBE-grown layers demonstrate more uniform characteristics. The main parameters of the developed staring FPAs are listed in Table 1.

Figure 9 shows a histogram of the distribution of the detectivity D^* over elements of a 128×128 FPA, which was recorded under a 50-mV reverse bias on the photodiodes, 60-μs integration time, and 60° field of view.

TDI FPAs for the spectral range 8–12 μm are developed in formats of 4×48, 2×96, 2×256, and 4×288 elements [22, 23]. The pitch along and across the strips

is 70 μm for each topology. The formats 4×48 and 4×128, in combination with a regular pattern of photodiodes, are destined for TID over 4 elements; in the case of integration over 2 elements, 2×96 and 2×256 formats with a staggered pattern are used. In a 4×288 FPA with a staggered pattern of photosensitive elements, the pitch along the scanning direction is 42 μm, and, in the reverse direction, it is 56 μm. The Si IC contains two mirror-positioned 4×144 MOS multiplexers with a channel pitch of 14 μm. The FPA has eight information outputs, four on each side.

Each photodiode is connected by In microcontact, via an intermediate contact grid on the sapphire substrate, to its cell in the Si multiplexers located on the same substrate. Signals are output via two channels on each side in the (4×48)–(2×256) FPAs and via four channels in the 4×288 FPA. The signals are transmitted to Si multiplexers, which are also connected via In microcontacts.

Figure 10 shows the topology of photosensitive elements in a cooled 2×256 FPA unit, and Fig. 11 shows the structure of a 4×288 FPA unit. Figures 12a and
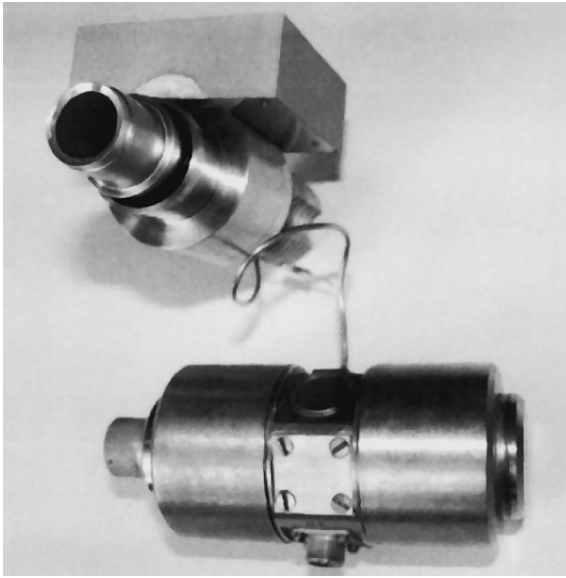
Fig. 13. 384×288 FPA with a microcryogenic cooler system.

Fig. 14. A thermal image.

12b, respectively, show the distributions of detectivity and voltage sensitivity of a 2×256 FPA at the photocurrent integration time of 25 μs. General parameters of the developed TID FPAs are listed in Table 2.

Processes in a large-scale IC (LSIC) are controlled by the multiplexer circuit. Signals from each strip of photosensitive elements are successively transmitted to an FPA output. The processes in the LSIC are maintained with four clock signals and four supply voltages, two of which bias the photodiodes and must have a low ripple. Silicon LSICs provide a speed of information output up to 10 MHz. The heat emission in the cooled FPA unit does not exceed 60 mW.

The FPA design is based on an evacuated cryostated case, which is connected to a microcryogenic cooler operating according to the Stirling cycle or to a throttled cooling system using the Joule–Thompson cycle (both developed at Cryogenic Engineering Scientific and Technological Open Joint-Stock Corp., Omsk, Russia). The heat inflow of the design is ~0.4 W. The incident light arrives at the array of photosensitive elements through a sapphire (for the 1–5 μm range) or germanium (8–12 μm) window with an antireflection coating. A getter, maintaining the necessary vacuum during the shelf life of the devices (up to 10 years), is mounted within the case. The cooled photodetector unit contains two Si-diode temperature sensors, one of which is used in the feedback circuit of the control unit of the microcryogenic cooler system while the other monitors the operation temperature. The temperature of ~80 K is maintained within 0.1 K. Figure 13 shows the outward appearance of a 384×288 FPA with a microcryogenic cooler.

The photodetector unit forms the standard TV output signal. The developed unit comprises an FPA, an interface subunit, and subunits for analog-to-digital conversion (ADC), digital processing, and a secondary power supply. The ADC subunit subtracts the dc component of the photosignals related to background irradiation, compensates for the scatter of the voltage sensitivity of the photosensitive elements via a two-point correction, performs interpolation or replaces defective or "inactive" elements, forms control and special marks, imparts (when necessary) pseudocolors to a thermal image, etc. For TID FPAs, the subunit also provides time delay and integration of signals, spatial superposition of even and odd lines in the staggered pattern and lines in the direct and reverse scanning, joining of scanning zones, etc. The unit can also include microcryogenic cooler system and calibration devices.

A thermal imager with a staring FPA for the 8−12 μm range is based on a 128×128 FPA [24]. The thermal imager includes an FPA, a Stirling cycle microcryogenic cooler system, interface units, ADC and digital processing units, an IR lens system with a focal length of 70 mm and aperture ratio 1 : 1.5, a case, and a display.

The average detectivity of the FPA used in the thermal imager is 4.5×10^{10} cm W^{-1} $\text{Hz}^{1/2}$. The interface unit controls the FPA operation, i.e., forms feeding voltages and clock pulses, amplifies the signals (two channels), and reduces them to the admissible input range of ADCs. The subunit for ADC and digital processing, developed in cooperation with the Siberian Research Institute of Optical Systems, Novosibirsk, Russia, performs analog-to-digital conversion of photosignals, corrects the scatter in the photosensitivity, eliminates defective or inactive elements in the thermal image, and forms a standard TV output signal. The noise-equivalent temperature difference ΔT at a zero spatial frequency is below 40 mK. Figure 14 shows a

thermal image obtained using this instrument. The thermal imager can be used in the detection and identification of heat leakages in heating systems, living and production areas, and for medical purposes, as well as in a wide range of industrial and specialized applications.

REFERENCES

1. V. I. Stafeev, Proc. SPIE **4340**, 240 (2000).

2. V. T. Khrypov, V. P. Ponomarenko, V. G. Butkevich, *et al.*, Opt. Eng. **31**, 678 (1992).

3. V. P. Ponomarenko and A. M. Filachev, Prikl. Fiz., No. 1, 13 (2002).

4. L. A. Bovina and V. I. Stafeev, Proc. SPIE **3819**, 37 (1998).

5. L. A. Bovina and V. I. Stafeev, Prikl. Fiz., No. 2, 58 (1999).

6. E. A. Salmin, V. P. Ponomarenko, and V. I. Stafeev, Fiz. Tekh. Poluprovodn. (Leningrad) **22**, 1142 (1988) [Sov. Phys. Semicond. **22**, 722 (1988)].

7. E. A. Salmin, I. V. Shimansky, Y. P. Ponomarenko, and V. I. Stafeev, Acta Phys. Pol. A **77**, 237 (1990).

8. V. V. Bogoboyashchiĭ and I. I. Izhnin, Izv. Vyssh. Uchebn. Zaved., Fiz., No. 8, 16 (2000).

9. V. I. Stafeev, Fiz. Tverd. Tela (Leningrad) **2**, 488 (1960) [Sov. Phys. Solid State **2**, 454 (1960)].

10. V. P. Ponomarenko and V. I. Stafeev, Tr. Mosk. Fiz.–Tekh. Inst., Ser.: Radiotekh. Élektron. **7**, 57 (1974).

11. K. O. Boltar and N. I. Iakovleva, Proc. SPIE **3819**, 40 (1999).

12. L. A. Bovina, K. O. Boltar', I. D. Burlakov, *et al.*, Prikl. Fiz., No. 3, 32 (1999).

13. L. A. Bovina, V. P. Ponomarenko, V. I. Stafeev, and Y. M. Logunenko, in *Abstracts of 10th International Opt.–Electron. Congress* (Germany, 1991), p. 137.

14. I. S. Virt, Izv. Vyssh. Uchebn. Zaved., Fiz., No. 41, 117 (1998).

15. L. A. Bovina, V. I. Stafeev, K. O. Boltar', *et al.*, Prikl. Fiz., No. 3, 41 (1999).

16. L. A. Bovina, K. O. Boltar, V. I. Stafeev, *et al.*, Proc. SPIE **3819**, 73 (1999).

17. P. A. Bakhtin, S. A. Dvoretskiĭ, V. S. Varavin, *et al.*, in *Abstracts of Meeting on Actual Problems in Semiconductor Photoelectronics* (Novosibirsk, 2003), p. 52.

18. V. M. Akimov, K. O. Boltar', I. D. Burlakov, *et al.*, Prikl. Fiz., No. 2, 83 (2003).

19. V. M. Akimov, K. O. Boltar', E. A. Klimanov, *et al.*, Prikl. Fiz., No. 2, 80 (2003).

20. L. A. Bovina, K. O. Boltar', I. D. Burlakov, *et al.*, Opt. Zh. **63** (6), 74 (1996) [J. Opt. Technol. **63**, 478 (1996)].

21. K. O. Boltar', N. I. Yakovleva, S. V. Golovin, *et al.*, Prikl. Fiz., No. 5, 95 (2003).

22. L. A. Bovina, I. D. Burlakov, Yu. K. Il'in, *et al.*, Opt. Zh. **63** (6), 62 (1996) [J. Opt. Technol. **63**, 466 (1996)].

23. L. A. Bovina, I. D. Bourlakov, V. I. Ivanov, *et al.*, Proc. SPIE **3819**, 2 (1999).

24. K. O. Boltar', L. A. Bovina, L. D. Saginov, *et al.*, Prikl. Fiz., No. 2, 50 (1999).

Translated by D. Mashovets

PHYSICS OF SEMICONDUCTOR DEVICES

Structural Mechanisms of Optimization of the Photoelectric Properties of CdS/CdTe Thin-Film Heterostructures

G. S. Khrypunov

Kharkov Polytechnical Institute (National Technical University), Kharkov, 61002 Ukraine
e-mail: khrip@ukr.net
Submitted January 24, 2005; accepted for publication February 3, 2005

Abstract—Comparative studies of the effect of chloride treatment of CdS/CdTe thin-film heterostructures on the output characteristics of ITO/CdS/CdTe/Cu/Au solar cells and the crystal structure of their base CdTe layer are carried out. Structural mechanisms determining variation in the efficiency of photoelectric processes in ITO/CdS/CdTe/Cu/Au thin-film solar cells produced by varying the thickness of the $CdCl_2$ layer during the chloride treatment are suggested. It is shown for the first time by X-ray diffractometry that the metastable hexagonal CdTe phase transforms into a stable cubic modification during the chloride treatment. This circumstance provides a substantial improvement in the photoelectric properties of CdS/CdTe thin-film heterostructures. © 2005 Pleiades Publishing, Inc.

1. INTRODUCTION

The potential to solve energy-related environmental problems lies in the wide-scale use of environmentally clean ground-based renewable energy sources, specifically, photoelectric converters of solar radiation [1]. Currently, the efficiency of the best laboratory samples of CdS/CdTe thin-film solar cells approaches the efficiency of conventional solar cells based on single-crystal Si [2]. However, thin-film solar cells are more economical due to their low material and energy cost [3].

From the point of view of solid-state physics, CdS/CdTe-based solar cells are new objects, specifically, multilayer polycrystalline thin-film heterostructures. Due to the developed grain-boundary surface of the base CdTe layer and the high temperatures required to obtain such device structures, phase interaction significantly affects the solar cell efficiency [3]. Chloride treatment is an obligatory technological operation in the fabrication of high-efficiency CdS/CdTe-based thin-film solar cells [2]. This treatment increases the solar cell efficiency by a factor of 5–6 due to the phase interaction of the base layer with $CdCl_2$ [2]. One of the main causes of an increase in solar cell efficiency is an increase in the minority-carrier lifetime [4]. This increase is usually attributed to the experimentally identified decrease in the degree of development and inhibition of the grain-boundary surface of the CdTe layer [5, 6]. However, the structural variations inside the grains have not been analyzed in sufficient detail. This circumstance has impeded further optimization of the design and technology for CdS/CdTe-based thin-film solar cells [2]. Thus, study of the structural mechanisms of optimization of the photoelectric properties of CdS/CdTe thin-film heterostructures during chloride treatment solves a concrete applied problem. At the same time, such studies are of interest for physical materials science of a new class of solid objects.

2. EXPERIMENTAL

In order to obtain laboratory samples of ITO/CdS/CdTe/Cu/Au solar cells, 0.4-μm-thick CdS films were deposited by thermal evaporation at 200°C on glass substrates with a preliminarily deposited 0.5-μm-thick ITO (indium–tin oxide) layer. Then, 4-μm-thick CdTe films were deposited without a vacuum break at a substrate temperature of 300°C. After that, the chloride treatment of the base layers was carried out. For this purpose, $CdCl_2$ films were deposited by thermal evaporation in a vacuum chamber on the surface of the CdTe layer without heating the substrate. The obtained ITO/CdS/CdTe/$CdCl_2$ heterostructures were thermally treated in air in a closed volume at 430°C for 25 min. Then, the annealed heterostructures were etched in a bromomethanol solution to remove the by-products of the phase interaction, and two-layer Cu–Au contacts were formed by thermal evaporation on the CdTe surface.

The efficiency (η) and output parameters of the solar cells, specifically, the open-circuit voltage U_{oc}, the density of the short-circuit current I_{sc}, and the filling factor (FF) of the current–voltage (I–V) characteristics under illumination, were determined from the I–V characteristic under illumination at a luminous flux density of 100 W/cm^2.

In order to reveal the specific structural features of the CdTe base layers prior to and after the chloride treatment, we used the following complex of procedures for detecting and recording the diffraction spectra [7, 8]:

(i) The diffraction spectrum was automatically recorded under continuous 2θ scanning in the angle range 2θ = 20°–120° using Bragg–Brentano focusing of radiation from a copper anode. During such recording, the diffraction pattern is formed by the grains with reflection planes [*hkl*] parallel to the sample surface.

(ii) The diffraction reflections from the planes of the sphalerite and wurtzite modifications of CdTe, which are not revealed by the above detection method due to the fact that such samples are textured, were detected and point-by-point recorded in radiation from an iron anode by the method of θ/2θ scanning according to the procedure of so-called skew recording. For this purpose, a sample was rotated relative to its initial position by the corresponding angle between the plane that formed the most intense diffraction peak under the Bragg–Brentano focusing and the specified plane. The use of softer X-ray radiation allowed us to increase the angle spacing between the diffraction peaks.

(iii) The point-by-point recording of the profiles of the diffraction peaks was carried out by the method of ω scanning in order to determine the degree of texture scattering, which is expressed in terms of the half-width of the diffraction profile (in arc degrees) in the ω curve.

The precise determination of the lattice period was carried out using the extrapolation function $(\cos^2\theta/\sin\theta) + (\cos^2\theta/\theta)$ [9].

3. RESULTS AND DISCUSSION

We measured the *I–V* characteristics exhibited under illumination for the ITO/CdS/CdTe/Cu/Au solar cells obtained using CdCl$_2$ layers of various thicknesses (Fig. 1). Three characteristic intervals can be separately identified in the dependences of the output characteristics and efficiency on the thickness of the CdCl$_2$ layer. An increase in the thickness of the CdCl$_2$ layer up to 0.06 μm leads to an increase in the solar cell efficiency from η = 1.1% to η = 7.4% (Fig. 1, curves *1*, *2*). This increase in the efficiency is equally governed by an increase in all the output parameters. As the thickness of the CdCl$_2$ layer increases from 0.06 to 0.35 μm, the solar cell efficiency increases from η = 7.4% to η = 10.3% due to an increase in the open-circuit voltage and filling factor of the *I–V* characteristic under illumination (Fig. 1, curves *2*, *3*). A further increase in the CdCl$_2$ layer thickness from 0.35 to 1.20 μm leads to a decrease in the solar cell efficiency from 10.3 to 5.4%, which is caused by a decrease in the filling factor of the *I–V* characteristic under illumination (Fig. 1, curves *3*, *4*).

Two diffraction maxima are revealed at the angles 2θ = 23.56° and 2θ = 75.92° in the X-ray diffraction pattern of the ITO/CdS/CdTe heterostructure without the chloride treatment, which was recorded using Bragg–Brentano focusing (Fig. 2a). According to ASTM File no. 15-0770, these reflections can be identified with those from the (111) and (333) planes of cubic CdTe, which indicates that the base layer is tex-
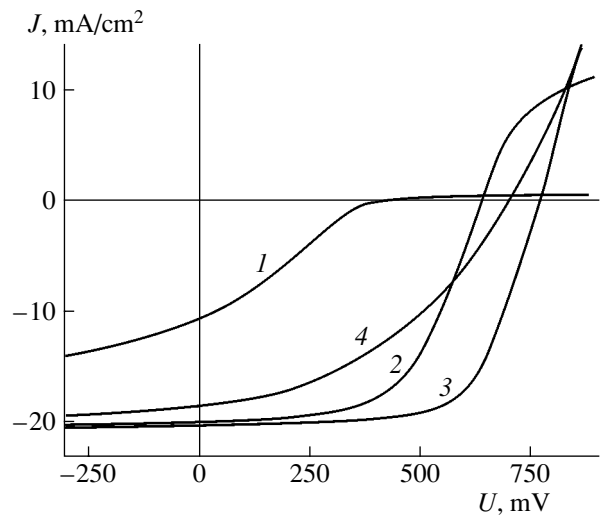

Fig. 1. *I–V* characteristics exhibited under illumination for ITO/CdS/CdTe/Cu/Au solar cells in relation to the thickness of the CdCl$_2$ layer. (*1*) No CdCl$_2$ layer: U_{oc} = 400 mV, J_{sc} = 10.7 mA/cm^2, FF = 0.280, and η = 1.19%; (*2*) the CdCl$_2$ layer is 0.06 μm thick: U_{oc} = 645 mV, J_{sc} = 19.0 mA/cm^2, FF = 0.576, and η = 7.4%; (*3*) the CdCl$_2$ layer is 0.35 μm thick: U_{oc} = 773 mV, J_{sc} = 20.1 mA/cm^2, FF = 0.670, and η = 10.3%; and (*4*) the CdCl$_2$ layer is 1.20 μm thick: U_{oc} = 702 mV, J_{sc} = 19.0 mA/cm^2, FF = 0.414, and η = 5.5%.

tured. The texture axis is the [111] direction, and the degree of texture scattering is 10°. Since we failed to reveal reflection from the CdS layer in the X-ray diffraction pattern of the ITO/CdS/CdTe heterostructure, we also recorded the X-ray diffraction pattern of an ITO/CdS heterostructure. It was found that these CdS films, which belong to a hexagonal crystal system, are textured along the [0002] direction. The application of scanning microscopy to a transverse cleaved surface of the ITO/CdS/CdTe device heterostructure showed that the CdTe and CdS layers are columnar and that the grain size for CdTe is governed by the grain size for CdS. Thus, the emergence of texture in the base layers is governed by oriented growth of CdTe on the textured CdS layers. According to [1], the columnar structure of the base layers provides a substantial decrease in the deleterious effect of the grain-boundary surface on photoelectric processes. However, the ITO/CdS/CdTe/Cu/Au solar cells that were not subjected to the chloride treatment had η of about 1% (Fig. 1, curve *1*).

The data of ASTM File no. 19-0193 show that the reflections revealed by the structural analysis of the ITO/CdS/CdTe heterostructures can also be identified with those from the (002) and (006) planes of metastable hexagonal CdTe. In this case, the texture axis for the base layer is the [0001] direction. In order to resolve the problem of which of the two modifications occurs in the sample under study, we carried out skew recordings. It was found that an attempt to introduce the (105) plane
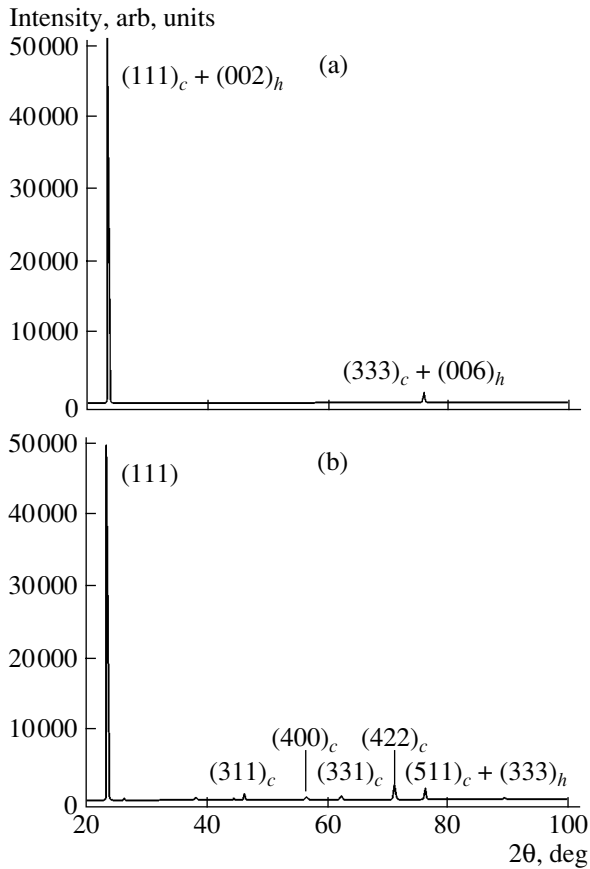
Fig. 2. X-ray diffraction patterns of ITO/CdS/CdTe hetero-structures exposed to radiation from a copper anode with Bragg–Brentano focusing (a) prior to the chloride treatment and (b) after the chloride treatment with the use of a CdCl$_2$ layer 0.06 μm thick.

Fig. 3. X-ray diffraction patterns of ITO/CdS/CdTe hetero-structures exposed to radiation from an iron anode after sample rotation by 22° (a) prior to the chloride treatment, and (b) after the chloride treatment with the use of a CdCl$_2$ layer 0.06 μm thick.

of the hexagonal modification into the reflecting position also introduces the (331) and (422) planes of the cubic modification into this position (Fig. 3a). This circumstance is associated with the fact that the angles between the (002) and (105) planes of the hexagonal modification and the angles between the (111) and (331) planes and the (111) and (422) planes of the cubic modification differ only slightly. Their magnitudes are 20.7°, 22.0°, and 19.5°, respectively. Thus, in the initial state, the CdTe base layer is two-phase, and the solar cell efficiency is low. A two-phase state, twinning, and a high density of stacking faults are characteristic of CdTe films (see, for example, [9]) because of the insignificant (about 1% [10]) difference between the energies at which the cubic and hexagonal crystal lattices are formed and the low energy at which stacking faults are formed.

Using the method of skew recording, we showed that the chloride treatment of the CdTe films when the thickness of the CdCl$_2$ layer was equal to 0.06 μm leads to the formation of single-phase layers with a stable cubic modification (Fig. 3b). We observed a decrease in the width of the diffraction peaks for reflections from
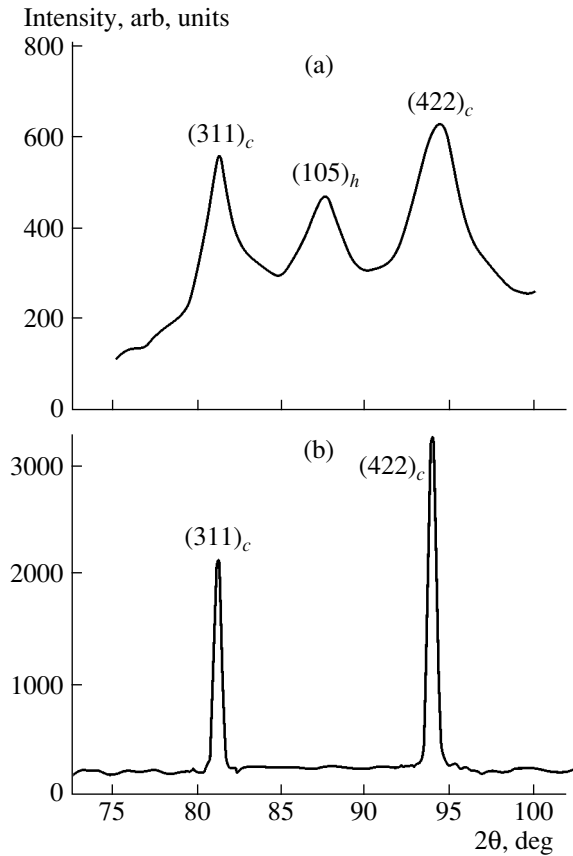
the (331) and (422) planes. This result qualitatively demonstrates that, along with a decrease in microstrain and an increase in the coherent scattering region, the density of stacking faults also decreases. The sensitivity of these lines to stacking faults is associated with the fact that $|h + k + l| = 3N \pm 1$ for them.

The reflections from planes (331), (400), (331), (422), and (511) + (333) of the cubic modification are revealed in the X-ray diffraction pattern, recorded using Bragg–Brentano focusing, of the CdS/CdTe heterostructure with a CdCl$_2$ layer 0.06 μm thick and subjected to chloride treatment (Fig. 2b). This observation indicates that the texturization of the base layer decreases. The degree of texture scattering is 5° (Fig. 3b). The experimentally observed decrease in the degree of texture scattering from 10° to 5°, despite a decrease in the structure quality, is associated with the fact that a texture of only one type is formed in the base CdTe layer after the chloride treatment, specifically, in the [111] direction.

We found that an increase in the thickness of the CdCl$_2$ layer from 0.06 to 0.35 μm leads to an increase

in the degree of texture scattering to 9.3°. The angular width of the (331) and (422) reflections decreases, which suggests a further decrease in the microstrain and density of stacking faults and to an increase in the sizes of the coherent scattering region. We also observed a decrease in the lattice constant of CdTe from $a = 6.494$ Å to $a = 6.488$ Å. According to ASTM File no. 15-0770, the lattice constant of strain-free CdTe layers of high structural quality is 6.481 Å. Therefore, the base CdTe layers subjected to chloride treatment with the use of a $CdCl_2$ layer 0.35 μm thick exhibit less lattice strain than when a $CdCl_2$ layer 0.06 μm thick is used. The experimentally observed lattice constant of the CdTe layer is larger than its theoretical value. This circumstance can be attributed to a difference of 9.7% between the lattice constants of the CdS and CdTe layers [11]. Due to this difference, an oriented CdTe layer grown on a CdS layer is strained. The strain causes an increase in the lattice parameter of the base layer.

According to the phase diagram of the $CdTe$–$CdCl_2$ system, the Cl atoms possess subatomic solubility in CdTe at the chloride treatment temperatures [12]. Therefore, after the chloride treatment, Cl is experimentally observed on the grain surface of the base layer rather than in the grain bulk [13]. The physical mechanism by which Cl causes structural variations in the CdTe layers relies on the formation of CdO and $TeCl_2$ compounds on the grain-boundary surface of the base layer in the course of annealing in air [14]. Since $TeCl_2$ is a gas under the annealing temperatures used, its presence leads to an increase in mobility of the Cd and Te atoms. This increased mobility leads to nucleation in the spacings between the CdTe grains [15]. It is evident that the nuclei are formed in the intergrain spacings near which the Cl content necessary for the above-mentioned structural transformations of CdTe is required. Therefore, CdTe starts to recrystallize from the surface [16]. This phenomenon causes the experimentally observed decrease in the texturization of the CdTe base layers after the chloride treatment. Since the base layer grows on the CdTe layer during recrystallization, this circumstance causes a decrease in the lattice strain and, correspondingly, lowers the lattice period. Such recrystallization also causes a decrease in the stacking fault and twin density and an increase in the sizes of the coherent scattering region, which leads to the experimentally observed decrease in the width of the diffraction maxima corresponding to the (331) and (422) planes of cubic CdTe (Fig. 3b).

As the thickness of the $CdCl_2$ layer is further increased from 0.35 to 1.20 μm, the lattice constant increases from $a = 6.488$ to 6.494 Å. This increase is accompanied by a decrease in the degree of texture scattering from 9.3° to 8.2°, while the angular width of reflections (331) and (422) increases. It has been shown that the Cl atoms are segregated on the CdS/CdTe interface if the $CdCl_2$ layer is excessively thick [17]. Therefore, nucleation can also start near this interface and not just in the bulk during recrystallization of the base layer in this case. As a result, there is an increase in the orienting effect of CdS on the crystal structure of the CdTe layer. We experimentally revealed the crystal lattice strain of the base layer, which leads to an increase in the lattice constant. The probability of emergence of stacking faults and twins in the base layer also increases. An increase in their concentration in the base layer causes the observed increase in the width of the diffraction peaks that correspond to the (331) and (422) planes of cubic CdTe.

4. CONCLUSIONS

As the thickness of the $CdCl_2$ layer increases to 0.06 μm, transformation of the two-phase CdTe base layer to a single-phase one exerts a determining effect on the intensification of the photoelectric properties of CdS/CdTe thin-film heterostructures. Metastable hexagonal CdTe transforms into a stable cubic phase.

A further increase in the thickness of the $CdCl_2$ layer to 0.35 μm leads to optimization of the photoelectric properties of CdS/CdTe heterostructures due to a decrease in the crystal-lattice strain, a decrease in the stacking fault and twin concentration, and an increase in the sizes of the coherent scattering regions of the base layer. This behavior is caused by the specific features of recrystallization of CdTe during chloride treatment, which leads to a decrease in the orienting effect of the CdS layer on the crystal structure of CdTe.

Excess thickness of the $CdCl_2$ layer (above 0.35 μm) causes a decrease in the efficiency of the photoelectric processes in the CdTe layer. This decrease is caused by the fact that, as the Cl content at the CdS/CdTe interface increases, cubic CdTe can nucleate near the CdTe surface. Due to this circumstance, during rectystallization of the base layer, the orienting effect of CdS on the crystal structure of the base layer is enhanced.

REFERENCES

1. M. A. Green, Prog. Photovoltaics **9**, 123 (2001).
2. X. Wu, J. C. Keane, R. G. Dhere, *et al.*, in *Proceedings of 17th European Photovoltaic Solar Energy Conference* (Munich, Germany, 2001), p. 995.
3. K. Durose, P. R. Edwards, and D. P. Halliday, J. Cryst. Growth **197**, 733 (1999).
4. H. R. Moutinho, F. S. Hasoon, F. Abulfotuh, and L. L. Kazmerski, J. Vac. Sci. Technol. **13**, 2877 (1995).
5. B. E. McCandless, Mater. Res. Soc. Symp. Proc. **668**, H1.6.1 (2001).
6. P. R. Edwards, S. A. Galloway, and K. Durose, Thin Solid Films **372**, 385 (2000).
7. A. Taylor and H. Sinclair, Proc. Phys. Soc. London **57**, 126 (1945).
8. P. A. Panchekha, O. G. Alaverdova, and V. I. Gnidash, Ukr. Fiz. Zh. **45** (1), 75 (2000).
9. P. A. Panchekha, Funct. Mater. **4**, 199 (1997).

10. I. P. Kalinkin, V. V. Alekseevskiǐ, and A. I. Simash-kevich, *Epitaxial Films of the II–VI Compounds* (Leningr. Gos. Univ., Leningrad, 1978), p. 54 [in Russian].

11. R. H. Bube, *Properties of Semiconductor Materials: Photovoltaic Materials* (Imperial College Press, USA, 1999), Vol. 1, p. 136.

12. G. S. Oleinik, P. A. Mizetskii, and T. P. Nuzhnaya, Inorg. Mater. **22**, 164 (1986).

13. M. Terheggen, H. Heinrich, G. Kostorz, *et al.*, in *Proceedings of EMRS Spring Meeting* (Strasburg, France, 2002), B-X4.

14. B. E. McCandless, Mater. Res. Soc. (Warrendale, PA, 2001), H1.6.1.

15. H. R. Moutinho, M. M. Al-Jassim, F. A. Abulfotuh, *et al.*, in *Proceedings of 6th IEEE Photovoltaic Specialist Conference* (Anaheim, USA, 1997), p. 431.

16. A. Romeo, A. N. Tiwari, and H. Zogg, in *Proceedings of 2nd World Conference and Exhibition on Photovoltaic Solar Energy Conversion* (Vienna, 1997), p. 1105.

17. M. Terheggen, H. Heinrich, G. Kostorz, *et al.*, in *Proceedings of 17th European Photovoltaic Solar Energy Conference* (Munich, Germany, 2001), p. 1188.

Translated by N. Korovin

PHYSICS OF SEMICONDUCTOR DEVICES

Electroluminescent Properties of Strained *p*-Si LEDs

N. A. Sobolev*^, A. M. Emel'yanov*, E. I. Shek*, O. V. Feklisova**, and E. B. Yakimov**

*Ioffe Physicotechnical Institute, Russian Academy of Sciences, St. Petersburg, 194021 Russia
^e-mail: nick@sobolev.ioffe.rssi.ru
***Institute of Microelectronics Technology and High Purity Materials, Russian Academy of Sciences,
Chernogolovka, 142432 Russia*

Submitted February 21, 2005; accepted for publication March 14, 2005

Abstract—Electroluminescence (EL) in the range 1.0–1.65 μm from LEDs strained by four-point bending at 700°C has been studied at currents up to 400 mA. The LEDs are fabricated by implantation of B and P ions into *p*-Si wafers grown by the floating-zone (*FZ*-Si) and Czochralski (*Cz*-Si) methods followed by annealing at 700 and 1100°C. The intensity of dislocation-related EL is higher in the *FZ*-Si than in the *Cz*-Si samples. It is also higher in the samples subjected to low-temperature post-implantation annealing than in those that underwent the same annealing at a high-temperature. The current-related transformation of the *FZ*-Si EL spectra is described well by eight Gaussian lines. The peak positions are 1.22, 1.244, 1.26, 1.316, 1.38, 1.42, 1.52 and 1.544 μm, and they are independent of current. Dependences of the integral intensity and line width on current are studied. © 2005 Pleiades Publishing, Inc.

1. INTRODUCTION

The needs of modern optoelectronics have stimulated the development of silicon-based LEDs, which has, in turn, increased the intensity at which this problem is being studied [1]. A promising approach is the development of LEDs based on single-crystal Si with dislocation-related electroluminescence (EL). Until recently, the EL quantum efficiency of such structures was about 10^{-3}% [2, 3]. In 2004, LEDs with an external quantum efficiency of dislocation-related EL equal to ~0.1% were reported [4]. Hopes for a further rise in quantum efficiency are based on the fact that the EL mechanism has not been thoroughly studied and on the great variety of fabrication methods used in the production of LEDS with dislocation-related EL, namely, uniaxial compression [2, 4], bending deformation [5], laser recrystallization [3], and implantation of rare-earth ions combined with high-temperature annealing of Si supersaturated with intrinsic point defects [6, 7]. The overwhelming majority of studies concern dislocation-related photoluminescence (PL). This approach significantly restricts the information that can be obtained; in particular, it limits the possibility of studying the effect of excitation levels on luminescence spectra. In [5], to reveal the specific features of PL spectral lines related to bending deformation, a variety of initial samples were studied, including different orientations of wafers, types of dopants, concentrations of oxygen, and conditions of deformation and subsequent annealing. In our earlier study [8], virtually identical EL spectral lines were observed for LEDs fabricated by implantation of B and P ions into (100) *n*-Si grown using the floating-zone method (*n-FZ*-Si) and strained according to the four-point bending method. The goal of the present study was to investigate the effect of deformation on the EL of LEDs formed in *p*-Si by ion implantation and subsequent annealing.

2. EXPERIMENTAL

In order to produce n^+–p junctions, phosphorus ions with an energy $E = 75$ keV were implanted into (100) *p*-Si wafers at a dose $\Phi = 1 \times 10^{15}$ cm^{-2}. The Czochralski-grown (*Cz*-Si) samples to be studied had a resistivity $\rho = 15$ Ω cm and thickness of 400 μm (sample series *5*). The *FZ*-Si samples had $\rho = 100$ Ω cm and a thickness of 310 μm (sample series *10*). Ohmic contacts were produced by implantation of B ions ($E = 40$ keV and $\Phi = 1 \times 10^{15}$ cm^{-2}) into the back of the wafers. Isochronous (20 min) post-implantation annealing treatments were performed in an Ar atmosphere at temperatures of 700 or 1100°C. Extended rodlike {311} structural defects, Franck's loops, and perfect prismatic dislocation loops were found in the samples annealed at the lower temperature of 700°C (sample nos. 5-700 and 10-700), but were not observed in the samples annealed at the higher temperature of 1100°C (sample nos. 5-1100 and 10-1100) [9]. In order to introduce dislocations, rectangular samples ~4 × 15 mm^2 in size were deformed by four-point bending at a load of 3.5 kg/mm^2 for 30 min at 700°C in a setup including a sapphire sample holder. The surface with the n^+–p junction was stretched. The dislocation density after the deformation attained values up to ~10^6 cm^{-2}. LEDs with a mesa-type edge configuration were fabricated using standard technology, with Al deposited onto both sides of the samples. The diameter of the n^+–p junctions was 0.8 mm.
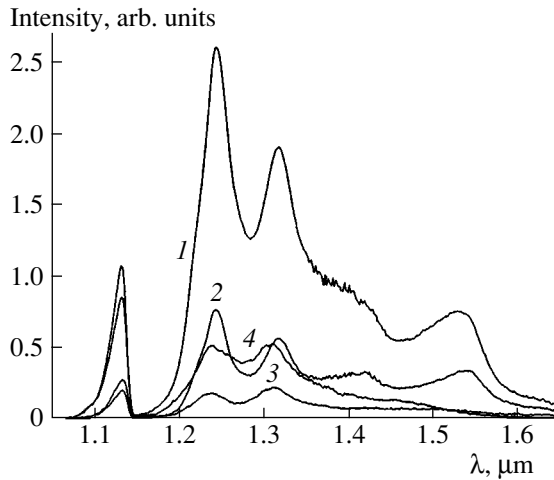
Fig. 1. EL spectra of sample nos. (*1*) 10-700, (*2*) 10-1100, (*3*) 5-1100, and (*4*) 5-700 measured at a current of 200 mA.

Fig. 2. EL spectra of LED no. 10-700. Current: (*1*) 10, (*2*) 40, (*3*) 80, (*4*) 200, and (*5*) 400 mA.

In all the samples, EL was studied under the maximum deformation at 80 K and amplitudes of forward current pulses up to 400 mA. The pulse width was 1−5 ms, and the repetition rate, 33 Hz. EL spectra were recorded in the range 1.0–1.65 μm using an MDR-23 monochromator with a 7-nm resolution, an InGaAs photodetector, and a lock-in nanovolmeter. All the spectral characteristics presented below are corrected for the spectral response of the detector and the whole optical path.

3. RESULTS AND DISCUSSION

Figure 1 shows spectra of all the samples under study at a current of 200 mA. In all the samples, dislocation-related EL was observed in the range 1.2–1.6 μm. The intensity of dislocation-related EL in the *FZ*-Si LEDs was higher than in the identically fabricated *Cz*-Si ones. A similar result was observed for the intensity of dislocation-related PL in the strained *p*-type *FZ*-Si and *Cz*-Si wafers [10] and for the intensity of dislocation-related EL in the strained *n*-type *FZ*-Si and *Cz*-Si LEDs [8]. The intensity of dislocation-related EL in the LEDs annealed at the above-specified lower temperature and containing extended structural defects (sample nos. 5-700 and 10-700) was higher than in the LEDs annealed at the higher temperature and free of extended structural defects (nos. 5-1100 and 10-1100). A similar effect of the temperature of post-implantation annealing on the intensity of dislocation-related EL has been observed for *n*-type *FZ*-Si and *Cz*-Si LEDs [8].

Figure 2 shows the EL spectra for sample no. 10-700, which were recorded at different driving currents. At low currents, the well-known dislocation-related EL lines *D*1, *D*2, *D*3, and *D*4 are dominant (their positions are marked by vertical dotted lines). Edge luminescence peaks can be seen at currents ≥40 mA. As the current increases, the *D*1 and *D*2 lines are asymmetrically
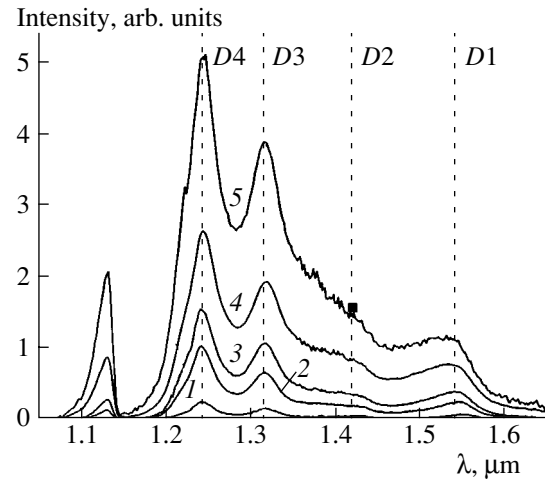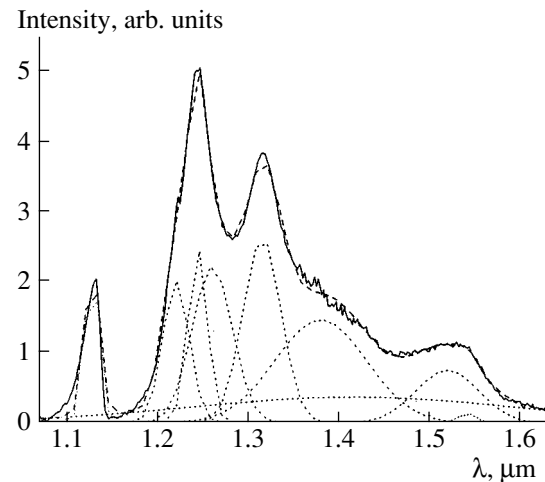

Fig. 3. Decomposition of the EL spectrum of sample no. 10-700 at a current of 400 mA. The solid line indicates the experiment; the dotted lines, Gaussian curves; and the dashed line, the overall approximating curve. Peak positions are listed in the text.

broadened. Similar transformations of the spectra of dislocation-related PL are usually attributed to the appearance of additional luminescence lines [5]. The current-induced transformation of EL spectra is described well by decomposition of the spectrum into eight Gaussian lines. The corresponding peak positions, 1.22, 1.244, 1.26, 1.316, 1.38, 1.42, 1.52 and 1.544 μm, were obtained in [8]. Figure 3 shows an example of such decomposition of the dislocation-related EL spectrum for sample no. 10-700 at 400 mA. Figures 4 and 5 show current dependences of the EL integral intensity *A* and FWHM for each line in the case of LED no. 10-700. The integral intensity was calculated as the product of the peak intensity and FWHM.
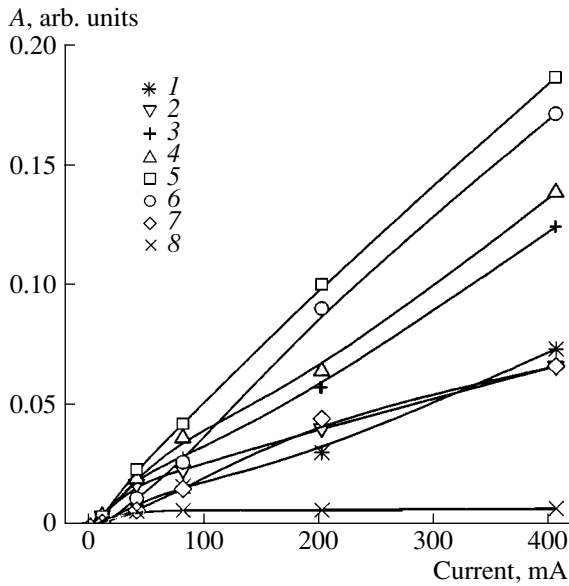
Fig. 4. Current dependences of the integral EL intensity for the Gaussian lines at (*1*) 1.22, (*2*) 1.244, (*3*) 1.26, (*4*) 1.316, (*5*) 1.38, (*6*) 1.42, (*7*) 1.52, and (*8*) 1.544 μm. Sample no. 10-700.

Fig. 5. Current dependences of the FWHM of the Gaussian lines at (*1*) 1.22, (*2*) 1.244, (*3*) 1.26, (*4*) 1.316, (*5*) 1.38, (*6*) 1.52, (*7*) 1.542, and (*8*) 1.42 μm. Sample no. 10-700.

Similar behavior is observed for *p-FZ*-Si LED no. 10-1100, which was annealed at the higher temperature: as the current increases, the *D*1 and *D*2 lines are asymmetrically broadened, and the current-induced transformation of the EL spectra can be described by eight Gaussian curves with current-independent peak positions, which coincide with those listed above for LED no. 10-700. It is noteworthy that all the listed lines, with the exception of those at 1.22 and 1.26 μm, were observed in the PL spectra of strained samples in [5]. The peak positions coincide within experimental accuracy in spite of significant differences in the sample technology, luminescence excitation mode, and temperature of PL observation. In order to obtain the complete set of PL lines in [5], it was necessary to fabricate several samples under different conditions, whereas each of our *FZ*-Si samples demonstrates all the lines.

The obtained data on current dependences of the integral intensity and FWHM in LEDs belonging to the no. 10 series, based on *p-FZ*-Si, can be compared with the *n-FZ*-Si LED we studied earlier [8]. In this sample, the 1.38-μm line with a FWHM ≈ (40–90) nm was dominant, while the second largest in intensity was the 1.52-μm line with a FWHM ≈ (65–85) nm. Two more lines should be mentioned: the 1.42 μm line with a FWHM ≈ (30–50) nm and the 1.542-μm line with a FWHM ≈ 20 nm. In *p-FZ*-Si LED no. 10-700, the line at 1.38 μm also dominates and has virtually the same FWHM (see Figs. 4 and 5). However, at a high current, the second largest in intensity is the line at 1.42 μm, which demonstrates significant broadening (FWHM ≈ 365 nm). The FWHMs for the 1.52- and 1.544-μm lines virtually coincide for the *n*- and *p-FZ*-Si LEDs. The
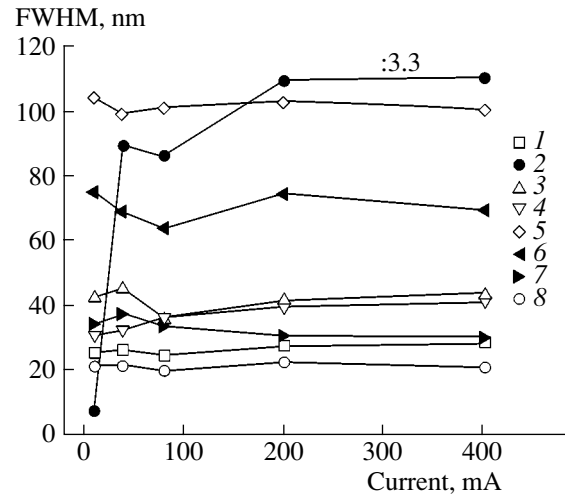
1.38-μm line, with nearly the same FWHM, also dominates in *p-FZ*-Si LED no. 10-1100 (corresponding figures are not presented here). The second largest in intensity at a high current is the line at 1.544 μm, but it is significantly broadened (FWHM ≈ 118 nm). The two above-mentioned 1.52- and 1.42-μm lines are characterized by FWHM values that remain nearly the same as in the *n-FZ*-Si LED. We believe that the observed broadening of the 1.42- and 1.544-μm lines can be attributed to differences in the spectra of the structural defects and electrically active centers formed in LEDs as a result of interaction between growth-, implantation-, and deformation-induced defects and impurity atoms contained in the initial Si or entering it during the thermal treatment. Changes in the charge state of the existing centers can also make a considerable contribution. In the spectra of the *p-Cz*-Si LEDs annealed at both the temperatures applied in our study and strained, the *D*3 and *D*4 peaks, which are observed against the background of a broad EL band, dominate (see Fig. 1). Unambiguous decomposition of this band into peaks was not achieved. We believe that the formation of the broad band can be attributed to an effect produced by the high concentration of oxygen atoms in *Cz*-Si, as broadened dislocation-related PL lines have previously been observed in *Cz*-Si with a high concentration of oxygen [5, 10].

4. CONCLUSION

Under study were the spectra of dislocation-related EL in LEDs fabricated by ion implantation on *p-FZ*-Si and *p-Cz*-Si and subjected to four-point bending. The effect of the method of Si growth, temperature of post-implantation annealing, and current in the diode on the intensity of dislocation-related EL was revealed. The well-known dislocation-related spectral lines *D*1–*D*4

dominate in *FZ*-Si LEDs at low currents. As the current increases, the *D*1 and *D*2 lines broaden.

The transformation of EL spectra under the effect of current is reasonably well described using eight Gaussian lines with current-independent peak positions. The dependences of the EL integral intensity and line width on the current have been studied.

REFERENCES

1. L. Pavesi, J. Phys.: Condens. Matter **15**, R1169 (2003).
2. V. V. Kveder, E. A. Steinman, S. A. Shevchenko, and H. G. Grimmeiss, Phys. Rev. B **51**, 10520 (1995).
3. E. O. Sveinbjornsson and J. Weber, Appl. Phys. Lett. **69**, 2686 (1996).
4. V. Kveder, V. Badylevich, E. Steinman, *et al.*, Appl. Phys. Lett. **84**, 2106 (2004).
5. S. Pizzini, E. Leonti, S. Binetti, *et al.*, Solid State Phenom. **95–96**, 273 (2004).
6. N. A. Sobolev, O. B. Gusev, E. I. Shek, *et al.*, Appl. Phys. Lett. **72**, 3326 (1998).
7. A. M. Emel'yanov and E. I. Shek, Fiz. Tverd. Tela (St. Petersburg) **46**, 1751 (2004) [Phys. Solid State **46**, 1810 (2004)].
8. N. A. Sobolev, A. M. Emel'yanov, E. I. Shek, *et al.*, Phys. Status Solidi C, No. 6, 1842 (2005).
9. N. A. Sobolev, A. M. Emel'yanov, E. I. Shek, and V. I. Vdovin, Physica B (Amsterdam) **340–342**, 1031 (2003).
10. M. Acciari, S. Binetti, O. V. Feklisova, *et al.*, Solid State Phenom. **95–96**, 453 (2004).

Translated by D. Mashovets

================================ **ERRATA** ================================

Erratum: "Interpretation of the Visible Photoluminescence of Inequisized Silicon Nanoparticles Suspended in Ethanol" [*Semiconductors* **39, 884 (2005)**]

V. E. Ogluzdin

The correct title of Section 2 (p. 885) should read A MODEL OF MULTIPHOTON-RELATED INCREASE IN THE TRANSMITTANCE OF A MEDIUM: OBSERVATION OF LUMINESCENCE IN A MEDIUM CONSISTING OF AN ENSEMBLE OF CLASSICAL LORENTZ OSCILLATIONS WITH DIFFERING FREQUENCIES. A RETARDATION OF THE PROPAGATION OF LUMINESCENT EMISSION PHOTONS IN A BROADENED MEDIUM. In this section, in the 11th line from the bottom (left column), multiphonon should read multiphoton. Also, in this page in line 5 from the top (right column), the subscripts j should read subscripts i. In p. 888, line 10 from the bottom (right column), anti-Stokes should read Stokes. In p. 889, line 7 from the bottom (left column), multiphonon should read multiphoton.